Diss. ETH No. 19052

On Radiofrequency Aspects of Magnetic Resonance Imaging at Ultra-High Fields

A dissertation submitted to the
SWISS FEDERAL INSTITUTE OF TECHNOLOGY
ZURICH

for the degree of
Doctor of Sciences

presented by
DAVID OTTO BRUNNER
Dipl. Phys. ETH
born March 23, 1980
citizen of Lyss BE

accepted on the recommendation of
Prof. Dr. Klaas P. Prüssmann, examiner
Prof. Dr. Andrew G. Webb, co-examiner
Prof. Dr. John M. Pauly, co-examiner

2010

Contents

Summary

Since the very early days of nuclear magnetic resonance (NMR) there was a continuous trend towards higher main magnetic field strengths. This development is mainly driven by the higher signal to noise ratio gained from the higher nuclear magnetization present in thermal equilibrium. In many applications, there is even a gain in specificity on top of the increased baseline signal levels such as for instance stemming from higher spectral line separation from chemical shifts or weakly coupled spin systems, higher contrast ratios as found in functional imaging applications relying blood oxygenation level dependent signal changes, different relations between relaxation times and spin exchange processes and many more. In the past, the main technical difficulties to overcome for increasing the field strength were inflicted by the necessity to establish a very high and in the meantime very uniform and stable static magnetic field over the volume of interest. Also the correction of susceptibility induced inhomogeneities in the main field was at the core of this development. Current superconductive magnets and elaborate correction systems and routines allow the main field to reach up to 21 T in commercial high resolution spectrometers. In the field of human medical magnetic resonance imaging (MRI) systems up to 4 T are nowadays in wide routine use. However, with upcoming human whole body systems with field strengths of 7 T and beyond the focus of the technical difficulties shifted to radiofrequency (RF) interaction between the nuclear magnetization and the probe. While all previously existing NMR and MRI systems worked within an electrodynamic regime, where the radiofrequency wavelength is longer than the extent of the sample to be imaged, this relation is drastically altered on the newest generation of human tomography systems. This shortening of the wavelength was shown to cause the RF field to exhibit a major increase in filed nonuniformity over the volume of interest and also makes the construction of RF probes as such more cumbersome as well as their safety assessment. Although there are sequences and pulses that offer an astonishingly high robustness against spatial variations in the induced spin nutation, resolving the RF related problems occurring with ultra-high frequencies are key to many applications of current and future ultra-high field systems.

The subject work explores basic methodology that help to resolve these difficulties by advances in hardware and its validation but also in measurement and pulse design methodology.

In order to manipulate and tailor the RF field within a volume resonator, an 8 channel parallel transmission setup consisting of a passive high power RF splitter with variable phase and amplitude adjustment capability and a transmit receive head coil was built. The head coil was based on 8 decoupled stripline resonators. Problems with cable loading and routing could be reduced by centrally feeding the striplines as it is shown in Chap. 2. Furthermore the axial extent of the field of view reported from such designs could be increased by this approach. The gained stability of the system was essential in order to perform reproducible quantitative parallel transmission experiments. This setup and the experience gained from it provided the basis for the deduction of figures of merits for parallel RF probes in MRI that will allow optimization and comparison of upcoming designs. As described in Chap. 3, these theoretical findings provide further insight into the encoding capabilities of RF arrays and their role in different applications in parallel transmission but also reception.

The methodology developed for the validation and application of RF arrays requires an accurate measurement of the excitation field distribution of each channel in the sample in order to be put into practice. Furthermore, accurate measurements of the RF excitation field provide crucial information for the validation of electromagnetic simulations needed for compliance testing but also for further development and optimization of the probe design principles. Unfortunately transmission arrays and the conditions at ultra-high fields impose both very hard requirements for excitation field measurement techniques. First, the excitation produced by a single element of the array exhibits a very large dynamic range that has to be covered compared to volume resonators. And second, compared to lower field strengths the measurement itself is increasingly hampered by confounding effects induced by higher local off-resonances, longer longitudinal relaxation times and more restrictive power limitations. In order to provide reliable measurements over a larger dynamic range at ultra-high fields a novel mapping technique based on comprehensive signal modeling was introduced. Additionally, an interferometric measurement scheme of the excitation field for transmission arrays is suggested in order to reduce the dynamic range and to increase the power efficiency of any mapping sequence applied. By these two approaches it was possible to acquire consistent calibration data of transmit arrays in comparably short time as demonstrated in Chap. 4.

The analysis of the performance and restrictions imposed by technical limitations and safety of transmit coil arrays leads to the conclusion that these considerations must be explicitly taken into account in applications, especially in the case of parallel (spectral)-spatial pulse design. Pulse design approaches presented so far

made use of the analogies between signal reception and excitation in order to balance between optimal spin nutation fidelity provided by the calculated waveform and the concomitant power consumption. However, these relations break down in the presence of explicit restrictions that represent hard constraints instead of equivalent optimization goals. Therefore, a mathematical framework and the necessary algorithmic solution for the design of such pulses under hard constraints is given in Chap. 5.

In the main, the problems occurring at ultra-high field strengths with RF excitation and devices were found to be related to upcoming wave propagation phenomena. Since this is a very unusual regime for NMR devices, NMR excitation and detection with propagating RF waves could be initially explored. The fact that propagating modes can persist within the bore of a 7 T magnet lead to the idea that RF probes could be constructed, that do not rely at all on near field interactions with the sample. As shown in Chap. 6, an antenna system located at distances of more than a meter can indeed excite and detect NMR signals with reasonable sensitivity compared to an inductive near field detection. As such, this is very astonishing being a very rare feature in NMR detection which usually relies on a very intimate coupling between the nuclear spin and a detecting media. The most common detection scheme of NMR relies indeed on Faraday induction apparent in the probe due to a close mutual coupling of nuclear magnetization to a RF detector. Alternative methods presented so far rely either on direct magnetic coupling to a SQUID or magnetic force detector, or on the spin-orbit coupling to optically active atoms as in atomic magnetometers, which both make a close proximity of the sample and the detection media necessary. The remote detection mediated by propagating RF waves offers in the context of ultra-high field MRI the advantage that a reactive loading of the antenna by the sample is not essential. Avoiding the sample dependence of the load seen by the probe renders the RF system more stable in that respect. Furthermore, placing the feeding structure at a certain distance reduces the risk of strong local tissue heating induced by high electric fields emanating from the feeding structure. This novel approach also frees up valuable space within the magnet bore. The main advantage provided by travelling waves however is expected to be an increase in field uniformity. According to the underlying equations of electromagnetism the fields have to exhibit a curvature corresponding to the wavenumber given by the frequency and dielectric properties of the material. Since both, the amplitude and the phase distribution of the field, can contribute to the total curvature, a variation in the phase can therefore lead to a more uniform distribution in the amplitude. For instance, a propagating plane wave would be very preferential for MRI of electrically very large samples because all curvature of the field is provided by its phase term. Exciting a travelling wave in a MR system could therefore be shown to yield very uniform coverage in the

resulting images over large volumes as long as the longitudinal distribution of the dielectric properties of the sample in the bore was axially tapered smoothly enough.

The novel regime of travelling wave interaction with NMR was found to be exceptional since first, a propagation phase delay can be measured dependent on the axial propagation direction for excitation and detection and second, the NMR signal retrieved is actually linked to the radiation of electromagnetic power. These facts yield prospects of very efficient radiofrequency spatial encoding on the scale of the wavelength. Furthermore, it could be shown that the radiation of the spin ensemble can be directed by induction of gradient moments. These concepts prompt strong analogies to other fields such as laser physics or nonlinear optics that can be further explored. Also the design of waveguide systems and antennas needed for this kind of experiments is very elaborate in microwave, communication and radar technology which could yield valuable input for future applications and improvements of NMR/MRI systems.

The approach of travelling wave NMR/MRI was furthermore shown to be extendable to parallel imaging and transmission approaches analogous to closely coupling arrays. A dielectric filling of the feeding section extending the bore of the magnet was used to allow multiple modes to be distinctively excited and carried to the sample. Although the setup constructed for these experiments is quite bulky, no variable lumped elements had to be used that are commonly a weak spot with respect to high power withstanding capabilities. Besides the successful demonstration of basic applications of parallel transmission and reception such as RF shimming and sensitivity encoded accelerated imaging, it could be experimentally shown, that the encoding capability provided by the radiofrequency fields is directly linked to the number of propagating modes within the feeding section.

In contrast to most traditional RF probe designs, RF devices relying on travelling wave mechanisms for the excitation of NMR have very good prospects for even higher frequencies of operation where the propagative electromagnetic waves become even more prominent. The possibility to design RF devices for NMR that do not necessarily rely on close inductive coupling could open the field for conceptually new classes of RF probes that allow, probably in conjunction with other parallel transmission techniques, for even higher static magnetic field strengths in the future.

Zusammenfassung

Schon seit der Entdeckung der frühesten Nuklearresonanzspektroskopie-Verfahren (NMR) wurde versucht das statische magnetisch Feld zu erhöhen. Diese Entwicklung wird hauptsächlich durch die höhere Signalausbeute getrieben, welche hauptsächlich von einer höheren nuklearen Magnetisierung im thermischen Gleichgewicht herrührt. Bei vielen Anwendungen wird durch das höhere Feld sogar unabhängig vom höheren Signal-zu-Rausch (SNR) Verhältnis die Spezifität erhöht, so z. B. resultiert von chemischen Verschiebungen oder schwach gekoppelten Systemen eine höhere Linienseparation, es wird ein höherer Kontrast gemessen in der funktionellen Magnetresonanz-Bildgebung, welche auf der blutoxygenierungsabhängigen Dephasierung beruht, leichte Verschiebungen der Relaxationszeiten und Raten von Spin-Austausch Prozessen ergeben ein verändertes Kontrastverhalten und eine Menge mehr. Früher wurde der Einsatz höhere Feldstärken hauptsächlich von den technischen Problemen bei der Herstellung eines sehr starken und gleichzeitig sehr homogenen Magnetfeldes gebremst. Mechanismen für die Korrektur von den durch das Objekt selbst induzierten Verzerrungen des Feldes mussten immer weiter verfeinert werden um die Kontrolle bei höheren Feldern zu gewährleisten. Moderne Supraleitertechnologie erlaubt daher heute NMR Messungen mit hoher Güte bei bis zu 21 T in kommerziellen Systemen zu betreiben. In der medizinischen Bildgebung am Menschen werden Felder bis zu 4 T heute routinemässig eingesetzt. Seit jedoch solche Systeme mit Feldstärken von 7 T und mehr betrieben werden, hat sich der Fokus der technischen Probleme auf die Wechselwirkung zwischen dem Detektor und dem Objekt bei sehr hohen Radiofrequenzen (RF) verschoben. Während bei allen anderen NMR-Spektrometern die Wellenlänge der RF-Felder viel länger ist als die Ausdehnung des Objektes, so hat sich dieses Verhältnis in den neuesten ultrahochfeld Tomographen drastisch verschoben. Es wurde sehr schnell festgestellt, dass diese Verkürzung der Wellenlänge zu grossen Varianzen der RF-Felder über das Objekt führt, welches einerseits die Bildgebung behindert und andererseits das Risiko sehr konzertierter und daher potenziell gefährlicher Leistungsdeposition erhöht. Letztlich führen die kurzen Wellenlängen auch dazu, dass die Herstellung verlässlicher Detektoren drastisch erschwert wird. Damit hängt die Nutzbarkeit der gegenwärtig stärksten und in

Zukunft noch grösseren Systemen entscheidend von der Lösung dieser RF Probleme ab.

In dieser Arbeit sollen daher diese Probleme von verschiedener Seite her angegangen werden. Dabei sollen Fortschritte im Bau der Detektoren und deren Sicherheitsvalidierung, aber auch Entwicklungen in der Puls- und Sequenzgestaltung angegangen werden.

Die Entwicklung eines passiven 8-Kanal Sendeaufbaus ermöglichte eine höheres Mass an Kontrolle über die RF-Felder im Objekt. Das System bestand aus einem passiven Leistungsteiler, dessen Ausgänge jeder über individuelle Phasenschieber und Abschwächer verfügten um die Anregung kanalweise zu steuern. Für die Leistungseinkopplung ins Objekt wurde ein Prototyp eines 8-Kanal Volumenresonators gebaut, welcher auf dem Prinzip der Streifenleiter Technologie beruhte (siehe Kapitel 2). Probleme mit der Beladung der Kabelummantelungen in Abhängigkeit der Kabelführung und des variablen Lastwiderstandes des Streifenleiters, welche einen stabilen und reproduzierbaren Betrieb oft verhinderten, konnten mit Hilfe einer zentralen Speisung behoben werden. Durch diese Neuerung konnte auch die longitudinale Abdeckung signifikant erhöht werden im Vergleich zu seitengetriebenen Pendants. Dieser Aufbau erlaube vorallem aufgrund seiner hohen elektronischen Stabilität sehr genaue und reproduzierbare Mehrkanalexperimente. Die Erfahrungen, welche mit diesem Aufbau gesammelt wurden, lieferten die Grundlagen für Gütekriterien von solchen Geräten, welche die Leistungsfähigkeit neuer Konzepte und Vergleiche untereinander zulassen. Wie in Kapitel 3 gezeigt wird, geben diese Kriterien weitere Einsicht in die räumliche Kodierfähigkeit eines Arrays und dessen Rolle in verschiedenen Anwendungen preis.

Es wurde gefolgert, dass die Leistungskriterien, aber auch die unter technischen und sicherheitsrelevanten Aspekten abgeleiteten Limiten, direkt in die Anwendung mit einbezogen werden müssen. Dies wurde im speziellen Fall der räumlich und spektral selektiven Mehrkanal-Anregung gezeigt. Bisherige Ansätze bedienten sich Methoden zur Rausch Untedrückung in Analogie zum Empfangsfall. Allerdings brechen diese Analogien unter Einbezug expliziter Schranken zusammen und die angewendeten Algorithmen können nicht verwendet werden, da sie Rauschen und Abbildungstreue als gleichwertige Optimierungsziele sehen. Daher wurden der mathematische Rahmen und die algorithmische Basis geschaffen, Pulskalkulationen mit Einbezug expliziter Schranken schnell durchzuführen, wie in Kapitel 5 gezeigt wird.

Die Methoden zur Berechnung oben genannter Leistungskriterien aber auch die Mehrkanal-Pulsberechnung benötigen genaue quantitative Messungen des NMR aktiven Radiofeldes im Objekt. Die exakte Messung der Feldverteilung liefert zudem wertvolle Hinweise für die Validation nummerischer Feldsimulationen. Jedoch stellen die Bedingungen bei hohen Feldern als auch Sende-Arrays an sich sehr hohe

Anforderungen an MR-basierte Messmethoden. Erstens ist der dynamische Bereich des Anregungsfeldes eines einzelnen Elementes des Arrays sehr gross. Zweitens behindern im Vergleich zu niedrigeren Feldstärken vor allem die hohen suszeptibilitätsinduzierten Resonanzverschiebungen, die längeren longitudinalen Relaxationszeiten und die viel strikteren Leistungslimitationen eine Messung mit den bestehenden Methoden. Um trotzdem genaue Messungen zu ermöglichen wurde eine Methode entwickelt, welche auf der vollständigen Signalmodellierung einer speziellen Pulssequenz beruht. Zusätzlich wurde die Mehrkanalfähigkeit explizite durch einen interferometrischen Ansatz mit einbezogen um einerseits den dynamischen Bereich zu reduzieren und andererseits die Leistungseffizienz zu erhöhen. Durch diese beiden Neuerungen konnten die Kalibrationsdaten von einem Array in vergleichsweise kurzer Zeit akquiriert werden, wie es in Kapitel 4 dargelegt ist.

Die meisten der oben diskutierten Probleme der Ultrahochfeld-MRT im Bereich der Radiofrequenz sind mit dem Aufkommen von Wellenpropagationseffekten verbunden. Dies ist einzigartig für NMR Systeme und es konnte daher erstmals gezeigt werden, dass klassische RF-Anregung und -Detektion mit Hilfe propagierender Wellen möglich ist. Die Tatsache, dass Wellenleitermoden in der Bohrung des 7 T -Magneten sich ausbreiten können, führte zu der Idee RF Detektoren zu bauen, welche hauptächlich über strahlende Feldanteile mit dem Objekt wechselwirken und so die problembehaftete Nahkopplung umgehen. Wie in Kapitel 6 gezeigt, sendet und empfängt eine Antenne, welche am Ende der Bohrung installiert ist, NMR Signale mit nennenswerter Sensitivität auch im Vergleich zu Resonatoren, welche über ihr induktives Nahfeld koppeln. Dies war ein sehr überraschender Befund, weil die Detektion von den sehr kleinen NMR-Signalen typischerweise eine sehr starke und daher nahe Kopplung ans Detektionsmedium verlangt. Tatsächlich beruhen die meisten Detektionsverfahren auf Faradayscher Induktion, welche durch eine Nahfeldkopplung der nuklearen Magnetisierung an einen naheliegenden Detektor auftritt. Alternative Methoden nutzen die direkte Kopplung der nuklearen Magnetisierung und einem Magnetometer, wie z.B. einem SQUID, einem Magnet-Kraft-Detektor oder einem Atommagnetometer. Die langreichweitige Wechselwirkung zwischen Detektor und Kernmagnetisierung über RF-Felder eröffnet für die Ultrahochfeld-MRT zahlreiche Möglichkeiten. So kann z.B. die resistive Beladung des Detektors durch das Objekt stark vermindert werden, was dessen Betrieb stabiler macht. Auch dass die getriebenen Elemente des Senders nicht in direkter Nähe des Objekts liegt, minimiert das Risiko hoher Feldkonzentrationen und daraus resultierender potenziell gefärlicher Erwärmungen. Eine der grossen Vorteile liegt aber in der Verbesserung der zu erwartenden Uniformität. Die dem RF-Feld zugrundeliegenden Gleichungen verlangen eine Kurvatur des Feldes entsprechend der Wellenzahl des Mediums. Eine propagierende Welle erlaubt nun zumindest einen Teil dieser Biegung in eine für die MRT nicht schädliche räumliche Varianz der Phase zu übertragen und dadurch kann eine uniformere Amplitude resultieren. Es konnte demfolgend experimentell gezeigt werden, dass eine propagierende Welle in einem MRT eine sehr hohe Uniformität der Sensitivität und eine sehr hohe Abdeckung liefert.

Das Regime propagierender Wellen, welche mit der Kernmagnetisierung wechselwirken, bringt auch neuartige Phänomene hervor, weil erstens nun eine Phasenverzögerung in Abhängigkeit der Propagationsrichtung auftritt und zweitens, weil das empfangene Signal direkt mit der Abstrahlung elektromagnetischer Leistung verbunden ist. Neben daraus resultierenden einzigartigen Möglichkeiten für die parallele Bildgebung in Anlehnung an die Holographie konnte auch gezeigt werden, dass sich die Abstrahlung des Spinsystems mit Hilfe der Gradienten steuern lässt. Diese Konzepte bringen starke Analogien zu anderen Gebieten hervor wie z. B. der Laserphysik oder der nichtlinearen Optik. Auch die Konstruktion und das Verständnis von Wellenleiter- und Antennensystemen sind in der Mikrowellen-, Kommunikations-, und Radartechnologie weit fortgeschritten, so dass hoffentlich viele Lösungen übernommen werden können.

Es wurde des weiteren gezeigt, dass der Ansatz einer propagierenden Welle für die Anregung und die Detektion von NMR auf bekannte Mehrkanalmethoden erweiterbar ist. Um mehrere, räumlich verschiedene Moden einspeisen zu können, wurde eine dielektrische Struktur in den Wellenleiter eingeführt. Obwohl der Aufbau ziemlich massiv ist, so benötigt er dennoch keinerlei konzentrierte oder abstimmbare Elemente, was ihn sehr Widerstandsfähig gegen hohe eingestrahlte Leistungen macht. Neben den wichtigsten Anwendungen des parallelen RF Sendens und Empfangens, wie z. B. beschleunigte Bildgebung und RF shimming, konnte gezeigt werden, dass das durch die RF-Felder vermittelte räumliche Auflösungsvermögen mit der Anzahl der propagierenden Moden gekoppelt ist.

Im Gegensatz zu den allermeisten anderen RF-Detektorenkonzepten hat der Ansatz der propagierenden Wellen gute Aussichten auch bei noch höheren Frequenzen zu funktionieren, bei welchen der Strahlungsanteil am Feld sogar noch grösser ist. Die Möglichkeit beim RF-Detektorenbau auf eine Nahfeldkopplung verzichten zu können, erlaubt die Entwicklung einer neuen Klasse von RF-Konzepten, welche vielleicht in Zukunft mit anderen Verbesserungen den Betrieb bei noch höheren Frequenzen erlaubt.

Chapter 1

Introduction

1.1 The Unique Proposition of NMR

Nuclear magnetic resonance (NMR)[1, 2] ranks among the most versatile experimental methods in chemistry, physics, and biology [3], providing insight into the structure and dynamics of matter at the molecular scale. Its imaging variant, magnetic resonance imaging (MRI)[4, 5], is widely used to examine the anatomy, physiology, and metabolism of the human body. The nuclear spins interact in a very strongly deterministic manner with their inter- and intramolecular surrounding, where most of these interactions are weak enough not to render the system chaotic but strong enough to produce precisely measurable effects that can be unambiguously allotted to various material properties. The dynamics of nuclear magnetization is one of the few phenomena in nature that are able to carry the inner microscopic order of matter from the molecular level to macroscopically detectable signals that can be well interpreted. This is very uncommon since the complex microscopic interactions do not gain critical relevance in most large complex systems but result only in a for the microscopic state unspecific thermodynamical variables. For example, the pressure and temperature of a gaseous system does not tell us very much about the intermolecular forces upon which they are based on. Indeed, other effects that directly represent the inner microscopic order in large complex systems can be enumerated in a short list: e.g. Meissner effect, quantum Hall effect, resistance quantization, atomic spectra, Moessbauer effect and a few others. Although all of these effects deliver very crucial insight into the structure and dynamics of matter, they cannot compete in analyzing biological systems and live organism because only the NMR signal, a radio wave, interacts both very weakly and especially innoxiously with the sample. The information carried from the spins by the radio signal and the accessibility of the signal in various materials are the very unique proposition of NMR which made methods employing NMR become almost ubiquitous in these fields.

1.2 The Race for Higher Fields

Although NMR as such gives very sensitive measurements of the surrounding of the nuclei, the detection of the NMR signal itself is not very sensitive compared with other analytic methods as for instance mass spectroscopy. This is mainly due to the very limited signal to noise (SNR) ratio present. While the noise contribution can only be lowered to the fraction that is introduced by the thermal motion of the charges in the sample itself, the signal gained from a sample is mainly dependent on the nuclear magnetization present in the sample. In thermal equilibrium, this magnetization is basically given by the polarization induced by the magnetic background field the sample is immersed in, the temperature and the gyromagnetic ratio of the considered nucleus. In order to increase the sensitivity of NMR either the magnetic field strength has to be increased or the thermal equilibrium has to be overcome if the temperature of the sample and the nucleus cannot be altered. Although increasing the net nuclear magnetization beyond the value in thermal equilibrium is in principle possible by magnetic transfer techniques, pre- or hyperpolarization, these methods are often prone to problems caused by the fact that the system returns irresistibly back to thermal equilibrium. Furthermore, the process of inducing additional polarization is often not well tolerated by the sample either due to the high switching rate of the magnetic field that would be needed, for instance, for pulsed prepolarization or due to the exposure to high power radiation or toxic chemicals in the case of most hyperpolarization schemes. Therefore, the prepolarization steps need to be applied ex-situ and the polarized material needs to be administered quickly to the sample. Astonishingly, it is much better tolerated by live organisms to be exposed to very high static magnetic fields. Even very complex organisms, such as humans, can sustain magnetic fields of several Tesla without any permanent adverse effects known to occur. Furthermore, increasing the background field does not only yield higher sensitivity due to the increased SNR but also the specificity of certain effects is increased such as in the case of the BOLD-effect [6], line separation resulting form chemical shifts or weak couplings [3], relaxation and magnetic transfer induced tissue contrast [7] and many more. Since adverse effects of high static fields such as the increased dephasing due to susceptibility induced field inhomogeneities, higher bandwidth of operation, higher RF induced losses and the increased RF non-uniformity could be well surmounted in the past, there was a constant trend towards higher magnetic fields since the beginning of NMR and MRI methodology.

The latest development resulted in magnets of 7 T [8] and 9.4 T [9] field strengths. Although these systems proved to be advantageous in many applications, the problem of nonuniform spin nutation throughout the sample became prohibitive in many circumstances. This nonuniformity is mainly based on the critical shortening of the RF wavelength due to the increased frequency of operation, that became comparable or even smaller than the object size. Therefore, the impact of the increase in field strength from 3 T to 7 T and beyond on the RF interaction between the system and the nuclear magnetization in the sample is much more drastic than the in relative scales comparable increase from 1.5 T to 3 T. The fact that the wavelength of the RF wave can be significantly shorter than the extent of the imaging volume is indeed very unique to NMR instruments since higher field strengths are usually only applied in smaller systems (see Fig. 1.1). The wave-length related problems concerning local sample heating, RF probe design and establishing a uniform excitation are thus unique to the newest generation of ultra-high field human MRI systems and have accordingly been researched for only a short period of time.

1.3 Basics of NMR and Electromagnetic Interaction

The spin of a particle represents an inner degree of freedom which has a great impact on its quantum mechanical behavior, either by its quantum statistical implications in many body problems, by its angular momentum, by the presence of an associated magnetic moment and many more. In the case of atomic nuclei however, the coupling to the net magnetic moment associated with the spin provides the most important interaction considered in NMR. Therefore, the Hamiltonian (H) of an atomic nucleus, in this case with spin $\frac{1}{2}$, describing the motion of the spin in Schrodinger's equation is dominated by the interaction term with the local magnetic field:

$$\begin{aligned} H &= \frac{\gamma}{2}\vec{\sigma}_{\text{Pauli}} \cdot \vec{B} \\ \vec{\sigma}_{\text{Pauli}} &= (\mathbf{S}_x, \mathbf{S}_y, \mathbf{S}_z) \\ \frac{\partial}{\partial t}|\Psi> &= H|\Psi> \end{aligned} \tag{1.1}$$

whereas $\mathbf{S}_i$ represent the Hermitian Pauli matrices being the generators of $SU(2)$. For practical applications and especially in MRI the Bloch equation describing the motion of the net nuclear magnetization of a isochromat in the external magnetic field is often used:

$$\begin{aligned} \frac{\partial}{\partial t}\vec{M} &= \gamma\vec{B} \times \vec{M} \\ &= \gamma\vec{B} \cdot (\mathbf{L}_x, \mathbf{L}_y, \mathbf{L}_z) \cdot \vec{M} \end{aligned} \tag{1.2}$$

whereas $\mathbf{L}_i$ are the anti-symmetric generators of $SO(3)$. Written in this form, neglecting relaxation for simplicity, it becomes clear by comparing to Eq. 1.1 that Bloch's equation describes the motion of the observable nuclear magnetization of the thermodynamical ensemble in a classical limit of the quantum mechanical equation of motion. But it is also very tempting to confuse the motion of the magnetization with the motion of a single spin state itself and it is therefore very important to keep always in mind that the measured NMR signal represents the coherence within an ensemble of spins as expressed by the density operator and not single spin states as the next paragraph touches on.

In the classical formulation, the signal retrieved from a magnetization processing around the main magnetic field (usually defined to be aligned along the z-axis of the system) at the precession frequency is proportional to the transverse magnetic moment being the only part of the magnetic moment acting at this frequency. In this classical picture, the NMR signal generation on the RF probe can be understood as simple induction generated by the electromotive force of a precessing magnetic dipole. It is nevertheless worth noting that a quantitative correspondence between the signal expected from a quantum mechanical description and its classical limit was and still is a topic of ongoing debates with low frequency but high intensity [10, 11, 12, 13] in the field of NMR. The problem of the quantum mechanical description of the NMR signal starts out in the fact that by calculating the probability of a single excited nuclear spin coupled to the electromagnetic quantum field to decay by spontaneously emitting a photon results in about 10^8 times the age of the universe. Therefore, the usual road map to the explanation of the NMR signals is to consider the quantum mechanical evolution of the spin system separately from the surrounding, not directly NMR related, background electromagnetic field and explaining the emitted signal by the dynamics of the net magnetization in the classical limit. Therefore the NMR signal is usually considered as an electromotive force present in the material studied proportional to the first order quantum transitions resulting in conjunction with relaxation in a free induction decay (FID). But the net energy transfer out of the spin system into the electromagnetic field is usually not considered at all. Nevertheless, calculations of relaxation times deliver even quantitatively good correspondences to the experiments without considering the coupling to the background electromagnetic field or the electrons in the detectors in that sense. The robustness of this formulation diminished the need of a more detailed quantum theory for the explanation of NMR experiments, however it will be of great interest when further increase in sensitivity in principle would allow the detection of the NMR signal of very few or even single spins where I would not expect to see a FID representing a transition of a single spin state. Such experiments will certainly help to understand the quantum mechanical interactions between single nuclear spins and the electromagnetic background field. By the way, this is one of the main differences between NMR and analogous resonance phenomena known in atomic systems, laser physics and non-linear optics, where the relaxation due to spontaneous emission is a dominant factor and hence this interaction can be studied in larger ensembles.

Considering the nuclear spin system as a classical net magnetization when describing its interaction with externally induced electromagnetic fields proved to be very reliable and is therefore one of the prerequisites for the most recognized methodology for the calculation of NMR signal generation in radiofrequency detectors; the concept of reciprocity. The reciprocity relations are commonly applied in the calculation of the efficiency of many kinds of linear signal transceive systems based on electromagnetic waves, mechanical waves or forces and many other systems. The idea is to calculate the reception sensitivity and noise floor of a detector from its transmission efficiency. This approach is of course especially useful if the transmission properties are much easier to determine than the reverse signal path. One of the main prerequisites for the application of this theory is that the NMR signal is excited and measured through one or several well defined ports on the detector with a well defined scalar current and voltage in each of them. Therefore, the concept of reciprocity is very useful in NMR applications, where well defined ports can be provided on the detector and where the effect on the nuclear magnetization of the power induced on a NMR coil is much easier to calculate than the signal induced during reception by the distributed nuclear magnetization. The reciprocity relations most often used in NMR [14, 15, 16] refer distinctly to both the NMR signal and the concomitantly acquired noise.

The reciprocity relation for the signal describing the relation between the frequency of nutation induced by a NMR probe and nuclear induction received at the same port differs from the Lorenz reciprocity well known from antenna theory because of the breaking of the isotropic symmetry in the system induced basically by the main magnetic field. It can be directly deduced from Eq. 1.2 that for RF fields that are small compared to the main field and for small total nuclear magnetization the nutation frequency is proportional to the transverse circularly polarized component rotating with the motion of precession of the nuclear magnetization vector. Based on this definition, this component is denoted as B_1^+ and its polarization is termed right-handed. This definition does not only depend on the polarization of the main magnetic field but equally on the sign of γ. However, B_1^+ reflects the sensitive part of the RF field produced by the probe and by this the two transverse circular polarizations of the magnetic field are inherently distinguished in terms of NMR activity causing the above mentioned breaking of the system's isotropy. For these so called gyrotropic linear systems [17] reciprocity relations are well establish and also used in other fields such as for studying propagation of weak electromagnetic waves in ferromagnetic materials or gaseous plasma. This relation can also be applied to nuclear magnetization. It is therefore found that the nutation frequency is proportional to B_1^+ and the received signal amplitude is proportional to B_1^- which is correspondingly the complex conjugate of the counter-rotating magnetic field the coil produces in transmission. The two entities are calculated from the linear complex magnetic field amplitudes B^{Lab} the coil produces per unit input power at the frequency of the rotating frame:

$$\begin{aligned} B_1^+ &= \frac{\left(B_x^{\mathrm{Lab}} + iB_y^{\mathrm{Lab}}\right)}{2} \\ B_1^- &= \frac{\left(B_x^{\mathrm{Lab}} - iB_y^{\mathrm{Lab}}\right)^*}{2}. \end{aligned} \tag{1.3}$$

The approximations mentioned above are rarely violated under normal conditions but it has to be mentioned that excessively high RF fields can induce effects like a Bloch-Siegert shift [18] where the counter-rotating circular polarization induces a frequency shift which is not predicted in the linear reciprocity model. Furthermore, high amounts of nuclear magnetization would render the entire electromagnetic system nonlinear which violates one of the basic assumptions. However, it is key to this consideration, that the amount of coupling of an RF based NMR detector to the nuclear magnetization for excitation and reception is directly given by the two transverse components of the magnetic field produced by the coil when it is driven at its port.

The reciprocity relation determining the noise received concomitantly with the NMR signal by the losses of the probe during transmission is based on the fluctuation-dissipation theorem. This fundamental theorem of statistical mechanics states that the power dissipation of a thermodynamical system is directly linked to the noise fluctuations seen on this thermodynamical variable. It is usually a very good assumption that the total losses of the system in transmission are ohmic losses in the coil, the sample or losses due to radiation basically dissipating outside the considered system. All these losses cause that a net resistance R is seen at the coil's port and if the entire system is at equal temperature T the noise amplitude N per unit bandwidth is basically given by:

$$\begin{aligned} R &= 2 \underbrace{\oint_{\partial V} \Re\left(\mu_0(\vec{r})\vec{E}(\vec{r}) \times \vec{B}(\vec{r})^*\right) \cdot d\vec{A}(\vec{r})}_{\text{radiation loss}} + \underbrace{\int_V \vec{E}^*(\vec{r})\sigma(\vec{r})E(\vec{r})dV}_{\text{Ohmic losses}} \\ N &= \sqrt{4k_BTR} \end{aligned} \tag{1.4}$$

where $\vec{E}$ and $\vec{B}$ represent the electric and magnetic field produced by the probe when driven by unit power on the port, k_B is the Bolzmann constant and $\sigma(\vec{r})$ is the distribution of the electrical conductivity in the system. As a subtlety, it can be mentioned that the fact that the net losses are considered to be only ohmic it is also assumed that the nuclear magnetization is not adsorbing any power whether dissipatively or reactively by storing it in the deflection of the magnetic moment relative to the main field. First, this is again expressing that the interaction between nuclear magnetization and electromagnetic field is considered not to transfer any energy and second, regarding its reciprocal implication means that the nuclear magnetization itself is considered to be consequently noiseless. This is of course not the case as for instance demonstrated in e.g. Ref. [19]. In contrast to the relation of excitation and signal reception relying on the magnetic components, the second part of the reciprocity relation states that in most situations encountered in NMR the electric field generated by exciting the port of the coil is determining the loss and noise characteristics in transmission and reception respectively.

Beside the fact that the losses induced by the electric fields produced by the coil are usually dominating the noise floor of NMR signals retrieved and need to be globally minimized in the design process of RF probes, the ohmic losses, especially within the sample, cause heating of conductive substances investigated. Particularly in applications with live samples, the heating of the tissue induced during transmission imposes a serious constraint to the total transmission power that can be applied for excitation. Therefore avoiding strong electric fields inside the sample is a major concern in NMR coil design and while for reception it is sufficient to minimize the total ohmic resistance, the local power absorption has to be rigourously monitored to prevent strong local heating at least in thermally large samples in transmission.

1.4 Radiofrequency Problems Rising with High Frequencies

The (vector)-potentials of the electric and magnetic fields which are relevant for NMR excitation and detection obey both the same type of equation[1]:

$$\left(\nabla^2 + k(\omega)^2\right) \Psi(\vec{r},\omega) = -4\pi f(\vec{r},\omega) \tag{1.5}$$

where Ψ stands for the vector potential or the scalar potential, $k(\omega)$ is the complex wavenumber and $f(\vec{r},\omega)$ is the spectral-spatial distribution of the source current or charge. This Helmholtz equation is solved by Green's functions G of the type:

$$G(\vec{R} = \vec{r} - \vec{r}',\omega) = \frac{e^{\pm i\vec{k}\cdot\vec{R}}}{R}. \tag{1.6}$$

If the product of the wavenumber and the maximum extent of the system $(\vec{k} \cdot \vec{R})$ is much smaller than 1, G is approximately the same as for electro- and magnetostatic problems. This regime is called quasistationary which means that there is no propagation phase delay between the driving source and the field. Most NMR systems work within that range as it is shown in Fig. 1.1. The quasistationary regime brings some important consequences to the design of RF probes. First, there exists always a sheet current distribution running on the nappe of convexly bound lossless volumes that produce a uniform transverse magnetic field inside the volume. In the case of a circular cylinder this is realized by the first order harmonic azimuthal distribution as it is well approximated by birdcage and TEM volume resonators [20, 21]. There exist even analytical approaches to the design of

---

[1] For simplicity, the Helmholtz equation is employed instead of the full set of Maxwell's and dielectric material's equations. The presented form is only valid if the dielectric parameters are piecewise constant in a rigorous way. However, gradual changes of material parameters can be approximated by appropriately fine meshing to a usually sufficient extent.

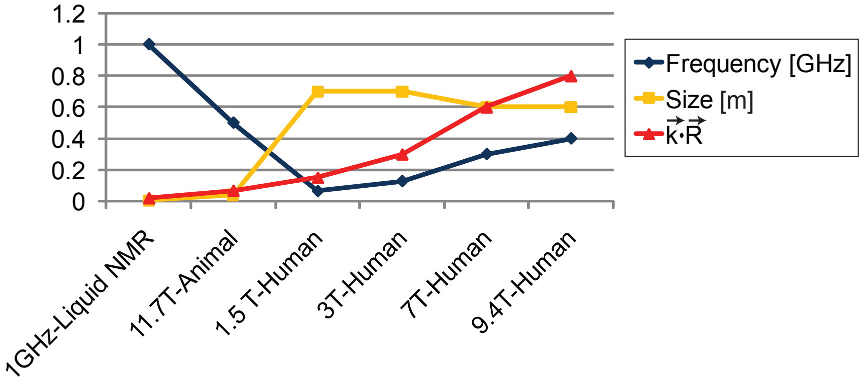

Figure 1.1: Typical NMR systems work within the quasistationary RF regime where $\vec{k} \cdot \vec{R} \ll 1$. The only exceptions are represented by the newest generation of ultra-high field human whole body MRI systems.

noncircular cylindrical volume lattice resonators as in Ref. [22]. Second, the field produced within the sample is reactively bound to the current carrying element on the coil and are therefore directly affecting the net reactance and resistance of the probe. Losses in the sample are therefore either inductively induced by the eddy currents generated by the RF magnetic field in the sample or by so called conservative electric fields [23] that are traditionally linked to stationary charge gradients present on the probe structure capacitively coupling to the lossy sample. The losses induced by the right-hand circularly polarized transverse magnetic field in a lossy sample are inevitable and consequently they should dominate in an optimal coil design. These in that sense ideal losses scale with $(\omega B_1)^2$ showing that the power deposition will drastically increase with the frequency of operation even under ideal circumstances. Using resistive conductors for the probe, the dominance of the ideal sample losses cannot be ensured for very small volumes where the losses on the coil are more important when using normal resistive conductors. With increasing size, the sample losses become dominant and the conductance of the coil itself becomes of less importance. This shows that even the quasistationary regime is not scale invariant because the RF probe consists of a 1 or 2 dimensional current distribution confined at the surface of the conductor by the skin depth but the sample is a 3 dimensional volume in most applications. This difference in dimensionality causes a different scaling of the loss contributions of the various parts. Another consequence of the strong reactive binding between the field inside the sample and the current on the probe in conjunction with the relatively moderate conductivities encountered in biological samples is that the magnetic field distribution inside the sample is not significantly altered as long as the current distribution on the probe is not affected by the loading. This fact renders the resulting excitation of a probe robust with respect to slightly altering shapes and sizes of the loads and a simple scaling of the input power is sufficient for compensation.

The breakdown of this quasistationary approximation in human ultra-high field systems causes these basic assumptions underlying the designs of RF probes loose validity. First, a truly uniform solution driven from the shell of the sample volume does not exist anymore in general, even theoretically. Second, the fields within the volume are not necessarily bound reactively to the conductor of the probe. Therefore the radiative contribution becomes more significant. Consequently, the field distributions are more strongly affected by the presence and the shape of the sample since aberrations and reflections can occur at dielectric boundaries leading to strong field interferences. This causes the field the RF probe produces within the sample to depend more strongly on the exact distribution of dielectric properties in the sample. Furthermore, wave propagation effects on the probe conductor itself make it more difficult to establish the targeted current distribution around the sample especially in conjunction with variable loading situations. These effects render the performance of large RF probes in practice less stable which not only affects their performance but also raises harder problems for safety and compliance testing.

1.5 Solutions to the RF Problem

Many solutions exist for optimizing a sequence to reduce its RF power consumption e.g. by reduction of flip angles as often practiced in multiple spin echo sequences [24], by reduction of the bandwidth of RF pulses [25] etc. Also, many techniques are well established that are inherently robust against RF field non-uniformities and main magnetic field inhomogeneities such as by the use of adiabatic pulses [26] or composite pulses [27] and many others. Alternatively, the sequence or single pulses can be optimized to tolerate specific imperfections in the field distributions [28]. Especially the localization of the nutation induced by the pulse by gradients can be applied not only for spatial encoding of the signal but to render a uniform spin manipulation within a nonuniform RF field [29, 30]. Unfortunately, most techniques for correction of RF non-uniformities inflict a significantly higher RF power consumption, an increased duration and/or a reduction in bandwidth whereby their application to ultra-high field systems often inflicts serious restrictions in acquisition speed and robustness.

Besides the approaches optimizing sequences and pulse waveforms, development of RF hardware is needed to help to resolve the problems occurring at ultra-high fields. The shortening of the wavelength makes developments on the existing designs necessary, although these devices are well proven and widely used at lower frequencies. The strong dependence of the field distribution in the sample on the distribution of the dielectric and conductive materials raised the necessity for RF excitation probes that allow adaptation of their field to each individual sample. This was realized by the usage of phased arrays for transmission [31]. The advantages of the parallelization of RF probes were well known for reception, where higher local SNR [32] and even spatial encoding [33, 34, 35] can be achieved by acquiring the signals from a plurality of decoupled receivers. Unfortunately, a lot of these designs cannot be directly applied for transmission because one of the main methods applied to decouple the individual elements from each other relies on the reflection induced by the preamplifier present at the port of each coil. While reflective, linear, low noise, small-signal amplifiers are widely available, most power amplifiers need a matched output to provide high efficiency, linearity and stability. Therefore, the isolation among the elements of a transmission array has to rely on reduction of mutual couplings. Furthermore, the downside of the adaptivity gained in the magnetic field is the variability of the concomitant electric field and thereby of the power deposition within the sample. In contrast to receive arrays, optimization and control of the total power losses does not ensure a safe operation for the sample because the distribution of the power deposition can drastically change. This makes new safety and compliance concepts necessary which was not the case when introducing the parallelization of signal reception.

However, one of the main advances made for MRI in the last decade was parallel imaging. It resulted from bringing together the encoding capabilities provided by the gradient system and by the receive coil array. This combination is very attractive since it merges the instantaneous encoding capability of the coil array with the high degree of spatial freedom and resulting resolution potential provided by the sequential encoding imposed by the gradients. This approach can also be applied to transmission in order to accelerate spatial localization of the spin nutation induced by RF pulses by the gradients [36, 37]. The long duration of such pulses inflicted by the sequential gradient encoding is indeed one of the main reasons for the rare application of pulses localizing the excitation by gradient encoding in several dimensions. The possibility to reduce this encoding time brings such pulses closer to practically applicable durations. Particularly the increased encoding capability provided by RF arrays at higher operation frequencies [38] brought these techniques into the focus of recent developments working on this problem.

Although the emergence of wave effects causes serious troubles to existing RF probe designs, it also offers the possibility of new concepts for the excitation and reception of NMR signals that do not rely on an intimate coupling between the nuclear magnetization and the detector. Unsurmountable problems could be encountered by trying to adapt the existing concepts of RF probes to a regime for which they initially have not been designed for, especially when facing even higher frequencies. Therefore the exploration of new RF probe concepts tailored to the new regime of RF interaction gains importance for current ultra-high field systems but also future, potentially even stronger generations.

Bibliography

[1] Bloch F, Hansen WW, and Packard M. The Nuclear Induction Experiment. Phys Rev 1946; 70(7-8):474–485.

[2] Purcell EM, Torrey HC, and Pound RV. Resonance Absorption by Nuclear Magnetic Moments in a Solid. Phys Rev 1946; 69(1-2):37–38.

[3] de Graaf RA. NMR Spectroscopy. West Sussex, England. John Wiley & Sons Ltd; 2 edition; 2007.

[4] Lauterbur PC. Image Formation by Induced Local Interactions: Examples Employing Nuclear Magnetic Resonance. Nature 1973; 242:190–197.

[5] Kumar A, Welti D, and Ernst RR. NMR Fourier Zeugmatography. J Magn Reson 1975; 18:69–83.

[6] Harel N, Ugurbil K, Uluda K, and Yacoub E. Frontiers of brain mapping using MRI. J Magn Reson Imag 2006; 23(6):945–957.

[7] Wyss M, Brunner DO, Morel A, and Pruessmann KP. T1 contrast in the human brain at 7T. In Proc ESMRMB 2008. p. 252.

[8] Vaughan JT, Garwood M, Collins CM, Liu W, DelaBarre L, Adriany G, Andersen P, Merkle H, Goebel R, Smith MB, and Ugurbil K. 7T vs. 4T: RF power, homogeneity, and signal-to-noise comparison in head images. Magn Reson Medicine 2001; 46(1):24–30.

[9] Vaughan T, DelaBarre L, Snyder C, Tian J, Akgun C, Shrivastava D, Liu W, Olson C, Adriany G, Strupp J, Andersen P, Gopinath A, Moortele P-Fvd, Garwood M, and Ugurbil K. 9.4T human MRI: Preliminary results. Magn Reson Med 2006; 56(6):1274–1282.

[10] Dicke RH. Coherence in spontaneous radiation processes. Phys. Rev 1954; 93:99–110.

[11] Macomber JD. How does a crossed-coil NMR spectrometer work? Spectrosc. Lett 1968; 1:131–137.

[12] Hoult DI and Ginsberg NS. The Quantum Origins of the Free Induction Decay Signal and Spin Noise. J Magn Reson 2001; 148(1):182–199.

[13] Hoult DI. The Origins and Present Status of the Radio Wave Controversy in NMR. Conc Magn Res A 2009; 34A(4):193–216.

[14] Hoult D and Lauterbur P. The sensitivity of the zeugmatographic experiment involving human samples. J Magn Reson 1979; 34:425–433.

[15] Hoult DI. The principle of reciprocity in signal strength calculations: a mathematical guide. Conc Magn Reson 2000; 12:173–187.

[16] Tropp J. Reciprocity and gyrotropism in magnetic resonance transduction. Phys Rev A 2006; 74(6):062103.

[17] Harrington RF and Villeneuve AT. Reciprocity Relationships for Gyrotropic Media. IRE Trans Microwave Theory and Techniques 1958; 6(3):308–310.

[18] Bloch F and Siegert A. Magnetic Resonance for Nonrotating Fields. Phys Rev 1940; 57:522.

[19] Mueller N and Jerschow A. Nuclear spin noise imaging. PNAS 2006; 103(18):6790–6792.

[20] Hayes CE, Edelstein WA, Schenk JF, Mueller OM, and Eash M. An efficient, highly homogeneous radiofrequency coil for whole-body NMR imaging at 1.5 T. J Magn Reson 1985; 63:622–628.

[21] Vaughan JT, Hetherington HP, Otu JO, Pan JW, and Pohost GM. High frequency volume coils for clinical NMR imaging and spectroscopy. Magn Reson Med 1994; 32(2):206–218.

[22] Riauka TA, De Zanche NF, Thompson R, Vermeulen FE, Capjack CE, and Allen PS. A numerical approach to non-circular birdcage RF coil optimization: Verification with a fourth-order coil. Magn Reson Med 1999; 41(6):1180–1188.

[23] Park B, Webb AG, and Collins CM. A method to separate conservative and magnetically-induced electric fields in calculations for MRI and MRS in electrically-small samples. J Magn Reson 2009; 199(2):233–237.

[24] Hennig J. Multiecho Imaging Sequences with Low Refocusing Flip Angles. J Magn Reson 1988; 78(3):397–407.

[25] Hargreaves BA, Cunningham CH, and Nishimura DG. Variable-rate selective excitation for rapid MRI sequences. Magn Reson Med 2004; 52:590–597.

[26] Garwood M and DelaBarre L. The Return of the Frequency Sweep: Designing Adiabatic Pulses for Contemporary NMR. J Magn Reson 2001; 153(2):155–177.

[27] Levitt MH and Freeman R. Compensation for Pulse Imperfections in NMR Spin Echo Experiments. J Magn Reson 1982; 48:234.

[28] Boulant N, Bihan DL, and Amadon A. Strongly Modulating Pulses for Counteracting RF Inhomogeneity at High Fields. Magn Reson Med 2008; 60:701–708.

[29] Pauly J, Nishimura D, and Macovski A. A k-Space Analysis of Small-Tip-Angle Excitation. J Magn Reson 1989; 81:43–56.

[30] Saekho S, Yip C-y, Noll DC, Boada FE, and Stenger VA. Fast-k_z Three-Dimensional Tailored Radiofrequency Pulse for Reduced B_1 Inhomogeneity. Magn Reson Med 2006; 55:719–724.

[31] Adriany G, Van de Moortele P-F, Wiesinger F, Moeller S, Strupp JP, Andersen P, Snyder C, Zhang X, Chen W, Pruessmann KP, Boesiger P, Vaughan T, and Ugurbil K. Transmit and receive transmission line arrays for 7 Tesla parallel imaging. Magn Reson Med 2005; 53(2):434–445.

[32] Roemer PB, Edelstein WA, Hayes CE, Souza SP, and Mueller OM. The NMR phased array. Magn Reson Med 1990; 16(2):192–225.

[33] Sodickson DK and Manning WJ. Simultaneous acquisition of spatial harmonics (SMASH): Fast imaging with radiofrequency coil arrays. Magn Reson Medicine 1997; 38(4):591–603.

[34] Pruessmann KP, Weiger M, Scheidegger MB, and Boesiger P. SENSE: sensitivity encoding for fast MRI. Magn Reson Med 1999; 42:952–962.

[35] Griswold MA, Jakob PM, Heidemann RM, Nittka M, Jellus V, Wang JM, Kiefer B, and Haase A. Generalized Autocalibrating Partially Parallel Acquisitions (GRAPPA). Magn Reson Medicine 2002; 47(6):1202–1210.

[36] Katscher U, Boernert P, Leussler C, and van den Brink JS. Transmit SENSE. Mag Res Med 2003; 49(1):144–150.

[37] Zhu Y. Parallel excitation with an array of transmit coils. Magn Reson Med 2004; 51(4):775–784.

[38] Wiesinger F, Van de Moortele P-F, Adriany G, Zanche ND, Ugurbil K, and Pruessmann KP. Parallel imaging performance as a function of field strength - An experimental investigation using electrodynamic scaling. Magn ResonMed 2004; 52(5):953–964.

Chapter 2

Construction of a Transmit-Receive Coil Array and a Parallel Transmit Feed System for Test Purposes

Partially published in:

D. O. Brunner, N. De Zanche, J. Froehlich, D. Baumann and K. P. Pruessmann. *"A Symmetrically Fed Microstrip Coil Array for 7T"*. Proc Intl Soc Magn Reson Med 2007, Berlin. p. 448

J. Froehlich, D. Baumann, D. O. Brunner, K. P. Pruessmann and R. Vahldieck. *"Computational Analysis and Validation of Coil Arrays for Whole-Brain MR-Imaging at 7 T"*. International Microwave Symposium Digest 2007, Honolulu. p. 2217-2220

N. DeZanche, D. O. Brunner and K. P. Pruessmann. *"An Inexpensive Versatile RF Power Splitter, Attenuator and Phase-Shifting System for Array Transmit at 7T"*. Minnesota High-Field Workshop 2007, Minnesota. p. 87

2.1 Introduction

There is a large multitude of designs allowing for uniform NMR excitation of larger volumes up to frequencies of operation of about 140 MHz. Historically, the evolution started from solenoidal and Helmoltz coils and went over to butterfly and saddle coils. Later, the class of actual volume resonators emerged from the slotted cylinder resonator [1] and the slotted tube resonator [2]. These structures would be called in modern terms TEM resonators because the field is produced by longitudinal transmission lines which are capacitively shortened to resonance within a shielded cavity containing the sample. The Alderman-Grant resonator [3] was then developed placing the tuning capacitance at the endrings of the slotted tube instead to the ground plane. It was realized that a first order azimuthal harmonic current distribution on a cylinder ideally realizes a uniform transverse magnetic field within the inner volume in a quasistationary regime. This current distribution is therefore usually dubbed as homogeneous mode of the resonator but its realization turned out not to be trivial. However, the targeted sheet current distribution could successfully be approximated by currents on the rungs of lattice resonators. The result of this development is the class of so called Birdcage resonators [4, 5] that became very widely used in almost all applications of NMR. But the inherently high inductance of the native Birdcage designs renders a rather low self resonance frequency of the structure which becomes critical for larger dimensions of the coils as used in human medical applications. If the conductor structure itself gets close to resonance, a controlled tuning and matching of the coil by introduced lumped or distributed capacitances becomes increasingly hard to realize. Close shielding of the volume coil however proved to reduce this problem such that Birdcages became the standard even for body imaging up to 150 MHz. An alternative proposition to resolve this problem is the TEM resonator design [6], which is, as the slotted tube resonator, a transmission line based construction. Therefore, the inherent limitation with respect to size and frequency of operations are given by the wavelength effects of the currents on the transmission line that reduce the longitudinal uniformity and can also render the design self resonant [7]. The pros and cons of birdcage and TEM resonator designs have been furiously discussed over the last years and the vast amount of designs and topologies that were spurred by these types of resonators makes even a clear classification and nomenclature a substantial task. The main difference between both designs that allows for best classification is the nature of the coupling between the current carrying rungs/transmission lines; in the case of a birdcage there is a line inductance or capacitance connecting neighboring rungs whereas a TEM resonator relies solely on a mutual inductive coupling between the elements.

With upcoming ultra-high field systems it was found that a harmonic current distribution does not render anymore a uniform excitation field. Some arguments arose about the exact reason of this phenomenon. Dielectric resonances excited in portions of the human body, destructive and constructive interferences between the fields produced by the individual rungs and many other effects have been evaluated and found to be a reasonable cause. However, what can be definitely said is that the quasistationary approximation on which the conclusion relies on that the homogeneous mode renders a uniform excitation field is just not valid anymore. In general, the regime in between the very close range coupling and far field situations is found to be very difficult, since no robust and mainly "omni-valid" approximation is known comparable to a quasistationary or a far-field approximation. This makes a simple and intuitive interpretation very hard and every phenomenon occurring can be explained with either point of view. Therefore it is not expected that this discussion will dissolve in a broad consensus. However, a drastic consequence of the break down of the quasistationary approximation is that the sample inside the coil does not only cause small disturbances in the magnetic field pattern and in the current distribution on the coil anymore. While at lower frequencies and smaller coils the sample entering the coil can be handled in first order approximation, which means that the sample just adds a serial resistive load but leaves the shapes of the fields basically unchanged, the effects can be much more complicated and more importantly strongly dependent on the detailed dielectric structure of the sample at high frequencies. Therefore, it is very useful to have more variable control over the current distribution on a coil. This is provided by the usage of phased array coils for transmission. Although coil arrays are standard for receive applications, the adaptation of those designs for transmission is not trivial since the mutual couplings among the individual elements of the array cannot be suppressed with reflective (pre-)amplifiers as it is usually done in the receive case. Additional reduction of mutual couplings beyond the isolation delivered by geometrical or lumped decoupling strategies is provided by reduction of the evanescent field of the single array elements by close shielding. Inherently, this is realized by the rungs of TEM coils, which have a very concentrated field between the conductor and the shield. This leads to the design of stripline resonator based transmit array coils [8]. Nevertheless it is remarkable, that the most mentioned potential weaknesses of the TEM volume resonator compared to the birdcage - the weak coupling among the rungs and the smaller loading factor- were now mentioned as one of the great advantages over loop topology based array designs.

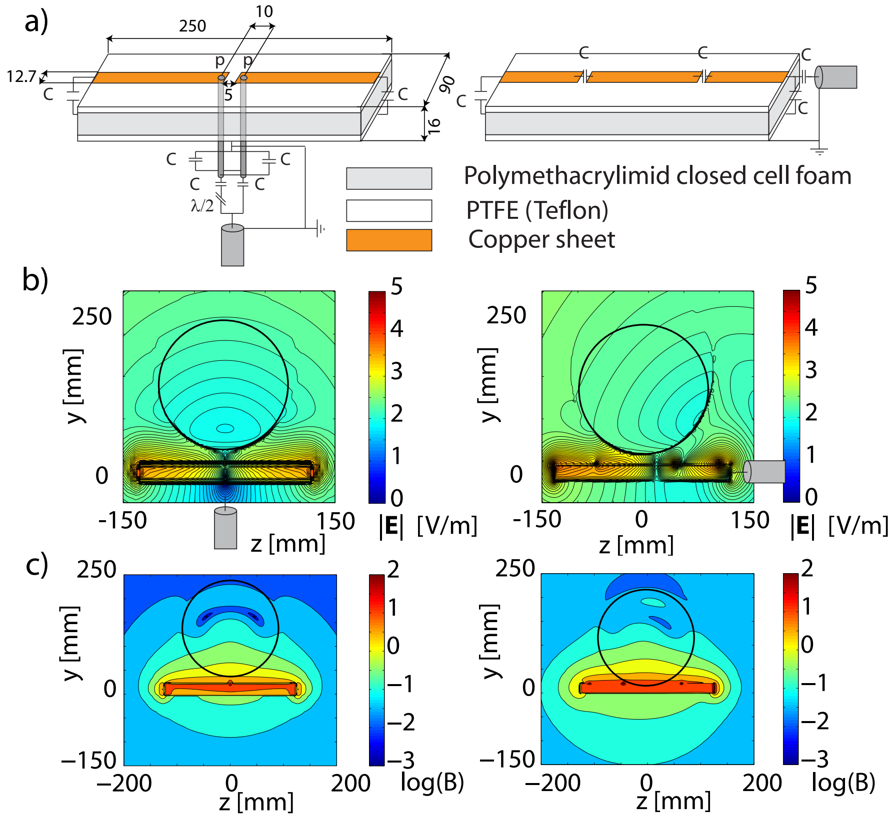

Figure 2.1: Schematic a) shows the construction and dimensions of the centrally fed stripline (left) and the side-fed version (right). All dimensioning is denoted in mm. The results of the FDTD simulations of a single element loaded by a tissue dielectric 20 cm sphere are plotted in b) and c) for the central axial plane. Plot b) shows the norm of the electric field and c) is a logarithmic plot of the B_1^+ field.

2.2 Construction and Design Considerations

2.2.1 Array Element Design

Based on the experiences collected in the group of Gregor Adriany in Minnesota it was decided to start our coil design based on their state-of-the-art stripline array coils. The geometry of each element was chosen to target an 8 channel array with full head coverage and is depicted in Fig. 2.1. The sandwich construction consisting of PTFE sheets at the surfaces and polymethacrylimid closed cell foam inside provides high mechanical stability with a very low dielectric loss tangent and permittivity. Furthermore this material combination is lighter and cheaper than a solid PTFE former usually employed for these purposes.

One of the main problems reported were the low coverage in the longitudinal dimension and the robustness of the tuning and matching situation. The axial current distribution is -at least in a uniformly loaded case- given by the effective wavelength on the stripline. The situation can be improved similarly as in loop coils by distributing the tuning capacitance by splitting [9]. The problem of tuning and matching stability however has certainly several aspects. First, as mentioned above, the loading induced by the sample is higher at higher frequencies and also the dependence on the sample geometry is stronger. This factor makes it inherently harder to come up with a robust design for higher frequencies for such coils. Second, the cabling and the grounding of each element is very critical. Usually the matching circuitries of NMR coils are targeted to be balanced which means actually that when attaching the coil to the cable, the currents should only flow inside the cable in a differential current mode leaving the potential of the cable's shield fixed. Otherwise common mode cable currents running on the shield of the RF cables increase radiation losses and stray reactance of the coil which reduces not only the net efficiency but also renders the setup touchy with respect to small changes in cable routing and its environment. In the case of transmit arrays the prevention of strong induction into ground loops formed by the feeding cables gains special importance to that respect because it is not trivial to bring the cables out of the hot areas where strong fields emanating from the coil elements reside. In the case of a traditional stripline resonator this task is especially not easy to fulfill because the cable is attached at the end of the resonator, where there are strong electric fields loading the cable. Furthermore, the large range of loadings the elements have to be matched to make it hard to achieve matching and balancing for all situations [10]. Therefore, a design was developed that is inherently symmetric and that allows the cables to be attached at a point with low electric fields. This concept is compared to elements that are fed from the side. In order to maintain similar current distributions on both elements, the tuning capacitance of the side-fed version was split into four segments and for this two additional lumped capacitances were equally distributed on the strip.

Single elements of both designs loaded by a tissue dielectric, 20 cm sphere have been simulated using FDTD. The resulting electric field and B_1^+ fields of both designs are shown in Fig. 2.1. Indeed it can be seen that the side-fed resonator would load the cable shield (not included in the simulation) by its strong electric field emanating from the end of the stripline. Moving the point where the cable ground is attached to the coil element to the center helps already to solve this problem. Furthermore, the novel design requires a balanced feeding which has to be provided by a balun. The common current mode rejection provided by most common balun designs delivers additional blocking of potential shield currents induced by unbalanced feeding.

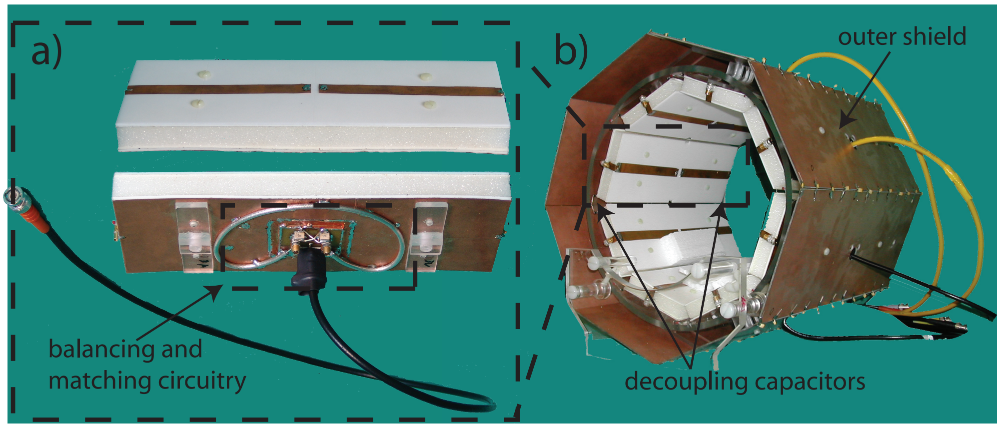

Figure 2.2: Photographs of a manufactured single element and the modular 8 channel array construction. Neighboring elements are decoupled by capacitors connecting the ends of the backplanes on both sides. An additional outer shield provides additional protection of the feed cables from stray fields.

It was concluded from these considerations about the design of single elements, that the central feeding offers significant advantages over a side-fed design especially for the targeted test and validation purposes and therefore a cylindrical array of 8 centrally fed elements was constructed.

2.2.2 Array Construction

A 30 cm diameter PMMA tube was used to hold the eight individual elements. This modular design allows to quickly exchange single elements of the array, which offered great advantages in the development process. Next neighboring elements are decoupled by a pair of capacitors of which are mounted between the edges of the backplanes of adjacent resonators. By this, the long sides of the backplanes of neighboring elements form a loop structure that is providing some mutual reactance between the two elements. This reactance can be tuned to compensate the mutual coupling among the adjacent elements. However, the choice of the decoupling capacitances was found to be not trivial. If the decoupling was adjusted for maximum isolation between neighboring elements, the coupling to next neighbors and even elements at further distances got increased. This is shown in Fig. 2.3 where 1 pF and 1.2 pF decoupling capacitors were employed for comparison. Before the measurement, the array was loaded by a 30 cm long, tissue dielectric cylinder with diameter of 20 cm and matched to it. For higher comparability between the two setups, the tuning capacitors of the array stood unchanged and the center frequency of the array was set to the frequency the elements showed minimum reflection after rematching to 50 Ω. In order to evaluate the influences of the decoupling capacitance, the scattering matrix has been analyzed using the formalisms presented in Section 3.1.1.

Although the 1.2 pF capacitances reduce the neighbor coupling, next neighbor couplings become enhanced and the maximum coupling is even higher than with 1 pF. Thus the power adsorption efficiency for quadrature driving even decreases by 10 % by increasing the decoupling of adjacent elements. Furthermore, 7 eigenvalues of the power scattering loss matrix ($\mathbf{\Phi}^S$ in Eq. 3.3) are below 0.5 for 1 pF . This means that the array is able to adsorb the power with an efficiency of more than 50 % for 7 out of 8 possible eigenmodes. One mode is almost completely reflected by the array and will therefore only produce marginal excitation. Using 1.2 pF decoupling capacitances only 6 modes of the array can be excited with less than 50 % reflection. It was therefore concluded that a lower decoupling capacitance is advantageous and thus a higher coupling among neighboring elements is worth being tolerated.

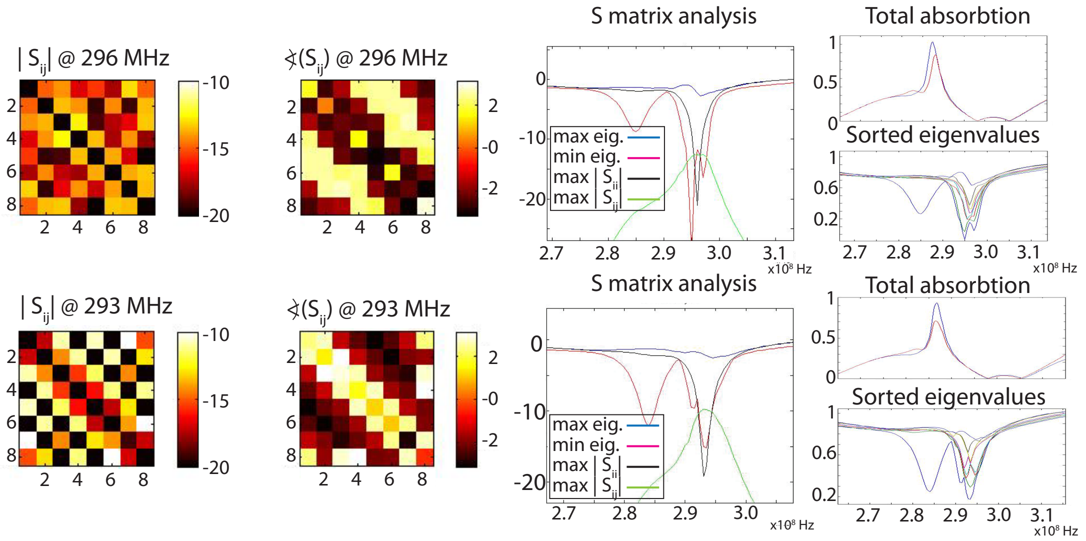

Figure 2.3: Comparison of two different values of decoupling capacitors. The upper plots were measured using 1 pF whereas the lower plots correspond to 1.2 pF. The plots show the color coded magnitude and phase of the array's scattering matrix (**S**) at the frequency the array was tuned to. The column in the middle shows plots of the maximum and minimum reflection, coupling and eigenvalue of **S** around the tuning frequency. The column on the right shows the total power adsorption of the array (see Eq. 3.6 for quadrature driving (red line) and uncorrelated mean input signals (blue line). Furthermore, the eigenvalues of the scattering loss matrix $\mathbf{\Phi}^S$ in Eq. 3.3 are plotted for both capacitances.

2.2.3 Construction of a RF Feed System

In order to apply RF shimming, a high power RF feed system had to be constructed that delivers control over the relative phases and amplitudes of the voltages feeding the array. In order to perform simple RF shimming experiments, the amplitudes and phases do not need to be altered at a high switching rate, nor fully independent waveforms need to be fed to each channel. Therefore, an approach was chosen splitting the output power of the system's standard RF power amplifier and mechanically adjusting each individual channel's phase delay and attenuation. For this, a partial Butler matrix [11] splits the power incident at its input port equally to the 8 output ports with 45 ° phase increments. The matrix consisted of 7 quadrature hybrids (Anaren, USA), 7 high power dump load terminations (KDI, USA) and appropriate fixed phase shifting delay lines mounted on a 3 mm thick copper plate providing large heat dissipation capabilities. In order to adjust the amplitude of each channel high power attenuators (ATM, USA) have been employed allowing for a maximum attenuation of -60 dB in steps of 1 dB. Phase adjustments have been provided by mechanical screw drive phase shifters (ATM, USA) allowing for a maximum phase shift of 120 °. In cases higher phase differences had to be applied, a course adjustment by appropriately lengthened cables has been introduced. The entire construction is depicted in Fig. 2.4.

To ensure that the RF excitation produced by each channel of the coil is highly linear with respect to the phase delays and attenuations applied, multiple scattering between the array and the RF splitter must be avoided. Occurring standing waves in the variable phase shifters and attenuators would make precise adjustments of RF shims very delicate and significant errors would be introduced in methods that explicitly rely on the linearity of the system with respect to the phase and amplitude settings as in Chapter 4. Since the coupling and the reflection from an array cannot be suppressed sufficiently in all cases, the outputs of the splitter must adsorb all scattered power from the array. This is already very well provided by the high isolation $> 23\,\text{dB}$ and the good input matching $\mathbf{S}_{ii} < 20\,\text{dB}$ of each splitting unit (hybrid plus termination) of the Butler matrix. Therefore, incoming waves at the output port are mainly dissipated in the high power terminations and only a small amount is transmitted back to the power amplifier but almost none of the power is scattered back to the array. The transmission in phase and amplitude of the feed system consisting of splitter, phase shifters, attenuators and $8 \times 12\,\text{m}$ of cables leading to the coil have been measured using a network analyzer. The results are plotted in Fig. 2.4. The total loss in each channel was below 30 % with a maximum imbalance of 0.26 dB. The maximum phase unbalance was 2 °.

In order to connect the RF coil to the feed system and to the receive chain of the scanner, eight low voltage pin diode TR switches were constructed providing

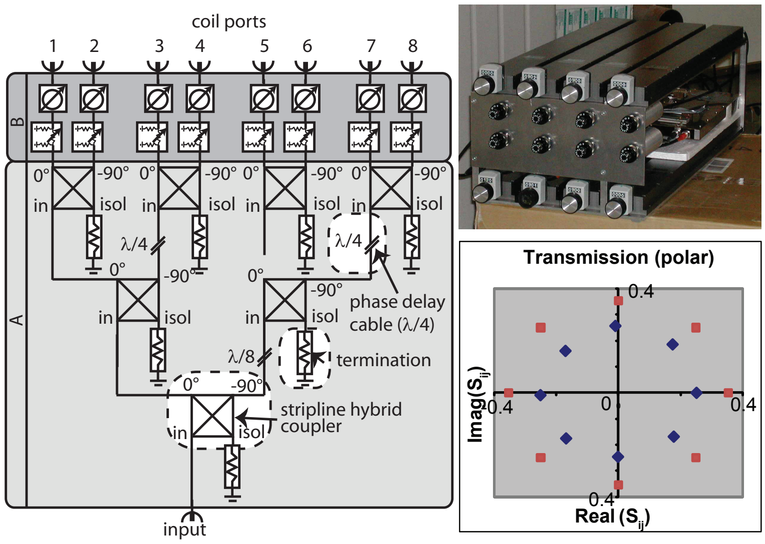

Figure 2.4: Schematic of the partial Butler matrix. The omitted parts of the original design have been replaced by 50 Ω terminations. The photograph shows the final assembly of the splitter, the attenuators and the phase shifters. The polar graph below shows the transmission from the input port to the coil ports of the entire unit.

an isolation of more than 60 dB between the receive and the transmit port in transmission state. Preamplification was provided by the scanners 16 channel interface box (Philips Healthcare, Cleveland, Oh., USA).

2.3 Experiments & Results

2.3.1 Bench Measurements

For these bench measurements, a tissue conductive saline water sphere of 15 cm diameter was employed as load. The loaded/unloaded Q factors of the elements was about 210/100 which represents not a very high Q drop ratio for this relatively small phantom. However, it is expected that significant contributions of the field inside the sample especially at the center can originate from radiative field components which is not reflected by the Q drop. The ability to tune and match each element in the array is demonstrated in Fig. 2.5a) for the loaded array. It can be seen that all elements behave similarly, that the remnant coupling does not lead to serious peak splitting and that each element can be matched providing reflections of less than -20 dB in the imaging band.

The dependence of the s-parameters of the array on the load is shown in Fig. 2.5b). Although the array is loaded by the sphere, now strong shifting of the adsorption peak occurs, which hints at a low capacitive coupling of the array to the sample.

The quality of the cable grounding was experimentally tested by measuring the reflection and the coupling of two neighboring elements once with the grounds of all connectors floating and ones with shorted grounds. In the first case, all feed cables, except the ones of the two elements being measured, have been routed radially away from the array. Then all connectors have been attached to a copper plate equipped with eight bulkhead jacks. By this all cables were set to common ground at the connector. In a span of 50 MHz around the imaging band almost no deviation occurs neither by rerouting the cables, nor by changing their grounding. A similar result was found by comparing the response of the coil when equipping the measured channels with tuned cable traps blocking remnant currents on the shield. This demonstrates that the cable shields are not significantly loaded by the array.

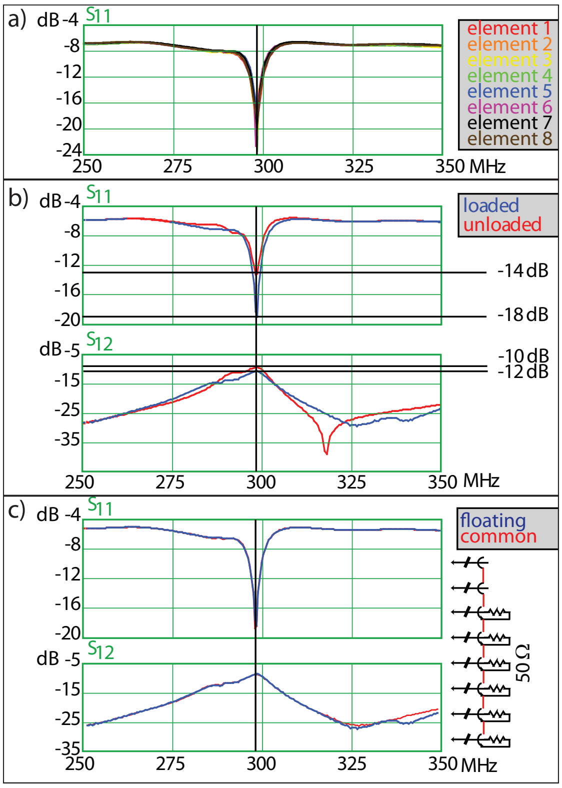

Figure 2.5: Bench tests of the array using a spherical loading phantom. The plots in a) show the magnitude of the reflection present in each port. b) shows the load dependence of the reflection and the coupling for the elements 1 and 2. Plot c) compares the s-parameters for floating grounds of all receive cables and for the case all grounds of the connectors were shorted during the measurement.

2.3.2 Imaging Experiments

Imaging experiments have been performed on a watermelon. In a first experiment, the RF shimming capability has been tested trying to remove local signal voids from transverse slices. Figure 2.6 shows root mean squares reconstructed images taken with different RF shims. The image on the left represents the nominal quadrature (homogeneous mode). It is seen that the excitation pattern within the

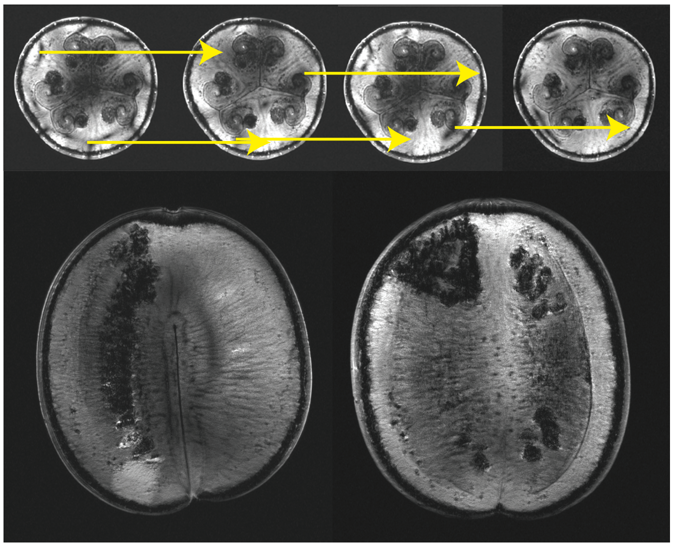

Figure 2.6: Results of RF shimming and imaging experiments using the feed system and the 8 channel coil array. The upper row of transverse slices shows that signal voids stemming from low RF excitation can be locally removed. The lower two images are sagittal and coronal images demonstrating the axial extent of the field of view of the coil. These images have been acquired by a gradient echo sequence with a repetition time of 60 ms on a 800 × 800 matrix and a field of view of 300 mm

coil can be drastically altered by RF shimming. However, a globally uniform RF shim was not found by this heuristic series of settings.

The axial coverage of the coil was demonstrated on central sagittal and coronal slices using RF shimming for optimizing the uniformity of the image. It is seen that uniform axial coverage can be achieved over the length of the melon ($\approx 25\,\text{cm}$). Additional experiments showing the RF shimming capability and precision of the array and the feed system are shown in Chapter 4.

2.4 Discussion & Conclusion

The presented setup consisting of an 8 channel transmit-receive array and an RF shimming capable feed system provided the basis for initial explorative experiments with parallel RF transmission. The implementation of a parallel RF feed system by a splitter matrix using passive components yielded high stability and an easy connection to the scanner at very low cost compared to electronically controlled systems but with the drawback of manual operation.

The central feeding employed on the 8 channel array provided high robustness to cable routing and grounding issues, which is a very important prerequisite for precise and reproducible measurements. Furthermore, grounding issues are expected to have a high impact on compliance testing of such a setup. Simulation and estimation of the power deposition in the sample is relying on well defined boundary conditions which cannot be provided if the cable shields, that can usually not be explicitly included in the model, are carrying high currents that even strongly depend on the exact configuration. Finally, it is well known that strong cable currents as such can be very harmful to the subject but also to the system itself. The centrally fed coil also allowed a high axial field of view due to the more uniform current distribution on the stripline compared to side-fed versions without capacitive splitting. As drawbacks, a slightly more complicated topology and a higher number of degrees of freedom for tuning and matching have to be mentioned. Furthermore, the intrinsic losses induced by the balun can be another disadvantage compared to feeding from the side.

The stripline topology of the array yields sufficiently low mutual coupling among the elements to prevent peak splitting and to allow for stable tuning and matching with a certain tolerance to variations in the loading. By capacitive decoupling of neighboring elements, the maximum coupling was kept below -12 dB. This value is comparable to those presented in literature [8, 9] when taking the smaller inner diameter (24 cm) and the longer axial extent of the presented coil into account. Nevertheless, it was found by the analysis of the scattering behavior of the coil, that by using the empirically found optimum values for the decoupling capacitor only 7 of 8 modes of the resonator can be coupled to the feed lines with a power efficiency of more than 50 %. Further improvement of the capacitive neighbor decoupling was not found to be an effective counter measure, because the coupling to elements at further distances became increased. The numerical structure of the S-matrices seen in Fig. 2.3 show that the coupling magnitude exhibits an alternating behavior being high for every pair of elements with an odd number of elements in between them. Also the phase of the coupled signal shows a distinct behavior by a fixed phase increment with increasing distance between coupling elements adding up to 2π around the array. Therefore it is assumed that the coupling behavior cannot be explained alone by the pairwise mutual inductances of only two elements in the array but must be found in the fact that the entire array structure forms in fact a volume TEM resonator with its distinct and in principle well known modal structure. Recalling that the same resonator structure is also used as a single channel volume resonator by relying on the mutual couplings between the single transmission lines, makes it plausible that simple neighbor decoupling might in certain situations not yield sufficient decoupling among all elements.

A further drawback of the TEM design found were the very high voltages across the tuning capacitors of up to $60\,{}^{\mathrm{V}}\!/\!\sqrt{\mathrm{W}}$. The consequently required withstanding voltage rating of the variable capacitances becomes therefore very challenging and opposing the needed compactness of such devices. The occurrence of such high voltages is closely linked to the high loaded Q-factors inherently encountered in TEM resonators due to their low loading fraction. While the impact of the low Q drop on the efficiency needs certainly more investigation especially in the context of very high frequencies where also radiative field components are expected to deliver significant contributions to B_1^+ without being directly linked to sample loading, the impact of the resulting narrow bandwidth in operation is more obvious. Especially the very steep phase gradient with respect to frequency in the transmission characteristic of a high Q LCR resonant circuit causes potentially high changes in the phase of the RF signal with respect to slight changes of the loading e.g. induced by sample motion. This effect can cause large inconsistencies in parallel transmission experiments if it occurs after or during the acquisition of the needed reference data sets.

Bibliography

[1] Kan S, Gonord P, Duret C, Salset J, and Vibet C. Versatile and Inexpensive Electronic System for a High-Resolution NMR Spectrometer. Rev Sci Instr 1973; 44(12):1725–1733.

[2] Schneider HJ and Dullenkopf P. Slotted Tube Resonator - New NMR Probe Head at High Observing Frequencies. Rev Sci Instr 1977; 48(1):68–73.

[3] Alderman DW and Grant DM. Eefficient Decoupler Coil Design Which Reduces Heating in Conductive Samples in Superconducting Spectrometers. J Magn Reson 1979; 36(3):447–451.

[4] Hayes CE, Edelstein WA, Schenk JF, Mueller OM, and Eash M. An efficient, highly homogeneous radiofrequency coil for whole-body NMR imaging at 1.5 T. J Magn Reson 1985; 63:622–628.

[5] Tropp J. Theory of the birdcage resonator. J Magn Reson 1989; 82:51–62.

[6] Vaughan T, Vaughan T, Garwood M, and Ugurbil K. Volume coils for highest field MRI. In Garwood M., editor, *Antennas and Propagation Society International Symposium, 2001. IEEE*; volume 1 2001. p. 378–381 vol.1.

[7] Bogdanov G and Ludwig R. Coupled microstrip line transverse electromagnetic resonator model for high-field magnetic resonance imaging. Magn Reson Med 2002; 47(3):579–593.

[8] Adriany G, Van de Moortele P-F, Wiesinger F, Moeller S, Strupp JP, Andersen P, Snyder C, Zhang X, Chen W, Pruessmann KP, Boesiger P, Vaughan T, and Ugurbil K. Transmit and receive transmission line arrays for 7 Tesla parallel imaging. Magn Reson Med 2005; 53(2):434–445.

[9] Vernickel P, Roschmann P, Findeklee C, Ludeke KM, Leussler C, Overwag J, Katscher U, Grasslin I, and Schunemann K. Eight-channel transmit/receive body MRI coil at 3T. Magn Reson Medicine 2007; 58(2):381–389.

[10] Mispelter J, Lupu M, and Briguet A. NMR Probeheads for Biophysical and Biomedical Applications. London, GB. Imperial College Press; 2006.

[11] Butler J and Lowe R. Beam-Forming Matrix Simplifies Design of Electronically Scanned Antennas. Electronic Design 1961; 97:170–173.

Chapter 3

Figures of Merit and Applications of Array Coils

partially published in:

D. O. Brunner, N. De Zanche and K. P. Pruessmann. *"A Comparison of Matching Strategies for RF Transmission Arrays Based on Network Theory"*. Proc Intl Soc Magn Reson Med 2008, Toronto. p. 143

De Zanche, Nicola Jurek Antonin Nordmeyer-Massner, David Otto Brunner and Klaas Paul Pruessmann. *"Noise Correlation and Coupling Mechanisms: A Comparison of Overlapped and Non-Overlapped Surfaces Coils"*. Proc Intl Soc Magn Reson Med 2008, Toronto. p. 1073

D. O. Brunner, J. A. Nordmeyer-Massner and K. P. Pruessmann. *"Information Theory in MRI"*. Proc Intl Soc Magn Reson Med 2009, Honolulu. p. 2978

D. O. Brunner, J. Paska, J. Froehlich and K. P. Pruessmann. *"SAR Assessment of Transmit Arrays: Deterministic Calculation of Worst- and Best-Case Performance"*. Proc Intl Soc Magn Reson Med 2009, Honolulu. p. 4803

D. O. Brunner, J. A. Nordmeyer-Massner and K. P. Pruessmann. *"An Information Theory Approach to Array Detection in MRI"*. Proc ESMRMB 2009, Antalya. p. 322

D. O. Brunner, J. Paska, J. Froehlich and K. P. Pruessmann. *"Exact Calculation of the Worst-Case Local SAR and the Highest Safe B_1^+ of a Transmitter Array"*. Proc ESMRMB 2009, Antalya. p. 194

D. O. Brunner and K. P. Pruessmann. *"SVD Based Calibration of Transmit Arrays"*. Proc Intl Soc Magn Reson Med 2010, Stockholm. p. 242

In this chapter, design goals of transmit but also receive array coils shall be deduced from the targeted applications of such devices. It will be shown that well known figures of merits of single channel devices are not straight forward extendable to multi-port devices. In line with these explanations, the basic methodology behind these techniques will be introduced such as the fundamentals of pulse design and RF shimming. It is assumed throughout this chapter that the ports of the array are well defined and that other network components, such as matching networks, interact only over these ports with the array.

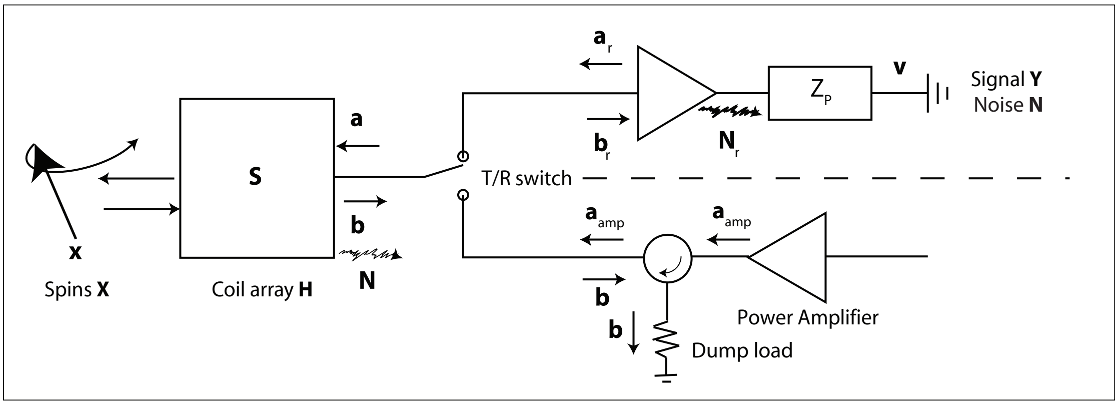

Figure 3.1: Block diagram of the setup considered. The coil array is represented by its scattering matrix **S**. The complex amplitudes of the waves incident on the array are collected in the vector **a** and the scattered waves correspondingly in **b** The channels of the array are connected over individual T/R-switches. The power amplifier are assumed to be reflection free which is in practice implemented by the usage of isolators at the outputs of the amplifiers. In receive mode, the array is connected to low noise preamplifiers for each individual channel.

3.1 Efficiency

3.1.1 Power Efficiency and SNR

From the first devices built for NMR measurements on, the power efficiency and SNR were the most important figure of merit of RF devices used. For NMR probes as such these performance measures are of course directly linked to the involved losses as it is explained in Chapter 1.3. It is defined as the ratio between the B_1^+ produced by a coil per square root of input power incident on the port of the coil (P):

$$\eta_P := \frac{B_1^+(P)}{\sqrt{P}}. \tag{3.1}$$

The advantage of the definition given above is that it is directly based on the application of an RF coil in NMR, namely exciting nuclear magnetism and receiving its signals. Since most NMR probe heads can be basically represented as a LCR circuit around the imaging band, the quality factor (Q) and the Q-drop ratio due to loading of the LC resonance is frequently used to represent their efficiency. Although the Q factor represents the loss fraction of a LC-resonator, some explicit assumptions[1] must be made on the coil topology and the field distribution of the probe in order to represent the real performance of the coil. Signal contributions retrieved over radiative field components of the coil are not taken into account by this approach, which is especially confounding at ultra-high frequencies. One of the main advantages of this approach is however, that it is directly measurable on the bench.

The generalization of the power efficiency metrics to multiple channels can be achieved by regarding the coil as a linear network of which each port is driven by a incident complex voltage wave which is collected in the vector **a** (see Fig. 3.1). Due to the non-uniform excitation produced by each channel, the efficiency is expected to be spatially variant and will therefore be defined as a local entity. The B_1^+ field produced by each individual coil c of the array per unit input power ($|\mathbf{a}_c|^2 = 1$) at a certain position ($B_{1,c}^+$) is linearly superimposing with the fields produced by the other channels and the resulting efficiency is therefore given by:

$$\eta_P := \max_{\mathbf{a}} \left(\frac{\sum_c B_{1,c}^+ (\mathbf{a})_c}{\sqrt{\mathbf{a}^H a}} \right) = \sqrt{\sum_c |B_{1,c}^+|^2}. \tag{3.2}$$

As a major difference to single channel devices, power incident on an array cannot only be reflected by mismatches of the port, but it can also be coupled into another port of the array. While the losses induced by this scattering (reflection + coupling) are negligible on reasonably matched single channel devices it can become a significant source of losses in arrays. Assuming that the feed lines ideally adsorb any power scattered by the array, a fact that is usually ensured by the presence of isolators at the output of each amplifier, we can calculate the scattering losses P_s and the effective power being dissipated in the array the array P^{diss} by measuring the scattering matrix $\mathbf{S}$ of the array by e.g. a network analyzer or

---

[1] The main confounding effects to be mentioned are basically that not all losses induced by the sample are actually linked to the NMR active field portions. Especially the influence of conservative electric field, longitudinal magnetic field components and especially at high frequencies radiated field portions are misinterpreted by this approach.

impedance meter. The S-parameters can in principle be measured quickly even while the subject is positioned inside the coil. $\mathbf{S}_{cc'}$ is defined as the amplitude of the s-wave emanating from port c of the array when driving port c' with unit amplitude. On this basis, assembling the instantaneous emanating and driving amplitudes of the array in the vectors $\mathbf{a}$, $\mathbf{b}$, respectively, the scattered waves are given by $\mathbf{b} = \mathbf{S}\,\mathbf{a}$. The power dissipated in the coil must be the difference between the power incident on the array and the power that is scattered back towards the amplifiers and ultimately into the dump loads:

$$\begin{aligned} P^{\mathrm{diss}} &= \sum_{c'} |\mathbf{a}_{c'}|^2 - \sum_{c} |\mathbf{b}_c|^2 = \mathbf{a}^H \mathbb{1} \mathbf{a} - \mathbf{a}^H \mathbf{S}^H \mathbf{S} \mathbf{a} = \mathbf{a}^H \underbrace{\left(\mathbb{1} - \mathbf{S}^H\ \mathbf{S}\right)}_{:=\boldsymbol{\Phi}^{\mathrm{diss}}} \mathbf{a} \\ P^S &= \mathbf{a}^H \underbrace{\mathbf{S}^H\ \mathbf{S}}_{:=\boldsymbol{\Phi}^S} \mathbf{a}. \end{aligned} \tag{3.3}$$

The power dissipation matrix $\boldsymbol{\Phi}^{\mathrm{diss}}$ and the scattering loss matrix $\boldsymbol{\Phi}^S$ are both positive (semi-)definite matrices. They fully describe the dissipation and scattering loss behavior of an array with respect to the incident voltage waves. From this, the array power efficiency can be defined relative to the dissipated and scattered power by the upper bound of B_1^+ that the array can produce per unit input power:

$$\begin{aligned} (\mathbf{B}_{\mathbf{1}}^+)_c &:= B_{1,c}^+ \\ \eta_{\mathrm{diss}} &:= \sqrt{\mathbf{B}_{\mathbf{1}}^{+\,H} (\boldsymbol{\Phi}^{\mathrm{diss}})^{-1} \mathbf{B}_{\mathbf{1}}^+} \\ \eta_S &:= \sqrt{\mathbf{B}_{\mathbf{1}}^{+\,H} (\boldsymbol{\Phi}^{S})^{-1} \mathbf{B}_{\mathbf{1}}^+}\,. \end{aligned} \tag{3.4}$$

These expressions are the analogues to the optimum SNR reconstruction for receive coil arrays as described in Ref. [1]. Of these two η_{diss} is of special importance, since it represents the effeciency of the array with respect to the power that is actually dissipated within the array and hence potentially in the sample.

The scattering losses on the other hand reflect the quality of the multi-channel matching and decoupling and can therefore be used to evaluate the effectiveness of matching networks. A main difference occurring compared to single channel devices is the dependence of the relative scattering losses on the input wave vector ($\mathbf{a}$). Therefore the losses have to be assessed in a time average or statistical manner with respect to the time dependent input wave vector $\mathbf{a}(t)$. In this case it can be found that:

$$\begin{aligned} \overline{\mathbf{P}^{\mathrm{diss}}(\mathbf{a}(t))} &= \frac{1}{T} \int_0^T \mathbf{a}(t)^H \boldsymbol{\Phi}^{\mathrm{diss}} \mathbf{a}(t) dt = Tr\left(\kappa_{\mathbf{a}(t)} \boldsymbol{\Phi}^{\mathrm{diss}}\right) \\ \overline{\mathbf{P}^{S}(\mathbf{a}(t))} &= Tr\left(\kappa_{\mathbf{a}(t)} \boldsymbol{\Phi}^{S}\right) \\ \text{where } \left(\kappa_{\mathbf{a}(t)}\right)_{c,c'} &:= \frac{1}{T} \int_0^T (\mathbf{a}(t))_c^* \cdot (\mathbf{a}(t))_{c'} dt. \end{aligned} \tag{3.5}$$

From this, the array excess power factor R can be defined expressing the extra power that has to be provided by the transmission chain due to imperfect matching and decoupling relative to an ideally matched and decoupled equivalent situation:

$$R := \frac{Tr\left(\kappa_{\mathbf{a}(t)}(\mathbf{\Phi}^{\text{diss}})^{-1}\right)}{Tr\left(\kappa_{\mathbf{a}(t)}\right)}. \tag{3.6}$$

As an alternative approach, which is also very often used in descriptions of array antennas for communication and RADAR purposes [2], an eigenvalue value decomposition of the scattering matrices, the dissipation and scattering loss matrices - which have common eigenvectors for the incident and the scattered wave ($\mathbf{a}^k_{\text{eig}}$, $\mathbf{b}^k_{\text{eig}}$ respectively) can be used to gain a more intuitive understanding of the matching and coupling behavior of an array. The eigenvectors represent driving vectors that stay up to a constant factor, given by the corresponding eigenvalue, unchanged when scattered by the array. Considering these eigenmodes of the array as ports by themselves, the array becomes ideally decoupled with respect to these ports and therefore each mode can be considered separately from all others. Therefore the eigenvector analysis of the scattering behavior of an array delivers clear information about the matching, dissipation and losses of each mode of the array in similar manner to a single channel device. Modes that have a very high reflection (represented by the scalar mode rejection ratio s^k) can therefore not be excited power efficiently, which will in most cases be reflected by the mode's coupling efficiency η^k_{eig}:

$$\begin{aligned} \mathbf{b}^k_{\text{eig}} =& \mathbf{S}\mathbf{a}^k_{\text{eig}} = s^k \mathbf{a}^k_{\text{eig}} \\ \eta^k_{\text{eig}} :=& \frac{\mathbf{B}^T \mathbf{a}^k_{\text{eig}}}{\|\mathbf{a}^k_{\text{eig}}\|} \\ \eta^k_{\text{eig opt}} :=& \eta^k_{\text{eig}} \frac{1}{\sqrt{1-|s_k|^2}}. \end{aligned} \tag{3.7}$$

The effective number of degrees of freedom inside the array is lower than the number of channels if η^k_{eig} is significantly lower for some k. If the mode rejection s_k for the same mode k is high, the degrees of freedom achievable in the array can be increased by decoupling and matching optimizations. The maximum achievable efficiency of each each mode is given by $\eta^k_{\text{eig opt}}$ above, which corrects for the mode reflection diminishing the efficiency.

A further aspect of the loss matrices is gained by expansion of the reciprocity relation for losses within an RF device and its noise behavior as described in section 1.3 to multiple port devices. It has been shown [3] that the noise voltage covariance matrix $\mathbf{\Psi}^{\text{noise}}$ of a matched multi port device is mainly given by the matrix representing the dissipative losses inside the device $\mathbf{P}^{\text{diss}}$ and the reference impedance R^{ref} of the s-parameter measurement and the uniform temperature of the system T:

$$\mathbf{\Psi}^{\mathrm{noise}} = 4k_B T R_{\mathrm{ref}} \mathbf{\Phi}^{\mathrm{diss}}. \tag{3.8}$$

This formula lets the target of decoupling a coil array to reduce the scattering losses and the reduction of noise correlation in the received signal coincide. It has to be noticed at this point, that this only applies to the noise emanating from the array and stays only valid if the preamplifiers are matched to the reference impedance of the system. The reflections of the preamplifiers would cause the net scattering of the array to change in receive mode.

These mathematical tools have been used in order to evaluate different matching strategies for transmission arrays in Ref. [4]. It is found that the scattering and dissipation losses become independent of the signal correlation among different channels if the corresponding loss matrices ($\mathbf{\Phi}^{\mathrm{diss}}$, $\mathbf{\Phi}^{S}$) are diagonal. Vice versa noise retrieved from the different channels becomes uncorrelated for these cases. Astonishingly, these matrices do not only become diagonal if a high isolation between the channels can be achieved but also by omitting any direct reflections in each channel ($\mathbf{S}_{ii} = 0$) or by matching each port to another eigenvalue of the array's impedance matrix. All these considerations stay only valid in this form, if the matching network itself is attached at well defined ports of the array. This means that the matching network itself must only interact with the array over the defined modes in the ports and must not alter for instance the current paths in the coil. Also if stray fields of variable elements of the matching network interact with the sample or with other coil elements the prerequisites of this kind of analysis is violated in a rigorous sense. In these cases full wave approaches taking the field changes of each variable element separately into account have to be used as shown in [5, 6] in order to determine the field strength and distribution within the coil and concomitantly the power efficiency measures.

3.1.2 SAR Efficiency and Safety

Having a highly power efficient coil is of great importance for transmission , if the achievable strength of the excitation is limited by the power that the RF amplifier can deliver. In most in-vivo applications, transmission power is not restricted by technical limitations of current designs of power amplifiers and RF probes, but by the potentially negative effects induced by the RF radiation incident on the tissue. The potential risk of electromagnetic radiation especially at RF frequencies are still the topic of currently ongoing discussion, not only in the field of MRI. Current safety guidelines [7] however do only impose restrictions on the RF power dissipation in the tissue and on the thermal heating resulting thereof, unlike for instance in the audio/DC frequency regime, where also limits with respect to the field strengths are set. At current status, it is therefore reasonable to base the validation and the compliance testing on the power deposition causing the heating. If these constraints are the most limiting ones, which is especially at high field strength often the case-, it is useful to define the efficiency according to the maximum tolerated specific power adsorption in the tissue. Since the RF power deposition is varying across the sample, the power is constrained ($P < P^{\max}$) for human MRI systems to the peak local and global SAR among all specified averaging volumes (Ω_p, $SAR(\Omega_p, P)$) as declared in the safety standards [7]. Therefore an efficiency of a SAR limited RF coil with respect to the maximum allowed SAR in all test volumes ($SAR_{\text{tol}}(\Omega_p)$)can be defined by:

$$\begin{aligned} P^{\max} &= \max_p \frac{SAR_{\text{tol}}(\Omega_p) \cdot P}{SAR(\Omega_p, P)} \\ \eta_{\text{SAR}} &:= B_1^+ \sqrt{P^{\max}}. \end{aligned} \tag{3.9}$$

Using a multichannel coil array, evaluation of these numbers becomes more intriguing, because the electric field distribution inside the sample is altering upon the relative input voltages applied to each port [8, 9]. Since the RF power dissipation is determined by the local, superimposed electric field of all coils and the local ohmic conductivity (σ), the SAR is given by:

$$\begin{aligned} SAR_p &= \frac{1}{2T_0 V_p} \int_0^{T_0} \int_{\Omega_p} \sum_{c,c'} \frac{\sigma(\vec{r})}{\rho(\vec{r})} (\mathbf{a})^*_{c'}(t) \vec{E}^*_{c'}(\vec{r}) \cdot \vec{E}_c(\vec{r}) (\mathbf{a})_c(t) \, dV \, dt \\ &= \sum_{c,c'} \frac{1}{2T_0 V_p} \int_{\Omega_p} \frac{\sigma(\vec{r})}{\rho(\vec{r})} \vec{E}^*_{c'}(\vec{r}) \cdot \vec{E}_c(\vec{r}) dV \int_0^{T_0} (\mathbf{a})^*_{c'}(t) (\mathbf{a})_c(t) \, dt \\ &= Tr\left(\mathbf{\Psi}^p \kappa_{\mathbf{a}(t)}\right) \text{ with } \mathbf{\Psi}^p := \frac{1}{2V_p} \int_{\Omega_p} \frac{\sigma(\vec{r})}{\rho(\vec{r})} \vec{E}^*_{c'}(\vec{r}) \cdot \vec{E}_c(\vec{r}) dV \end{aligned} \tag{3.10}$$

whereas $\vec{E}_c(\vec{r})$ determines the local electric field produced by coil c per square root of input power incident on the port, V_p denotes the volume of Ω_p and ρ is the mass density distribution of the tissue. Due to the temporal variation of the spatial SAR distribution, the maximum allowed power and the SAR efficiency have to be evaluated for each pulse sequence separately in the most general case. What comes in hand is that the evaluation of all the local SAR values can be based on the positive (semi-)definite SAR-matrices $\mathbf{\Psi}^p$ for each test volume. In the case the SAR-matrices are deduced from electromagnetic field simulations using Eq. 3.10, the calculation of the SAR based on the SAR-matrices will exhibit that the number of test volumes is for biological structures usually much lower than the number of cells used in the discretization of the electromagnetic calculation. Furthermore, the separation of the spatial integration (SAR-matrix) and the time domain integration

($\kappa_{\mathbf{a}(t)}$) performed in this calculation scheme restricts the calculation needed for different pulses and sequences to that in the time domain plus the matrix vector product in each test volume. The numerically very expensive spatial integration needs consequently only to be performed once.

For the evaluation of coil array designs it is very useful to know the maximum strength of B_1^+ that can be produced within the SAR boundaries. This value would not only allow a quantitative comparison among different arrays, the calculation would also directly yield optimum RF shims with respect to SAR efficiency. In contrast to single channel systems, the RF shim generating maximum excitation at minimum peak SAR has to be found. By this a upper bound for the local SAR efficiency $\eta_{\mathrm{SAR}}^{\mathrm{best}}$ is found and the following optimization problem has to be solved:

$$\begin{aligned} \eta_{\mathrm{SAR}}^{\mathrm{best}} &= \max_{\mathbf{a}} \left|\mathbf{B}^T \mathbf{a}\right| \\ \text{such that: } \mathbf{a}^H \mathbf{\Psi}^p \mathbf{a} &< SAR_{\mathrm{tol}}(\Omega_p) \ \forall p. \end{aligned} \tag{3.11}$$

Since this optimization problem is not convex in this formulation, it is very hard to solve without numerical ambiguities. Fortunately there is a formulation that is convex and can therefore be treated as a Semi Definite Programme (SDP). This class of numerical problems can be efficiently solved and with deterministic numerical bounds even for large scale problems:

$$\begin{aligned} SAR_{\mathrm{min}}^{\mathrm{rel}}(\vec{r}) &= \min_{\mathbf{a}} w \\ \text{such that: } \mathbf{a}^H \mathbf{\Psi}^p \mathbf{a} &\leq w \cdot SAR_{\mathrm{tol}}(\Omega_p) \ \forall p \\ \mathbf{B}^T(\vec{r})\mathbf{a} - 1\,\mu\mathrm{T} &= 0 \\ \eta_{\mathrm{SAR}}^{\mathrm{best}}(\vec{r}) &= \frac{1\,\mu\mathrm{T}}{\sqrt{SAR_{\mathrm{min}}^{\mathrm{rel}}(\vec{r}) \cdot SAR_{\mathrm{tol}}(\Omega_{\mathrm{max}})}}. \end{aligned} \tag{3.12}$$

As an alternative to an online SAR monitoring that needs to check each RF shim or multi-channel pulse, the worst-case SAR value could be used as an upper bound in order to limit the total power sent to the array to a globally safe value. This worst-case SAR (SAR_p^{worst}) would need to represent the exact maximum of power that can be safely induced with any configuration of driving voltages of unit power. This worst-case SAR can be determined by an eigenvalue decomposition of the SAR matrices ($\mathbf{\Psi}^P = \mathbf{U}^H \mathbf{\Lambda}^p \mathbf{U}$) yielding the maximum allowed total input power and a corresponding lower bound efficiency $\eta_{\mathrm{SAR}}^{\mathrm{worst}}$:

$$\begin{aligned} SAR_p^{\mathrm{worst}} &= \max_p \max_{\mathbf{a}} \left(\frac{\mathbf{a}^H \mathbf{\Psi}^p \mathbf{a}}{\mathbf{a}^H \mathbf{a}} \right) = \max_p \max_k \left(\frac{\mathbf{u}_k^H (\mathbf{\Lambda}^p)_{kk} \mathbf{u}_k}{1} \right) \\ &= \max_p \max_k (\mathbf{\Lambda}^p)_{kk} = \Lambda_{\max} \\ P^{\max} &= \max_p \frac{SAR_{\mathrm{tol}}(\Omega_p)}{SAR_p^{\mathrm{worst}}} = \frac{SAR_{\mathrm{tol}}(\Omega_p)}{\Lambda_{\max}} \\ \eta_{\mathrm{SAR}}^{\mathrm{worst}}(\vec{r}) &:= \|\mathbf{B}_1^+(\vec{r})\| \sqrt{P^{\max}}. \end{aligned} \tag{3.13}$$

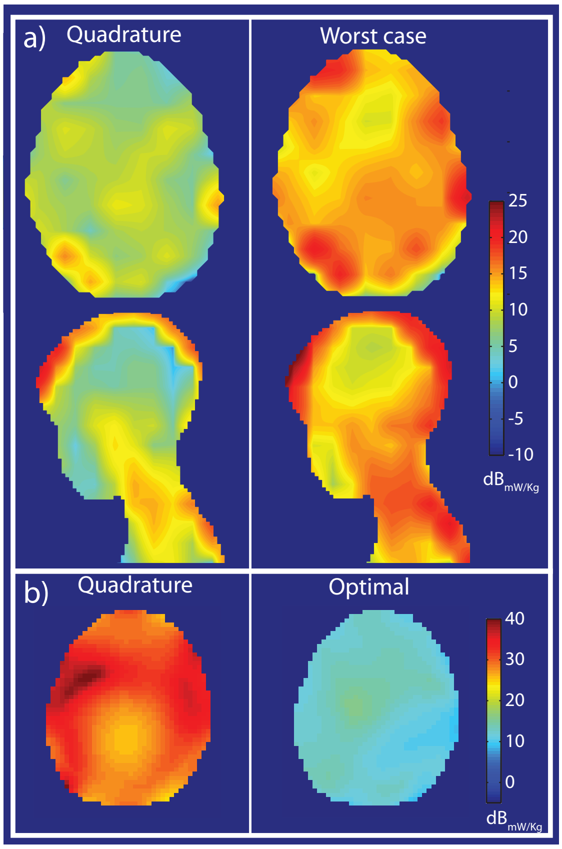

Figure 3.2: : Worst- and best-case scenarios for the 8 channel head array. Plot a) shows the SAR over 10 g distribution for 1 W total input power for the quadrature drive of the elements and in a worst-case scenario for each location. The minimum peak local SAR (SAR_{min}) needed to produce 1 μT is compared to the quadrature drive in b).

It can be seen, that if the electric field patterns and the conductivity distribution in the subject are known, the worst-case estimate boils down to the calculation of the maximum eigenvalue of all SAR matrices. It has to be noted that the worst case efficiency is defined as the maximum B_1^+ field that can be achieved assuming the worst case scenario. An even lower efficiency can of course be realized by locally superimposing the B_1^+ fields destructively, which however was not considered to render reasonable information on the performance of the array. Therefore the efficiency defined from the worst-case scenario can be regarded as a lower bound for the SAR efficiency of coil array for a reasonable but cautious user.

From a theoretical perspective it can be concluded that the SAR efficiency of a coil array is dependent on the RF shim that is applied. However, for quantitative comparisons close upper and the lower bounds of the SAR efficiency can be unambiguously calculated.

As an example of such analysis, the worst-case local SAR and the minimum peak local SAR needed for 1 μT ($SAR_{\min}$) have been calculated for the 8 channel head array based on field distributions calculated using FDTD. The FDTD cubicle mesh cells had a size of 2 mm and the SAR was determined for volumes with approximately 10 g of tissue. The local worst- and best-case scenarios are compared to quadrature driving. The results are collected in Fig. 3.2. The plots show the huge span in which the efficiency and correspondingly the potential local SAR can vary inside an array coil, depending if the array is driven in worst-case or optimally. In fact, the SAR peak value can be up to 10 dB higher per unit input power compared to a birdcage-like quadrature configuration. On the other hand, the SAR efficiency can be locally 15 dB higher than in quadrature.

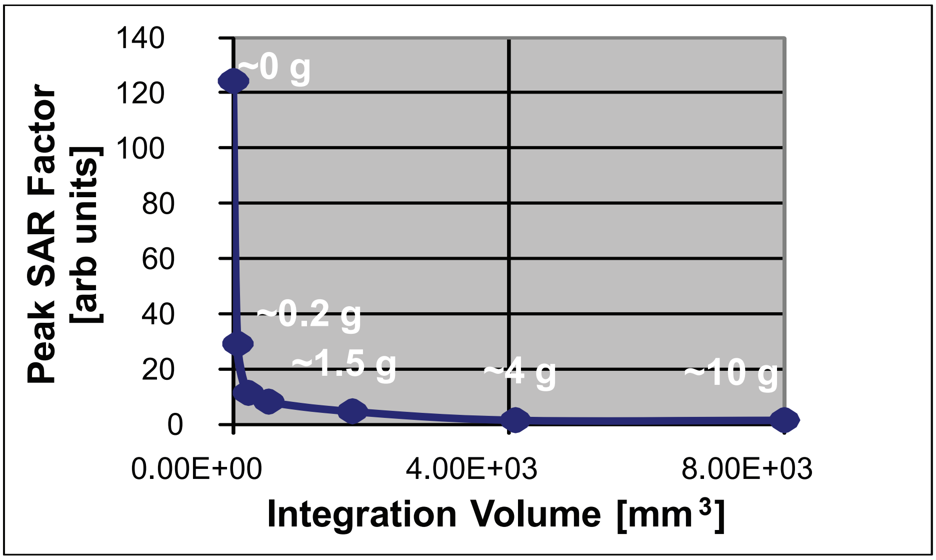

Figure 3.3: : Plot of the peak SAR in dependence of the size of the test volumes Ω_p.

Because of the very non-uniform distribution of the conductivity in the human body, e.g. there is a high dielectric contrast in the human head between the bone and the cerebrospinal fluid, the power deposition will consequently be very localized too. However, since the potentially resulting temperature increase is not expected to be so strongly localized due to the significant amount of heat transport present within the human body by heat conduction but also perfusion and blood flow, the SAR deposition must be considered within thermally relevant volume fractions. The current guidelines [7] recommend an averaging over volumes with 10 g of tissue mass. The effect of such an averaging is shown in Fig.3.3.

3.1.3 Conclusions

The presented results above indicate the potential problems that rigorous safety validations for routine use of parallel transmission are facing due to the huge dependence of the results on the driving configuration but also on the details of the guidelines. On top of that, variability in the considered electromagnetic model, such as the exact positioning of the head in the coil and the inter-individual differences, have not even been taken into account at this point. Of course the safety can be ensured by limiting the power to the most critical case, but this might inhibit many applications and destroy the advantages of coil arrays compared to single channel systems. On the other hand, the application of specific power limitations must rely on much more accurate knowledge of the power distribution and also the actual system state to alow a safe operation close to the SAR limitations than in a single channel case.

The fact that the spatial distribution of the power deposition gains a crucial importance represents as such a breaking of the symmetry between transmission and reception as stated by the reciprocity relation. The duality between transmission losses and received noise refers only to the total sum of the losses. As soon as strict constraints on the local power deposition are imposed, the efficiency of the probe does not follow simple reciprocity statements. This makes clear, that the methodology applied to determine optimal receive coil combinations are not generally yielding optimal results for transmission problems such as RF shimming or pulse design.

3.2 Spatial Encoding with Arrays

One of the main benefits gained from RF arrays in transmission is the possibility to change the effective field pattern during a NMR experiment. While the variability offered to the electric field is one of the main concerns for compliance of such devices, the steerability of the NMR active magnetic field is one of their most important abilities. The linear superposition of the magnetic fields allows to target the field pattern within the sample to a certain extend and allows the array not only to adapt its excitation pattern for multiple applications but it also renders some spatial encoding capabilities. In order to evaluate the performance of an array it is necessary to take this into consideration.

3.2.1 RF Shimming

The previously discussed calculations of the optimal array performance with respect to input power and SAR represent already two RF shimming approaches. However, those calculations are only considering the excitation field in one point within sample at the time. On the contrary, one of the prospectively most useful applications is to optimize the excitation field over a volume that is larger than the typical variation scale of the RF fields. Methods not relying on actual B_1^+ maps have been proven particularly useful in practice due to the simplicity of the acquisition of the reference data. A good comparison of various RF shimming methods for hands-on purposes can be found in Ref. [10].

However, when it comes to the question of the maximum uniformity that is achieved by an array within a specific target volume, there are two particular problems to be considered: Since usually in MRI the term uniformity is attributed to the magnitude of the B_1^+ field, the optimization problem to be solved in order to get a uniform excitation over the volume Ω with strength B_1^+ within the SAR (SAR_{tol}) and the power limitations of the amplifiers (per channel ($P_c^{\max}$) as well as in total ($P^{\max}$) over all channels) is of the following kind:

$$\begin{aligned} &\min \left(\int_\Omega \left| |\mathbf{B}^T(\vec{r})\mathbf{a}| - B_1^+ \right| d\vec{r} \right) \\ \text{such that/and: } &\mathbf{a}^H \mathbf{\Psi}^p \mathbf{a} \le \frac{w}{SAR_{\text{tol}}(\Omega_p)} \ \forall p \\ &\mathbf{a}^H \mathbb{1} \mathbf{a} \le P^{\max} \\ &|\mathbf{a}^H \cdot \mathbf{e}_c|^2 \le P_c^{\max}. \end{aligned} \tag{3.14}$$

The first obstacle to get the solution of the above problem arises by the non-convexity of the target function. These so called magnitude least squares problems are hard to solve unambiguously even neglecting the SAR and power constraints. Although there is the possibility to get some error bound by convex relaxation [11] there is no guarantee for the optimality of the numerical solution. While for many applications having a good but maybe not optimal shim is fully sufficient, inconsistent and misleading results might be obtained when comparing different array designs, tuning and matching options. The second problem is introduced by the fact, that in practice the power and SAR efficiency of the resulting RF shim is rapidly decreasing the more the uniformity is enforced. This makes it in general very difficult to judge the uniformity of an array with one single number in a meaningful manner and the relation between power and uniformity has to be compared in more detail as in Ref. [12] or even for every application separately.

For some applications such as for certain localized spectroscopy, the goal of an RF shim is just to maximize the signal power retrieved from a volume of interest.

Furthermore, in this situation a fixed coil combination for the received signals has to be found. For simplicity of the following derivation it is assumed, that the receive channels are already noise-prewhitened. In this case, the signal power retrieved out of a region of interest (P^{Signal}) in a linear transmission regime is given by:

$$\begin{aligned} P^{\text{Signal}}(\mathbf{w}, \mathbf{a}) &\propto \int_{\text{ROI}} M_0(\vec{r}) \sum_{c,c'} \mathbf{w}_{c'} B^-_{1,c'}(\vec{r}) B^+_{1,c}(\vec{r}) \mathbf{a}_c d\vec{r} \\ &= \mathbf{w}^H \mathbf{S}^{\text{ROI}} \mathbf{a} \text{ with } \mathbf{S}^{\text{ROI}} := \int_{\text{ROI}} M_0(\vec{r}) B^-_{1,c'}(\vec{r}) B^+_{1,c}(\vec{r}) d\vec{r}. \end{aligned} \tag{3.15}$$

The received signal power is characterized by a bilinear form represented by the signal matrix $\mathbf{S}^{\text{ROI}}$ weighted by the spin density M_0. This matrix can be acquired for instance by separately imaging the excitation induced by each channel or linearly independent sets of channel combinations (see Chapter 4) while receiving with all channels in parallel. Resulting from a singular value decomposition of the signal matrix, the optimal RF shim ($\mathbf{a}^{\text{opt}}$) and the optimal receive combination ($\mathbf{w}^{\text{opt}}$) are determined by the left and right singular vectors corresponding to the maximum eigenvalue. Therefore the calculation of signal power optimal coil combinations can be performed fast and unambiguously by a simple SVD $\mathbf{S}^{\text{ROI}} = \mathbf{U}\mathbf{\Sigma}\mathbf{V}^H$ in this case:

$$\begin{aligned} P^{\text{Signal}}(\mathbf{w}, \mathbf{a}) &\propto \mathbf{w}^H \mathbf{S}^{\text{ROI}} \mathbf{a} \\ &= \sum_k \mathbf{w}^H \mathbf{U}_k \mathbf{\Sigma}_{kk} \mathbf{V}_k^H \mathbf{a} \\ \max_{\|\mathbf{a}\|=1;\ \|\mathbf{w}\|=1} P^{\text{Signal}}(\mathbf{w}, \mathbf{a}) &\propto \max_k \Sigma_{kk} \\ \text{with } \mathbf{w}^{\text{opt}} = \mathbf{U}_{k^{\max}}&;\ \mathbf{a}^{\text{opt}} = \mathbf{V}_{k^{\max}} \end{aligned} \tag{3.16}$$

whereas $k^{\max} = \arg\max_k(P^{\text{Signal}}(\mathbf{w}, \mathbf{a}))$ and $\mathbf{U}_k$, $\mathbf{V}_k$ represent the kth column vector of $\mathbf{U}$ and $\mathbf{V}$ correspondingly.

The optimality of the RF shim derived above is determined relative to the amplifiers total output power $\|\mathbf{a}\|^2$. The optimality can also be referenced to any other positive definite power entity represented by a positive definite matrix $\mathbf{\Psi}$ by recombining the transmit channels analogously to noise prewhitening procedures in the receive case entering $\mathbf{\Psi}$ as "noise covariance" matrix of the transmit channels. However, the extension to several power constraints is not as trivial as in Eq. 3.12 since the equality constraint ensuring the excitation would become quadratic at its best.

If the signal retrieved out of an ROI has to be maximized for an imaging experiment, the problem has to be treated slightly differently because the resolution of the final image is usually much higher than the variation of the RF fields in the subject. The high resolution allows to adapt the receive coil combination on a per pixel basis during reconstruction in contrast to the RF shim which has to be applied globally for the entire image acquisition. The possibility to adjust the receive coil superposition a posteriori breaks the symmetry of transmission and reception in similar way as constraints on local power adsorption do as discussed in Section 3.1.3. By this receive array can cover large volumes without local losses in the total sensitivity due to destructive superposition of individual coil's sensitivity. This can be the case in transmission, where one superposition is applied for the whole volume at the time which can it make impossible to avoid such signal extinction. This must be taken explicitly into account when calculating signal optimal RF shims. This can be done if the signal matrix ($\mathbf{S}^\rho$) mentioned above is known for each voxel (ρ). The optimal receive coil combination for each voxel $\mathbf{w}_\rho^{\text{opt}}$ (and the corresponding optimum RF shim $\mathbf{a}_\rho^{\text{opt}}$) is determined from $\mathbf{S}^\rho$ the same way as in the single voxel case (Eq. 3.16. The optimum RF shim yielding the maximum signal after the voxel based reconstruction can be derived from the total sum of all voxel's signal power after optimal reconstruction:

$$\begin{aligned}
\max_{\|\mathbf{a}\|=1;\ \|\mathbf{w}_\rho\|=1} P^{\text{Signal}} &\propto \max_{\|\mathbf{a}\|=1;\ \|\mathbf{w}_\rho\|=1} \sum_{\rho\in ROI} \left|\mathbf{w}_\rho^H \mathbf{S}^\rho \mathbf{a}\right|^2 \\
&= \max_{\|\mathbf{a}\|=1} \sum_{\rho\in ROI} \left|\mathbf{w}_\rho^{\text{opt}} \mathbf{U}\mathbf{S}^\rho \mathbf{V}^H \mathbf{a}\right|^2 \\
&= \max_{\|\mathbf{a}\|=1} \sum_{\rho\in ROI} \left|\Sigma_{k^{\max}k^{\max}}\right|^2 \left|(\mathbf{a}_\rho^{\text{opt}})^H \mathbf{a}\right| \\
&= \max_{\|\mathbf{a}\|=1} \sum_{\rho\in ROI} \sum_{c,c'} \mathbf{a}_c^* (\mathbf{a}_\rho^{\text{opt}})_c (\mathbf{a}_\rho^{\text{opt}})^*_{c'} \mathbf{a}_{c'} \\
&= \max_{\|\mathbf{a}\|=1} \mathbf{a}^H \mathbf{\Omega} \mathbf{a} \\
\text{with } (\mathbf{\Omega})_{cc'} &:= \sum_{\rho\in ROI} \left|\Sigma_{k^{\max}k^{\max}}\right|^2 (\mathbf{a}_\rho^{\text{opt}})_c (\mathbf{a}_\rho^{\text{opt}})^*_{c'}.
\end{aligned} \tag{3.17}$$

The signal optimal RF shim $\mathbf{a}^{\text{opt}}$ can be found by an eigenvalue decomposition of the matrix $\mathbf{\Omega}$ and corresponds to the eigenvector with the eigenvalue of maximum magnitude analogously to the single voxel case. However, the summation of the optimal RF shims for each voxel weighted by their signal amplitude ensures that the signal yield of the computed global RF shim is maximized over the entire ROI with respect to the nominal input power. As discussed above in the spectroscopy case, the transmission power the optimality of the RF shim is referring to can be changed to any single definite power entity, but also here the extension to a plurality of power and SAR constraints is not trivial to solve without any numerical ambiguities.

Besides the ability to calculate signal optimal RF shims, the methodology derived above provides a way for bootstrapping the calibration of transmit arrays and reconstructing images acquired with different RF shims preserving the relative phase information. In order to optimally combine signals received from a receive array coil, the sensitivities of each element have to be known [1, 13]. Acquiring these receive sensitivities is especially challenging at ultra-high field conditions and in conjunction with transmit-receive arrays, since local signal voids induced by destructive interferences of the transmit B_1^+ fields cause strong local noise amplification in the obtained sensitivity maps. This noise propagates into the reconstructed images subsequently used e.g. as input for B_1^+ calculations, for the design of tailored RF pulses or other parallel imaging modalities. Magnitude based coil combination methods cannot be used in this context because the phase relation between the transmit channels have to be preserved by the reconstruction. When acquiring the transmit calibration data, this problem ends therefore in a tricky predicament: Signal voids in the transmit field corrupt the retrieved receive sensitivity profiles while the strong noise amplification arising thereof hampers the acquisition of the transmit sensitivities, which would be needed to shim the transmit field in order to get a reliable receive signal combination. Interestingly, $(\mathbf{w}_\rho^{\mathrm{opt}})^*$ and $(\mathbf{a}_\rho^{\mathrm{opt}})^*$ in Eqs. 3.16 represent as such noise optimally reconstructed coil sensitivity references for reception and transmission because they project on the maximum singular value of the voxel's signal matrix. Since a multitude of imaging acquisitions, that must only allow to span the entire linear space of possible excitations, is measured to acquire the signal matrices $\mathbf{S}^\rho$, a uniform RF shim for the reference measurement is not needed to begin with. Signal drop outs due to destructive interferences among elements of the array in one acquisition are noise optimally compensated if any RF shim exists exciting this portion of the sample sufficiently.

Since the maximum eigenvalue of each voxel represents not only the product of B_1^+ and B_1^- but depends also on the equilibrium magnetization present during the acquisition sequence, $\Sigma_{k\mathrm{max}}^\rho$ determines the signal-optimally reconstructed value of the voxel ρ fitting the bilinear signal model for any imaging sequence. As such, this approach can be understood as the generalization of a signal optimal receive array reconstruction [1] to transmit-receive arrays. The advantages of such an approach compared to a derivation of calibration data and reconstruction of images with quadrature excitation with the same baseline SNR is shown in Fig. 3.4.

3.2.2 Combination of gradient and array encoding

Since the beginning of MRI, the encoding capability of the RF receivers was used to restrict the field of view that needs to be encoded. More recently, upcoming parallel imaging techniques make an explicit use of the spatial RF encoding capa-

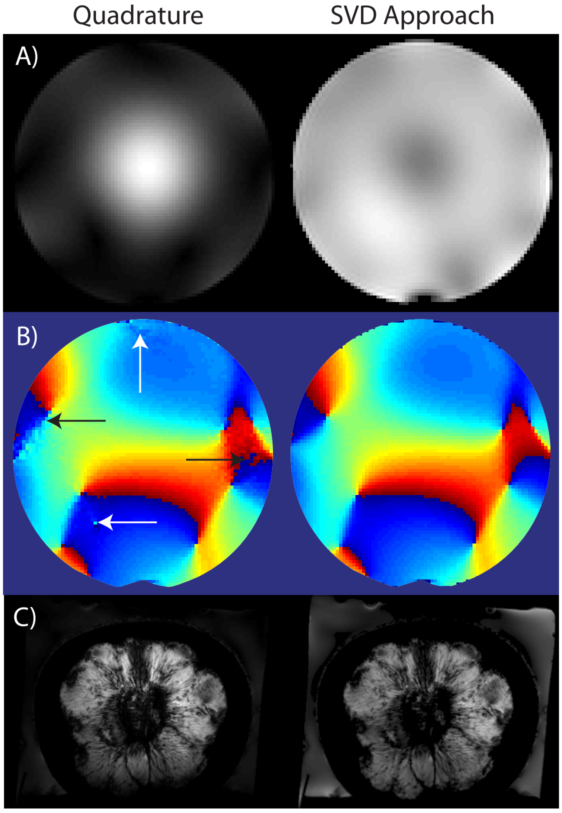

Figure 3.4: Comparison of the signal optimal approach to quadrature excitation for the calibration of a transmit arrays. Row A) and C) compare the reconstructed images retrieved for a 15 cm spherical saline water phantom and a grapefruit submerged in a 10 liter water container. The improvements of the image uniformity is obvious in both cases. Images B) show the spatial distribution of the relative receive phase derived for channel 1. In the case the phase is referenced to quadrature excitation, strong local noise enhancement occurs at positions of low excitation which is not the case using the SVD reconstruction on the same data set as indicated by the arrows.

bility of receive arrays concomitantly with the spatial encoding performed by the gradients [13, 14, 15]. The encoding provided by the RF fields and by the gradients complement each other in the sense that the RF encoding is instantaneous but of low spatial resolution and the gradient encoding can provide very high resolution but forces a sequential read out of the spatial information. While the exact influence of the gradients is sequence dependent, it is remarkable that the encoding performed by the receive array is entirely separable from all other encoding processes applied to the nuclear magnetization. This makes parallel receive methods in general very versatile and allows acceleration of almost every imaging sequence.

Signal Models and Reconstruction

The reconstruction approach discussed in this work relies on an algebraic inversion of the forward model representing the encoding process. The generality of this approach proved to provide a very high versatility and has some close relation to recent linear pulse design approaches. Therefore the methodology used for modeling the signal, its discretization and the numerical approaches commonly used for its inversion will be discussed to some extent in this short review.

The signal model and its discretization The signal $S_c(t)$ received by coil c can be expressed using the known spatial sensitivity modulation $s_c(\vec{r})$[2], the net phase term added by the gradient action $e^{i\vec{k}(t)\cdot\vec{r}}$ plus the phase induced by local offresonances $e^{i\omega_0(\vec{r})t}$ and the transverse magnetization density $\rho(\vec{r})$.

$$S_c(t) = \int_{\mathbb{R}^3} \rho(\vec{r}) s_c(\vec{r}) e^{i\vec{k}(t)\cdot\vec{r}} e^{i\omega_0(\vec{r})t} d\vec{r}. \tag{3.18}$$

The separability between the encoding induced by the gradients and the sensitivity modulation is one of the main reasons for the great impact of parallel imaging, because it gives the methodology inherently the versatility to be added to almost all kind of sequences with gradient modulation induced spatial encoding.

For compact notation the linear signal encoding distribution can be introduced as:

$$S_c[\rho(\vec{r})](t) := S_c(t) \tag{3.19}$$

The formal frame of distributions allows to conveniently operate on continuous test functions $\rho(\vec{r})$ and to have a closer look at the implications of the discretization made for algebraic reconstruction approaches. In the detector, the signal is usually sampled at a high temporal rate ($\geq 10\,\text{MHz}$), subsequently demodulated with the carrier frequency and filtered to the needed imaging bandwidth. This way, noise aliasing from outside the actual imaging band is suppressed and the width of the passband can be adapted noise optimally for every individual scan[3]. Furthermore, the oversampling at the first stage allows to increase the dynamic range of the sampled signal. However, modern spectrometers employed for NMR and MRI provide time discretized measurements of the detected signal with high stability and fidelity at sufficiently high bandwidth. The discretization imposed by the digital spectrometer taking samples at time points $t_\tau = \tau \cdot \Delta t$ with $\tau \in \mathbb{N}$ is thus trivial to introduce:

$$S_{c\tau}[\rho(\vec{r})] := S_c(t_\tau). \tag{3.20}$$

Another choice initially made in reconstruction (and most often made completely implicitly) is determining a set of spatial basis function $(i_\rho(\vec{r}))$ the reconstruction

---

[2] usually s_c denotes only the coupling between transverse magnetization at $\vec{r}$ and the coil c but in non-Fourier encoding schemes, reduced FOV applications and other techniques a known spatial modulation is imposed on the detected signal, which is also taken into account within this factor

[3] The bandwidth of the RF chain is mainly given by the Q ($\approx 20-100$) of the loaded coil $BW_{RF} = \frac{\omega_0}{2\pi Q} \approx 1-6\,\text{MHz@3 T}$, the bandwidth the sampling is usually more than 10 MHz, the bandwidth of the spin system is $BW_{Spin} \approx \frac{1}{T_2}$ and the one of the gradient induced broadening is $BW_{Image} := \max_{t,\vec{r}} \frac{d}{dt}\vec{k}(t)\cdot\vec{r} = \max \vec{G}(t)\cdot\vec{r} < 1\,\text{MHz}$. Therefore the bandwidth of the spin signal can be well covered avoiding unwanted temporal signal or noise correlations.

shall be referenced to. $\rho \in \mathbb{N}^3$ denotes the index of the voxel which refers to the spatial basis function. Usually they are orthonormal:

$$\int_{\mathbb{R}^3} i_\rho(\vec{r}) i_{\rho'}(\vec{r}) d\vec{r} = \delta_{\rho,\rho'} \tag{3.21}$$

and fulfill some sort of completeness which means one should be able to compose an image of $\rho(\vec{r})$ from the set of basis functions using appropriate weighting coefficients $\mathbf{m}_\rho$.

$$\rho(\vec{r}) \approx \tilde{\rho}(\vec{r}) := \sum_\rho \mathbf{m}_\rho i_\rho(\vec{r}). \tag{3.22}$$

At this point it is difficult to formulate mathematical criteria for the quality of such a choice since the effects of the errors induced by this approximation are dependent on the application and in most cases on human perception of the image. However, it is important to note that the further reconstruction process will not be able to outperform this approximation. $\tilde{\rho}$ will be referred as the reconstructed image. In most cases $i_\rho(\vec{r}) = b^3(\vec{r} - \vec{r}_\rho)$ where b^3 denotes the three dimensional box car function or alternatively a set of delta function is chosen. Both basis sets are orthonormal referring to the volume integral scalar product and moreover they have a pairwise discrete support. Referring to the spatial basis functions and the temporal discretization, we can therefrom derive the encoding matrix $\mathbf{E}$ which is usually concatenated for all coils c:

$$\mathbf{E}_{\tau,(c,\rho)} := S_c[i_\rho(\vec{r})](t_\tau) \tag{3.23}$$

and therefore

$$\mathbf{S}_{(c,\tau)} \approx \sum_\rho \mathbf{E}_{\tau,(c,\rho)} \mathbf{m}_\rho. \tag{3.24}$$

The approximation made here relates to the same topic as in Eq. 3.22. The extensive treatment of the spatial discretization is done to emphasize that the spatial discretization made by the choice of the basis functions is already a parameter of the reconstruction. Similar to the freedom to choose the coil combination a posteriori in image reconstruction mentioned in Section 3.2.1, the reconstruction problem sets the freedom of this choice to be done after the signal acquisition and it has therefore no direct impact on the experiment itself.

The goal of the reconstruction The problem of the reconstruction is finding a linear map $\mathbf{F}$ such that: First to have the least possible deviation between the reconstructed image and the measured signal. This means finding the set of $\mathbf{m}_\rho$ in

Eq. 3.22 that fit the measured signal the best under the application of $\mathbf{E}$. Secondly, there should be the least possible noise in the resulting image.

The first goal can be expressed mathematically, that $\mathbf{F}$ should be a (regularized) left inverse of $\mathbf{E}$:

$$\min_{\mathbf{F}} \|\mathbf{FE} - \mathbb{1}\|. \tag{3.25}$$

The second goal can be formulated by considering the noisy signal $\mathbf{s}_{c,\tau}^{noisy} = \mathbf{s}_{c,\tau} + \eta_{c,\tau}$ producing a noisy image $\tilde{\mathbf{m}}_\rho$ after reconstruction. The deviation to the ideal noise free image shall be minimized by the reconstruction:

$$\begin{aligned} \min_{\mathbf{F}} \sum_\rho \overline{|\tilde{\mathbf{m}}_\rho - \mathbf{m}_\rho|^2} &= \min_{\mathbf{F}} \sum_\rho \overline{|\mathbf{e}_\rho \cdot (\mathbf{F}\mathbf{s}^{noisy} - \mathbf{F}\mathbf{s})|^2} \\ &= \min_{\mathbf{F}} \sum_\rho \overline{|\sum_{c,\tau} \mathbf{F}_{\rho,(c,\tau)} \eta_{c,\tau}|^2} \\ &= \sum_\rho \sum_{(c,\tau),c',\tau'} \mathbf{F}_{\rho,(c,\tau)} \overline{\eta_{c,\tau} \eta *_{c',\tau'}} \mathbf{F}_{\rho,(c,\tau)} \\ &= \min_{\mathbf{F}} Tr(\mathbf{F}\mathbf{\Psi}\mathbf{F}^H) = \min_{\mathbf{F}} Tr(\mathbf{X}). \end{aligned} \tag{3.26}$$

The matrix $\mathbf{\Psi}$ represents the noise covariance measured. Since each channel is assumed to be sampled with full bandwidth, no temporal correlation should be visible. However, the noise among different channels of the arrays can still be correlated as stated in Section 3.1.1. Hence:

$$\mathbf{\Psi}_{(c,\tau),(c',\tau')} = \delta_{\tau,\tau'} \kappa_{\eta(t)}. \tag{3.27}$$

As in Eq. 3.6, $\kappa_{\eta(t)}$ denotes the noise covariance among the channels.

A remark about the off-diagonal elements of $\mathbf{X}$ can be made: Usually only the diagonal elements of $\mathbf{X}$ corresponding to the noise power in each pixel are considered when minimizing the noise power in an image. The off-diagonal elements however represent the noise correlation between voxels in the image and one could think to loose noise optimality by allowing this noise correlation. However, since $\mathbf{X}$ is positive definite, the off-diagonals are simultaneously minimized which can be seen from the following equations which hold for positive matrices in general[4]:

$$\begin{aligned} \mathbf{A} \in (C)^{n\times n} &\text{ pos. def.} \Rightarrow \\ |\mathbf{A}_{ij}| &\leq \frac{\mathbf{A}_{ii} + \mathbf{A}_{jj}}{2} \\ |\mathbf{A}_{ij}| &\leq \sqrt{\mathbf{A}_{ii}\mathbf{A}_{jj}} \\ \max_{i,j} |\mathbf{A}_{ij}| &\leq \max_i \mathbf{A}_{ii}. \end{aligned} \tag{3.28}$$

This is a welcome fact because it shows that the noise minimization in each voxel does not work against noise separation between voxels in principle. Therefore, the minimization of the diagonal elements optimizes in the mean time also the noise correlation between different voxels in the reconstructed image and this even with respect to various norms (arithmetic, geometric and max-norm).

The reconstructed result can be characterized by the Point Spread Function (PSF) and the Spatial Response Function (SRF). The PSF is the system's impulse response to the test function or a point source:

$$\left(PSF_{i_\rho}\right)_{\rho'} := \sum_{c,\tau} \mathbf{F}_{\rho',(c,\tau)} S_c[i_\rho](t_\tau). \tag{3.29}$$

In contrast to this, the SPF is the weighting by which a point in object space contributes to the value of a reconstructed voxel.

$$SRF_\rho(\vec{r}) := \mathbf{F}_{\rho,(c,\tau)} S_c[\delta(. - \vec{r})](t_\tau). \tag{3.30}$$

Two differences between SRF and PSF should be mentioned: First, the PSF acts in the space of the reconstructed image e.g. $\mathbb{N}^3$ whereas the SRF in the object space $\mathbb{R}^3$. Secondly, the PSF accounts for the choice of voxels functions i_ρ. This difference becomes important when the ideal signal distribution is replaced by a more realistic model of the signal to check for imaging artifacts occurring from e.g. partial volume effects.

Direct inversion (weak approach) This scheme forces $\mathbf{F}$ to be an exact inverse of $\mathbf{E}$ and sets therefore the constraint $\mathbf{FE} = \mathbb{1}$ to the noise minimization. The resulting Lagrangian function of this minimization problem is for each voxel ρ:

$$L_\rho^{\text{Constrained}} = \mathbf{X}_{\rho,\rho} + \mathbf{\Lambda}_\rho(\mathbf{FE} - \mathbb{1})_{\rho,\rho}. \tag{3.31}$$

Where $\mathbf{\Lambda}$ denotes the Lagrangian covector with entries for each voxel. From this it is clear that this method only works, if $\mathbf{E}$ has full rank. In this case

---

[4] The proof of these relations is easy when knowing that a pos. def. matrix has pos. def. diagonal submatrix-blocks and that the characteristic polynomial described by the ij-the submatrix must be positive i.e. the angular point must have a value bigger than zero.

$\mathbf{F} = (\mathbf{E}^H\mathbf{\Psi}^{-1}\mathbf{E})^{-1}\mathbf{E}^H\mathbf{\Psi}^{-1}$ which corresponds to the appropriate Moore-Penrose-Inverse.

Using this approach, we make sure that each voxel is separated from all others within the encoding model used. But the approximation of the discretization Eq. 3.24 can never be better than the encoding density since otherwise the problem is not feasible. In order to make sure the rank of $\mathbf{E}$ is sufficiently high, the imaging parameters must be chosen accordingly or the missing input data is often simply zero-padded.

A remark can be made on $\mathbf{\Lambda}$: The Lagrangian vectors are always orthogonal to the constraint manifold and points within this vector space towards the steepest increase of $L_\rho^{\text{Constrained}}$. Thus, $\mathbf{\Lambda} = (2\mathbf{E}^H\mathbf{\Psi}^{-1}\mathbf{E})^{-1}$ points into the direction where the noise and the reconstruction error will be most enhanced and can therefore deliver useful information about the robustness and conditioning of the reconstruction as found in Eq. 3.36.

Balanced reconstruction (strong or minimum norm approach) If both goals - minimization of the inversion's remainder and the noise in the reconstructed image - are considered to be equivalent a priori, up to a weighting, the following Lagrangian function is found:

$$L_\rho^{Balanced} = \parallel \left(\mathbf{W}(\mathbf{FE} - Id)\right)_\rho \parallel^2 + \lambda \mathbf{X}_{\rho,\rho} \tag{3.32}$$

where $\mathbf{W}$ is a positive matrix weighting each voxel. Since there are no hard constraints, there is always at least one solution. Therefore the reconstruction goals can be set much higher than the encoding in the experiment would suggest without running the risk of encountering a numerically infeasible problem. By this, the accuracy of the approximation made in 3.22 is increased and the inversion tries to reconstruct the maximum out of the data.

Another way to account for the imperfections of the sampling model is to directly ask for the minimum deviation of the SRF from the voxel function i_ρ:

$$\begin{aligned} \mathbf{F} &= \arg\min_{\mathbf{F}_\rho} \int_{\mathbb{R}^3} |SRF_\rho(\vec{r}) - i_\rho(\vec{r})|^2 d\vec{r} \\ \Rightarrow \mathbf{FC} &= \mathbf{E}^H \qquad\qquad (3.33) \\ \text{where } \mathbf{C}_{(c,\tau),(c',\tau')} &:= \int_{\mathbb{R}^3} (S_c[\delta(. - \vec{r}])(t_\tau)) * S_{c'}[\delta(. - \vec{r})](t_{\tau'}) d\vec{r}. \end{aligned}$$

Both approaches become equivalent, if the spatial discretization of the reconstruction grid becomes much finer than the resulting SRF, which can be verified ex-post.

However, although the balanced reconstruction offers greater versatility in choosing the reconstructed resolution and other options, the problem of a optimal and robust choice of the regularization parameters imposes some difficulties in practice. Some of these problems are again linked to the perception of image artifacts which is usually stronger if the errors show a strong spatial coherence.

Evaluating the Encoding Performance of an Array

The role of the array in parallel imaging reconstructions: In order to perform a successful reconstruction, the inverse problems posed above have to be solved. This inversion can involve high SNR losses depending on its conditioning. Especially in the cases where the encoding performed by the gradients alone is not sufficient, the encoding provided by the array becomes crucial. In the reconstruction however, there is the freedom to choose the inverse matrix **F** in order to keep the conditioning in bounds. The condition number in those cases is given by:

$$\begin{gathered}\mathbf{s} = \mathbf{E}\mathbf{m}; \\ cond(\mathbf{E}) = \|\mathbf{E}\|\|\mathbf{F}\|.\end{gathered} \tag{3.34}$$

The reconstruction error estimates can be expressed for small errors and normal statistics:

$$\tfrac{\|\tilde{\mathbf{m}}-\mathbf{m}\|}{\|\mathbf{m}\|} \leq cond(\mathbf{E})\left(\frac{\|\eta\|}{\|\mathbf{s}\|}+\frac{\|\Delta\mathbf{E}\|}{\|\mathbf{E}\|}\right)+(cond(\mathbf{E}))^2\frac{\|\mathbf{FE}-Id\|}{\|Id\|}. \tag{3.35}$$

The errors in the reconstruction stem therefore from three sources represented by the three summands above: The first is the noise acquired concomitantly with the received signal. The second summand represents the error introduced by errors of the encoding itself. These errors can have various sources such as gradient infidelities, off-resonances, incorrect assessment and noise on the coil sensitivities, geometrical inconsistencies and so forth. While the noise on the input signal is usually very well normally distributed, the errors on the encoding matrices can be very systematic. Therefore the resulting artifacts are mostly very coherent in the resulting image. The errors of these two terms are multiplied by the condition number of the system, which shows the importance of a well behaved inversion. However, the third term represents the error that stems from the deviation of **F** from a numerically exact inverse of **E**. This error competes in the case of regularized reconstructions with the goal of keeping the condition number low to control the first two terms. The dependence on the condition number represents the sensitivity of the reconstruction solution on the remainder. A high condition number causes therefore that little changes on the remainder have a big impact on the reconstructed solution. This of course imposes some problems on numerical algorithms trying to find this inverse. It has to be mentioned, that the equation above represents an upper bound for the error over all reconstructed pixels. Since the error varies spatially quite significantly, it often makes sense to study the spatial distribution of the error expectations. This can be achieved by considering for each pixel only the block of the matrices that multiply with the pixel under consideration.

Estimations of the condition number of typical reconstruction problems can serve as a figure of merit for the encoding capability of the array in conjunction with a specific acquisition scheme. The noise amplification due to the non-unitary encoding provided by the array can also be evaluated on a per pixel basis for a given acquisition. For this, the noise in the reconstructed pixel of the undersampled scan is compared to the fully sampled scan correcting for the shorter acquisition time [13]. This comparison requires that the resulting resolution of both reconstructions is equal and it is therefore only formulated for direct inversion approaches:

$$\frac{\mathbf{X}^{\text{reduced}}_{\rho,\rho}}{\mathbf{X}^{\text{full}}_{\rho,\rho}} = \sqrt{\frac{n_k^{\text{reduced}}}{n_k^{\text{full}}}}\;\underbrace{\sqrt{\left((\mathbf{E}^H\mathbf{\Psi}\mathbf{E})^{-1}\right)_{\rho,\rho}(\mathbf{E}^H\mathbf{\Psi}\mathbf{E})_{\rho,\rho}}}_{:=g_\rho}. \tag{3.36}$$

This is the so called g-factor and it is the most frequently used value to represent the spatial encoding capability of an array. Considering the last remark in Paragraph 3.2.2, the g-factor has a close relation to the Lagrangian multipliers used in a weak reconstruction approach. This makes again clear, that the g-factor is a local measure of the conditioning of the algebraic inversion. In the most general case this expression is hard to evaluate, but for Cartesian acquisitions the resulting block matrix structure of $\mathbf{E}$ and $\mathbf{\Psi}$ allows for reasonable calculation times. However, it has to be recalled that this figure of merit is strongly dependent on the k-space trajectory chosen and is only valid for the weak reconstruction method.

Information theoretical approach to spatial encoding: An alternative approach independent of any reconstruction method or acquisition scheme can be found by considering the amount of information about the object that is retrieved during a scan instead of the image quality/SNR as such [16, 17]. A measure for the information content of a signal is given by the Shannon theorem [18]. This theorem states, that the amount of mutual information I per unit time and per unit bandwidth that is transmitted from a sender - in our case the spin ensembles in a voxel - to a receiver is given by:

$$\begin{aligned} I(\mathbf{Y}) =& \log_2 \left(\frac{\det(\kappa_{\mathbf{Y}} + \mathbf{\Psi})}{\det \mathbf{\Psi}} \right) \\ \left(\mathbf{Y}(t)\right)_c :=& \int_{\text{ROI}} s_c(\vec{r}) e^{i\vec{k}(t)\cdot\vec{r}} e^{i\omega_0(\vec{r})t} \rho(\vec{r}) d\vec{r} \text{ detected signal} \end{aligned} \tag{3.37}$$

$$\begin{aligned} \kappa_\rho(\vec{r}, \vec{r}') :=& \frac{1}{T} \int_t^T \left(e^{i\vec{k}(t)\cdot\vec{r}} e^{i\omega_0(\vec{r})t} \rho(\vec{r}_\rho) \right)^* \\ & \cdot \rho(\vec{r}_{\rho'}) e^{i\vec{k}(t)\cdot\vec{r}'} e^{i\omega_0(\vec{r}')t} dt \text{ spin signal covariance} \end{aligned} \tag{3.38}$$

$$\begin{aligned} \left(\mathbf{H}\right)_{\rho,c} :=& s_c(\vec{r}_\rho) \text{ discrete transfer function} \\ \left(\kappa_\rho\right)_{\rho,\rho'} =& \kappa_\rho(\vec{r}_\rho, \vec{r}_{\rho'}) \text{ discrete spin signal covariance)} \\ \kappa_{\mathbf{Y}} :=& \mathbf{H}^H \kappa_\rho \mathbf{H} \text{ received signal covariance.} \end{aligned} \tag{3.39}$$

This formulation is in principle capable to quantify the information gained by the gradient encoding and by the RF encoding of the array dependent on the SNR of the signal. If the spins are assumed to be uniformly distributed $\rho(\vec{r}) = 1$, the spatial correlation function of the gradient modulated spin signals $(\kappa_\rho(\vec{r}, \vec{r}'))$ reflects the encoding performed by the k-space trajectory $\vec{k}(t)$. The performance of an array for a given trajectory can therefore be determined by straight forward computation of the equation above. The higher the amount of mutual information gained, the higher the SNR of the images can potentially be after reconstruction. In the case no gradient encoding is present, it can be argued that the spins itself are in principle spatially uncorrelated and therefore $\kappa_\rho = \mathbb{1}$. This corresponds to the assumption that no priors are known on the distribution of the nuclear magnetization. Doing some algebra, some similarity can be revealed between the mutual information the signals of a coil array deliver and the SNR yield in the Roemer [1] reconstructed fully sampled image:

$$\begin{aligned} SNR^2_{\text{Roemer}} =& Tr\left(\mathbf{H}^H \mathbf{H} \mathbf{\Psi}^{-1}\right) = \sum_j \mathbf{\Lambda}_{jj} \\ I(\kappa_\rho = \mathbb{1}) =& \log_2 \left(\det(\mathbf{H}^H \mathbf{H} \mathbf{\Psi}^{-1} + Id) \right) = \sum_j \log_2 \left(\mathbf{\Lambda}_{jj} + \mathbb{1} \right) \\ & \text{with } \mathbf{H}^H \mathbf{H} \mathbf{\Psi}^{-1} = \mathbf{Q}^H \mathbf{\Lambda} \mathbf{Q}; \mathbf{\Lambda} \text{ diagonal, } \mathbf{Q} \text{ unitary.} \end{aligned} \tag{3.40}$$

The eigenvalues of the matrix collecting the encoding of the array $\mathbf{H}$ and the noise covariance $\mathbf{\Psi}$ determine the SNR as well as the mutual information. In the case of the Roemer SNR, it does not depend on how the eigenvalues are distributed, it is only the total sum that counts. In the case of the mutual information however, the $\log_2$ function is not linear. Considering a fixed constant Roemer SNR, the distribution giving the maximum mutual information would be an even distribution among all eigenvalues. This corresponds to the situation, where the matrix $\mathbf{H}^H\mathbf{H}\mathbf{\Psi}^{-1}$ is unitary. Although this does not mean that the signal in each channel must be completely independent from all others, there must only exist a unitary transformation of the channels that renders the signals orthogonal. This shows that the mutual information not only accounts for the SNR in the signal, but also for the independence of the information yielded by each channel and thereby of the spatial encoding gained.

As an example, Fig. 3.5 shows a comparison of SNR, g-factors, and mutual information values retrieved from an eight channel wrist array by varying the impedance transformation ratios at the inputs of the individual preamplifiers. For this, a uniform phantom was used and the elements were split into two subgroups of next-neighboring coils. The adjustments started out from the settings providing the maximum isolation among all coil elements. The noise covariance and the sensitivity maps were acquired, which final results are denoted by "11". Then the matching network of the first subgroup was slightly varied delivering the data set "21". Then the second group was adjusted ("22") etc. The results show an optimum SNR for setting "21" but an optimum g-factor in "11". Furthermore, the SNR and the g-factor do not monotonically depend on the matching adjustments. The mutual information reveals a monotonically decreasing performance which shows that the baseline SNR as well as the encoding capability of the array are considered concurrently. Therefore the mutual information can be regarded as a valuable measure for the performance of a receive array coil independently of the acquisition and the reconstruction technique.

3.2.3 Concomitant Spatial Encoding by Gradients and Arrays for Transmission

Using the Fourier spectroscopic approach to NMR [19], RF pulses can be applied for various tasks, such as excitation, refocussing, quantum filtering, encoding by spectral or spatial selection an many more. The treatment of pulse design presented in this work will focus on spatially and spectrally selective RF pulses that are irradiated on the sample concomitantly with tailored waveforms fed to the gradient system. The design of RF pulses is basically an inverse problem trying to find the RF waveform that performs the intended spin manipulation. In order to find an appropriate inversion method, a short introduction into the forward model will be given. Furthermore, the small flip angle approximation will be derived and the span of its validity is declared. The inversion problem to be solve prompts some strong analogies to image reconstruction, however also some crucial differences between the two problems will be discussed.

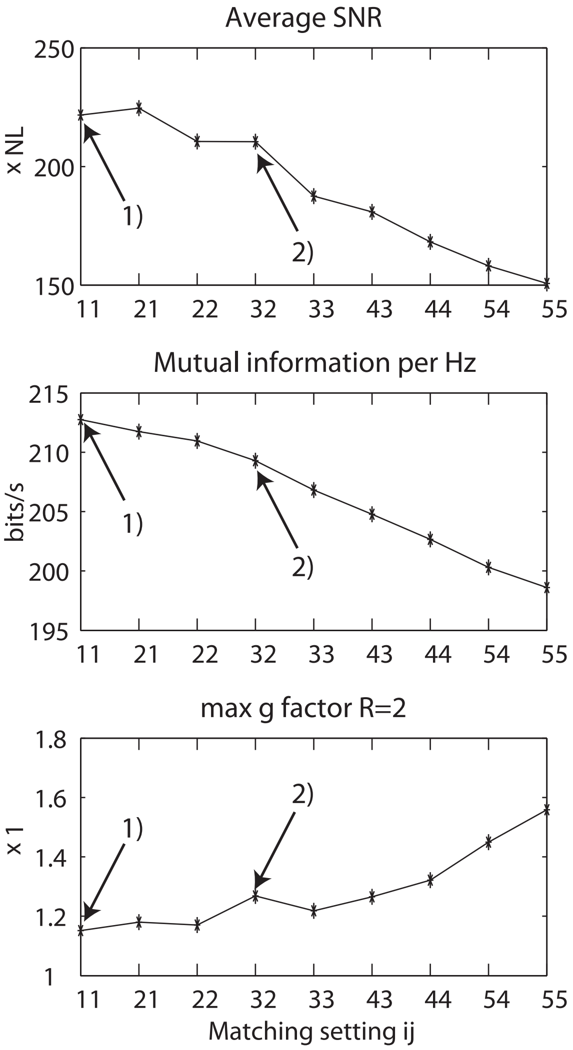

Figure 3.5: : SNR, mutual information and maximum g-factor for a rate 2 accelerated cartesian scan retrieved from a matching optimization procedure of an 8 channel array The mutual information reveals the peak performing setting unambiguously while the SNR and the g-factor consideration deliver contradictive results.

Nuclear Magnetization under RF Irradiation

Since the pulses to be designed are targeted mainly for MRI applications, only uncoupled spin systems will be considered, which allows to consider the nuclear magnetization as an ensemble of spatially and spectrally distributed individual isochromats each representable by its net magnetization vector in space. Therefore the motion of the resulting magnetization can be described by the Bloch equation, which predicts - neglecting relaxations during the RF pulse - that the motion of the magnetization is a rotation around the net magnetic field at the location of the magnetization (see Eq. 1.2). The resulting spin manipulation at the end of the pulse (T) is therefore a net rotation $\mathbf{R}(T) \in S0(3)$. Although the orthogonal 3×3 matrices are the most common representation of rotations, they will be studied in the complex $SU(2)$ group for compactness of notation as in [20]. The homomorphism used to map a rotation with axis vector $\vec{n}$ and angle ϕ are the well known Cayley-Klein parameters which are represented as 2×2 complex matrix $\mathbf{Q}(T) \in SU(2)$ and also termed as complex quaternions or spinors. The resulting net rotation is most frequently calculated by considering the RF waveform as piecewise constant for a time Δt. Each of these small subpulses results in a net rotation (hard pulse approximation). These considerations result in the following formulation for $\mathbf{Q}(T)$ resulting from a given gradient $\vec{G}(t)$ and B_1^+ waveform and position $\vec{r}$ (see [20]):

$$\begin{aligned} \mathbf{Q}(T) &= \mathbf{Q}_n \mathbf{Q}_{n-1} \cdots \mathbf{Q}_2 \mathbf{Q}_1 \\ \mathbf{Q}_i &= e^{\Delta t \mathbf{L}_i} \\ \mathbf{L}_i &:= \frac{i\gamma}{2} \begin{pmatrix} B_0 + \vec{G}(t_i) \cdot \vec{r} & (B_1^+(t_i))^* \\ B_1^+(t_i) & -(B_0 + \vec{G}(t_i) \cdot \vec{r}) \end{pmatrix}. \end{aligned} \tag{3.41}$$

On the basis of this decomposition, the Shinnar-Le Roux [21] algorithm, relying on the z-transform known from electrical filter design, allows the calculation of pulses with arbitrary spectral response for rotation angles < 180 °. The drawback of this design approach is that only spectral responses in one dimension can be treated. Pulses being targeted to be selective in multiple dimensions must allow to separate the problem into one dimensional subproblems which is possible in some special cases e.g. spectral-spatial selective pulses on oscillatory gradients or multidimensionally selective pulses on cartesian trajectories. However, generalization of this approach especially to multiple and non-uniform excitations fields is not known to date. Therefore, further approximations shall make the inverse problem numerically better treatable.

The topology of the $SU(2)$ group allows the usage of the Baker-Campbell-Hausdorff formula which can be stated for two consecutive rotations as:

$$e^{\Delta t(\mathbf{L}_1+\mathbf{L}_2)} = e^{\Delta t \mathbf{L}_1} e^{\Delta t \mathbf{L}_2} e^{\frac{-(\Delta t)^2}{2}[\mathbf{L}_1,\mathbf{L}_2]} e^{\frac{(\Delta t)^3}{6}(2[\mathbf{L}_2,[\mathbf{L}_1,\mathbf{L}_2]]+[\mathbf{L}_1,[\mathbf{L}_1,\mathbf{L}_2]])} \cdots \tag{3.42}$$

where the square brackets express the commutator between matrices. It can be seen from this formula that the concatenation of the rotations/pulses can be approximated by the sum of the rotation vectors if the rotation angle is either small (all commutators are $O((\Delta t)^2)$) or if the rotations commute ($\|[\mathbf{L}_1, \mathbf{L}_2]\| \ll 1$) which is for instance the case if they take place around approximately parallel axes.

$$e^{\Delta t(\mathbf{L}_1+\mathbf{L}_2)} \approx e^{\Delta t L_1} \, e^{\Delta t L_2}. \tag{3.43}$$

This means for example, that pulses that nutated the magnetization around the same axis at each position across the entire sample just add up if they are played after each other. In Ref. [20] those pulses are called inherently refocused under the action of the gradients.

Considering the rotations induced by the off-resonance terms $\mathbf{L}_i^z$ within one subpulse and the nutation induced by the RF field $\mathbf{L}_i^{xy}$ as separate rotations and $\mathbf{L}_i^{xy}$ being small we find:

$$\begin{aligned}
\mathbf{L}_i^z &:= \frac{i\gamma}{2}\begin{pmatrix} B_0 + \vec{G}(t_i)\cdot\vec{r} & 0 \\ 0 & -(B_0 + \vec{G}(t_i)\cdot\vec{r}) \end{pmatrix} \\
\mathbf{L}_i^{xy} &:= \frac{i\gamma}{2}\begin{pmatrix} 0 & (B_1^+(t_i))^* \\ B_1^+(t_i) & 0 \end{pmatrix} \\
\mathbf{L}_i^k &:= \frac{i}{2}\begin{pmatrix} k_i & 0 \\ 0 & -k_i \end{pmatrix} \\
k_i &:= -\gamma \int_{t_i}^{T} (\vec{G}(t)\cdot\vec{r} + B_0)dt
\end{aligned} \tag{3.44}$$

$$\begin{aligned}
\mathbf{Q}(T) &\approx \mathbf{Q}_n \cdots e^{\Delta t \mathbf{L}_{i+1}^z} e^{\Delta t \mathbf{L}_{i+1}^{xy}} e^{\Delta t \mathbf{L}_i^z} e^{\Delta t \mathbf{L}_i^{xy}} \cdots \mathbf{Q}_1 \\
&= \mathbf{Q}_n \cdots \underbrace{e^{\Delta t \mathbf{L}_i^z} e^{i\mathbf{L}_i^k}}_{=e^{i\mathbf{L}_{i+1}^k}} \underbrace{e^{-i\mathbf{L}_i^k} e^{\Delta t \mathbf{L}_i^{xy}} e^{i\mathbf{L}_i^k}}_{=e^{\mathbf{L}_i^{kxy}}} \underbrace{e^{-i\mathbf{L}_i^k} e^{\Delta t \mathbf{L}_{i-1}^z}}_{=e^{-i\mathbf{L}_{i-1}^k}} \cdots \mathbf{Q}_1
\end{aligned} \tag{3.45}$$

$$\begin{aligned}
\mathbf{L}_i^{kxy} &= \frac{i\gamma}{2}\begin{pmatrix} 0 & (\Delta t B_1^+(t_i) e^{ik_i})^* \\ \Delta t B_1^+(t_i) e^{ik_i} & 0 \end{pmatrix} \\
\mathbf{Q}(T) &\approx e^{\mathbf{L}_n^{kxy}} \cdots e^{\mathbf{L}_i^{kxy}} \cdots e^{\mathbf{L}_1^{kxy}} e^{i\mathbf{L}_1^k} \\
&\approx \exp\left(\sum_{i=1}^{n} \mathbf{L}_i^{kxy}\right) e^{i\mathbf{L}_1^k}.
\end{aligned} \tag{3.46}$$

The approximation introduced in Eq. 3.43 is applied twice; once to decompose the nutation and the off-resonance induced precession in Eq.3.45 of each subpulse, and a second time in Eq. 3.46 in order to represent the total rotation of the pulse as the sum of the subpulses' net rotations. Clearly, the second approximation is rather prone to inaccuracies for realistic pulses since the rotation within each subpulse is usually much smaller than the rotation induced by the entire pulse. Furthermore, the first approximation can always be improved by reduction of the time discretization step Δt but not the latter. If we look at the limit of $\Delta t \to 0$ we get:

$$\begin{aligned}
\mathbf{Q}(T) \approx{}& \exp\left(\frac{1}{2}\begin{pmatrix} 0 & \theta^* \\ \theta & 0 \end{pmatrix}\right) e^{i\mathbf{L}_1^k} \\
\theta :={}& i\gamma \int_0^T B_1^+(t) e^{-\gamma \int_{t'}^{T} (\vec{G}(t')\cdot\vec{r} + B_0)dt'}).
\end{aligned} \tag{3.47}$$

Therefore we can see that the rotation produced by the pulse in the low flip angle regime as it is represented by the quaternion $\mathbf{Q}(T)$ decomposes in a net precession (rotation around n_z) with an effective angle $-\gamma\int_0^T(\vec{G}(t)\cdot\vec{r}+B_0)dt$ and a nutation around an axis in the transverse plain described by the complex angle θ. Please note that the angle of the rotation attributes to the double of the net angle in the quaternion.

This result can be expanded to the case of a multi-channel transmission array by using the fact that the local B_1^+ field is given by the superposition of the fields produced by each channel $B_{1,c}^+(\vec{r})$ that is driven with the waveform $(\mathbf{v}(t))_c$:

$$\begin{aligned}\theta =& i\gamma\sum_c\int_0^T B_{1,c}^+(\vec{r})(\mathbf{v}(t))_c e^{-i\gamma\int_t^T(\vec{G}(t')\cdot\vec{r}+B_0)dt'})\\ & i\gamma\sum_c B_{1,c}^+(\vec{r})\int_0^T(\mathbf{v}(t))_c e^{i\vec{k}(t)\cdot\vec{r}-i\gamma B_0(T-t)}dt' \\ \vec{k}(t) :=& -i\gamma\int_t^T\vec{G}(t')dt'.\end{aligned} \tag{3.48}$$

This expansion does not directly rely on any further approximations since the linearity of B_1^+ is well assured and has as such no implications in any of the assumptions and approximations made. In the special case where the magnetization M_0 is aligned along n_z at the beginning of the pulse we get a resulting magnetization of:

$$\begin{aligned}M_x &= \sin(\Re(\theta))M_0\\ M_y &= \sin(\Im(\theta))M_0\\ M_z &= \cos(|\theta|)M_0.\end{aligned} \tag{3.49}$$

If $|\theta|\ll 1$ and therefore $\sin\theta\approx\theta$ we get the well known small flip angle approximation found in [22]. In this formulation the close relation between encoding in the receive case and excitation localization in transmission becomes clear; both have algebraically analogous formulations. Although in the traditional derivation a small total flip angle has to be assumed, it is well known that many pulses designed by inversion of the linear relation in Eq. 3.48 hold up to much higher flip angles, in some cases even up to 90 °. The slightly more complicated derivation above should make clearer that in deed not the size of the flip angle is determining the limitation of the approximation, but the remnant commutator terms in Eq. 3.42. As mentioned in [20], the approximation stays valid for high nutations, if a pulse consists of self refocused subpulses with coaxial nutation axes. To achieve this, it is suggested in this work, that all the subpulses shall have Hermitian k-space weighting. In this case we can find another beneficial effect: The commutators of the nutation corresponding to the Hermitian symmetry in k-space cancel out if the gradient is reversed between the two locations. The only malicious terms surviving are therefore $O(\Delta t^3)$. This explains why pulses designed on e.g. spiral trajectories by inversion of Eq. 3.48 are usually very robust towards higher flip angles, even though the refocused subpulses displayed in each revolution of the spiral do not have a small flip angle by themselves. These considerations show, that the validity of the small tip angle approximation will not mainly depend on the net flip angle of the pulse itself, but also strongly on the gradient waveform used, the nutation induced in total during the pulse etc.

The Role of Conditioning in Linear Pulse Design

In 3.2.2 it was found that the conditioning of the inverse problem posed for the reconstruction has a crucial impact on the resulting images and further that in the case the spatial encoding delivered by the gradients is not complete, the spatial encoding has to be provided by the array. As stated above, the equation to be inverted for low flip angle pulse design is analogous to the one to be solved for reconstruction. This means that a potential ill-conditioning of the problem results in excessive power requirements of the resulting pulse and jagged waveforms. It is important to note that it does -beside numerical inaccuracies- not lead to noise enhancement, because the target pattern is given noise free up to numerical precision. Since the primary result, the magnetization profile at the end of the pulse, is retrieved after applying the forward equation again, the ill conditioning does not directly result in higher noise/error levels in the resulting magnetization profile up to the limits of the fidelity of the transmit chain. But by the higher power consumption also the power deposition in the sample is raised and since higher nutations are performed during the pulse, violations of the small-flip-angle approximation become more prominent. It can therefore be concluded that the conditioning, and therefore also the encoding capability of the array play an equally important role as in the receive case even though not for the same reason. However, the numerical control over the condition of the inverse problem is not primarily driven by the quality of the result in the image space, but mainly by the capability to handle the power requirements of the resulting pulse. Furthermore, RF power limits can in most cases not be considered as optimization goals but are subject to hard constraints. A methodology for this approach shall be derived therefore in the next chapter.

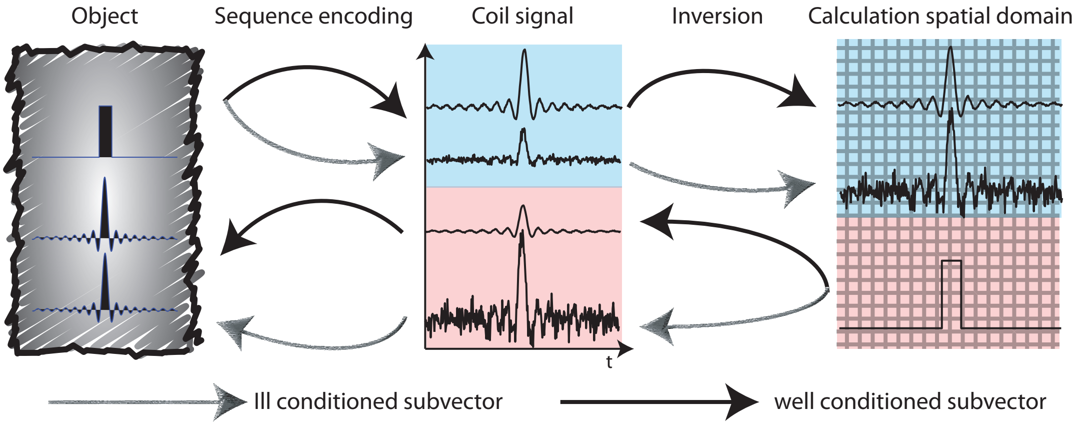

Figure 3.6: The effect of the conditioning of the inverse problem is different in image reconstruction and pulse design but its control is equally important. In reconstruction, an ill-conditioned subspace of the signal has a small signal yield but is strongly amplified by the inversion resulting in a strong noise enhancement in the final image. In pulse design, the ill-conditioning causes the resulting pulse to have a high power consumption due to the strong amplification of the inverse. However, the effect of the ill-conditioned subspace is small in the forward model, which is the reason for the strong amplification imposed by the inversion. Thus, it is not directly leading to a noise enhancement in the object space. However, the resulting high power consumption is potentially rendering the pulse not executable on system due to power and SAR restrictions, but also the violation of the small-flip-angle approximation is increased due to the occurring larger total nutation within the pulse.

Bibliography

[1] Roemer PB, Edelstein WA, Hayes CE, Souza SP, and Mueller OM. The NMR phased array. Magn Reson Med 1990; 16(2):192–225.

[2] Chaloupka HJ, Wang X, and Coetzee JC. A superdirective 3-element array for adaptive beamforming. Microwave and Optical Technology Letters 2003; 36:425–430.

[3] Bosma H. On the theory of linear noisy systems. Philips Res Rep Suppl 1967; 10.

[4] Brunner DO, Zanche ND, and Pruessmann KP. A Comparison of Matching Strategies for RF Transmission Arrays Based on Network Theory. In Proc Intl Soc Magn Reson Med 2008. p. 143; Toronto; 2008.

[5] Paska J, Froehlich J, Brunner DO, Pruessmann KP, and Vahldieck R. Field Superposition Method for RF Coil Design. In Proc Intl Soc Magn Reson Med 2009. p. 3038; Honolulu, Hawaii, USA; 2009.

[6] Kozlov M and Turner R. Fast MRI coil analysis based on 3-D electromagnetic and RF circuit co-simulation. J Magn Reson 2009; 200(1):147–152.

[7] International Commission on Non-Ionizing Radiation Protection, Guidelines for Limiting Exposure to Time-Varying Electric, Magnetic, and Electromagnetic Fields (up to 300 GHz). Health Physics 1998; 74(4):494–522.

[8] Brunner DO, Paska J, Froehlich J, and Pruessmann KP. SAR assessment of transmit arrays: Deterministic calculation of worst- and best-case performance. In Proc Intl Soc Magn Reson Med 2009. p. 4803; Honolulu, Hawaii, USA; 2009.

[9] Brunner DO, Paska J, Frohlich J, and Pruessmann KP. Exact calculation of the worst-case local SAR and the highest safe B1+ of a transmitter array. In Proc ESMRMB 2009. p. 194; Antalya, Turkey; 2009.

[10] Van de Moortele PF, C S, L D, G A, JT V, and K. U. Calibration tools for RF shim at very high field with multiple element RF coils: from ultra fast local relative phase to absolute magnitude B1+ mapping. In Proc Intl Soc Magn Reson Med 2007. p. 1676; Berlin; 2007.

[11] Kassakian P. Kassakian PW. Convex approximation and optimization with applications in magnitude filter design and radiation pattern synthesis. University of California at Berkeley 2006.

[12] Van den Berg CAT, van den Bergen B, Van de Kamer JB, Raaymakers BW, Kroeze H, Bartels LW, and Lagendijk JJW. Simultaneous B_1^+ homogenization and specific absorption rate hotspot suppression using a magnetic resonance phased array transmit coil. Magn Reson Med 2007; 57(3):577–586.

[13] Pruessmann KP, Weiger M, Scheidegger MB, and Boesiger P. SENSE: sensitivity encoding for fast MRI. Magn Reson Med 1999; 42:952–962.

[14] Sodickson DK and Manning WJ. Simultaneous acquisition of spatial harmonics (SMASH): Fast imaging with radiofrequency coil arrays. Magn Reson Medicine 1997; 38(4):591–603.

[15] Griswold MA, Jakob PM, Heidemann RM, Nittka M, Jellus V, Wang JM, Kiefer B, and Haase A. Generalized Autocalibrating Partially Parallel Acquisitions (GRAPPA). Magn Reson Medicine 2002; 47(6):1202–1210.

[16] Brunner DO, Nordmeyer-Massner JA, and Pruessmann KP. Information Theory in MRI. In Proc Intl Soc Magn Reson Med 2009. p. 2978; Honolulu, Hawaii, USA; 2009.

[17] Brunner DO, Nordmeyer-Massner JA, and Pruessmann KP. An information theory approach to array detection in MRI. In Proc ESMRMB 2009. p. 322; Antalya, Turkey; 2009.

[18] Biglieri E. Coding for Wireless Channels. Springer US; 2005.

[19] Ernst RR and Anderson WA. Application of fourier transform spectroscopy to magnetic resonance. Rev Sci Instr 1966; 37:93–102.

[20] Pauly J, Nishimura D, and Macovski A. A Linear Class of Large-Tip-Angle Selective Excitation Pulses. J Magn Reson 1989; 82:571–587.

[21] Pauly J, Roux PL, Nishimura D, and Macovski A. Parameter Relations for the Shinnar-Le Roux Selective Excitation Pulse Design Algorithm. IEEE Trans Med Imag 1991; 10(1).

[22] Pauly J, Nishimura D, and Macovski A. A k-Space Analysis of Small-Tip-Angle Excitation. J Magn Reson 1989; 81:43–56.

Chapter 4

B_1^+ Interferometry for the Calibration of RF Transmitter Arrays

published in:

D. O. Brunner, S. Heinzer-Schweizer and K. P. Pruessmann. *"Fast Mapping of Highly Inhomogeneous RF Fields"*. Proc Intl Soc Magn Reson Med 2007, Berlin. p. 353

D. O. Brunner and K. P. Pruessmann. *"A Matrix Approach for Mapping Array Transmit Fields in Under a Minute"*. Proc Intl Soc Magn Reson Med 2008, Toronto. p. 354

D. O. Brunner and K. P. Pruessmann. *"An Interferometric Approach for B_1^+ Mapping of RF Transmitter Arrays"*. Proc ESMRMB 2008, Valencia. p. 94

D. O. Brunner and K. P. Pruessmann. *"B_1^+ Interferometry for the Calibration of RF Transmitter Arrays"*. Magn Reson Med 2009; 61(6): p. 1480-1488

4.1 Introduction

The increasing variety of current multi-channel transmission (MCT) approaches can be roughly divided into two categories. In one class of methods the elements of a transmitter array are driven with fixed relative phase and amplitude, an approach that is frequently referred to as RF shimming [1, 2]. The second kind of MCT methods applies fully individual RF waveforms to different transmitter channels, enabling even more tailored excitations such as Transmit SENSE [3, 4]. A common feature of all of these methods is the fundamental need to know RF characteristics of the individual array elements. For full control of RF interference in MCT each array element needs to be characterized in terms of its B_1^+ field distribution within the region of interest (ROI). Unless reliable model calculations are available such calibration must be performed by in-situ B_1^+ field mapping. Compared with volume-coil mapping at lower field strengths, B_1^+ mapping for MCT at ultra-high-field is substantially more demanding. Firstly, large dynamic ranges must be covered due to the strong inhomogeneity of single-element B_1^+ fields. Secondly, increased B_0 inhomogeneity at high field complicates the interpretation of B_1^+ reference scans. Thirdly, the higher SAR deposition of RF pulses at high field limits the use of large-angle pulses for B_1^+ mapping purposes. And finally, MCT is extremely demanding in terms of the speed of B_1^+ mapping. For each element of the transmit array an individual B_1^+ map needs to be obtained for each subject and target region.

One popular class of MRI-based B_1^+ mapping techniques relies on the acquisition of two sets of signals prepared with different RF pulses or different sequence timing. The actual rotation angles involved are then obtained by interpreting the observed signals within analytic models of the signal formation. The two signals may be gradient echoes excited with two different nominal flip angles [5] or repetition times [6]. The former approach is commonly referred to as the double-angle method and was originally proposed in the form of a spin-echo sequence with variable-angle excitation [7, 8]. Further early B_1^+ mapping methods were based spin echo and a stimulated echo [9] or generally on two different echoes produced with a three-pulse sequence [10]. However, while widely used for traditional B_1^+ mapping tasks the use of only two test signals does not offer sufficient dynamic range. Another approach makes use of large-flip-angle composite pulses for MR excitation [11] or refocusing [12]. At high field these methods are very time-consuming because the high SAR values of such composite pulses imposes long repetition times. A recently presented approach using the 180° signal null in a 3D gradient-echo sequence [13] is not applicable for 2D readouts of single or few slices, inflicting the long scan times of a full 3D acquisition. The methods that are known to offer the largest dynamic range rely on the acquisition of multiple data sets using a series of excitation flip angles in a spin echo [14] or gradient-echo [15] sequence. The methods described thus far are very time consuming, because they require full relaxation between successive image acquisitions. Furthermore, with slice-selective excitation pulses for 2D mapping the actual flip angle varies across the slice profile, precluding the use of large test angles.

This survey of existing methods illustrates the challenges of calibrating a transmit array for ultra-high-field MRI accurately, within SAR limits, and within a time frame acceptable for the preparation stage of an actual MR exam. The underlying difficulty is closely connected with two key aspects of the B_1^+ mapping task. One is the necessity to disambiguate B_1^+ during transmission and the sensitivity of signal detection, which is not possible in the small flip-angle regime. Therefore every part of the region of interest must undergo large-angle nutation in at least part of the mapping procedure. It is mainly this requirement that makes large dynamic B_1^+-ranges and SAR limits a challenging combination. The other important point is that the relationship between B_1^+ and received MR signals is additionally entangled with a range of other factors, particularly saturation and relaxation, the spatial response of the RF pulses involved, and B_0 inhomogeneity. It is due to these complications that B_1^+ mapping frequently uses very long repetition times and time-consuming 3D schemes, and lacks accuracy at high field.

In the present work we revisit these problems and propose novel ways of solving them. Firstly, the need for large nutation angles is addressed by the adoption of an interference approach for B_1^+ assessment. Instead of mapping the B_1^+ fields of single array elements directly it is proposed to rather measure the interference of each single-element B_1^+ with a SAR-efficient baseline RF field distribution. In this fashion the net sensitivity of array B_1^+ mapping is boosted by already exploiting array transmission. Secondly, the complex behavior of B_1^+ mapping signals is addressed by interpreting them within a parametric model that includes all relevant signal dependencies. In conjunction with an efficient 2D imaging sequence this comprehensive model permits fast and highly accurate slice-wise B_1^+ assessment. It is demonstrated that combining these approaches enables the accurate B_1^+ calibration of an 8-channel transmission system at 7T in less than a minute.

4.2 Methods

4.2.1 Materials

All experiments were performed on a Philips Achieva 7T whole-body MR system (Philips Healthcare, Cleveland, Ohio). On this system the power output of the RF amplifier is set in terms of a nominal B_1^+-value according to initial power calibration. For the sake of simplicity all B_1^+ mapping results will be given relative to this nominal value and denoted as B_1^{rel}. The proposed methods were tested

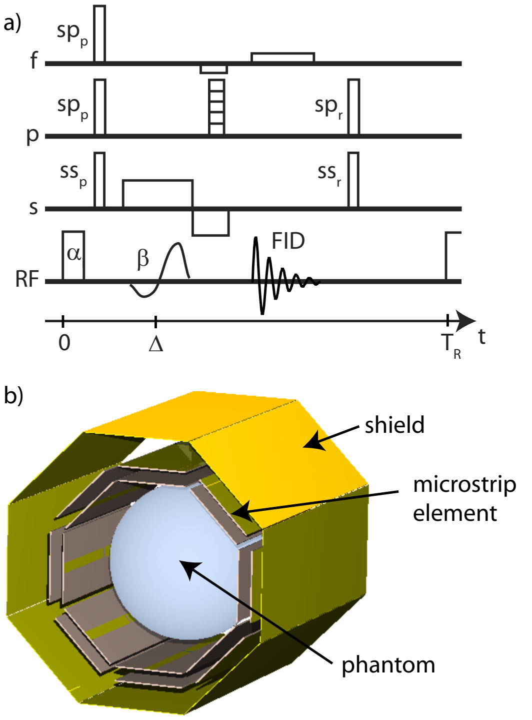

Figure 4.1: a) Diagram of the pulse sequence implemented for the frequency encode gradient (f), phase encode (p), slice selection (s) and RF signals. The sequence consists of a non-selective saturation block pulse followed by a slice-selective, small flip angle, gradient echo recalled readout of the magnetization pattern produced by the prepulse. In this schematic a spinwarp readout is depicted which was replaced by a single-shot EPI readout for MCT calibration experiments. b) CAD drawing of the 8 channel microstrip array and phantom used for the measurements.

with three different RF devices: an end-capped, shielded, tight-fitting transmit-receive head birdcage resonator, which will be referred to as ’T/R head’ (Philips Healthcare, Cleveland, Ohio). ’TX volume’ was a shielded, open and wider (30 cm inner diameter) birdcage resonator, which was combined with a 16-channel receive-only surface coil array insert (Nova Medical Inc, Wilmington, Massachusetts). The ’T/R array’ was a custom-built 8-channel transmit-receive array (see Fig. 4.1.b) and [16, 17]) driven by an equally custom-built RF-shim feed system [18]. For all experiments the average and peak forward power at the RF amplifier output were limited to 10 W and 2.4 kW, respectively. For SAR considerations the RF electric fields produced by the T/R array were simulated using a finite-integral time-domain method. Details of the simulation and its validation are described in [17].

Two different phantoms were used: A 15 cm-diameter sphere and a 12 cm-diameter cylindrical phantom, both containing aqueous 41 mM KCl solution. The cylindrical phantom was subdivided into compartments of different T_1 relaxation times ranging between 150 ms and 800 ms (see Tab. 4.1). T_1 adjustment was achieved by doping with Gd-DOTA (DOTAREM®, Laboratoire Guerbet, Roissy CDG, France). B_1^+ maps were generally acquired in the central transverse plane of each phantom.

4.2.2 Interferometry for B_1^+ mapping

MRI-based B_1^+ mapping generally relies on observing how the target B_1^+ manipulates the nuclear magnetization in a suitable pulse sequence. In such an experiment the signal received from a certain position depends not only on the local B_1^+ and the available magnetization but also on the local sensitivity of the receiver used. To disambiguate B_1^+ from the other two factors it is generally necessary to establish a nonlinear relationship between the received signal and B_1^+ [10]. This is achieved by large-angle nutation at some stage of a mapping sequence. To achieve high B_1^+ sensitivity and full spatial coverage, nutation angles well beyond 30° must be reached throughout the region of interest (ROI). For mapping B_1^+ fields of large dynamic range this means that high drive powers must be used to reach B_1^+ sensitivity also in regions of low B_1^+ . At ultra-high-field this requirement translates into very time consuming procedures due to stringent SAR constraints.

This problem is illustrated in the left column of Fig. 2. Driving only a single element c $(1 \leq c \leq C)$ of the T/R array results in a $B_{1,c}^+(\vec{r})$ distribution with a sharp maximum close to the element Fig. 4.2.3.a). In much of the phantom the B_1^+ of the single element is very small yielding low B_1^+ sensitivity.

To overcome this problem we propose a conceptual separation between the need to work in the large flip-angle regime and the aim to measure small B_1^+ . These two goals can indeed be reconciled by measuring B_1^+ distributions of large dynamic range not by themselves but superimposed on a less dynamic baseline B_1^+ . Such a baseline field can be thought of as shifting the nutation angle to a favorable working point where small interference by the superimposed, dynamic field can be better sensed.

With a transmit array the interference approach can be readily implemented by choosing some suitable driving configuration to generate the baseline field and then causing interference by varying the contribution of individual channels. The resulting driving configurations are characterized by the complex-valued relative current amplitudes $(\mathbf{I})_{m,c}$, where $1 \leq m \leq M$ and $1 \leq c \leq C$ enumerate the driving configurations and the array elements, respectively. The net excitation field of configuration m $(B_{1,m}^+)$ is then given by the complex superposition of the excitation fields of the individual elements $(B_{1,c}^+)$:

$$B_{1,m}^+(\vec{r}) = \sum_{c=1}^{C} (\mathbf{I})_{m,c} B_{1,c}^+(\vec{r}). \tag{4.1}$$

Given a sufficient number of such configurations, yielding a set of M configuration maps $B_{1,m}^+$, single-coil maps $B_{1,c}^+$ can be calculated by applying the inverse of the matrix **I** on a pixel-by-pixel basis:

$$B_{1,c}^+(\vec{r}) = \sum_{m=1}^{M} \left((\mathbf{I}^H \mathbf{W} \mathbf{I})^{-1} \mathbf{I}^H \mathbf{W} \right)_{c,m} B_{1,m}^+(\vec{r}) \tag{4.2}$$

where ^{H} denotes the Hermitian conjugate of a matrix.

The positive definite diagonal matrix $\mathbf{W}$ permits weighting the measured $B_{1,m}^+$ by their confidence if more configurations are mapped than channels are present in the array. Note that this weighting can be done individually for each pixel, which is important because noise levels can vary significantly in single-configuration maps. Generally, good numerical conditioning of the inversion step is crucial since both noise and mapping errors can otherwise be strongly amplified. In particular the number of configurations mapped must not be smaller than the number of array elements.

Based on these considerations the choice of driving configurations is governed by three partly competing objectives:

1. Maintaining large B_1^+ throughout the sample for all m.
2. Avoiding high local electric fields within the sample for all m.
3. Ensuring good conditioning of **I**

The optimal choice of configurations naturally depends on the individual array and imaging setup and cannot be made without detailed prior knowledge about $B_{1,c}^+$. However, favorable choices can also be derived heuristically. One generic option is to start from a quadrature configuration[1] and invert the input phase of single channels, one per configuration:

$$(\mathbf{I})_{m,c} = \begin{cases} -e^{i\frac{2\pi(c-1)}{C}}, & m = c; \\ e^{i\frac{2\pi(c-1)}{C}}, & m \neq c. \end{cases} \tag{4.3}$$

In this case, the quadrature configuration generates the baseline B_1^+ field considered above, permitting the sensitive mapping of field interferences by the individual array elements. This method was successfully applied in the present work, as reported in the subsequent section. Notwithstanding, a range of enhanced strategies can be conceived. For instance, if the generic scheme of Eq. [4.3] does not yield $B_{1,c}^+$ maps of sufficient quality, further configurations can be included.

---

[1] Driving the current of each port of the array with right-hand circular phase increment equivalently to the current distribution between the rungs of a birdcage resonator in ideal circular polarization (homogeneous mode) is denoted as quadrature.

Importantly, the choice of these additional configurations can be based on the existing $B_{1,c}^{+}$ estimates. For example, RF shim parameters could be calculated that focus B_1^+ field in regions of previously poor mapping quality. This RF shim could then serve as a new baseline configuration.

4.2.3 Mapping Sequence

For mapping the $B_{1,m}^{+}$ fields produced by individual driving configurations a multiple-flip-angle approach was used. The nutations that sensitize the mapping sequence to B_1^+ should be non-selective to circumvent confounding slice profile effects. At the same time the imaging sequence as such should be limited to 2 dimensions to be time-efficient. These goals were reconciled by using a 2D gradient-echo sequence with a non-selective, spoiled prepulse of varying nominal flip angle, similar to a scheme described in [19]. A schematic of this sequence is shown in Fig. 4.1.a. The rectangular prepulse had a duration of 2 ms, followed by spoiler gradient pulses of 4 ms. The nominal prepulse flip angle (α) was increased for simplicity in even steps from 0° to the maximum possible with the respective transmitter (typically 400° in 10 to 20 steps). The following slice excitation was performed with a low flip angle of typically 20° and a small slice thickness of 2 mm to prevent effects of through-plane B_0 inhomogeneity. Throughout, the drive configuration chosen for the saturation pulse was also used for applying the subsequent excitation pulse. Doing so removes the need to switch the configuration between the two pulses and thus reduces hardware requirements.

Due to the moderate spatial variation of B_1^+ the resolution of the image readout was set to 64×64. Two different acquisition schemes were used and compared. The first was a steady-state spin-warp scheme with a repetition time of $T_\mathrm{R} = 200\,\mathrm{ms}$ unless stated otherwise. Shorter T_R were prevented by SAR limits. The steady-state condition was ensured by 15 dummy runs before each actual image acquisition. The second acquisition variant was a single-shot echo-planar imaging (EPI) readout, which drastically reduces the overall scan time. No dummy runs were performed prior to EPI acquisition. EPI is susceptible to image distortion due to B_0 inhomogeneity. However, in the present application this effect is benign because it does not vary with driving configurations and prepulse flip angles.

Using either acquisition variant an image series with increasing prepulse angle was obtained for each driving configuration. This series was then fitted, pixel by pixel, to a signal model incorporating all relevant influences on the observable signal strength. Slightly different models were required for the steady-state spin-warp and the transient-state EPI data (Eq. [4.5] and Eq. [4.4], respectively). The detailed derivations are given in 4.5.1. The only free parameters of either signal model are the ratio of the actual and nominal flip angle, (B_1^{rel}), and T_1. Additionally the models incorporate the influence of the local static baseline field B_0. The latter was assessed in a standard fashion by gradient-echo imaging with two different echo times ($\Delta\mathrm{TE} = 0.5\,\mathrm{ms}, \mathrm{TR} = 100\,\mathrm{ms}$). In T/R array experiments the array was driven in quadrature for B_0 mapping.

The nonlinear model fitting was done in a least-squares sense by an initial coarse exhaustive search neglecting off-resonance effects ($\Delta B_0 = 0$), followed by iterative refinement of B_1^{rel} and T_1 values incorporating the influence of local off-resonance. The B_1^{rel} and T_1 fitting the data closest were stored in corresponding B_1^+ and T_1 maps.

The described mapping and fitting procedure yields the magnitude of B_1^+ in absolute terms (even though expressed here relative to a nominal value). It is not capable of measuring the absolute phase of B_1^+ fields. However, knowledge of absolute phase is not necessary for most practical applications of MCT. For controlling the RF field superposition in a transmit array it is sufficient to know the phases of the $B_{1,c}^+$ only up to an arbitrary phase offset, which must be the same for all array elements but which may vary in space. This reduced requirement is fulfilled by the net image phase obtained in the experiments described above. On this basis the phase of the first image, i.e. that obtained without prepulse, was used as the phase of B_1^+ for the respective drive configuration.

Data acquired with array reception generally required channel combination after reconstruction of single-channel images. Throughout, this combination was performed such as to optimize the SNR of the combined image [20]. The corresponding spatially varying combination coefficients were determined once initially from the data acquired for B_0 mapping.

4.2.4 Single-Channel Validation

In a first validation step, the B_1^+ mapping procedure was subject to basic tests, using a single-channel transmitter, namely the T/R head resonator, loaded with the spherical phantom. Robustness with respect to varying saturation and relaxation effects was then demonstrated with the cylindrical multiple-T_1 phantom in the same resonator. The T_1 values obtained as a side product of the fitting process were compared with reference values measured by a single-voxel inversion recovery method. The same setup was used to further test the validity of the signal model by varying sequence properties in the spin-warp scheme. First the repetition time T_{R} was varied between 200 ms and 800 ms. In a second experiment the number of different prepulse angles α was varied between 10 and 39, keeping the maximum angle constant. For further validation B_1^+ mapping in the spherical phantom was used to predict the signal nulls produced by a 180° excitation pulse in 3D gradient-echo imaging (as proposed by [13]). Finally, the B_1^+ maps obtained using the spin-warp and EPI schemes were compared using the TX volume coil and the spherical phantom.

4.2.5 RF-Shim Validation

Targeted excitation by superposition of $B_{1,c}^+$ produced by different transmitter elements forms the basis of all MCT methods such as RF shimming and Transmit SENSE. To be useful for MCT calibration, B_1^+ mapping must enable accurate predictions of such superpositions. In particular, the B_1^+ map of a driving configuration and the B_1^+ maps of the individual transmit channels involved must fulfill Eq. [4.1] to be consistent. Verifying this equality validates the proposed B_1^+ mapping approach also for transmit arrays and demonstrates its applicability for MCT calibration.

To perform this verification the T/R array was loaded with the spherical phantom and B_1^+ mapping data were obtained with the EPI readout. For each of the described 8 generic driving configurations (Eq. [4.3]) 20 flip-angle steps were performed at a repetition time of 300 ms, resulting in a total scan time of 48 s. Based on the mapping results RF shim factors were calculated such as to focus the net B_1^+ in a certain pixel, using nonlinear least-squares optimization. The resulting RF-shimmed driving configuration was then experimentally implemented and its B_1^+ was mapped in the same way as previously for the generic driving configurations. Following Eq. [4.1] the mapping result was predicted by the corresponding numerical superposition of the single-channel $B_{1,c}^+$ maps.

4.3 Results

4.3.1 Interferometry for B_1^+ mapping

Figure 4.2.1 shows B_1^+ maps produced by single-element excitation a), the full quadrature configuration b), and the first array drive configuration of Eq. [4.3] with inverted current amplitude in the array element at the top of the phantom c). In all three cases the RF pulse was scaled to the same amplitude at each element driven. It can be seen that single-element excitation hardly produces any signal in most of the ROI compared to quadrature excitation. The proposed array drive configuration yields a similar overall amount of excitation as quadrature. The concomitant electric fields, obtained by simulation, are depicted in the second row of this figure (Fig. 4.2.2), for equal total forward power delivered to the array. Single-element excitation causes the highest local electric field, which is 6 times higher than the maximum in the quadrature case and 2 times higher than with the proposed drive configuration.

Figure 4.2.3 shows B_1^+ maps of the same array element generated with the

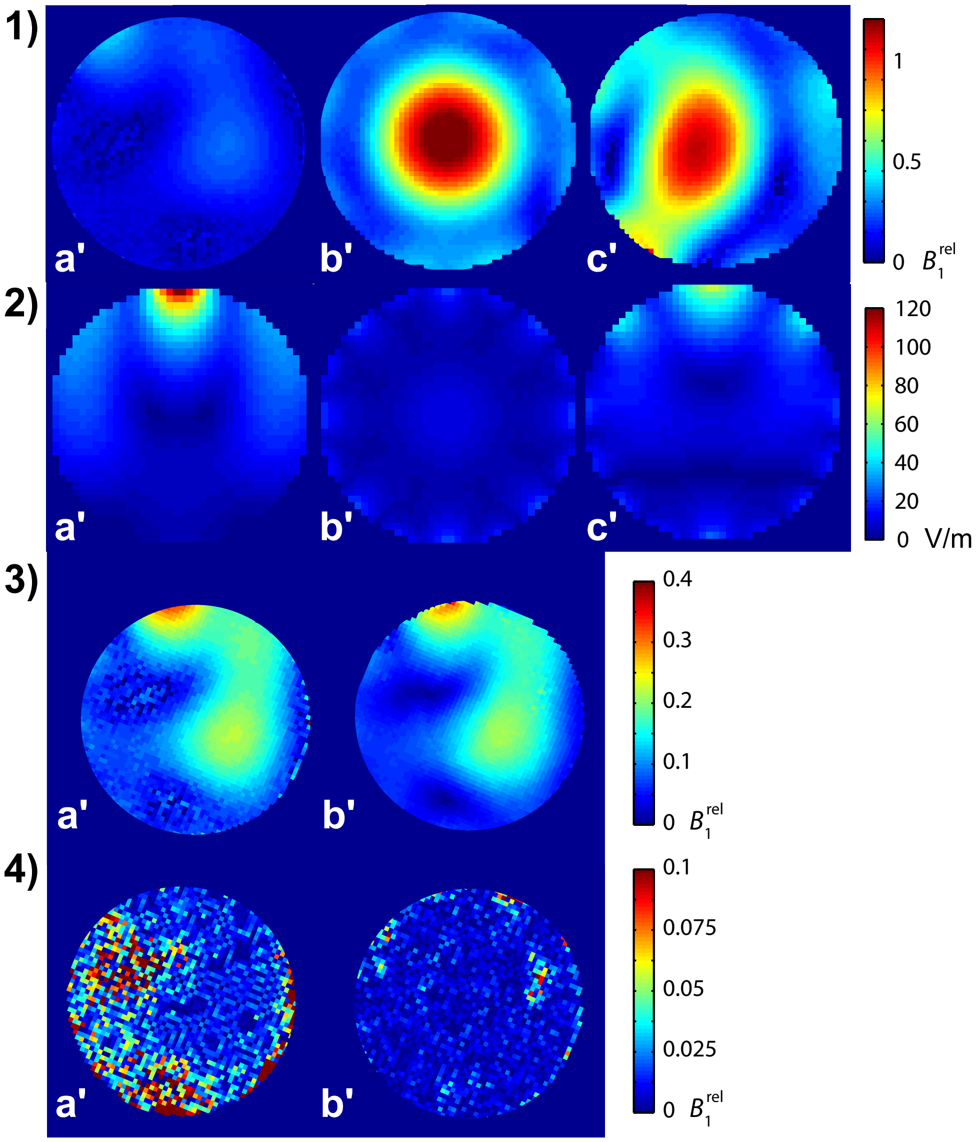

Figure 4.2: Comparison between single element excitation and improved array drive configuration for B_1^+ mapping. 1) B_1^+ field measured when exciting the phantom using a) single coil, b) quadrature and c) the configuration given by Eq. [4.3] inverting the phase of the top element (all images have equal color scaling). 2) full-wave numerical simulations of the electric fields produced by delivering equal total power to the coil array for taking the images in 1). 3) B_1^+ maps acquired using a) single coil excitation and b) the configuration described above. 4) noise maps estimated by substraction of a smoothed map corresponding to 3).

proposed mapping sequence and fitting approach. The first map was obtained with conventional single-channel excitation a). The second map was obtained with the proposed interference approach, using driving configurations as described above b). Figure 4.2.4 shows estimates of the noise content in these B_1^+ maps. The noise estimates were obtained by strongly smoothing the B_1^+ maps and subtracting the smoothed versions from the originals. It is seen that the interference approach reduces noise in the B_1^+ maps substantially, especially in regions where the the B_1^+ of the single element is low. Pixels close to the edge of the phantom are not accurately mapped by the novel method. This can be explained by the higher required consistency of the signal acquisition between different scans, which is challenged due to partial-volume effects in aforementioned regions.

4.3.2 Single-Channel Validation

The results of the single-channel validation experiments are shown in Fig. 4.3 and Fig. 4.4. Figure 4.3.a) shows typical signal fitting results for the spin-warp and EPI schemes, illustrating the adequacy of the underlying signal models. Independence of B_1^+ mapping results from T_1 is demonstrated by the B_1^+ map shown in Fig. 4.3.c), which does not exhibit any correlation with the corresponding T_1 map in d). Furthermore, the T_1 values obtained along with B_1^+ through joint fitting correspond reasonably well with reference values measured by single-voxel inversion recovery as summarized in Tab. 4.1. The fitted T_1 values were found to be more accurate for relaxation times comparable to the repetition time of the sequence. For longer relaxation times ($T_1 \gg 2\,T_\mathrm{R}$), the acquired signal depends less on T_1 variations. This results in the observed lower accuracy of fitted T_1 values, but actually improves the robustness of the B_1^+ fitting. Generally the accuracy of the fitted T_1 values is much less than that of the B_1^+ results and the proposed approach is hence not suited for high-performance T_1 mapping.

The proposed combination of imaging sequence and B_1^+ fitting proved robust also against variations of sequence properties as shown in Fig. 4.3.e) and f). Both for varying T_R and for varying flip angle series the obtained B_1^+ data show excellent congruence. The only exception are the two small indentations marked by arrows in f). These coincide with signal voids caused by the walls of the compartment in the middle of the phantom. It is therefore likely that these small errors are related to partial-volume effects. Figure 4.3.f) also shows that a rather low number of flip angles of about 10 to 12 are sufficient for very accurate B_1^+ measurements. Figure 4.3.b) confirms that the ring of zero signal in a 3D gradient-echo sequence was indeed accurately predicted by the proposed B_1^+ mapping method.

Finally Fig. 4.4 shows that the much faster single-shot EPI readout yielded a very similar B_1^+ map as the more robust but also much more time consuming spin-warp scheme. The minor degradation of the EPI data is due to lower SNR

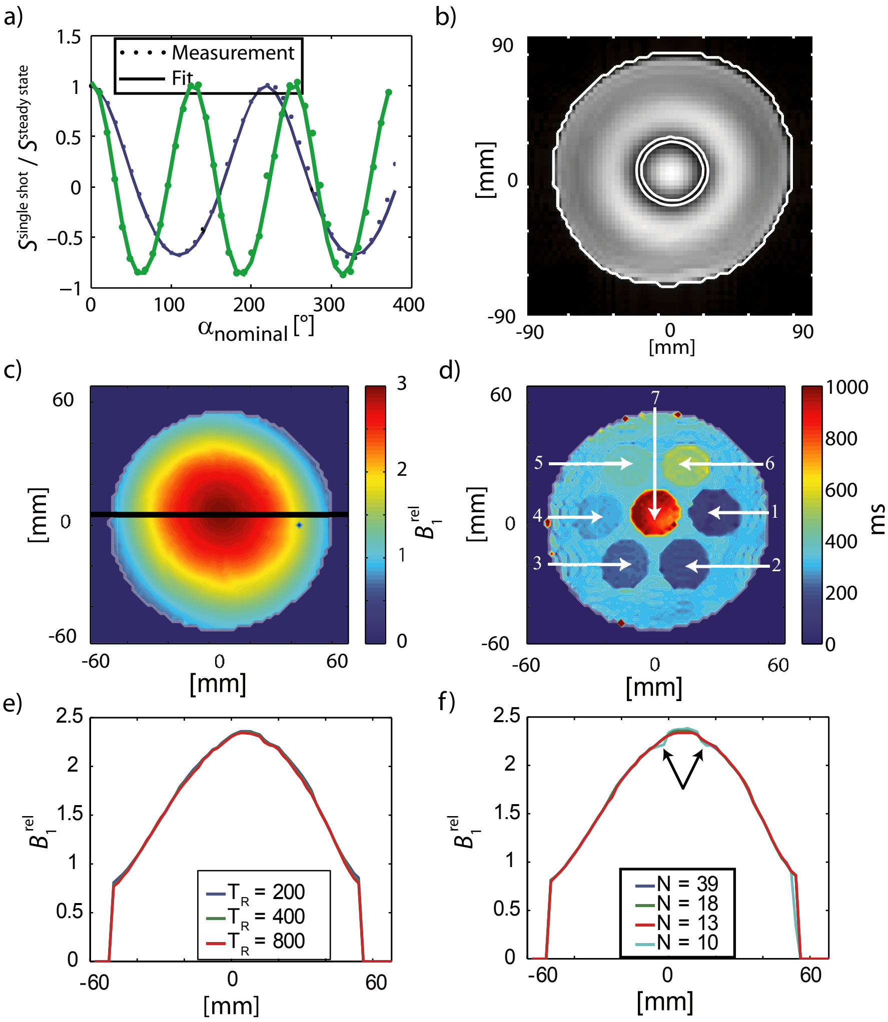

Figure 4.3: Validations of B_1^+ mapping sequence and evaluations. a) Example of fits (solid line) performed to the data (dots) using steady-state spinwarp readout (blue) and single-shot EPI (green). b) Using the measured B_1^+ map the signal null produced by a local flip angle of 180° is predicted (solid white lines) for a given nominal flip angle and compared to the corresponding (gray-scale plot) acquired 3D gradient echo image. c) B_1^+ map and d) corresponding T_1 map in the cylindrical phantom with compartments having different longitudinal relaxation times. The black line marks the position of the profiles taken for plots e) and f). e) Profile of B_1^+ maps from c) acquired using different repetition times TR in the sequence. f) Same profile as e) resulting from different total numbers (N) of flip angles acquired.

and geometrical distortion caused by B_0 inhomogeneity. Nevertheless the mapping quality achieved with the EPI readout is certainly sufficient for typical calibration tasks in MCT.

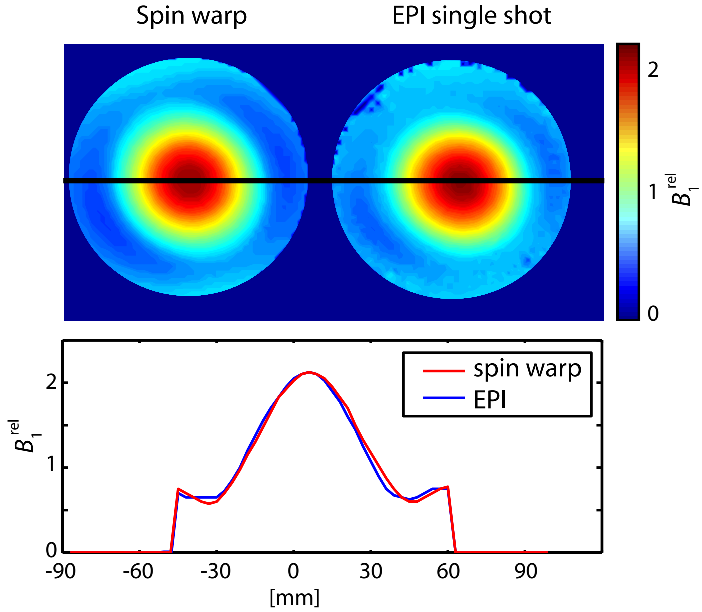

Figure 4.4: Comparison between spinwarp and EPI readout of B_1^+ maps inside the spherical phantom using the 'TX volume' coil. Both maps have a resolution of 64 × 64 pixels and a field of view of 180 mm. The profile shown below was taken along the line marked in both 2D plots.

4.3.3 RF Shim Results

The total scan time for mapping the 8-channel T/R array with EPI readouts was 40 s. The additional B_0 map was acquired in 6 s. The nonlinear fitting procedure took roughly 10 s per $B_{1,m}^+$ map under Matlab 7.1®(The Mathworks, Natick, Massachusetts) on a common PC. However, the fitting routines can be started as soon as scanning is completed for the first driving configuration and then run in parallel with data acquisition. In this fashion the whole B_1^+ mapping procedure was completed within less than a minute (56 s). It used 1.8 W average forward RF power per $B_{1,m}^+$ map acquired and a peak power of 2.1 kW. The RF shim parameters used for focusing B_1^+ in a given region are listed in Tab. 4.2. As shown in Fig. 4.5 the predicted and mapped RF shimming results coincide very closely. It should be noted that the small residual discrepancies in these results do not necessarily indicate inaccuracy of the B_1^+ mapping, but also reflect the finite accuracy of the custom-built RF shimming hardware.

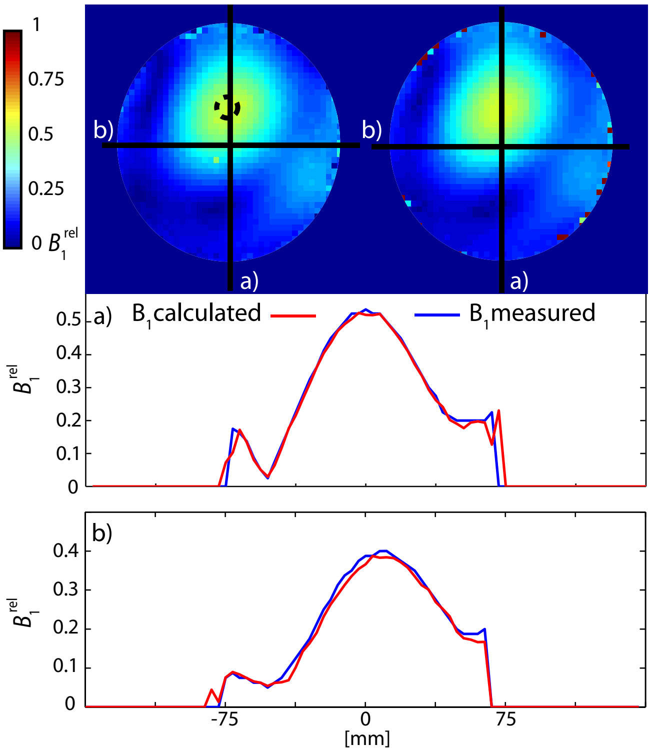

Figure 4.5: Example of an RF shim experiment planned using B_1^+ maps of the 'T/R array' acquired using the novel method and an EPI readout. The RF shim parameters are optimized to focus the excitation inside the dashed circle. The left image shows the B_1^+ field calculated by the superposition of the single array element B_1^+ maps. The right image shows the B_1^+ field measured adjusting these RF shim parameters to the array feed system. The two profile plots along the two axes indicated show the direct comparison between the two maps.

4.4 Discussion and Conclusion

The methodology introduced in this work combines an interference approach with a comprehensive parametric signal model to achieve accurate B_1^+ mapping of transmitter arrays within tight SAR and time constraints. It is important to note that the two underlying principles are conceptually independent and can each be readily used in other combinations. In particular, the interference approach could equally facilitate conventional B_1^+ mapping of transmitter arrays, e.g., using a double-angle method. For moderate dynamic ranges of B_1^+ this combination promises a further significant gain in mapping speed. Likewise the sequence and parametric model employed here can also serve for B_1^+ mapping of single-channel systems.

Using B_1^+ interferometry the B_1^+ fields of array elements are not measured directly but via their interference with a SAR-efficient baseline field. In this fashion even small B_1^+ fields can be observed in the large-flip-angle regime. This strategy could also be viewed as shifting the working point of the B_1^+ measurement from zero flip angle to a baseline angle at which MR signals change unambiguously with B_1^+ . As a result the numerical conditioning of extracting B_1^+ values improves significantly, reducing the propagation not only of thermal noise but also of systematic errors.

These benefits are confirmed by the experimental results obtained in this study.

Unlike previous techniques the interference method yields single-channel B_1^+-maps with an accuracy that is largely independent of the local RF field strength of the respective element. Importantly, the B_1^+ results were also found not to be biased by parameters of the mapping sequence or by the local T_1 and B_0 offset. Their accuracy was demonstrated by a high level of consistency between predicted and measured B_1^+ fields generated by RF shimming. This finding confirms the suitability of the extended signal model and nonlinear fitting procedure employed in this work. Besides B_1^+ maps it also yields T_1 maps as a byproduct. These maps are significantly less accurate than the B_1^+ results because the MR signal depends less sensitively on relaxation. However, such rough T_1 estimates could still be useful, e.g., for further sequence planning.

Measuring B_1^+ by interference relies on the ability to superimpose independent RF field components and to generate a reasonably homogeneous baseline field. It thus exploits the benefits of MCT already at the stage of calibrating the transmitter array. Doing so effectively requires a rough idea of the expected RF field distributions and is governed by the competing goals of achieving large flip angles, controlling the conditioning of the inverse problem, and limiting RF power deposition. Clearly, the design of the calibration experiments cannot rely on the B_1^+ maps that will only be the result of these scans. Therefore the choice of driving configurations for the mapping routine must be made heuristically or based on prior knowledge. In the present work a simple heuristic driving scheme has been found to work well for calibrating a circular coil array.

In cases where the initial driving scheme does not yield satisfactory mapping results it can be extended by complementary configurations that stabilize the inverse calculation in Eq. [4.2]. It is important to note that the choice of such additional configurations can actually be based on the B_1^+ estimates that are already available. The resulting incremental optimization of the calibration strategy is expected to arrive at robust B_1^+ maps fairly quickly for transmitter arrays of reasonable coverage. Such a process could be regarded as boot-strapping calibration of MCT systems and will likely also converge, if less quickly, after starting from an arbitrary set of initial configurations.

Ultimately, for each constellation of transmitter array, sample, and region of interest there exist optimal driving schemes that reach a given accuracy target with a minimal number of configurations. However, such optimal schemes are of largely academic interest because they can be identified only after exact B_1^+ maps have already been obtained in one way or another. Furthermore they depend on the exact local SAR characteristics of the respective setup, which cannot be assessed with present-day in-vivo methodology.

Based on the results of the present study the proposed mapping methodology is expected to enable accurately tailored RF shimming and Transmit SENSE.

The high B_1^+ sensitivity of the interference approach enables single-shot readouts, permitting 2D mapping of an 8-channel array in less than a minute. Due to the smooth spatial variation of B_1^+ it is expected that single-slice calibration will often be sufficient for applications to surrounding slabs of moderate thickness. For larger volumes, the B_1^+ mapping sequence could be extended to 3D operation by adding phase encoding in the slice direction. Alternatively, readouts of multiple slices could be performed successively after a single non-selective preparation pulse. For few slices this option would cause only a moderate increase in overall scan time. The duration of B_1^+ calibration is thus reduced to a range similar to that of other preparation steps, such as volume shimming. The proposed approach therefore promises to render fully calibrated array transmission truly practical, filling a key gap in current MCT methodology.

4.5 Appendix

4.5.1 Signal Model Calculation

Let B_1^{rel} denote the ratio between the actual and nominal B_1^+. Then the nominal flip angles α, β of the block prepulse and the slice-selective excitation pulse (Fig. 4.1) result in effective angles of $\alpha B_1^{\mathrm{rel}}$ and βB_1^{rel}. Note that B_1^{rel} is the same in both expressions, reflecting the fact that the same drive configuration is used for both pulses. Neglecting relaxation during these short pulses their effect can be represented by net rotation matrices, which depend not only on the effective angles but also on the static field offset ΔB_0. These matrices, say $P(\alpha B_1^{\mathrm{rel}}, \Delta B_0)$ and $Q(\beta B_1^{\mathrm{rel}}, \Delta B_0)$, were numerically calculated for relevant parameter ranges and stored in a look-up table.

Spoiling is assumed to be ideal. Hence the effect of the RF pulses is reduced to multiplying the z magnetization by, respectively, $P_{z,z}$ and $Q_{z,z}$. Longitudinal relaxation is assumed to occur only between the RF pulses, and modeled as exponential with a single effective T_1 value per image voxel. The evolution of longitudinal magnetization during a series of sequence repetitions can then be described recursively as follows.

Let $M_z^{(i-1)}$ denote the longitudinal magnetization of a given voxel before slice excitation in the $(i-1)$th sequence repetition. Undergoing the subsequent RF pulses and relaxation intervals it gives rise to:

$$\begin{aligned} M_z^{(i)} =& M_0\left(1-\exp\left(-\frac{\Delta}{T_1}\right)\right)+\exp\left(-\frac{\Delta}{T_1}\right)P_{z,z}(\alpha^{(i)}B_1^{\mathrm{rel}},\Delta B_0)\cdot \\ & \left(M_0\left(1-\exp\left(-\frac{T_{\mathrm{R}}-\Delta}{T_1}\right)\right)+\exp\left(-\frac{T_{\mathrm{R}}-\Delta}{T_1}\right)M_z^{(i-1)}Q_{z,z}(\beta B_1^{\mathrm{rel}},0)\right) \end{aligned} \tag{4.4}$$

where M_0 denotes the thermal equilibrium magnetization and $\alpha^{(i)}$ indicates an individual prepulse angle in each sequence repetition. $Q_{z,z}$ is generally taken equal to its value at zero B_0 offset, reflecting the assumption of a good M_z slice profile.

Consider a readout (e.g. single-shot EPI) that yields a full image in each sequence repetition (i). The pixel values of such an image will be proportional to the available $M_z^{(i)}$. They additionally scale with further factors, such as $\sin(\beta B_1^{\mathrm{rel}})$ and the sensitivity of the receiver coil. However these latter factors do not vary with the prepulse angle and can thus be eliminated by normalizing all images by a reference obtained with $\alpha = 0$. Such normalization also eliminates the unknown equilibrium magnetization M_0. Given ΔB_0 from a separately acquired B_0 map the only remaining free parameters of the recursive model are B_1^{rel} and T_1 of the pixel under consideration.

A slightly different model is required to analyze the standard case of many sequence repetitions per image. For this case the nominal prepulse angle α is kept constant while acquiring an image and the magnetization is assumed to be driven into steady state by initial dummy repetitions:

$$M_z^{(i+1)} = M_z^{(i)} \Rightarrow$$

$$M_z^{steady} = M_0 \frac{P_{z,z}(\alpha B_1^{\mathrm{rel}}, \Delta B_0) \exp\left(-\frac{\Delta}{T_1}\right)\left(1 - \exp\left(-\frac{T_{\mathrm{R}} - \Delta}{T_1}\right)\right) + 1 - \exp\left(-\frac{\Delta}{T_1}\right)}{1 - P_{z,z}(\alpha B_1^{\mathrm{rel}}, B_0) Q_{z,z}(\beta B_1^{\mathrm{rel}}, 0) \exp\left(-\frac{T_{\mathrm{R}}}{T_1}\right)} \tag{4.5}$$

Again, normalization by a reference image obtained with $\alpha = 0$ eliminates M_0 and other constant factors, leaving only B_1^{rel} and T_1 to be fitted.

Compartment	1	2	3	4	5	6	7
$T_1^{IR}[ms]$	150 ± 14	190 ± 14	220 ± 14	270 ± 14	380 ± 14	630 ± 14	800 ± 14
$T_1^{B_1}[ms]$	162 ± 20	204 ± 15	237 ± 13	303 ± 14	411 ± 14	513 ± 30	901 ± 73

Table 4.1: Comparison of T_1 values measured by single voxel spectroscopic inversion recovery (T_1^{IR}) to the values obtained by the B_1^+ mapping sequence ($T_1^{B_1}$). The error of the spectroscopic measurement was determined by the resolution of the stepping of the inversion time. The error of the $T_1^{B_1}$ values has been determined by the standard deviation of all pixels located entirely inside the compartment.

Element nr.	1	2	3	4	5	6	7	8
Attenuation [dB]	-15	-2	0	-4	-15	-16	-8	-16
Phase [°]	15	0	0	0	-15	180	0	180

Table 4.2: RF shim parameters used for the experiment depicted in Fig. 4.5. The phases and attenuation coefficients are denoted relative to the quadrature excitation current.

Bibliography

[1] Hoult DI. Sensitivity and Power Deposition in a High-Field Imaging Experiment. J Magn Reson Imag 2000; 12(1):46–67.

[2] Adriany G, Van de Moortele P-F, Wiesinger F, Moeller S, Strupp JP, Andersen P, Snyder C, Zhang X, Chen W, Pruessmann KP, Boesiger P, Vaughan T, and Ugurbil K. Transmit and receive transmission line arrays for 7 Tesla parallel imaging. Magn Reson Med 2005; 53(2):434–445.

[3] Katscher U, Boernert P, Leussler C, and van den Brink JS. Transmit SENSE. Magn Reson Med 2003; 49(1):144–150.

[4] Zhu Y. Parallel excitation with an array of transmit coils. Magn Reson Med 2004; 51(4):775–784.

[5] Cunningham CH, Pauly JM, and Nayak KS. Saturated Double-Angle Method for Rapid B_1^+ Mapping. Magn Reson Imag 2006; 55:1326–1333.

[6] Yarnykh VL. Actual Flip-Angle Imaging in the Pulsed Steady State: A Method for Rapid Three-Dimensional Mapping of the Transmitted Radiofrequency Field. Magn Reson Med 2007; 57:192–200.

[7] Insko EK and Bolinger L. Mapping of the radiofrequency field. J Magn Reson Series A 1993; 103:82–85.

[8] Stollberger R and Wach P. Imaging the Active B_1 Field in Vivo. Magn Reson Med 1996; 35:246–251.

[9] Akoka S, Franconi F, Seguin F, and Le Pape A. Radiofrequency map of an NMR coil by imaging. Magn Reson Imag 1993; 11:437.

[10] Carlson JW and Kramer DM. Rapid Radiofrequency Calibration in MRI. Magn Reson Med 1990; 15:438–445.

[11] Mugler JP and Miller GW. Rapid 3D Mapping of the B_1 Field Using a Low-Flip-Angle, Phase-Based Method with Improved Sensitivity. In Proc 15th annual meeting of ISMRM 2007. p. 351.

[12] Oh CH, Hilal SK, Cho ZH, and Mun IK. Radio frequency field intensity mapping using a composite spin-echo sequence. Magn Reson Imag 1990; 8:21–25.

[13] Dowell NG and Tofts PS. Fast, Accurate, and Precise Mapping of the RF Field In Vivo Using the 180° Signal Null. Magn Reson Med 2007; 58:622–630.

[14] Barker G, Simmons A, Arridge S, and Tofts P. A simple method for investigating the effects of non-uniformity of radiofrequency transmission and radiofrequency reception in MRI. Brit J Radiol 1998; 71:59–67.

[15] Kerr AB, Cunningham CH, Pauly JM, Giaquinto RO, Watkins RD, and Zhu Y. Self-calibratied transmit SENSE. In Proc 15th annual meeting of ISMRM 2006. p. 2561; Seattle; 2006.

[16] Brunner DO, Zanche ND, Froehlich J, Baumann D, and Pruessmann KP. A symmetrically fed microstrip coil array for 7T. In Proc 15th annual meeting of ISMRM 2007. p. 448; Berlin; 2007.

[17] Froehlich J, Baumann D, Brunner DO, and Pruessmann KP. Computational Analysis and Validation of Coil Arrays for Whole-Brain MR-Imaging at 7T. In International Microwave Symposium Digest 2007. p. 2217–2220; Honolulu, Hawaii, USA; 2007.

[18] DeZanche N, Brunner DO, and Pruessmann KP. An Inexpensive versatile RF power splitter, attenuator and phase-shifting system for array transmit at 7T. In Minnesota High-Field Workshop 2007. p. 87.

[19] Klose U. Mapping of the radio frequency magnetic field with a MR snapshot FLASH technique. Med Phys 1992; 19(4):1099–1104.

[20] Pruessmann KP, Weiger M, Scheidegger MB, and Boesiger P. SENSE: sensitivity encoding for fast MRI. Magn Reson Med 1999; 42:952–962.

Chapter 5

Optimal design of multiple-channel RF pulses under strict power and SAR constraints

published in:

D. O. Brunner and K. P. Pruessmann. *"Enforcing Strict Constraints in Multiple-Channel RF Pulse Optimization"*. Proc Intl Soc Magn Reson Med 2007, Berlin. p. 1690

D. O. Brunner and K. P. Pruessmann. *"Increasing Bandwidth of Spatially Selective Transmit SENSE Pulses using Constrained Optimization"*. Proc Intl Soc Magn Reson Med 2008, Toronto. p. 635

D. O. Brunner and K. P. Pruessmann. *"Optimal Design of Multiple-Channel RF Pulses Under Strict Power and SAR Constraints"*. Magn Reson Med 2010; in press: p.

5.1 Introduction

In traditional MRI, RF pulses with spatial selectivity in multiple dimensions [1, 2] are primarily used for volume-selective spin manipulations. In high-field MRI such pulses can also serve to compensate for increased non-uniformity of the RF fields produced by the transmit probe. However, their practical application is generally hampered by long pulse durations.

To accelerate multiple-dimensionally selective RF pulses parallel excitation with multiple transmitters (Transmit SENSE, [3, 4, 5]) has recently been introduced, following a close analogy with parallel imaging techniques. Several means of calculating accelerated multiple-channel pulses have been presented, e.g. in [3, 4, 6], building upon the analogies between signal reception and low-flip-angle excitation as well as that between noise in receive signals and power deposition in the transmit mode. It has been noticed that with excessive pulse acceleration the power dissipated in the tissue (specific absorption rate, SAR) tends to increase disproportionately in a way similar to noise amplification in the receive case [7]. Similar to ill-posed image reconstruction, this problem has been addressed by regularizing the matrix inversion involved in the pulse calculation [3, 8, 6]. Such regularization reduces the SAR and transmitter power levels at the expense of pulse profile fidelity.

These developments highlight the close conceptual similarity of spatially selective spin excitation and spatially resolved spin detection [9]. However, there are also important differences between the two perspectives, prompting rather different criteria for power and noise control in RF pulse optimization and image reconstruction, respectively. In image reconstruction, minimizing the noise level in the resulting image is a goal that competes with that of maximizing the fidelity of reconstructing the spin signal. As a consequence it can be rational, for instance, to tolerate stronger noise if this mitigates even stronger artefacts. By contrast, in RF pulse design the SAR as well as the average and the peak transmitter powers are subject to hard regulatory [10] and technical limits that cannot be violated in a trade-off for profile quality. Furthermore, in reconstructing an image value it is only the net noise variance that is relevant, while it does not matter how the noise is composed from different origins in the sample and apparatus. This, too, is different in RF pulse design, where it does matter how dissipated power is spatially distributed. SAR limits must be kept in every part of the body independently [11] and may vary between different anatomies. These considerations illustrate that RF pulse design is a different and arguably harder problem than image reconstruction since it involves a larger number of design criteria of which the majority must not be optimized but rather kept within given constraints.

It has been shown that multiple power and SAR constraints can be jointly fulfilled by sufficiently strong regularization [3, 4, 6], which however will generally fail to yield the bestpulse profile that is compatible with these constraints. In principle, this problem could be addressed by incorporating a separate regularization parameter for each constraint and searching for the optimal parameter set [8]. However, the latter would be extremely numerically demanding, which conflicts with the need to construct multiple-channel RF pulses on demand during imaging sessions.

In view of these difficulties the present work proposes an alternative design approach that uses semi-definite programming (SDP) for optimizing pulse profiles under multiple strict constraints [12]. Within viable computation times it permits the calculation of optimal multiple-channel RF pulses that comply with given global and local SAR limits as well as upper bounds for peak and average transmitter power.

5.2 Theory

RF pulses are usually designed by inverting the Bloch equations for a given target nutation pattern. The small-flip-angle approximation derived in Eq. 3.48 according to Ref. [1] linearizes these equations, permitting the design of spatially and spectrally selective pulses by linear inversion. It has been shown [4, 13] that this approach can be readily extended to multiple-channel transmission. Let a multiple-channel RF pulse be given by the complex-valued voltage waveforms $v_c(t)$ used to drive the ports of an array of n_c transmitter elements. Then the small-flip-angle analysis yields the following expression for the resulting complex-valued transverse magnetization M_{xy}:

$$\begin{aligned} M_{xy}(\vec{r}, T_0) =& i\gamma M_0(\vec{r}) \\ & \cdot \sum_c B_1^c(\vec{r}) \int_0^{T_0} e^{i\vec{k}(t)\cdot\vec{r}} e^{\overbrace{\left(i\omega_0(\vec{r}) + \frac{1}{T_2^*(\vec{r})}\right)(t - T_0)}^{:=\varphi}} v_c(t)dt \qquad (5.1) \\ \vec{k}(t) =& -\gamma \int_t^{T_0} \vec{G}(t')dt' \qquad (5.2) \end{aligned}$$

where $\vec{r}$ denotes position in space, t is time, T_0 is the total pulse duration, γ ($\approx 267.5 \cdot 10^6\,{}^{\mathrm{rad}}/_{\mathrm{T \cdot s}}$ for protons) is the gyromagnetic ratio of the nucleus of interest, $\omega_0(\vec{r}) = \gamma\Delta B_0(\vec{r})$ is the local off-resonance frequency, $T_2^*(\vec{r})$ is the macroscopic transverse relaxation time, and $B_1^c(\vec{r})$ is the voltage-normalized B_1^+ field of coil c. More precisely, B_1^c is understood to be the B_1^+ that results from driving the port to which coil c is connected. It thus includes any potential field contributions generated by other transmitter elements to which this coil may be coupled. The amplifier outputs are assumed to be protected by circulators with dump loads that absorb any power that is reflected by unmatched ports or otherwise scattered through the array. On this basis the amplifiers can be regarded as mutually isolated and as producing exclusively forward waveforms $v_c(t)$. The k-space trajectory $\vec{k}(t)$ describes Fourier encoding performed by concurrent gradient fields with time course $\vec{G}(t)$. A more accurate forward model is given in Appendix 5.7.1 taking the limited bandwidth of the gradient waveforms into account. The nominal resolution of the Fourier encoding is given by the maximum extent of the trajectory, k_{max}. The undersampling factor R is given by the maximum extent of the requested field of excitation, FOX, and the maximum sampling spacing Δk that the trajectory exhibits within its range of k-space coverage:

$$R = \frac{\Delta k \, FOX}{2\pi} \tag{5.3}$$

For a given body region $\Omega_p \subset \mathbb{R}^3$ the average SAR[1] of the RF pulse is given by the ohmic losses induced by the time-varying superposition of the individual coils' electric fields:

$$\begin{aligned} SAR_p &= \frac{1}{2T_0V_p} \int_0^{T_0} \int_{\Omega_p} \sum_{c,c'} \frac{\sigma(\vec{r})}{\rho(\vec{r})} v_{c'}^*(t) \vec{E}_{c'}^*(\vec{r}) \cdot \vec{E}_c(\vec{r}) v_c(t) \, dV \, dt \\ &= \sum_{c,c'} \frac{1}{2T_0V_p} \int_{\Omega_p} \frac{\sigma(\vec{r})}{\rho(\vec{r})} \vec{E}_{c'}^*(\vec{r}) \cdot \vec{E}_c(\vec{r}) dV \int_0^{T_0} v_{c'}^*(t) v_c(t) \, dt \end{aligned} \tag{5.4}$$

where $\vec{E}_c(\vec{r})$ denotes the voltage-normalized electric field phasor produced by driving port c, $\sigma(\vec{r})$ and $\rho(\vec{r})$ denote electric conductivity and mass density, respectively, V_p is the volume of Ω_p and the asterisk indicates the complex conjugate. The average and instantaneous forward power delivered to port c, P_c^{ave} and $P_c^{\text{inst}}(t)$, can be calculated from $v_c(t)$ using the channel's impedance Z_c:

$$P_c^{\text{ave}} = \frac{1}{2T_0Z_c} \int_t^{T_0} v_c^*(t) v_c(t) \, dt \leq \widehat{P}_c^{\text{ave}} \tag{5.5}$$

$$P_c^{\text{inst}}(t) = \frac{1}{2Z_c} v_c^*(t) v_c(t) \leq \widehat{P}_c^{\text{peak}} \tag{5.6}$$

with the upper limits $\widehat{P}_c^{\text{ave}}$, $\widehat{P}_c^{\text{peak}}$, which may be of technical nature or imposed by safety considerations.

---

[1] The exact calculation of the SAR from electromagnetic fields and material properties and the specification of the control volumes Ω_p may vary between different safety standards and protocols. However, the resulting SAR value will generally depend quadratically on the driving voltages, permitting any definition of the local and global SAR to be incorporated in the presented analysis.

To facilitate numerical pulse calculation the problem is discretized equidistantly in time, $t_j = (j-1)\cdot \Delta t,\ j = 1\ldots n_t$, and along a Cartesian grid in space, $\vec{r}_q,\ q = 1\ldots n_q$, prompting the vector definitions

$$\mathbf{v}_{(c,j)} = v_c(t_j) \tag{5.7}$$

$$\mathbf{m}_q = M_{xy}(\vec{r}_q, T_0)/M_0(\vec{r}_q) \tag{5.8}$$

where the double index of $\mathbf{v}$ indicates concatenation of all voltage values in a single vector. The sampling interval Δt must be small enough to capture all of the spin dynamics caused by the gradient fields:

$$\Delta t \ll \frac{\pi}{\gamma\, G_{\max} r_{\max}}, \tag{5.9}$$

where $r_{\max}$ denotes the largest distance from the isocenter that occurs within the sample. If short enough the pulse dwell time of the MR system used is a convenient choice for Δt. The spatial discretization must likewise be sufficiently fine to resolve all of the relevant structure of M_{xy} as well as B_1^c, ω_0 and T_2^*. It should usually be finer than the nominal resolution of the Fourier encoding ($k_{\max}\Delta x \ll \pi$) to account for subtle excitation effects such as Gibbs ringing.

After discretization, Eq. 5.1 can be rewritten in matrix-vector form with the transmit matrix $\mathbf{T}$ [6]:

$$\begin{aligned} \mathbf{m} &= \mathbf{T}\mathbf{v} \\ \mathbf{T}_{q,(c,j)} &= i\gamma B_1^c(\vec{\mathbf{r}}_q)\,\Delta t\, e^{i\vec{\mathbf{k}}(t_j)\cdot\vec{\mathbf{r}}_q}\, e^{\left(i\omega_0(\vec{\mathbf{r}}_q)+\frac{1}{T_2^*(\vec{\mathbf{r}}_q)}\right)(t_j-T_0)}. \end{aligned} \tag{5.10}$$

The discretization step also simplifies the notation of the SAR and power criteria (Eq. 5.4-5.6), which all assume the form of positive (semi-)definite quadratic forms of $\mathbf{v}$:

$$P_c^{\text{ave}} = \mathbf{v}^H \mathbf{\Phi}_c^{\text{ave}} \mathbf{v}, \qquad (\mathbf{\Phi}_c^{\text{ave}})_{(c',j),(c'',j')} = \frac{\Delta t}{2T_0 Z_c}\delta_{c,c'}\delta_{c,c''}\delta_{j,j'} \tag{5.11}$$

$$P_{c,j}^{\text{inst}} = \mathbf{v}^H \mathbf{\Phi}_{c,j}^{\text{inst}} \mathbf{v}, \qquad (\mathbf{\Phi}_{c,j}^{\text{inst}})_{(c',j'),(c'',j'')} = \frac{1}{2Z_c}\delta_{c,c'}\delta_{c,c''}\delta_{j,j'}\delta_{j,j''} \tag{5.12}$$

$$SAR_p = \mathbf{v}^H \mathbf{\Psi}^p \mathbf{v}, \qquad \mathbf{\Psi}^p_{(c',j),(c'',j')} = \delta_{j,j'}\tilde{\mathbf{\Psi}}^p_{c',c''} \tag{5.13}$$

$$\tilde{\mathbf{\Psi}}^p_{c',c''} = \frac{\Delta t}{2T_0 V_p}\int_{\Omega_p} \frac{\sigma(\vec{r})}{\rho(\vec{r})}\,\vec{E}^*_{c'}(\vec{r})\cdot\vec{E}_{c''}(\vec{r})\,dV \tag{5.14}$$

where δ denotes the Kronecker delta and the superscript H indicates the complex conjugate transpose.

In summary, the problem of linear pulse design can be stated as follows: For a given k-space trajectory find those pulse waveforms $\mathbf{v}_{\text{opt}}$ within all of the SAR and power constraints that best approximate a desired transverse magnetization profile $\mathbf{m}_{des}$:

$$\begin{aligned} \mathbf{v}_{\text{opt}} &= \underset{\mathbf{v}}{\operatorname{argmin}} \, \|\mathbf{W}(\mathbf{T}\mathbf{v} - \mathbf{m}_{des})\|_2^2 \\ \text{such that } SAR_p &= \mathbf{v}^H \mathbf{\Psi}^p \mathbf{v} \leq \widehat{SAR}_p \quad \forall p \\ P_c^{\text{ave}} &= \mathbf{v}^H \mathbf{\Phi}_c^{\text{ave}} \mathbf{v} \leq \widehat{P}_c^{\text{ave}} \quad \forall c \\ P_{c,j}^{\text{inst}} &= \mathbf{v}^H \mathbf{\Phi}_{c,j}^{\text{inst}} \mathbf{v} \leq \widehat{P}_c^{\text{peak}} \quad \forall c, j. \end{aligned} \tag{5.15}$$

Here the matrix $\mathbf{W}$ serves to introduce spatial weighting of deviations from $\mathbf{m}_{des}$ to express potentially varying importance of profile fidelity [6]. Most typically it is used to mask out regions outside the sample. The concept of SDP, which will be used in the following, is compatible with any choice of norm for measuring the weighted profile deviation. For the present work the ℓ_2-norm was chosen for two reasons. Firstly, it is arguably the most canonical option because it measures error power. Secondly, as detailed later on it permits numerical simplifications that greatly reduce the complexity of the optimization, which is essential to keep computation times in a feasible range for online pulse design.

It is noteworthy that the optimization problem (5.15) can be equivalently formulated as an unconstrained minimum-norm problem with suitable multiple-term regularization, using Lagrange multipliers as detailed in 5.7.3. However, such an approach only shifts the main difficulty from optimizing the RF pulse itself to optimizing the potentially numerous regularization parameters, which is a notoriously difficult task. Many ways of choosing regularization parameters have been developed [14, 15] but all of them work efficiently only for a small number of constraints and inflict a large number of matrix inversions. As a consequence the regularization parameters are often chosen heuristically, which however does not yield optimal solutions.

5.3 Methods

5.3.1 Constrained optimization and reduction of its complexity

According to Eq. 5.15 optimal pulse design amounts to minimizing a quadratic cost functional within quadratic constraints that define a convex search space because the SAR and power matrices are all positive (semi-)definite. In convex optimization theory problems of this kind are known as semi-definite programmes and a range of efficient strategies exist for solving them. Since the specific problem considered here exhibits only quadratic constraints it can even be addressed by the particularly efficient method of second-order cone programming (SOCP) [16, 17, 18, 19]. With this approach a global optimum, if it exists, is safely found within well-defined numerical error bounds. This is a key advantage over general nonlinear optimization, in which global optimality is often not guaranteed.

The amount of computation required for solving the SOCP given by Eq. 5.15 depends strongly on the number of dimensions of the search space, which is given by the length of $\mathbf{v}$ and thus very large to begin with. For more efficient computation we propose a two-stage algorithm in which the dimensionality of the search space is first reduced by least-squares projection as described in Refs. [17, 20]. The basic idea of this approach is to find a small set of $k \ll n_c n_t$ basis vectors spanning a reduced search space that still contains a very good approximation of the global optimum. The calculation of the reduced basis is described below (Eqs. [5.16-5.18]), leading to the reformulation of the optimization problem in reduced dimensions (Eq. [5.19]). The dimension reduction greatly speeds up the repeated evaluation of the cost functional and of the constrained power and SAR terms (Eq. [5.20]), permitting more efficient solution of the SDP in the second step.

Least-squares projection as described in Ref. [17] requires certain assumptions that cannot be strictly ensured for the most general pulse design tasks. However, they hold if the problem is overdetermined and if the sum of all power and SAR matrices is positive definite. In typical practical situations these requirements are fulfilled. Overdetermination results automatically when defining the target profile at sufficiently high resolution. Positive-definiteness is reached when for every nonzero pulse at least one of the constrained SAR and power terms is positive. This is ensured, for instance, by including constraints on the peak or average power of each channel. Building on these prerequisites, in the present work a reduced basis is found by least-squares projection with the Lanczos algorithm [20, 21]. To this end the cost functional to be minimized (5.15) is expanded according to

$$\begin{aligned}\phi(\mathbf{v}) :=& \|\mathbf{W}(\mathbf{T}\mathbf{v} - \mathbf{m}_{des})\|_2^2 \\ =& \mathbf{v}^H\mathbf{T}^H\mathbf{W}^H\mathbf{W}\mathbf{T}\mathbf{v} - \mathbf{m}_{des}^H\mathbf{W}^H\mathbf{W}\mathbf{T}\mathbf{v} \\ & - \mathbf{v}^H\mathbf{T}^H\mathbf{W}^H\mathbf{W}\mathbf{m}_{des} + \mathbf{m}_{des}^H\mathbf{W}^H\mathbf{W}\mathbf{m}_{des}s\end{aligned} \tag{5.16}$$

Lanczos tridiagonalization is performed on the leading quadratic form $\mathbf{A} := \mathbf{T}^H\mathbf{W}^H\mathbf{W}\mathbf{T}$ with the target vector $\mathbf{T}^H\mathbf{W}^H\mathbf{W}\mathbf{m}_{des}$ and starting vector 0 such that only basis vectors in the preimage of the target vector are found by the iteration. The underlying iterative procedure is described more closely in the subsequent section. After k iterations it yields a tridiagonal $k \times k$ matrix $\mathbf{\Delta}_k$[2] and an $(n_c n_t) \times k$

---

[2] This symbol was chosen to keep the notation consistent with the literature and is not to be confused with the k-space sampling distance Δk.

matrix $\mathbf{Q}_k$ whose unitary column vectors are the so-called Lanczos vectors. The eigenvalues of $\mathbf{\Delta}_k$ approximate the k eigenvalues of $\mathbf{A}$ whose eigenvectors contribute the most to the target vector (see App. 5.7.2). Correspondingly, the first k Lanczos vectors form a reduced basis as desired, i.e., one in which the cost functional $\phi(\mathbf{v})$ can be well approximated. For $\mathbf{A}$, $\mathbf{\Delta}_k$ and $\mathbf{Q}_k$ the following relation holds:

$$\mathbf{A}\mathbf{Q}_k = \mathbf{Q}_k\mathbf{\Delta}_k + \mathbf{r}_k\mathbf{e}_k^H \tag{5.17}$$

where $\mathbf{r}_k$ denotes the residual of the Lanczos iteration and $\mathbf{e}_k$ is the k^{th} canonical unit vector in $\mathbb{C}^k$.

The approximation is used by substituting $\mathbf{v} = \mathbf{Q}_k\mathbf{y}$ in Eq. 5.16, with $\mathbf{y}$ denoting the RF pulse waveform in the reduced basis. Using the Cholesky decomposition $\mathbf{\Delta}_k = \mathbf{L}_k^H\mathbf{L}_k$ the cost functional can be rewritten for the reduced basis as:

$$\begin{aligned}\phi(\mathbf{Q}_k\mathbf{y}) =& \mathbf{y}^H\mathbf{L}_k^H\mathbf{L}_k\mathbf{y} - \mathbf{y}^H\mathbf{Q}_k^H\mathbf{T}^H\mathbf{W}^H\mathbf{W}\mathbf{m}_{des} - \mathbf{m}_{des}^H\mathbf{W}^H\mathbf{W}\mathbf{T}\mathbf{Q}_k\mathbf{y} \\ &- \beta_0^2\mathbf{e}_1^H\mathbf{L}_k^{-1}(\mathbf{L}_k^{-1})^H\mathbf{e}_1 + \beta_0^2\mathbf{e}_1^H\mathbf{L}_k^{-1}(\mathbf{L}_k^{-1})^H\mathbf{e}_1 + \beta_0^2 \\ =& \|\mathbf{L}_k\mathbf{y} - \beta_0(\mathbf{L}_k^{-1})^H\mathbf{e}_1\|_2^2 - \beta_0^2\mathbf{e}_1^H\mathbf{L}_k^{-1}(\mathbf{L}_k^{-1})^H\mathbf{e}_1 + \beta_0^2\end{aligned} \tag{5.18}$$

where $\beta_0 = \|\mathbf{W}\mathbf{m}_{des}\|_2$. Here it has been exploited that the columns of $\mathbf{Q}_k$ are orthonormal and that $\mathbf{Q}_k^H\mathbf{T}^H\mathbf{W}^H\mathbf{W}\mathbf{m}_{des} = \mathbf{e}_1\beta_0$ because $\mathbf{T}^H\mathbf{W}^H\mathbf{W}\mathbf{m}_{des}$ is the first Lanczos vector and hence orthogonal to all other columns of $\mathbf{Q}_k$. Further simplification can be achieved by defining $\mathbf{e}_L := (\mathbf{L}_k^{-1})^H\mathbf{e}_1$ and dropping the constant terms, yielding the reduced-basis formulation of the design problem (5.15):

$$\begin{aligned}\mathbf{y}_{\text{opt}} &= \underset{\mathbf{y}}{\text{argmin}}\, \|\mathbf{L}_k\mathbf{y} - \beta_0\mathbf{e}_L\|_2^2 \\ \text{such that } SAR_p &= \mathbf{y}^H(\mathbf{Q}_k^H\mathbf{\Psi}^p\mathbf{Q}_k)\mathbf{y} \leq \widehat{SAR}_p \quad \forall p \\ P_c^{\text{ave}} &= \mathbf{y}^H(\mathbf{Q}_k^H\mathbf{\Phi}_c^{ave}\mathbf{Q}_k)\mathbf{y} \leq \widehat{P}_c^{\text{ave}} \quad \forall c \\ P_{c,j}^{\text{inst}} &= \mathbf{y}^H(\mathbf{Q}_k^H\mathbf{\Phi}_{c,j}^{\text{inst}}\mathbf{Q}_k)\mathbf{y} \leq \widehat{P}_c^{\text{peak}} \quad \forall c, j.\end{aligned} \tag{5.19}$$

It is important to note that despite the approximation involved the values of the power criteria are still exact for the RF pulse represented by $\mathbf{y}$, ensuring that the constraints are still strictly obeyed. The matrix multiplications between $\mathbf{Q}_k$ and the power matrices $\mathbf{\Phi}$ and $\mathbf{\Psi}$ need to be performed only once after the tridiagonalization. The SAR and average power matrices exhibit block-diagonal structure, which can be exploited to accelerate the matrix multiplications as shown here for the example of the SAR matrices:

$$(\mathbf{Q}_k^H\mathbf{\Psi}\mathbf{Q}_k)_{l,l'} = \sum_{j,c}\mathbf{Q}^*_{(j,c),l}\sum_{j',c'}\delta_{j,j'}\tilde{\mathbf{\Psi}}_{c,c'}\mathbf{Q}_{(j',c'),l'} = \sum_{c,c'}\tilde{\mathbf{\Psi}}_{c,c'}\underbrace{\sum_{j}\mathbf{Q}^*_{(j,c),l}\mathbf{Q}_{(j,c'),l'}}_{:=\kappa^{l,l'}_{c,c'}} \tag{5.20}$$

where the computationally expensive calculation of $\kappa_{c,c'}^{l,l'}$ needs to be performed only once to represent all these power matrices in the new basis.

Using the reduced-dimensional power matrices and provided sufficiently small k the remaining optimization problem (5.19) can be solved fast, using a variety of established solvers. The solver used in this work was SDPT3 [22], which was interfaced by YALMIP [23].

5.3.2 Lanczos iteration

The Lanczos algorithm is widely used to solve large, sparse, symmetric eigenvalue problems. One key advantage of this algorithm over other methods, e.g., the Householder algorithm, is that it does not generate any large matrices. The Lanczos algorithm is closely related to the method of conjugate gradients, which has been used in MRI reconstruction [24, 25, 26, 27, 28] as well as RF pulse design [29, 30]. Both kinds of algorithms belong to the family of Krylov space based methods and share beneficial convergence and recovery properties [31]. Details of the specific Lanczos algorithm used in the present work are provided in the Appendix (5.7.2).

The computationally most expensive step within the Lanczos iteration is multiplying the matrices $\mathbf{T}$, $\mathbf{T}^H$ with temporary vectors. It is performed by gridding and Fast Fourier Transform [25, 30] (Fig. 5.1), using a Kaiser-Bessel convolution kernel [32, 33]. The static frequency offsets $\omega_0(\vec{r})$ were incorporated by multiple-frequency interpolation (MFI) [34, 26, 35]. The MFI module was expanded to also account for T_2^* decay by adding a corresponding imaginary part to the local frequency offset [36]. The modulation and demodulation frequencies ω_μ $(1 \leq \mu \leq L_\omega)$ of the MFI were chosen as described in Ref. [34] and maps of the spatially varying interpolation coefficients $c_{\mu,q}^{(\omega)}$ were calculated by least-squares fitting. The number of support values for T_2^* interpolation, L_{T_2}, was chosen such as to limit the interpolation error ϵ in the transverse magnetization at the end of the pulse to a given maximum $\epsilon_{\max}$. Based on the strongest and weakest relaxations that occur in the sample, $\alpha_{\min} = e^{-T_0/T_2^{\min}}$, $\alpha_{\max} = e^{-T_0/T_2^{\max}}$, it was determined as:

$$\epsilon \leq \frac{(\alpha_{\max} - \alpha_{\min})}{L_{T_2}} \leq \epsilon_{\max} \;\Rightarrow\; L_{T_2} = \left\lceil \frac{\alpha_{\max} - \alpha_{\min}}{\epsilon_{\max}} \right\rceil . \tag{5.21}$$

The support values T_η $(1 \leq \eta \leq L_{T_2})$, were then calculated such as to obtain equidistant relaxation factors:

$$T_\eta = -\frac{T_0}{\ln\left(\alpha_{\min} + \frac{\eta-1}{L_{T_2}-1}\left(\alpha_{\max} - \alpha_{\min}\right)\right)}. \tag{5.22}$$

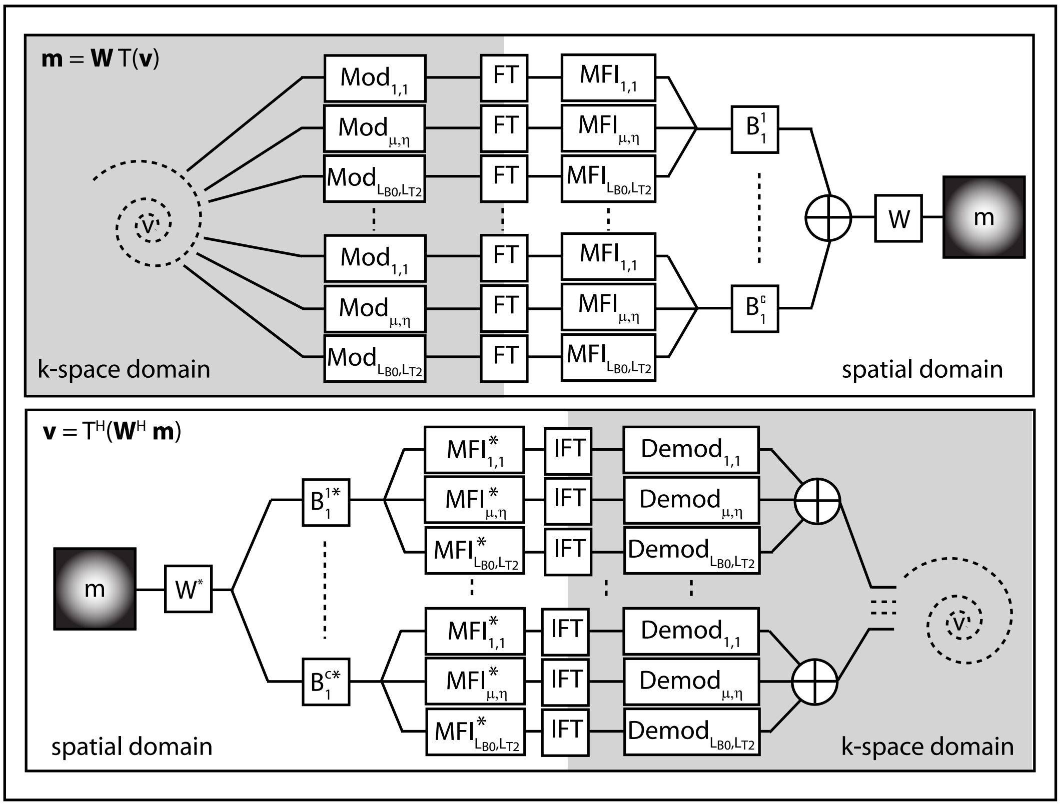

Figure 5.1: Fast multiplication of the matrices $\mathbf{WT}$ and $\mathbf{T}^H\mathbf{W}^H$ with temporary vectors. FT/IFT denote forward and reverse non-Cartesian Fourier transform based on gridding. Mod/Demod and MFI denote the temporal modulations and multiplications by coefficient maps that are involved in multiple-frequency interpolation for off-resonance and T_2^* correction.

The corresponding coefficient maps $c_{\eta,q}^{(T_2)}$ were obtained by next-neighbor interpolation. Finally, MFI modulation and demodulation as well as the coefficient maps were cast into net arrays for use in the Lanczos iteration:

$$\begin{aligned} \mathrm{Mod}_{(\mu,\eta),j} &= e^{(i\omega_\mu + \frac{1}{T_\eta})(t_j - T_0)}, \quad \mathrm{Demod}_{(\mu,\eta),j} = \mathrm{Mod}^*_{(\mu,\eta),j} \\ \mathrm{MFI}_{(\mu,\eta),q} &= c_{\mu,q}^{(\omega)}\, c_{\eta,q}^{(T_2)}. \end{aligned} \tag{5.23}$$

Jointly these methods permit the numerically efficient procedural approximation of the matrix-vector multiplications involving $\mathbf{T}$, $\mathbf{T}^H$. Multiplication with $\mathbf{W}$ and $\mathbf{W}^H$ was performed straightforwardly, which is fast because these matrices are diagonal.

5.3.3 Simulations

The proposed pulse design strategy was explored in numerical simulations. The k-space trajectory for all pulse designs was a 5 ms 3-turn constant-density outside-in spiral with $k_{max} = \frac{16\pi}{\mathrm{FOX}}$ and undersampling by a factor of $R \approx 2.7$ (Fig. 5.2). The maximum gradient strength applied during the trajectory was below $10\,{}^{\mathrm{mT}}/_{\mathrm{m}}$ and the maximum gradient slew rate used was $85\,{}^{\mathrm{mT}}/_{\mathrm{ms\,m}}$. The FOX had a size of 0.2 m and a 64×64 Cartesian grid was used for spatial discretization, corresponding to 4-fold oversampling with respect to the Fourier encoding. The desired magnetization pattern was a flat square at the center of the FOX with a flip angle of 0.2 rad. The sampling interval of the temporal discretization was 6.4 μs. Unless stated otherwise 50 iterations were performed in the Lanczos algorithm.

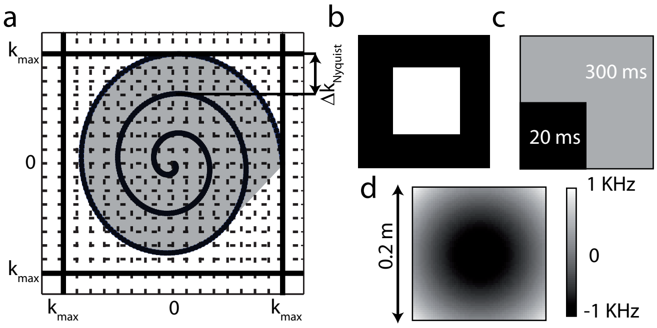

Figure 5.2: a) k-space trajectory used for numerical experiments. The extent of the trajectory in k-space was chosen according to a resolution of $FOX/16$. b) Desired excitation pattern (m_{des}). c) T_2^* map and d) off-resonance distribution.

The modeled transmitter was an 8-channel stripline array dimensioned for the human head and loaded by a homogeneous sphere with a diameter of 20 cm, dielectric properties similar to those of brain tissue ($\varepsilon_r = 52, \mu_r = 1, \sigma = 0.55\,{}^{\mathrm{S}}/_{\mathrm{m}}$), and mass density of $\rho = 960\,{}^{\mathrm{Kg}}/_{\mathrm{m}^3}$ (Fig. 5.3). The weighting matrix $\mathbf{W}$ was diagonal with unit diagonal entries for positions inside the sphere and zeros otherwise. The array's RF fields at the Larmor frequency were calculated with the Finite Integration Technique (FIT) detailed in Ref. [37], driving one port at a time while terminating all others with matched loads. The relevant right-hand circularly polarized RF magnetic field (B_1^+) inside the object was then calculated for each transmitter element according to

$$B_1^c = \frac{1}{2}\left((\vec{B}_1^c)_x + i(\vec{B}_1^c)_y\right). \tag{5.24}$$

To demonstrate the ability to control both global and local power deposition, SAR constraints were set for three different compartments of the phantom. Ω_1 encompassed the entire sphere, giving rise to a total SAR constraint. Ω_2 was a $(40 \times 40 \times 40)\,\mathrm{mm}^3$ cube close to the first array element. The SAR induced in this volume is expected to depend mainly on the power supplied to channel 1. Ω_3 was a $(60 \times 50 \times 40)\,\mathrm{mm}^3$ cuboid close to elements 5 and 6 (Fig. 5.3b). The power matrices $\mathbf{\Psi}^p$ of these three compartments are plotted in Fig. 5.3. The actual excitation profiles of resulting pulse waveforms were calculated by forward integration of the Bloch equations, performing recursive hard-pulse rotations with a dwell time of $6.4\,\mu$s. All calculations were carried out using Matlab® (The Mathworks, Natick, Massachusetts) on a standard PC (Pentium4, 3GHz, 2GB RAM).

5.4 Numerical experiments and results

5.4.1 Convergence of the Lanczos algorithm

A first validation experiment served to study the role of the number k of Lanczos iterations, which is equal to the number of dimensions of the reduced search space for pulse optimization. The Lanczos algorithm was carried out for the pulse design task described in the previous section, performing a total of 500 iterations. After each iteration the current Lanczos basis was used to perform a constrained pulse design with the total SAR limited to a maximum of 1 W/Kg. For comparison, a second pulse was constructed using the same basis but without the SAR constraint, i.e., by direct inversion of $\mathbf{\Delta}_k$. For both pulses the resulting deviation from the target profile was determined within the linear model, where it is given by $\sqrt{\phi(\mathbf{v})}$, as well as based on the actual pulse profile obtained by Bloch integration. In addition the conditioning of the reduced design problem was monitored by determining the maximum and minimum eigenvalues of $\mathbf{\Delta}_k$ and calculating the condition number according to

$$\mathrm{cond}(\mathbf{\Delta}_k) = \frac{\lambda_{\max}}{\lambda_{\min}}. \tag{5.25}$$

The results of this study are shown in Fig. 5.4. The first plot illustrates that the largest eigenvalue is found early while gradually smaller eigenvalues occur during the iteration and cause the conditioning to deteriorate. The profile quality improves rapidly during early iterations and converges quickly as indicated by the error measures in the second plot. The unconstrained pulses reach somewhat higher profile fidelity than their constrained counterparts. However, this improvement comes at the expense of gradually increasing and eventually very high SAR, which reflects deteriorating conditioning. Interestingly, the corresponding increase in power of the unconstrained pulses also causes the actual profile error to diverge while the error measure $\phi(\mathbf{v})$ of the linear picture converges as expected. This is due to increasing violation of the small-flip-angle approximation as ever

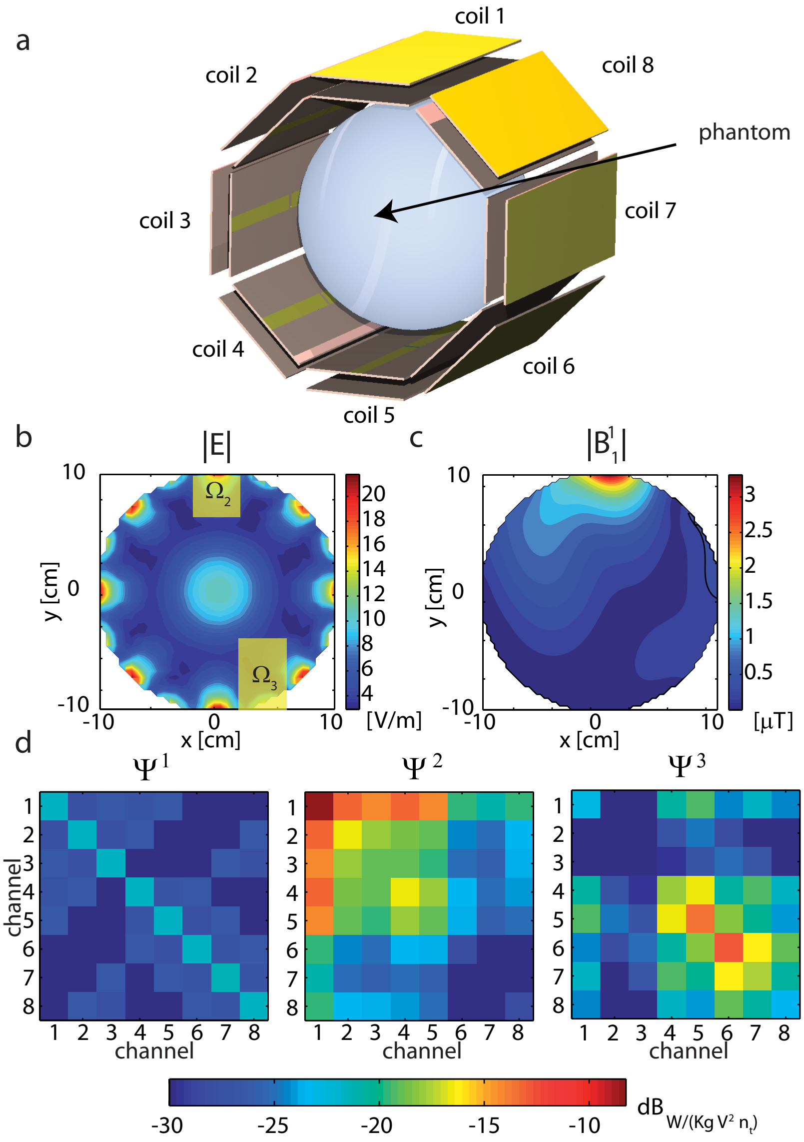

Figure 5.3: Setup and RF fields: a) Simulated 8-channel transmitter array and phantom. b) Electric RF field (magnitude) generated in the center of the phantom by quadrature operation. c) B_1^+ (magnitude) obtained by driving only port 1. Both field plots are scaled to 1 W forward power per channel. d) Resulting SAR matrices ($\mathbf{\Psi}^1$, $\mathbf{\Psi}^2$, $\mathbf{\Psi}^3$) for the entire sphere and the two sub-regions marked in b).

larger nutations occur during the pulses. As intended, the SAR of the constrained pulses remains within the prescribed limit and constant once the limit is reached. Correspondingly, the actual profile error converges and the SAR limit and the eventual profile quality are reached fast, indicating that relatively few iterations are sufficient. For the typical case studied here, both measures of profile error remain practically constant after about 20 iterations. On this basis the number of iterations was fixed at $k = 50$ for the rest of this work.

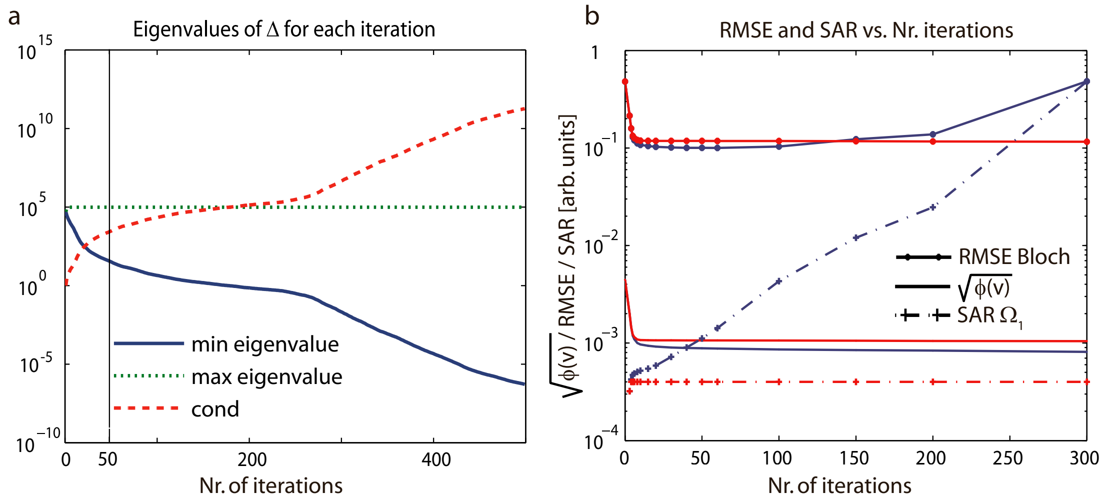

Figure 5.4: a) Eigenvalues and condition number of the tridiagonal matrix $\mathbf{\Delta}_k$ calculated by Lanczos iteration. b) After each iteration pulses were constructed with constraints (red) and without constraints (blue). The graphs show the resulting remaining error in Eq. 5.15 ($\sqrt{\phi}$), the root-mean-square error (RMSE) of the pulse profile according to Bloch simulation (RMSE Bloch) and the implied total SAR. Note the use of arbitrary units for better visualization.

A second set of test examples served to confirm the ability to account for local resonance offsets and T_2^* decay in the proposed design procedure. Simple, schematic B_0 and T_2^* distributions were used for the demonstration purpose (Fig. 5.2). Bloch integration was first used to study how the profile of an unconstrained pulse is affected by these B_0 and T_2^* distributions when ignoring them at the design stage. Then the pulse design was repeated with either or both of the error mechanisms incorporated and Bloch integration was again used to determine the resulting pulse profiles. In the design of the corrected pulses the SAR in all three compartments $\Omega_1, \Omega_2, \Omega_3$ was constrained to the levels previously obtained without the corrections. The resulting pulse profiles are shown in Fig. 5.5. They illustrate that fast T_2^* decay results in a lack of transverse magnetization at the end of the pulse and slight loss of edge definition, both of which were largely compensated for by the T_2^*-corrected design (Fig. 5.5b). Substantial profile distortion due to B_0 inhomogeneity was successfully corrected by including MFI in the design algorithm (Fig. 5.5c). The minor reduction in overall flip angle in this example likely reflects a trade-off between profile shape and amplitude, which was indirectly imposed by the SAR constraint. Finally, the simultaneous correction of both error mechanisms was equally effective (Fig. 5.5d).

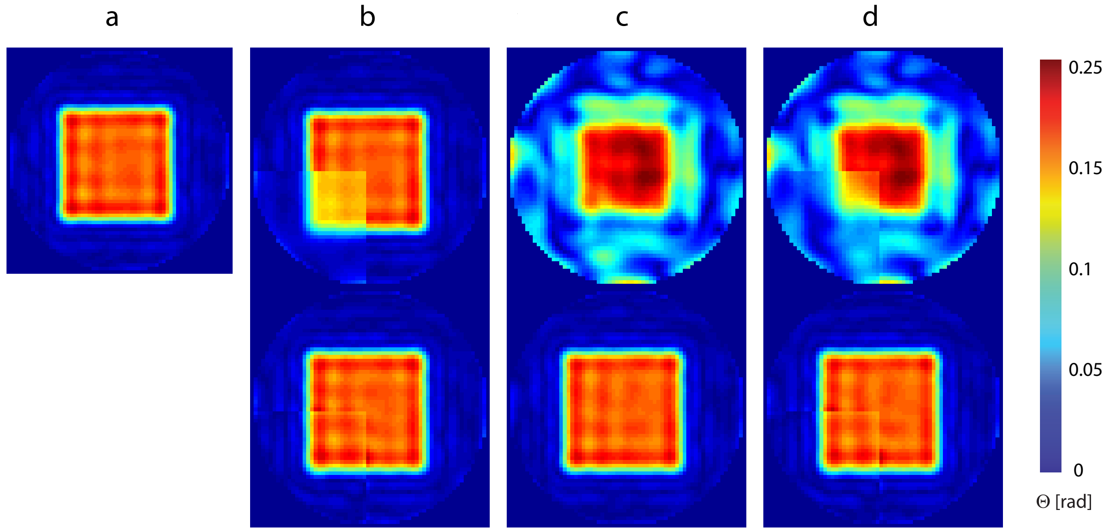

Figure 5.5: a) Excitation profile produced by a pulse obtained after 50 Lanczos iterations. The profile was then perturbed by the effects of T_2^*(b), off-resonance (c) or both (d) as specified in Fig. 5.2. Incorporating these effects in the pulse design resulted in the corrected profiles shown in the bottom row.

5.4.2 Control of SAR and amplifier power

The main advantage of the presented optimization strategy is the ability to exert direct control over the SAR in multiple compartments and safely stay within amplifier limits without having to choose any regularization parameters. These benefits are demonstrated in the following example, assuming the SAR limits of $\widehat{SAR}_1 = 1\,\mathrm{W}/\mathrm{Kg}$, $\widehat{SAR}_2 = 1\,\mathrm{W}/\mathrm{Kg}$ and $\widehat{SAR}_3 = 0.5\,\mathrm{W}/\mathrm{Kg}$ as well as limits of $\widehat{P}^{\mathrm{ave}} = 45\,\mathrm{W}$ and $\widehat{P}^{\mathrm{peak}} = 900\,\mathrm{W}$ for the average and peak forward power per channel. Unconstrained pulse design using 50 iterations resulted in the amplitude modulation waveforms given in Fig. 5.6a, which exceed the given limits in various ways. The dashed red line in this plot indicates the point in time when any of the SAR limits is first violated. The yellow bars highlight those parts of the individual waveforms that exceed the limit on average forward power per channel. Vertical red bars mark those parts of the waveforms that exceed the peak power limit. By contrast, incorporating the various limits as constraints in the SDP approach yielded an actually viable set of waveforms, namely that with minimal profile error within the Lanczos basis (Fig. 5.6b). Figure 5.6c-f shows the magnitude and phase of the corresponding transverse magnetization profiles, indicating that the necessary power reduction comes at a relatively minor expense in profile quality in this case. The main difference between the constrained and unconstrained pulses is a small drawback in profile sharpness of the former, reflecting that most power savings were realized early in the waveforms, i.e. in the k-space periphery.

The bar graph in Fig. 5.6.g details the power consumption of the two pulses in terms of their channel-wise average and peak powers as well as their SAR values. Each bar is scaled relative to the corresponding power limit. As indicated by arrows the constrained pulse actually reaches the limits only for a few criteria, namely the average forward power in channels 3 and 8 as well as the SAR in Ω_3. Exhausting all limits simultaneously apparently could not have improved the resulting excitation profile, reflecting the fact that the power criteria are not entirely independent.

The computation time required by the proposed method consists of two main contributions. The first part, i.e., the Lanczos iteration, is dominated by gridding and FFT operations whose computational cost varies greatly with the pulse duration, the temporal and spatial discretization, and the extent of the MFI. For the shown examples the Lanczos decomposition with 50 iterations took about 2 s for uncorrected pulses and up to 10 s when incorporating the B_0 and T_2^* maps. The time required for the second step, i.e., solving the resulting SDP, depends mainly on the number of constraints applied. With all SAR and average power constraints included it took less than 1 s to cast the problem to the solver plus about 0.5 s of actual solver time. Constraining the peak power is more demanding as it requires separate constraints for each time point. Doing so increased the time for casting the problem to the solver to roughly 2 min along with about 30 s of solver time. These values can certainly be reduced with enhanced CPU power and more refined implementation. For instance, the process of casting the SDP to the solver still contains a number of generic validation and transformation steps that could readily be eliminated.

5.5 Discussion and Conclusion

The results presented in the previous section confirm the feasibility and effectiveness of the proposed SDP approach to constrained multiple-channel RF pulse design. Its foremost strength is the combination of optimality and guaranteed feasibility of resulting pulses without requiring a costly search for suitable regularization parameters. The SDP method readily accommodates an arbitrary number of constraints, which enables simultaneous control over various power criteria, including the local SAR in sub-volumes of the sample. It has also been shown to be

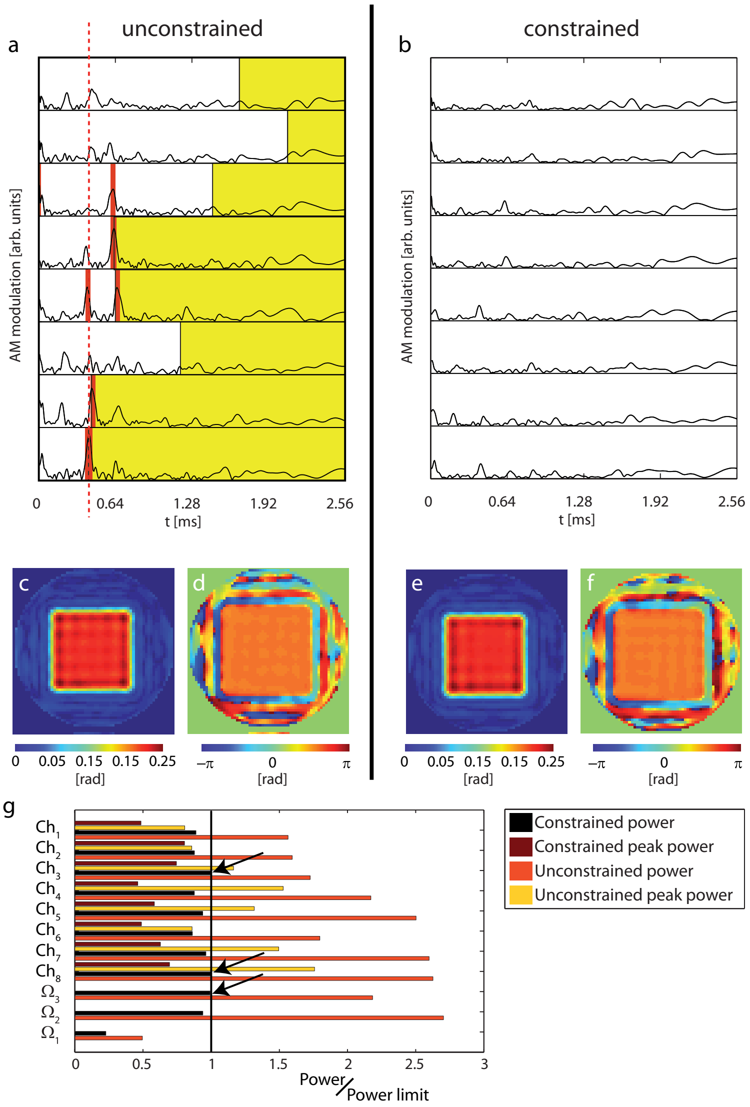

Figure 5.6: Constrained versus unconstrained pulse design. a, b) Resulting RF amplitude modulations for the eight channels. The red dashed line indicates the moment in time when the unconstrained pulse first violates any of the SAR limits. The yellow bars show those parts of the pulse that are in excess of the per-channel average power limit, while red bars indicate excessive peak power. The constrained pulse (b) does not exceed any of the limits. c-f) Magnitude and phase of the excitation profiles obtained with these pulses. g) Power demand and SAR deposition of the two pulses relative to the limits set. The constrained pulse is within all of the limits, exhausting three of them (arrows).

compatible with enhanced models of the magnetization dynamics. In particular, local off-resonance and T_2^* decay have successfully been compensated for, which may prove useful especially at high static magnetic field.

The proposed two-step strategy consisting of initial dimension reduction and then solving a relatively small SDP renders constrained pulse optimization numerically viable. In principle, it can be applied to every constrained convex pulse optimization with a quadratic target functional. For example, alternatively to the present implementation a SAR criterion could form the optimization target and strict limits on profile errors could be set as constraints. In such an approach the profile error could be measured with alternative norms such as the ℓ_1 or maximum norms, leading to problems that can still be solved efficiently with SOCP algorithms as shown in Ref. [16]. As demonstrated in this work, the proposed strategy is readily applicable for strongly overdetermined pulse design tasks and is thus expected to work well for sparse 3D k-space trajectories [38]. It has already proven useful for optimizing the spectral-spatial response of RF pulses, which can be used to enhance their bandwidth as shown in Ref. [39]. Constrained pulse optimization as described here could also be used to replace regularized inversion in magnitude-least-squares pulse design [40].

Within the scope of the presented performance tests the proposed combination of algorithms has proven numerically robust and efficient, optimizing, e.g., a typical 2D selective pulse in a few seconds unless peak power needs to be constrained. At this speed it will be suitable for ad-hoc pulse calculations during scanning sessions. Notwithstanding, it is an open question how many different SAR compartments need to be considered for ensuring the safety of a given in-vivo application. While this number could be substantial it would not necessarily result in a massive increase in computation time because some constraints will always be implied by other, effectively harder ones, focusing the bulk of the SDP computation on a limited number of critical constraints. Clearly, it remains a general and major challenge to suitably measure, model, or estimate the RF magnetic and electric fields of the transmitter elements as well as the material properties that enter the pulse optimization. At least the power matrix corresponding to the global SAR can be estimated quite reliably based on properties of the RF chain and the coil array (see 5.7.4).

Finally, it is noteworthy that the prerequisite of small flip angles can be relaxed under certain conditions that ensure linear pulse superposition also at large flip angles [2]. Based on this principle, which implies certain restrictions on k-space trajectories, constrained pulse design can equally be extended to large angles [41].

5.6 Spectral-Spatial Pulse Design for multiple-channel RF Transmission

5.6.1 Theory and Methods

A major remaining problem is the small bandwidth of such localized pulses. Small off-resonances - either induced by B_0 inhomogeneities or spectroscopic frequency shift - deteriorate the produced magnetization profile. Especially on ultra-high field systems ($> 4\,\mathrm{T}$) the off-resonances are increased as well as the frequency offset induced by chemical shifts and weak couplings. It is therefore important to have explicit control of the bandwidth of multiple-channel transmission pulses in either application, imaging and spectroscopy.

Strictly speaking, the reason for the frequency offset found in traditional imaging and spectroscopy do not have the same cause. In imaging, the off-resonance is mainly attributed to local differences of the main magnetic field within the sample stemming most prominently from the non-uniform distribution of susceptible materials in the sample but also to a minor extent from non-uniformities of the main magnet. On the contrary, the volume of a localized spectroscopic experiment has to be well shimmed to much higher degree (in the range of a few Hz) and therefore the frequency offset can be in a first order approximation attributed to slight variations $\Delta\gamma$ of the gyromagnetic ratio due to chemical shift or couplings among the spins. Considering the effect of variation in γ and B_0 on the phase term of the produced magnetization in Eq. 5.1, we see:

$$\begin{aligned}\varphi(\gamma + \Delta\gamma, B_0 + \Delta B_0, t) = \left(\vec{k}(t) + \frac{\Delta\gamma}{\gamma}\vec{k}(t)\right) \cdot \vec{r} + \quad (5.26)\\ \left(\gamma B_0 + \Delta\gamma B_0 + \Delta\gamma\Delta B_0\right)(t - T_0)\,. \quad (5.27)\end{aligned}$$

Since the fraction of chemical shift ($\frac{\Delta\gamma}{\gamma}$) induced changes in the gyromagnetic ratios is in the ppm range for the most in-vivo relevant compounds and nuclei, the effective k-space trajectory is almost equal among the different isochromats. The rest of the phase terms act in an equivalent manner as a simple B_0 off-resonance. Therefore, designing broadband multidimensional pulses for spectroscopy and imaging attributes to the same rules. However, it has to be mentioned, that this consideration stays only true, as long as the nutation behavior of the spin coupling does not become relevant.

Spectral-spatial pulse design has been introduced to MRI by Meyer et al. [42]. It was shown that the design rules for low flip angle pulses can be expanded to the spectral dimension by adding a virtual gradient, along which the desired spectral response can be defined analogously to the spatial case.

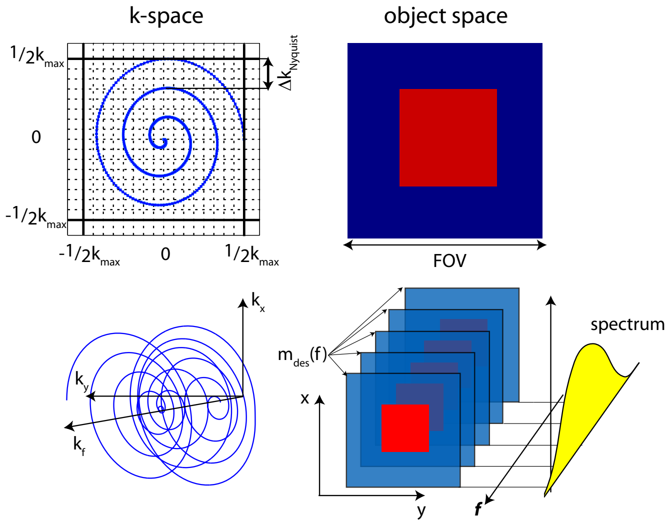

Figure 5.7: Graphical example of 2D spatial pulse design (upper half) that is expanded to a spectral-spatial design (lower half).

The virtual gradient strength G_f was chosen according to the FOV given and the bandwidth (BW) of the desired magnetization profile $m_{des}(\vec{r}, f)$:

$$BW = \max(f) - \min(f) \tag{5.28}$$

$$G_f = \frac{BW}{\gamma \cdot FOV} \tag{5.29}$$

$$k_f(t) = \gamma G_f(t - \frac{T_0}{2}). \tag{5.30}$$

The frequency component of the k-space trajectory was centered around the origin of the k-space in order to allow for a self refocused spectral response. In this work, the algorithm presented above was expanded to solve the spectral-spatial problem by adding the spectral dimension to the gridding engine. This way, the fast gridding Fourier transform can be employed, which allows for solving large scale problems numerically efficiently. Since the inverse problem to be solved is heavily overdetermined, the regularization of the inversion has crucial importance to keep the resulting pulses executable on the system. Under these circumstances, the calculated solution depends strongly on the chosen regularization which renders the adjustment of the regularization parameters for optimal performance a hard task. Constraining the power and SAR consumption of the pulses inherently yields well behaved solutions and is therefore considered to be an effective approach to solve the inverse problems posed by such a overdetermined spectral-spatial pulse design approach. In [43], the spectral response was incorporated in the forward model by allotting several different off-resonance terms (B_0 in Eq. 5.1) to each voxel. This approach exhibits of course great flexibility in choosing spectral sampling points, but for large spectral-spatial resolutions it becomes numerically very expensive to treat the problem in such an explicit manner preventing numerically efficient fast Fourier approaches from being applied also in the spectral dimension.

In order to reach the needed bandwidth of most spectroscopical applications of around 1 kHz, parallel transmission can be of great help. The mere shorting of the spatial encoding renders an increase in bandwidth. Beyond that, the pulse is expected to offer further optimization potential by the additional degrees of freedom offered by parallel transmission, especially when the acceleration as such is not pushed to the limits of the spatial RF encoding as such. Further increase in spectral selectivity can be achieved, by investing the time gained by acceleration in spectral encoding. By repeatedly sampling the spatial k-subspace, a more dense sampling of the spectral dimension can be achieved. This is especially desired, since the parallel transmission does not provide any encoding in the spectral dimension per se.

5.6.2 Experiments and Results

Two examples have been calculated and simulated using the same setup and system parameters as above. Both pulses were targeted to have constant spectral response and to spatially localize the excitation in a square as shown before. The pulses were calculated using the same power and SAR limitations as the pulses, that were calculated without taking the spectral response into consideration for comparison. In the first example, the spatial part of the k-space was 2 fold undersampled by a 2.6 ms constant density outside-in spiral and a bandwidth of 500 Hz was targeted. In a second experiment, a 3 fold accelerated spiral was used to target a bandwidth of 1 kHz which would allow to encompass water/fat frequency separation as well as the spread of most metabolites of interest in MR spectroscopy at 7 T. This pulse is compared to a pulse designed without regards to the spectral response. A third pulse was then constructed on a trajectory that is rehearsing the gradient waveform of the spiral three times, from which the second repetition had a reversed gradient waveform. By this, the pulse has the same duration as non accelerated spatially selective pulse, but it exploits the freedom given by the spatial diversity of the array channels to optimize the spectral response. The results of these experiments can be seen in Fig. 5.8. It can be seen, that under the given circumstances, the bandwidth of moderately accelerated pulses can be more than doubled with only moderately sacrificed spatial performance. However, the needed 1 kHz bandwidth can be achieved by employing an actual spectral-spatial k-space sampling pattern. However, time penalties due to spectral encoding can be compensated by the acceleration of the spatial encoding by parallel transmission.

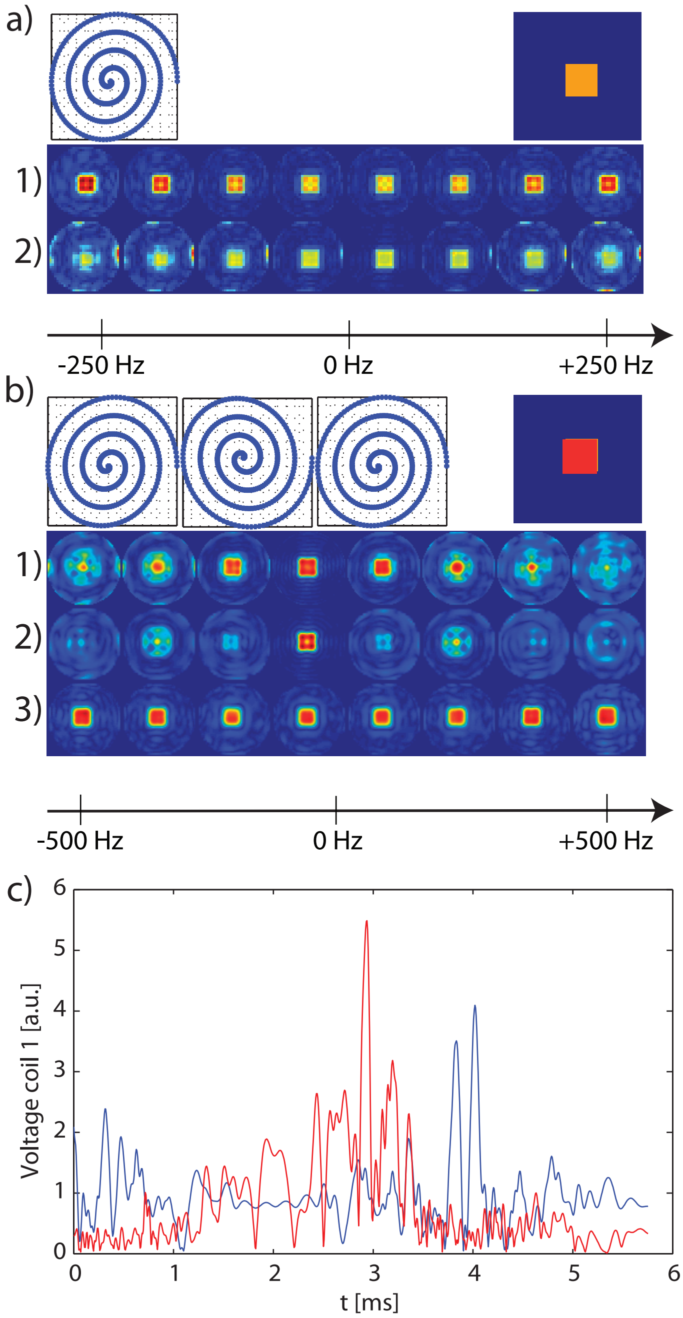

Figure 5.8: Examples of spectral-spatial pulses. a) shows the results the 2 fold accelerated pulses targeting a bandwidth of 500 Hz (1) and without spectral considerations (2). Both pulses were constrained to the same amount of total power. b) shows the results for a 3 fold undersampling over a total bandwidth of 1 kHz. 1) shows the performance of a spectral-spatially designed pulse on one single spiral. 2) was a spatial only design on the same trajectory whereas 3) results from a spectral-spatial pulse designed on 3 repetitions of the same spiral as above. Plot c) shows the voltages feed to coil 1 for generating the magnetization profiles plotted in b) where the blue line corresponds to 2) and the red to 3).

5.7 Appendix

5.7.1 Discretization of SFA

The input to the RF-amplifier and the gradient system is given for a dwell time of Δt. The played RF waveform can be considered as constant within this time, since its bandwidth is mainly given by the quality factor Q of the coils, which corresponds to several MHz. Therefore, $v(t)$ can be written as composition of the dwells $D_i(t)$.

$$\begin{aligned} D_j(t) &= \begin{cases} 1, & j \cdot \Delta t \leq t < (j+1) \cdot \Delta t \\ 0, & \text{else} \end{cases} \\ v(t) &= \sum_j v_j D_i(t). \end{aligned} \tag{5.31}$$

This is a difference to the receive case, where the output bandwidth of the spectrometer is adapted to the scan. If this choice was made appropriately, the data can be represented as points in the k-space. However, technically the dwell time during transmission is on most system fixed and in most cases significantly longer than in reception compared to the needed bandwidth. In many cases this difference may be considered as factoide but e.g. using cartesian trajectories this can get some relevance and producing a visible amount of aliasing.

In general, the gradient waveforms $\vec{G}(t)$ should be approximated more smoothly than in the hard pulse approximation, since their bandwidth is much smaller (due to the high inductances involved in the gradient system). They should therefore be interpolated at least linearly in each interval $t_j \leq t < t_{j+1}$:

$$\begin{aligned} \vec{k}(t) &= -\gamma \int_t^{T_0} \vec{G}(\tau) d\tau = -\gamma \int_{t_{j+1}}^{T_0} \vec{G}(\tau) d\tau - \gamma \int_t^{t_{j+1}} \vec{G}(\tau) d\tau \\ &= \vec{\mathbf{k}}(\mathbf{t}_{j+1}) - \gamma \vec{G}_0(\mathbf{t}_j) t' - \gamma \vec{G}_1(\mathbf{t}_j) \frac{t'^2}{2}. \end{aligned} \tag{5.32}$$

Whereas $t' = \mathbf{t}_{j+1} - t$ and $\vec{G}_0$, $\vec{G}_1$ denote the constant and the linear coefficient of the gradient channel-wise linear time interpolation of the gradient waveform in the j^{th} dwell. Inserting this into Eq. 5.1 (neglecting off-resonance and T_2^* decay for simplicity) yields at the end of the pulse ($t = T_0$):

$$\begin{aligned} M_{xy}(\vec{r}) =& i\gamma \sum_{c,j} B_1^c(\vec{r}) \mathbf{v}_{(c,j)} \int_0^{T_0} D_i(t) e^{i\vec{k}(t)\cdot\vec{r}} dt \\ =& i\gamma \sum_{c,j} B_1^c(\vec{r}) \mathbf{v}_{(c,j)} \int_{t_j}^{t_j+\Delta t} e^{i\left(\vec{k}(\mathbf{t}_{j+1}) - \gamma t' \vec{G}_0(\mathbf{t}_j) - \gamma \frac{t'^2}{2} \vec{G}_1(\mathbf{t}_j)\right)\cdot\vec{r}} dt = *. \end{aligned}$$

Since the quadratic phase can not be expressed analytically, we make an average phase approximation assuming the quadratic term adds only a small constant phase to the integrand, but does not change its amplitude. The average phase within a time dwell is $-\frac{(\Delta t)^2}{6}\bar{\gamma}\vec{G}_1(\mathbf{t}_j)\cdot\vec{r}$ and therefore:

$$\begin{aligned}
* =& -i\gamma\sum_{c,j} B_1^c(\vec{r})\mathbf{v}_{(c,j)} e^{i\left(\vec{k}(\mathbf{t}_{j+1})-\frac{\gamma\Delta t^2}{6}\vec{G}_1(\mathbf{t}_j)\right)\cdot\vec{r}}\int_0^{\Delta t} e^{-i\gamma t\vec{G}_0(\mathbf{t}_j)\cdot\vec{r}}dt \\
=& i\gamma\sum_{c,j} B_1^c(\vec{\mathbf{r}}_q)\mathbf{v}_{(c,j)} e^{i\left(\vec{k}(\mathbf{t}_{j+1})-\frac{\gamma}{2}\vec{G}_0(\mathbf{t}_j)\Delta t-\frac{\gamma\Delta t^2}{6}\vec{G}_1(\mathbf{t}_j)\right)\cdot\vec{\mathbf{r}}_q} \\
&\cdot\frac{1}{i\gamma\vec{G}_0(\mathbf{t}_j)\cdot\vec{\mathbf{r}}_q}\left(e^{\frac{i\gamma}{2}\vec{G}_0(\mathbf{t}_j)\cdot\vec{\mathbf{r}}_q\Delta t}-e^{\frac{-i\gamma}{2}\vec{G}_0(\mathbf{t}_j)\cdot\vec{\mathbf{r}}_q\Delta t}\right) \qquad (5.33)\\
=& i\gamma\sum_{c,j} B_1^c(\vec{r}_q)\mathbf{v}_{(c,j)} e^{i\left(\frac{1}{2}(\vec{k}(\mathbf{t}_j)+\vec{k}(\mathbf{t}_{j+1}))+\frac{\gamma}{12}\vec{G}_1(\mathbf{t}_j)\Delta t^2\right)\cdot\vec{r}_q}\text{sinc}\left(\frac{\gamma}{2}\vec{G}_0(\mathbf{t}_j)\cdot\vec{\mathbf{r}}_q\Delta t\right). \qquad (5.34)
\end{aligned}$$

Equation 5.34 is the generalized forward model for transmission with smooth gradient waveforms and RF waveforms approximated by square pulses. The k-space trajectory is then calculated by $\vec{\mathbf{k}}_j^s := \frac{1}{2}\left(\vec{\mathbf{k}}(\mathbf{t}_{j+1})+\vec{\mathbf{k}}(\mathbf{t}_j)\right)+\frac{\gamma}{12}\vec{G}_1(\mathbf{t}_j)\Delta t^2$. The averaging between the k-space position of two consecutive dwell times occurs due to the definition of the time of the dwell at its beginning. The term $O(\Delta t^2)$ takes the change of the gradient field within the dwell into account. If we choose the dwell time Δt according to the gradient strength such that:

$$\max_{\mathbf{t}_j}\left(\frac{\gamma}{2}\vec{G}_0(\mathbf{t}_j)\cdot\vec{\mathbf{r}}_q\Delta t\right)\leq\max_{\mathbf{t}_j}\left(\|\frac{\gamma}{2}\vec{G}_0(\mathbf{t}_j)\|\right)\cdot r_{\max}\Delta t\ll\pi \qquad (5.35)$$

i.e. the sinc function can be approximated as constant 1 over the entire FOX. It should be mentioned that the dwell time of the system should be kept short enough to satisfy this condition, otherwise artifacts of the dwelling will appear inside the FOX. With this approximation, the transmit matrix $\mathbf{T}$ linking the voltage vector $\mathbf{v}$ to the magnetization vector $\mathbf{m}$ is found to be:

$$\begin{aligned}
\mathbf{T}_{q,(c,j)} :=& i\gamma B_1^c(\vec{\mathbf{r}}_q)\Delta t e^{i\vec{\mathbf{k}}_j^s\cdot\vec{r}} \\
\mathbf{m} =& \mathbf{T}\mathbf{v}.
\end{aligned} \qquad (5.36)$$

5.7.2 Lanczos algorithm

The implementation used in this work included the following steps (see [21] chapter 9.2.1.):

Initialization

```
  $\mathbf{w} = \tilde{T}^H(\mathbf{W}^H\mathbf{W}\mathbf{m}_{des})$
  $\mathbf{v}(1 : n_c \cdot n_t) = \mathbf{0};\ \beta_0 = \|\mathbf{w}\|_2;\ j = 0;\ \mathbf{w} = \mathbf{w}/\beta_0$
Iteration
  while $j < k$
    if $j \neq 0$
      $\mathbf{temp} = \mathbf{w};\ \mathbf{w} = \mathbf{v}/\beta_j;\ \mathbf{v} = -\beta_j\,\mathbf{temp}$
    end if
    $\mathbf{v} = \mathbf{v} + \tilde{T}^H(\mathbf{W}^H\mathbf{W}\tilde{T}(\mathbf{w}))$
    $j = j + 1;\ \alpha_j = \mathbf{w}^H\mathbf{v};\ \mathbf{v} = \mathbf{v} - \alpha_j\mathbf{w}$
    reorthogonalization
      for $l = 1 : (j - 1)$
        $\mathbf{v} = \mathbf{v} - \frac{\mathbf{v}^H\mathbf{Q}_k(1:n_c \cdot n_t,l)}{\mathbf{Q}_k(1:n_c \cdot n_t,l)^H\mathbf{Q}_k(1:n_c \cdot n_t,l)} \cdot \mathbf{Q}_k(1 : n_c \cdot n_t, l)$
      end for
    $\beta_j = \|\mathbf{v}\|_2; \mathbf{Q}_k(1 : n_c \cdot n_t, j) = \mathbf{w}$
  end while
```

As mentioned in Ref. [44], loss of orthogonality among the search directions often limits the performance of the Lanczos algorithm. Therefore, a reorthogonalization step was introduced that improves the algorithm's convergence and ensures the unitarity of the Lanczos vectors, which can be exploited in Eq. 5.20. Reorthogonalization also suppresses so-called ghosting of the eigenvalues in $\mathbf{\Delta}_k$, which would otherwise increase the apparent number of significant eigenvectors, slowing down the subsequent optimization.

The result of the algorithm is given by the column-wise unitary $((n_c \cdot n_t) \times k)$ matrix $\mathbf{Q}_k$ whose columns are the Lanczos vectors and by the $(k \times k)$ tridiagonal matrix $\mathbf{\Delta}_k$:

$$\mathbf{\Delta}_k = \begin{pmatrix} \alpha_1 & \beta_1 & 0 & \cdots & 0 \\ \beta_1 & \alpha_2 & \ddots & & \vdots \\ 0 & \ddots & \ddots & \ddots & 0 \\ \vdots & & \ddots & \ddots & \beta_{k-1} \\ 0 & \cdots & 0 & \beta_{k-1} & \alpha_k \end{pmatrix} \tag{5.37}$$

An advantage of Krylov space based methods such as Lanczos iteration is their inherent efficient choice of search directions. In contrast to singular value decomposition (SVD) methods an early-stopped Lanczos algorithm yields a basis that is tailored to the target vector (in our case $\mathbf{T}^H\mathbf{W}^H\mathbf{W}\mathbf{m}_{des}$). As Refs. [20, 31] show the k-th step of the Lanczos method solving $\mathbf{b} = \mathbf{A}\mathbf{x}$ aims to find the k-th order polynomial $\zeta(\mathbf{A}) \in \Pi_k$ such that the norm of the initial residual $\mathbf{r}_0 = \mathbf{b}$ (since $\mathbf{x}_0 = 0$) is minimized. The resulting regularization behavior can be studied by considering the diagonal form of $\mathbf{A} = \mathbf{U}\mathbf{\Lambda}\mathbf{U}^H$ with $\mathbf{\Lambda} = \mathrm{diag}(\ldots, \lambda_i, \ldots)$ containing its eigenvalues and the unitary matrix $\mathbf{U}$ containing its eigenvectors $\mathbf{u}_i$. The norm of the remainder $\mathbf{r}_k = \mathbf{b} - \mathbf{A}\mathbf{x}_k$ after the k-th step can then be analyzed as follows:

$$\begin{aligned}\|\mathbf{r}_k\| =& \|\mathbf{x} - \mathbf{x}_k\|_{\mathbf{A}} = \|\zeta_k(\mathbf{A})(\mathbf{x} - \mathbf{x}_0)\|_{\mathbf{A}} = \min_{\zeta \in \Pi_k} \|\zeta(\mathbf{A})(\mathbf{x} - \mathbf{x}_0)\|_{\mathbf{A}} \\ =& \min_{\zeta \in \Pi_k} \|\zeta(\mathbf{A})\mathbf{r}_0\|_{\mathbf{A}^{-1}} = \min_{\zeta \in \Pi_k} \{ \sum_{i=1}^{dim(\mathbf{A})} \frac{(\mathbf{r}_0 \cdot \mathbf{u}_i)^2}{\lambda_i} \zeta^2(\lambda_i) \}^{1/2}\end{aligned} \tag{5.38}$$

where it has been used that the positive-definite matrix $\mathbf{A}$ induces a norm denoted as $\| \; \|_{\mathbf{A}}$. This shows how the scalar product $(\mathbf{r}_0 \cdot \mathbf{u}_i)$ between the first residual and the eigenvectors determines, together with the eigenvalues, in which order the Lanczos vectors are chosen. In this fashion the resulting reduced basis is effectively tailored to the target vector $\mathbf{b} = \mathbf{r}_0$. For truncated SVD only the matrix $\mathbf{A}$ is considered and singular values are involved based on their magnitude but irrespective of how the corresponding singular vectors relate to the given residual. This approach may worsen the overall conditioning of the problem and could result in the need to construct relatively large reduced bases as has been reported in Ref. [45] for the case of multiple-channel RF pulse design.

5.7.3 Relation between regularized and constrained pulse design

The constrained optimization problem stated in Eq. 5.15 can also be solved using Lagrange multipliers $\lambda_p^{(1)}, \lambda_c^{(2)}$ and $\lambda_{(c,j)}^{(3)}$, one for each power and SAR term to be controlled:

$$\begin{aligned} L =& \|\mathbf{W}(\mathbf{T}\mathbf{v} - \mathbf{m}_{des})\|_2^2 \\ &+ \sum_p \lambda_p^{(1)} \mathbf{v}^H \mathbf{\Psi}^p \mathbf{v} + \sum_c \lambda_c^{(2)} \mathbf{v}^H \mathbf{\Phi}_c^{\mathrm{ave}} \mathbf{v} + \sum_{(c,j)} \lambda_{(c,j)}^{(3)} \mathbf{v}^H \mathbf{\Phi}_{(c,j)}^{\mathrm{inst}} \mathbf{v}^H \\ \Rightarrow \hat{\mathbf{v}} =& \left(\mathbf{T}^H \mathbf{W}^H \mathbf{W} \mathbf{T} + \sum_p \lambda_p^{(1)} \mathbf{\Psi}^p + \sum_c \lambda_c^{(2)} \mathbf{\Phi}_c^{\mathrm{ave}} + \sum_{c,j} \lambda_{(c,j)}^{(3)} \mathbf{\Phi}_{(c,j)}^{\mathrm{inst}} \right)^{-1} \\ & \mathbf{T}^H \mathbf{W}^H \mathbf{W} \mathbf{m}_{des} \end{aligned} \tag{5.39}$$

The Lagrange approach thus amounts to regularizing the straightforward inverse problem with a large number of regularization parameters given by the Lagrange multipliers. Each of the regularization parameters permits controlling the corresponding cost term as previously pointed out in Ref. [8]. The choice of the parameters is usually made and refined heuristically until the result is considered satisfactory. However, an optimal set of regularization parameters, leading to optimal exploitation of the given constraints, is very costly to calculate. Nevertheless, if the optimal solution $\mathbf{v}$ is known, matching values of the regularization parameters can be readily identified. Assembling them in the vector $\boldsymbol{\lambda}$, the minimum of the Lagrange function is characterized by:

$$\frac{\partial}{\partial \mathbf{v}^H} L = \mathbf{T}^H \mathbf{W}^H \mathbf{W} \mathbf{T} \mathbf{v} + \mathbf{P} \boldsymbol{\lambda} - \mathbf{T}^H \mathbf{W}^H \mathbf{m}_{des} = 0 \tag{5.40}$$

where the matrix $\mathbf{P}$ was defined as

$$\mathbf{P} := \left(\; \boldsymbol{\Psi}^1 \mathbf{v}, \; \cdots, \boldsymbol{\Psi}^p \mathbf{v}, \; \cdots, \boldsymbol{\Phi}_c \mathbf{v}, \; \cdots, \boldsymbol{\Phi}_{c,j} \mathbf{v}, \; \cdots, \boldsymbol{\Phi}_{n_c, n_t} \mathbf{v} \; \right) \tag{5.41}$$

Solving Eq. 5.40 for $\boldsymbol{\lambda}$ yields:

$$\Rightarrow \mathbf{P} \boldsymbol{\lambda} = \mathbf{T}^H \mathbf{W}^H \mathbf{m}_{des} - \mathbf{T}^H \mathbf{W}^H \mathbf{W} \mathbf{T} \mathbf{v} \tag{5.42}$$

$$\Rightarrow \boldsymbol{\lambda} = \mathbf{P}^+ \left(\mathbf{T}^H \mathbf{W}^H \mathbf{m}_{des} - \mathbf{T}^H \mathbf{W}^H \mathbf{W} \mathbf{T} \mathbf{v} \right) \tag{5.43}$$

where $^+$ denotes the Moore-Penrose pseudo-inverse. If $\mathbf{P}$ does not have full rank the set of regularization parameters is not unique, reflecting that the underlying cost terms are not independent. In this case the pseudo-inverse yields the matching $\boldsymbol{\lambda}$ that has the smallest ℓ_2-norm, assigning zero weight to combinations of constrainst that are not actually limiting. Therefore, solving for the optimal $\boldsymbol{\lambda}$ based on a known optimal $\mathbf{v}$ can serve to check sets of constraints for redundancy. In addition, optimal Lagrange multipliers, once calculated, could serve for subsequent optimization of large-angle pulses as proposed in [46]. Furthermore, as proposed in Ref. [17], they could be used to refine the choice of the reduced basis by tridiagonalization of the regularized $\mathbf{A}$, followed by also repeating the SDP. Such a recursive approach could serve to minimize the size of the eventual basis.

5.7.4 Experimental determination of SAR matrices

The power matrices used for the constraints can easily be found for the forward power ($\boldsymbol{\Phi}_c^{\text{inst}}$, $\boldsymbol{\Phi}_c^{\text{ave}}$) since the load impedance Z_c used in Eqs. 5.5 and 5.6 is usually known and can also readily be measured. Determining the total and especially the local SAR matrices ($\boldsymbol{\Psi}^p$) is more challenging since the imaging volume is not accessible for power measurements. Electromagnetic field simulations are hence the method of choice for safety and compliance testing of multiple-channel RF transmission [47, 48]. From simulation data the power matrices can be readily derived as done in this work. Alternatively, the total loss of the coil array, as calculated from the scattering matrix in Eq. 3.3, can be used as a safe upper bound for the total SAR. This upper bound is a good estimate of the total SAR when losses in the sample dominate those in the coil materials and due to radiation. Assuming that the mass density inside the body is homogeneous on a thermally relevant scale, the total SAR matrix is obtained using the total mass of the object m_{tot}:

$$\Rightarrow \tilde{\mathbf{\Psi}}^{total} = \frac{\Delta t}{2 Z_0 T_0 m_{\mathrm{tot}}} \left(\mathbb{1} - \mathbf{S}^H \mathbf{S} \right) \tag{5.44}$$

where Z_0 denotes the reference impedance of the S-parameter measurement, which needs to be accounted for because S-parameters refer to normalized power waves, whereas the signal fed to the array was described in voltage terms in this work. Power scattering as reflected by $\mathbf{S}^H\mathbf{S}$ results from imperfect matching of individual coil ports and from coupling between transmitters. Accounting for it will improve pulse designs that are limited by SAR constraints.

Bibliography

[1] Pauly J, Nishimura D, and Macovski A. A k-Space Analysis of Small-Tip-Angle Excitation. J Magn Reson 1989; 81:43–56.

[2] Pauly J, Nishimura D, and Macovski A. A Linear Class of Large-Tip-Angle Selective Excitation Pulses. J Magn Reson 1989; 82:571–587.

[3] Katscher U, Boernert P, Leussler C, and van den Brink JS. Transmit SENSE. Magn Reson Med 2003; 49(1):144–150.

[4] Zhu Y. Parallel excitation with an array of transmit coils. Magn Reson Med 2004; 51(4):775–784.

[5] Ullmann P, Junge S, Wick M, Seifert F, Ruhm W, and Hennig J. Experimental analysis of parallel excitation using dedicated coil setups and simultaneous RF transmission on multiple channels. Magn Reson Med 2005; 54(4):994–1001.

[6] Grissom W, Yip C-Y, Zhang Z, Stenger VA, Fessler JA, and Noll DC. Spatial domain method for the design of RF pulses in multicoil parallel excitation. Magn Reson Med 2006; 56(3):620–629.

[7] Katscher U, Roehrs J, and Boernert P. Basic considerations on the impact of the coil array on the performance of Transmit SENSE. Magn Reson Mater Phy 2005; 18:81–88.

[8] Yip C-Y, Fessler JA, and Noll DC. A Constrained Minimization Approach to Designing Multi-dimensional, Spatially Selective RF Pulses. In Proc Intl Soc Mag Reson Med; volume 11 2004. p. 188; Kyoto; 2004.

[9] Zhu Y. An Analysis of Reciprocity in Parallel MRI. In Proc Intl Soc Mag Reson Med; volume 15 2007. p. 1684; Berlin; 2007.

[10] International Commission on Non-Ionizing Radiation Protection, Guidelines for Limiting Exposure to Time-Varying Electric, Magnetic, and Electromagnetic Fields (up to 300 GHz). Health Physics 1998; 74(4):494–522.

[11] van den Berg CAT, van den Bergen B, Van de Kamer JB, Raaymakers BW, Kroeze H, Bartels LW, and Lagendijk JJW. Simultaneous B_1^+ homogenization and specific absorption rate hotspot suppression using a magnetic resonance phased array transmit coil. Magn Reson Med 2007; 57(3):577–586.

[12] Brunner DO and Pruessmann KP. Enforcing strict constraints in multiple-channel RF pulse optimization. In Proc Intl Soc Mag Reson Med 2007. p. 1690; Berlin; 2007.

[13] Katscher U, Boernert P, and van den Brink JS. Theoretical and numerical aspects of transmit SENSE. IEEE Trans Med Imag 2004; 23(4):520–525.

[14] Hansen PC. Analysis of Discrete ill-posed problems by means of the L-curve. SIAM Rev 1992; 34:561–580.

[15] Hanke M and Hansen PC. Regularization Methods for Large-Scale Problems. Surv Math Ind 1993; 3:253–315.

[16] Lobo MS, Vandenberghe L, Boyd S, and Lebret H. Applications of second-order cone programming. Linear Algebra Appl 1998; 284(1-3):193–228.

[17] Golub GH and von Matt U. Quadratically Constrained Least Squares and Quadratic Problems. Numer Math 1991; 59:561–580.

[18] Thoai NV. Duality Bound Method for the General Quadratic Programming Problem with Quadratic Constraints. J Opt Theor Appl 2000; 107(2):331–354.

[19] Vandenberghe L and Boyd S. Semidefinite Programming. SIAM Review 1996; 38(1):49–95.

[20] Hanke M. On Lanczos Based Methods for the Regularization of Discrete Ill-Posed Problems. BIT 2001; 41(5):1008–10018.

[21] Golub GH and Loan CFV. Matrix Computations. The Johns Hopkins University Press 1996; (Third Edition).

[22] Toh KC and al e. SDPT3 – A Matlab Software Package for Semidefinite Programming.

[23] Loefberg J. YALMIP: A Toolbox for Modeling and Optimization in MATLAB. In Proceedings of the CACSD Conference 2004; Taipei; 2004.

[24] Kannengiesser SAR, Brenner AR, and Noll TG. Memory and time efficient deconvolution of B_0 field inhomogeneity effects. In ESMRMB; volume 8 1999. p. 67–68; Seville; 1999.

[25] Pruessmann KP, Weiger M, Boernert P, and Boesiger P. Advances in sensitivity encoding with arbitrary k-space trajectories. Magn Reson Med 2001; 46(4):638–651.

[26] Sutton BP, Noll DC, and Fessler JA. Fast, iterative, field-corrected image reconstruction for MRI. IEEE Tr Med Im 2003; 22(2):178–188.

[27] Sánchez-González J, Tsao J, Dydak U, Desco M, Boesiger P, and Pruessmann KP. Minimum-norm reconstruction for sensitivity-encoded magnetic resonance spectroscopic imaging. Magnetic Resonance in Medicine 2006; 55(2):287–295.

[28] Qu P, Luo J, Zhang B, Wang J, and Shen GX. An improved iterative SENSE reconstruction method. Conc Magn Reson B 2007; 31B(1):44–50.

[29] Yip C-Y, Fessler JA, and Noll DC. Iterative RF Pulse Design for Multidimensional, Small-Tip-Angle Selective Excitation. Magn Reson Med 2005; 54(4):908–917.

[30] Graesslin I, Katscher U, Schweser F, Niemann M, and Boernert P. Iterative solution of Transmit SENSE using a conjugate gradient method. Proc Intl Soc Mag Reson Med 2006; 14.

[31] Strakos Z and Tichy P. On Error Estimation in the Conjugate Gradient Method and why it Works in Finite Precision Computations. Elec Trans on Numer Anal 2002; 13:56–80.

[32] Jackson JI, Meyer CH, Nishimura DG, and Macovski A. Selection of a Convolution Function for Fourier Inversion Using Gridding. IEEE Trans Med Imag 1991; 10(3):473–478.

[33] Beatty PJ, Nishimura DG, and Pauly JM. Rapid gridding reconstruction with a minimal oversampling ratio. IEEE Trans Med Imag 2005; 24(6):799–808.

[34] Man L-C, Pauly JM, and Macovski A. Multifrequency Interpolation for Fast Off-resonance Correction. Magn Reson Med 1997; 37:758–792.

[35] Barmet C, Tsao J, and Pruessmann KP. Sensitivity encoding and B_0 inhomogeneity - A simultaneous reconstruction approach. In Proc Intl Soc Mag Reson Med 2005; Kyoto; 2005.

[36] Mentrup D and Eggers H. Signal Decay Correction in 2D Ultra-Short Echo Time Imaging. Magn Reson Mater Phy 2006; 19(2):62–70.

[37] Froehlich J, Baumann D, Brunner DO, Pruessmann KP, and Vahldieck R. Computational Analysis and Validation of Coil Arrays for Whole-Brain MR-Imaging at 7 T. In Intl Microwave Symposium Digest 2007. p. 2217–2220; Honolulu, Hawaii, USA; 2007. IEEE-MTT-S.

[38] Saekho S, Yip C-y, Noll DC, Boada FE, and Stenger VA. Fast k_z three-dimensional tailored radiofrequency pulse for reduced B_1 inhomogeneity. Magn Reson Med 2006; 55(4):719–724.

[39] Brunner DO and Pruessmann KP. Increasing bandwidth of spatially selective transmit SENSE pulses using constrained optimization. In Proc Intl Soc Mag Reson Med 2008. p. 635; Toronto; 2008.

[40] Setsompop K, Wald LL, Alagappan V, Gagoski BA, and Adalsteinsson E. Magnitude least squares optimization for parallel radio frequency excitation design demonstrated at 7 Tesla with eight channels. Magn Reson Med 2008; 59(4):908–915.

[41] Xu D, King KF, Zhu Y, McKinnon GC, and Liang Z-P. A noniterative method to design large-tip-angle multidimensional spatially-selective radio frequency pulses for parallel transmission. Magn Reson Med 2007; 58(2):326–334.

[42] Meyer CH, Pauly JM, Macovskiand A, and Nishimura DG. Simultaneous spatial and spectral selective excitation. MagnReson Med 1990; 15(2):287–304.

[43] Setsompop K, Alagappan V, Gagoski BA, Potthast A, Hebrank F, Fontius U, Schmitt F, Wald LL, and Adalsteinsson E. Broadband slab selection with B_1^+ mitigation at 7T via parallel spectral-spatial excitation. Magn Reson Med 2009; 61(2):493–500.

[44] Greenbaum A and Strakos Z. Predicting the Behavior of Finite Precision Lanczos and Conjugate Gradient Computations. SIAM J Matrix Anal Appl 1992; 13(1):121–137.

[45] Zelinski AC, Wald LL, Setsompop K, Alagappan V, Gagoski BA, Goyal VK, Hebrank F, Fontius U, Schmitt F, and Adalsteinsson E. Comparison of three algorithms for solving linearized systems of parallel excitation RF waveform design equations: Experiments on an eight-channel system at 3 Tesla. Conc Magn Reson B 2007; 31B(3):176–190.

[46] Xu D, King KF, Zhu Y, McKinnon GC, and Liang Z-P. Designing multichannel, multidimensional, arbitrary flip angle RF pulses using an optimal control approach. Magn Reson Med 2008; 59(3):547–560.

[47] Mao W, Wang Z, Smith MB, and Collins CM. An improved iterative SENSE reconstruction method. Conc Magn Reson B 2007; 31:127–131.

[48] Ibrahim TS and Tang L. Insight Into RF Power Requirements and B_1 Field Homogeneity for Human MRI Via Rigorous FDTD Approach. J Magn Reson Imag 2007; 25:1235–1247.

Chapter 6

Travelling Wave Nuclear Magnetic Resonance

partially published in:

D.O. Brunner, N. DeZanche, J. Paska, J. Frï¿œhlich and K.P. Pruessmann. *"Travelling Wave MR on a Whole-Body System"*. Proc Intl Soc Magn Reson Med 2008, Toronto. p. 434

D.O. Brunner, N. DeZanche, J. Paska, J. Frï¿œhlich and K.P. Pruessmann. *"Travelling-Wave MR: Comparison with a Volume Resonator at 7T"*. Proc ESMRMB 2008, Valencia. p. 91

D.O. Brunner, J. Paska, J. Frï¿œhlich and K.P. Pruessmann. *"Travelling-Wave MRI: Initial Results of In-Vivo Head Imaging at 7T"*. Proc Intl Soc Magn Reson Med 2009, Honolulu. p. 500

D.O. Brunner and K.P. Pruessmann. *"Reciprocity Relations in Travelling Wave MRI"*. Proc Intl Soc Magn Reson Med 2009, Honolulu. p. 2943

D.O. Brunner and K.P. Pruessmann. *"Phase Delay Effects in Travelling-Wave MRI"*. Proc ESMRMB 2009, Antalya. p. 347

D.O. Brunner, N. DeZanche, J. Frï¿œhlich, J. Paska and K.P. Pruessmann. *"Travelling Wave Nuclear Magnetic Resonance"*. Nature 2009; 475(7232): p. 994-998

D.O. Brunner, J. Paska, J. Frï¿œhlich and K.P. Pruessmann. *"Travelling Wave Parallel Imaging"*. Proc Intl Soc Magn Reson Med 2010, Stockholm. p. 646

J. Paska, D.O. Brunner, J. Frï¿œhlich and K.P. Pruessmann. *"A Travelling Wave Setup for Parallel Transmission"*. Proc Intl Soc Magn Reson Med 2010, Stockholm. p. 3795

6.1 Basic Conception and Demonstration

Uniform spatial coverage in NMR and MRI is traditionally achieved by tailoring the reactive near field of resonant Faraday probes [1, 2, 3, 4]. This approach is valid when the RF wavelength at the Larmor frequency is substantially larger than the target volume, which does not hold for modern, wide-bore, high-field systems. At the currently highest field strength that is used for human studies, 9.4 tesla [5, 6], the resonance frequency of hydrogen nuclei reaches 400 MHz, corresponding to a wavelength in tissue on the order of 10 cm. At such short wavelengths head or body resonators form standing-wave field patterns, which degrade MRI results by causing regional signal losses and perturbing the contrast between different types of tissue.

The non-uniformity of standing waves is due to the underlying electrodynamics, which require that the magnetic field exhibit curvature according to its frequency and the ambient material. Standing waves fulfill this condition by spatial variation of the field magnitude (Fig. 6.1a). However the required field curvature can also be translated, partly or wholly, into phase variation. Causing the underlying field pattern to propagate through space such phase variation reduces the variation of the field magnitude. Notably, the limiting case of a plane wave exhibits perfectly uniform magnitude at any wavelength. In addition, travelling RF waves offer a natural means of exciting and detecting NMR across large distances (Fig. 6.1b).

Despite these attractive features travelling-wave NMR has not been explored so far. In traditional cylindrical setups the formation of travelling waves at the NMR frequency is suppressed by structures surrounding the sample, such as gradient coils, cryostats, and RF screens. Their conductive surfaces admit axially travelling waves only beyond some cut-off frequency which is roughly reciprocal to the bore width. Therefore travelling-wave NMR requires a high-field magnet that also has a wide bore in order to bring the cut-off frequency below the NMR frequency.

To fulfill this requirement we used a cylindrical, superconducting 7.0-tesla magnet with a 58 cm-diameter bore lined with an RF screen (Fig.6.1c). The screen was made from a stainless steel mesh designed to provide high conductance at RF frequencies while blocking audio-frequency eddy currents induced by the surrounding gradient coils. When enclosing only air the bore has a cut-off frequency of 303 MHz, which is still just above the proton Larmor frequency of 298 MHz. However, the frequency limit is reduced when dielectric material is brought into the bore. Even small amounts of dielectric loading enable the formation of axially travelling waves at the NMR frequency, effectively using the RF screen as a waveguide. A human body in particular - containing large amounts of water, which is a strong dielectric - reduces the cut-off frequency sufficiently to clearly enter the travelling-wave regime.

NMR via such travelling waves requires a new type of probe. Instead of the

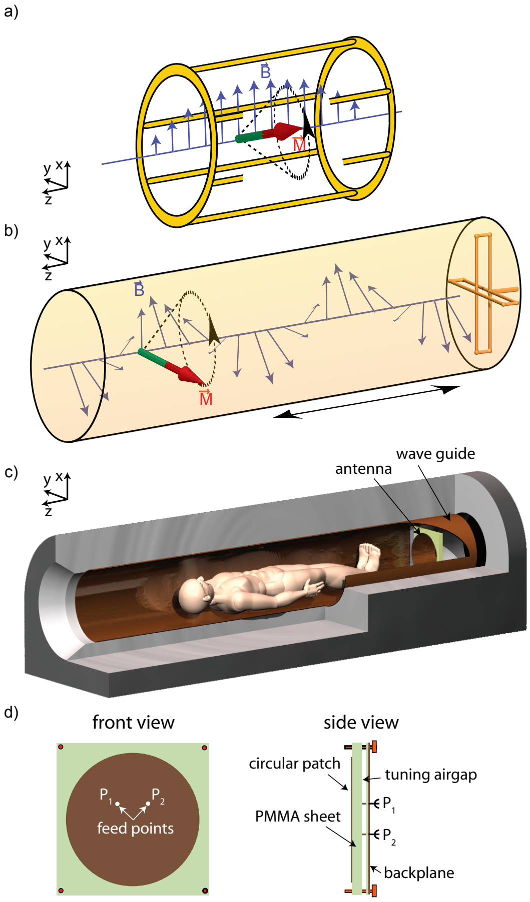

Figure 6.1: Working principles of traditional and travelling-wave NMR. a) Traditional resonant probes form a standing RF wave within the sample. Its magnetic component B causes nutation of the nuclear magnetization M and governs the probe's receive sensitivity. b) In the novel approach an antenna probe interacts with the sample via a travelling wave. c) In a wide-bore, high-field magnet such waves can be guided by a conductive lining, permitting remote NMR excitation and detection with an antenna at the end of the magnet. d) Schematic of the circularly polarized patch antenna used for the initial implementation of this concept.

reactive near field of the sample a travelling-wave probe must couple to the propagating modes of the waveguide. To do so it no longer needs to be close to the sample but can be placed anywhere along the bore. Requirements of this sort are well known in microwave engineering and can be addressed by a range of technical solutions. For the present work the NMR probe was implemented in the form of a circularly polarized patch antenna (Fig. 6.1d).

Using this setup the principle of travelling-wave NMR was first demonstrated by spectroscopy of an aqueous 10% ethanol solution. Proton NMR was excited and detected by the patch antenna, which was initially mounted at the end of the RF screen, 70 cm from the sample. The resulting spectrum (Fig. 6.2a) shows the expected dominant water peak as well as the methyl and methylene resonances of the ethanol molecule. The experiment was then repeated with gradually increasing antenna distances. As the magnified methyl triplets in Fig. 6.2b show, consistent spectrum quality was obtained with the probe placed well outside the magnet and a well-resolved spectrum was still detected at a distance of 2.6 m from the sample.

The evident loss of sensitivity at large distance reflects the expected decrease in coupling between the antenna and the modes of the bore. Higher sensitivity at large distances would be achieved with an antenna of greater directivity or a longer waveguide.

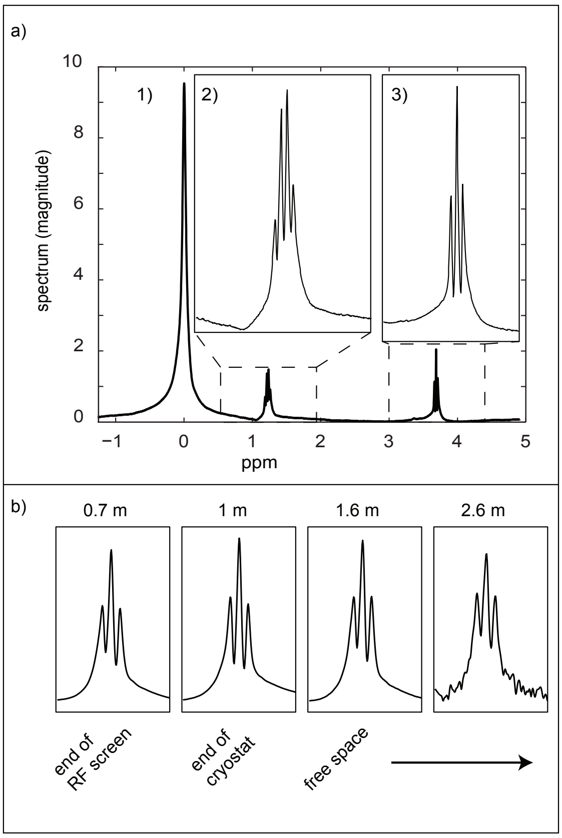

Figure 6.2: Demonstration of travelling-wave NMR in an aqueous 10 % ethanol solution. a) NMR spectrum obtained at an antenna distance of 70 cm, showing water (1), methylene (2), and methyl (3) resonances. b) Details of the methyl triplet as observed with increasing distance.

The spatial uniformity of the travelling waves was studied in an extended sample of 50 cm in length, formed by two adjacent bottles filled with mineral oil. On its own, this arrangement did not yield completely uniform RF coverage, as illustrated by the imaging results shown in Fig. 6.3a. The residual non-uniformity indicates the presence of a standing RF wave superimposed on the intended travelling component. It is caused mainly by slight reflections at the transitions between the bottles and the empty sections of the bore, which entail changes in wave impedance. The reflections can be mitigated by wave-impedance matching and additional loading. To demonstrate this two further bottles were added at the far end of the sample, the second one containing a conductive water solution to act as a termination dissipating incident wave energy. This modification indeed rendered the MRI results substantially more uniform, indicating the presence of almost purely travelling RF waves (Fig.6.3b).

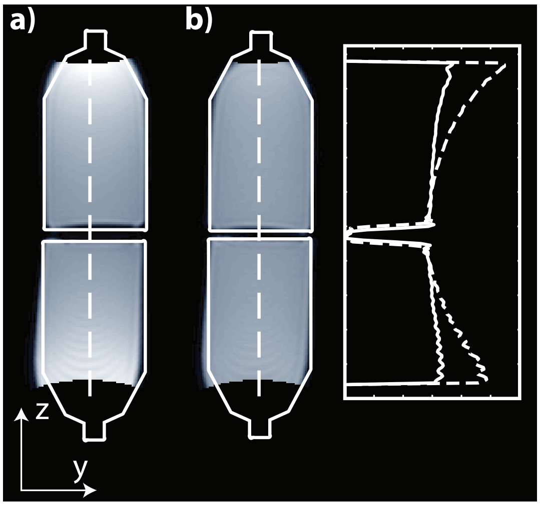

Figure 6.3: : Example of wave-impedance matching in travelling-wave MRI: a) Non-uniform coverage of two phantom bottles is caused by residual standing RF waves, which can be suppressed by b) wave-impedance matching and dissipation in a termination load.

For reasons of safety, initial invivo experiments targeted only a volunteer's lower extremities ensuring that the chest and head remained outside the waveguide. The antenna was placed at the opposite end of the bore, 70 cm from the ankle. The resulting magnetic-resonance image (Fig. 6.4a) shows the right lower leg with good uniformity over a large volume. The field of view of 50 cm is the maximum possible with the gradient system used and is not limited by the travelling-wave concept. Wave-impedance matching was not necessary in this case because the leg per se forms a sufficiently smooth, tapered impedance transition. For comparison the same imaging procedure was repeated with a commercially available birdcage resonator optimized for head MRI at 7 tesla. The result thus obtained (Fig.6.4b) exhibits smaller coverage, reflecting inherent limitations of resonant probes. The standing-wave nature of its rung currents limits the feasible length of the birdcage probe, which is 17 cm for this model. On longer rungs the RF current would become even more non-uniform [7], causing a similar axial sensitivity drop-off and rendering the resonator unstable [8].

While it was possible to cover the lower legs uniformly, significant RF attenuation is expected to occur along the full length of a human body. Simulations of the setup in Fig. 6.1c, assuming an adult male subject, indicate that in total the body absorbs approximately 90 % of the RF power coupled into the waveguide and only the remaining 10 % are radiated off its far end. Less attenuation is expected for shorter or slimmer subjects or when using an even wider bore. Based on the same simulations the coupling efficiency of the patch antenna was estimated at 80 %, a value that can certainly be improved by optimizing the strategy of driving the waveguide modes.

Besides coverage and uniformity the travelling-wave concept will also affect the sensitivity and RF power efficiency of NMR experiments. According to the reciprocity of NMR signals [9] the sensitivity of an RF probe is closely related to its efficiency, i.e., its yield of circularly polarized RF magnetic field at reference

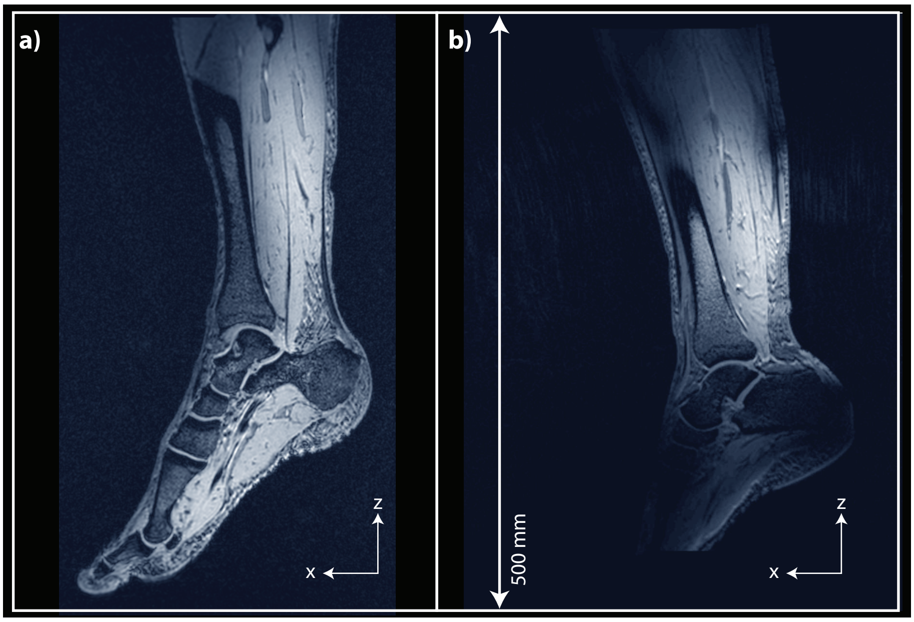

Figure 6.4: : In-vivo results: a) Travelling-wave MRI of a human lower leg in-vivo. b) Identical scan performed with a traditional resonant probe.

input power. Resonant near-field probes achieve high efficiency by concentrating RF energy and dissipation in the sample and the probe itself. By contrast, the travelling-wave approach relies on RF energy flowing through the setup, requiring that part of it be absorbed beyond the target volume. This can be done by a dedicated absorber device or diffusely outside the waveguide as was the case in our initial experiments. With either solution the necessary absorber losses will take some toll in terms of efficiency and sensitivity, constituting a drawback of travelling-wave probes compared with resonators.

Reduced probe efficiency is the lesser concern because it can be addressed by using higher driving power. In-vivo MRI is usually not limited by technical RF power constraints but rather by sample heating, to which the absorber losses do not contribute.

The corresponding sensitivity loss, caused by thermal noise originating from any material that absorbs RF power during transmission, is more limiting. One potential way of avoiding this loss is to use a cryogenically cooled absorber structure. For MRI applications it is also conceivable to combine travelling-wave excitation with local detection by an array of detunable surface resonators [3]. Such a hybrid approach will reconcile the improved coverage and safety advantage of travelling-wave excitation with the sensitivity benefit of close-range array detection.

With respect to net sensitivity another potential concern is the phase delay that results from signal propagation to and from the resonant nuclei. For large samples it will give rise to significant phase differences between signals travelling different distances. This effect is illustrated in Fig. 6.5a, showing travelling-wave MRI of a long, water-filled cylinder with antennas placed at both ends of the waveguide. Using the same antenna for transmission and reception ($1 \rightarrow 1$ or $2 \rightarrow 2$) results in a linear distribution of the image phase. MRI will not be hampered by such phase variation as long as it is resolved by the imaging process. However spectroscopic experiments could suffer from delay-related dephasing. To address this problem the transmit and receive antennas should generally be designed and positioned such that the total phase delay is the same across the volume of interest. In the previously mentioned experiment this situation was accomplished by using either of the two antennas for transmission and the opposite one for reception. As shown in Fig. 6.5a the linear phase patterns nearly vanished in these configurations ($1 \rightarrow 2$ or $2 \rightarrow 1$). Alternatively, after travelling-wave excitation from either side a gradient encoding blip could be applied to compensate for variable phase delay, effectively refocusing the spin radiation for reception by the same antenna as used for RF transmission. Since the signal received in a travelling wave setup is directly linked to the radiation of electromagnetic power, this experiment shows that the radiation from spin ensembles can be steared by magnetic field gradients [10, 11]. Furthermore, the distinct phase gradient modulated on the NMR signal dependent on the direction of the signal propagation delivers as such the possibility for spatial signal localization. In the case ideal linear phase gradients can be established for each detector, the signal received by each antenna corresponds to the signal acquired after a phase encoding gradient moment dependent on the direction of propagation. This means that in a spin warp acquisition each antenna can acquire a different line in k-space simultaniously to antoher antenna if the phase encoding is chosen in the direction of propagation. Considering an accelerated SENSE scan [12] the encoding provided by the RF is ideal corresponding to a g-factor of 1.

Entering the far-field realm, travelling-wave NMR prompts analogies with electron spin resonance [13] and nonlinear optics [14]. Adopting principles and devices from these fields may enable the study of phenomena analogous to, e.g., photon echoes [15], four-wave mixing [16], and self-induced transparency [17]. Potentially useful analogies can also be drawn with the large variety of more widespread technologies that rely on travelling-wave phenomena, including manifold imaging modalities, radar, and telecommunication. The above discussed spatial localization by the propagation phase delay can for instance directly be related to holographic techniques. In the present work, the established concepts of waveguides and antennas have already proven useful.

Clearly, by adopting propagating waves NMR also incurs known complications of this realm, such as material-dependent diffraction and attenuation. These effects will likely be encountered, e.g., in MRI of the human torso, exhibiting pronounced dielectric interfaces such as the shoulders. Figure 6.5b shows an initial experimental illustration of dielectric perturbations in a phantom of similar size and shape as a human torso. One way of countering these effects is wave-impedance matching, which has been demonstrated here in a basic form. Analogously to index matching in microwave and optical technology, wave-impedance matching can be achieved using a wide range of distributions of dielectric, magnetically permeable, or conductive material and thus offers great inherent freedom for tailoring resulting RF field distributions.

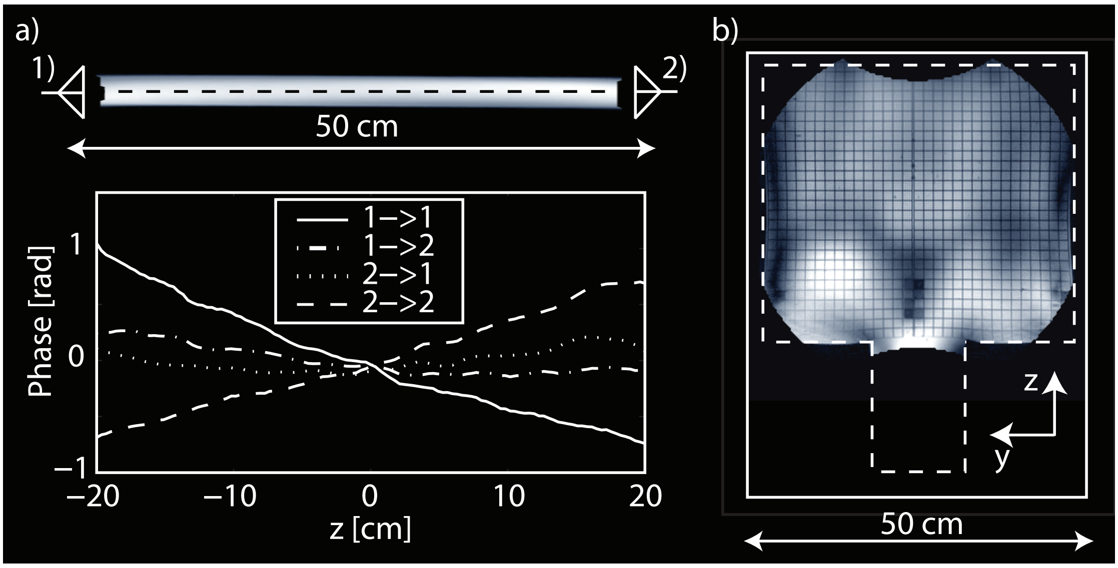

Figure 6.5: : Travelling-wave MRI of very large samples. a) Two antennas, one at each end of the waveguide, were used to image a long water cylinder. Transmission and reception with the same antenna ($1 \rightarrow 1$, $2 \rightarrow 2$) give rise to linear phase delays, as shown in graphs of the image phase along the phantom. Constant net phase delay is achieved by transmitting with either of the antennas and receiving with the opposite one ($1 \rightarrow 2$, $2 \rightarrow 1$). b) Image of a human torso phantom. Dielectric boundaries introduce discontinuities of the wave impedance, causing field perturbations that diminish towards the lower regions of the phantom.

By improving the extent and uniformity of spatial coverage travelling-wave MRI promises to facilitate the exploration of the highest currently available field strengths for human studies. A further promising area of application is high-field screening. The ability to perform spatially resolved NMR in larger volumes may simplify studies of large numbers of small animals [18] or inanimate samples in parallel.

Finally, introducing a significant distance between the sample and the NMR probe has multiple beneficial side-effects. In such a configuration the probe is not loaded by losses in the sample, which simplifies impedance matching and renders the probe performance substantially more robust than that of near-field high-frequency probes. This situation also simplifies safety considerations in human studies by avoiding exposure to strong short-range electric fields emanating from the probe. Furthermore, placing the probe far away frees up space in the center of costly high-field magnets [19], may improve the comfort of human subjects and facilitates bringing in alternative equipment, such as stimulation devices for studies of brain function.

6.1.1 Methods

All experiments were performed in a cylindrical superconducting 7.0-tesla magnet (Philips Healthcare, Cleveland, Ohio), equipped with a three-axis gradient system and lined with an RF screen made from a stainless-steel mesh (diameter = 58 cm, length = 135 cm). NMR and MRI data acquisition was performed with an integrated console and spectrometer (Achieva, Philips Healthcare). Throughout, the RF transmitter power was limited to the same values as for human head exposure with a local resonator, i.e., 10 W average forward power and 1.4 kW peak power.

The custom-designed patch antenna is shown in Fig. 6.1d. Its front plane is a 350-mm diameter disk made of copper sheet glued onto a 25 mm-thick acrylic (PMMA) former. The backplane is formed by a square copper sheet mounted on 5 mm acrylic. Acrylic yields negligible proton NMR signal at the echo times used in this work. A variable gap between the two planes was used to tune the antenna to the proton NMR frequency of 298 MHz. The antenna was driven at two points in the front plane forming a right angle with the center of the disk. The radial positions of the feed points were chosen such as to match the impedance of the 50 Ω feed lines. To produce circular polarization in the transmission mode the two ports were fed through a 90 ° hybrid splitter. In receive operation the two channels were connected to independent receive lines of the spectrometer and combined digitally. Switching between transmit and receive operation was performed by TTL-controlled diode switches.

The spectra shown in Fig. 6.2 were obtained from a 10% solution of ethanol in water, contained in a 1-litre glass beaker. To support the formation of axially travelling waves bottles of distilled water were added on either side of the beaker as dielectric loads. NMR spectra were acquired with a localized STEAM sequence (stimulated echo acquisition mode) with an echo time of 11 ms and a repetition time of 3 s. Low-flip-angle RF pulses were used such that the selected volume of 9 cm^3 changed negligibly with the RF amplitude. The acquisition bandwidth was 2 kHz and 16 phase cycles were performed to cancel spurious echoes. When changing the position of the RF probe all console and spectrometer settings were kept constant.

The data shown in Fig. 6.3 were obtained from bottles filled with 3 litres Marcol 82 mineral oil, using a gradient-echo sequence with an echo time of 2.9 ms, a repetition time of 42 ms, and a bandwidth per pixel of 338 Hz. A very small flip angle was chosen to ensure that the image intensity depends linearly on the transmit and receive sensitivities of the probe.

The in-vivo images of a volunteer's right lower leg (Fig. 6.4) were acquired with a 3D gradient-echo sequence, yielding an isotropic resolution of 1 mm in 6 minutes. The echo time was 3.1 ms, the repetition time was 12 ms, and the bandwidth per pixel was 376 Hz. All sequence parameters were kept the same for the two probes, except for the transmit power, which was reduced to 25 % for the resonator to obtain similar flip angles in the center. The axial length of the field of view of 500 mm was again limited by the gradient system. The resonant probe was a commercially available birdcage resonator with a diameter of 30 cm and a length of 17 cm (Nova Medical Inc., Wilmington, MA). Both legs resided within the resonator to keep the volunteer in the same position.

Electromagnetic simulations of the in-vivo setup were performed using the finite difference time domain (FDTD) technique (SEMCAD®, Schmid&Partner Engineering AG). The cylindrical RF screen was modeled as a perfect electrical conductor and an anatomical model of an adult male [20], featuring in-vivo dielectric tissue properties, was positioned at its center. The patch antenna was placed equally as in the in-vivo experiment, i.e., at a distance of 70 cm from the ankle. The flow of RF energy through the waveguide was assessed by integrating the Poynting vector over transverse control planes. A first control plane between the antenna and the human served to determine the power coupled into the waveguide. A second one in the loss-free region close to the end of the waveguide was used to calculate the power that is radiated off the far end of the waveguide. The power difference was validated by volume integration of ohmic losses over the entire body.

In the experiments reported in Fig. 6.5a, an RF-spoiled 2D gradient-echo sequence was used to image a 2 m long, water-filled cylinder of 7 cm in diameter. Two antennas were used simultaneously, one at each end of the bore, at a distance of 10 cm from the respective end of the waveguide to minimize reflections. In these experiments only a single port of each antenna was used for RF transmission and signal reception to avoid any phase perturbation by imperfect port combination. In two successive sets of experiments either of the antennas was used for transmission while receiving image signals with both. All scans were performed twice with an echo time difference of 0.5 ms, permitting to estimate and remove any phase contributions from local frequency offsets.

The remaining image phase results exclusively from RF propagation, including unknown constant offsets of various sources, such as cabling and spectrometer calibrations. To eliminate these arbitrary offsets each phase plot was offset corrected to null the phase in the center ($z = 0$). The nominal field of view was 50 cm. In order to avoid phase distortions by potential gradient delays, the readout direction was orthogonal to the cylinder axis and no correction for gradient non-linearity was applied. The range of meaningful phase values was thereby reduced to approximately 35 cm.

Figure 6.5b shows a torso phantom made of PMMA as proposed by the American Society for Testing and Materials (ASTM), filled with gelled water ($\epsilon_r = 80$, $\sigma = 0.47\,{}^{\mathrm{S}}\!/_{\mathrm{m}}$). Imaging of this phantom was performed by a low-flip-angle, multiple-slice, RF-spoiled 2D gradient-echo sequence with a repetition time of 50 ms per slice, yielding an effective resolution of 1 mm in-plane and a slice thickness of 4 mm.

6.2 Parallel MRI by Travelling Waves

6.2.1 Introduction

The advantage offered by the otherwise problematic shortening of the wavelength, is the enhanced parallel imaging capability found at ultra-high fields [21]. This cannot be exploited by the travelling wave approach discussed above. The higher degree of freedom of the RF fields inside the imaging area renders the possibility of highly accelerated imaging. In transmission, the higher spatial variability of the NMR active fields became assessable by multi-port transmission coils, which allowed tailoring the RF field by RF-shimming [22, 23] or accelerating gradient limited spatially selective RF pulses [24]. These parallel transmission approaches have shown to be able to improve the efficiency with respect to input power but also tissue absorption of the RF transmission, as well as mitigating the problem of non-uniform excitation within the targeted region of interest [22, 25, 26].

Although transmission arrays offer the possibility to adaptively change the excitation field to each application without having to design a specific coil each time, many problems regarding close range coupling between the coil structure and the sample remain. Furthermore, most designs need to be tuned and matched individually for each subject. Moreover, safety validation concerning the local power deposition in the tissue (SAR) stays a major challenge, due to the possibility of very strong and localized electric fields emanating from the coil residing closely to the tissue. Finally, it is not clear, whether especially the axial extension of the coverage of such coil designs can readily be sized up even for whole head coverage, as suggested by the study presented in [27].

Therefore the technical feasibility and the prospects of a combination of the parallel transmission and the travelling wave idea shall be explored. The diversity of the field patterns provided by each port of the array is the key ability that transmit and also receive arrays must deliver. It is a prerequisite for all kinds of parallel transmission and imaging modalities. In a classical close fitting array, this is ensured by decoupled localized resonant structures, e.g. loops or striplines. Using the travelling wave approach localization of the electromagnetic fields close to the feed structure does not directly deliver any RF encoding in the distant sample, because it does not reside within the steeply decaying near field of the exciters. But if a waveguide is used that is able to carry multiple propagating modes in the travelling wave approach, the distinct field pattern of each mode delivers spatial diversity. The prerequisite to access this diversity is that several modes or distinct mixtures of modes can be excited by each feeding port. The field distribution inside the scanner could thereby be manipulated similarly as in the case of a transmission array because the transverse vectoral field distributions of the modes offer special diversity. The key goals in order to allow parallel imaging in a travelling wave approach are therefore: First, ensuring that a significant number of modes are below cut-off at the NMR frequency. Second, that the modes can be fed as orthogonally between the ports as possible. By this, all kinds of parallel RF methods can in principle be adapted to be used in conjunction with a travelling wave system.

6.2.2 Theory

Approximating the bore of a human MRI system as a hollow cylindrical perfect electrical conductor allows describing the electromagnetic fields inside the bore in terms of the guided waves formalism [28]. As a result of such analysis the homogeneous solutions of the Helmholtz problem with the corresponding boundary conditions form the so called waveguide modes. Each mode is characterized by its transverse vectorial field distribution ($\vec{B}_T, \vec{E}_T \in \mathbb{R}^3$) and the longitudinal propagation wave number k_z or alternatively to the latter its cut-off frequency ω_c. The fields of each mode at the frequency ω are then given by:

$$\begin{aligned} \vec{E}(\omega) &= \vec{E}_T(\omega) \cdot e^{ik_z(\omega)\cdot z} \\ \vec{B}(\omega) &= \vec{B}_T(\omega) \cdot e^{ik_z(\omega)\cdot z} \\ \text{with } k_z(\omega) &= \sqrt{\mu\epsilon}\sqrt{\omega^2 - \omega_c^2}. \end{aligned} \tag{6.1}$$

In the case of a hollow waveguide the modes can be divided canonically into two disjoint subgroups depending on the longitudinal components of their transverse field distribution: The transverse magnetic (TM) for which $(\vec{B}_T)_z = 0$ in the volume and the boundary condition $(\vec{E}_T)_z = 0$ at the perfectly conducting surface of the waveguide. This means that the magnetic field of a TM mode is purely transverse and therefore NMR active. On the downside, the TM modes of lowest cut off frequencies have a magnetic field minimum at the centre. Their counterpart, the transverse electric modes (TE) have $(E_T)_z = 0$ with boundary condition $\frac{\partial(\vec{B}_T)_z}{\partial\vec{n}} = 0$. Although the magnetic field of these modes is not purely transverse, the transverse components increase with the propagation wave number k_z. Furthermore, the first TE modes have the lowest cut off frequency in a circular waveguide and exhibit a magnetic field maximum at the centre. All modes are commonly numbered first by the number of circumferential variation and the second digit denotes the number of radial variation. Two modes are termed degenerate if they have the same cut-off frequency and if their transverse field distributions are geometrically congruent up to a global phase. It can be seen from Equation 1 that each mode starts to propagate if the frequency is higher than the cut-off frequency. If the cut-off frequency is higher than the frequency of operation, the wave number k_z becomes imaginary reflecting that the wave dies off longitudinally.

In order to generate a field inside the waveguide, the modes are excited by a coupling element, which corresponds to an inhomogeneity in the Helmholtz equation. This source couples power into a superposition of modes that travels away from the source. In [29] the source was realized by a patch antenna, that basically impresses an approximately fixed current distribution at one end of the waveguide creating a fixed mode superposition. However, since the resulting field distribution in the bore cannot be altered by the source, the only way shown to implement parallel transmission and imaging approaches was by the usage of the longitudinal phase variation of two antennas located at opposite ends of the waveguide [10]. But variations in the transverse field distribution cannot be exploited for parallel transmission and reception using such an approach.

For the case that several modes are above cutoff in the waveguide, several ports can be used to impress an altering current distribution [30] that excite an altering superposition of modes that in turn lead to an altering field distribution in the sample depending on the amplitudes and phases applied to the ports. By these means such a waveguide can be considered analogously as a transmit and/or receive array coil.

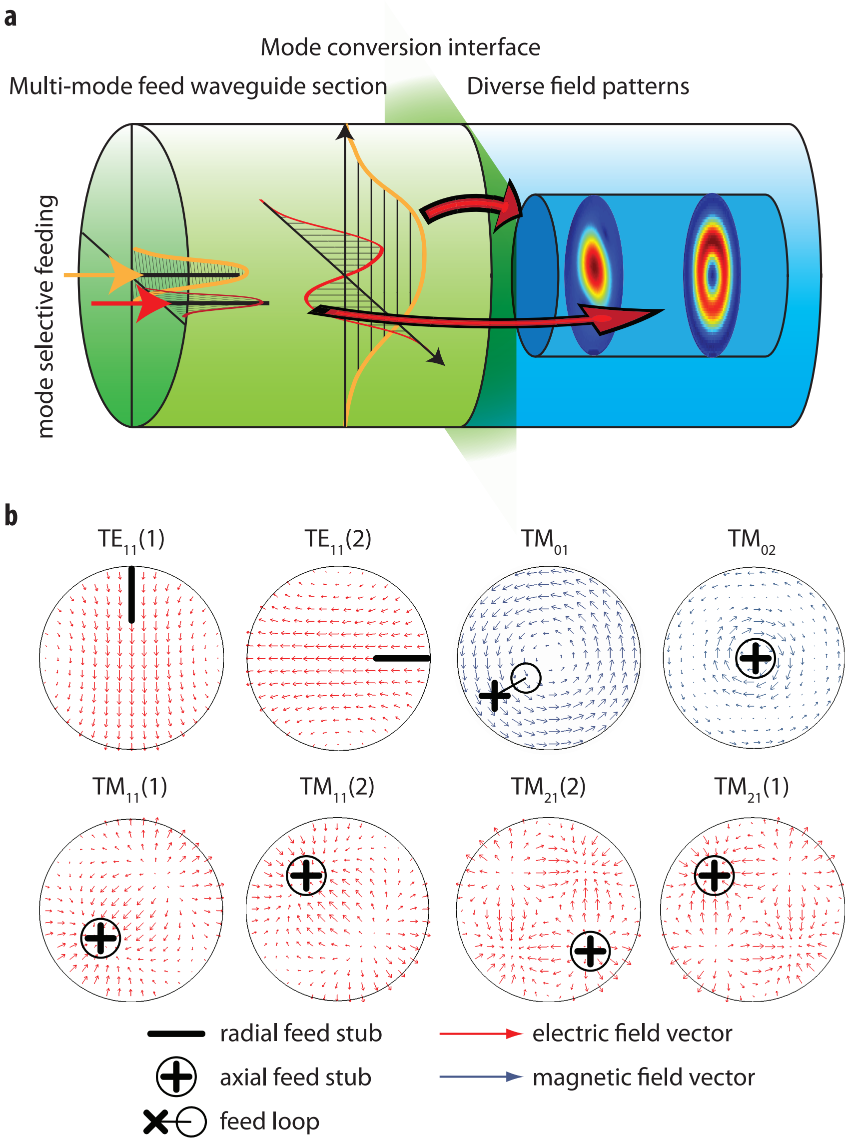

Figure 6.6: : Schematic of the functional principle. a) A waveguide section that is able to carry several modes is attached in front of the waveguide that is loaded by the sample. Each single mode that is selectively fed is expected to induce a different field pattern inside the sample due to its distinct coupling at the mode conversion interface between the feed waveguide and the sample. b) shows the transversal field distributions of the basic modes for a uniformly filled waveguide. The schematic shows how these individual modes were targeted to be selectively fed each by a copper stub or a loop.

In current ultra-high field systems such an approach is not directly applicable. First, the empty bore does not support the propagation of several modes. Second the bore is usually too short in order to allow the modes to fully establish from the feeding structure before reaching the lossy sample. The latter problem is mitigated in this work by adding a feed waveguide section (see Fig. 6.6) extending the bore. This feed section must be able to carry several modes from the exciters to the sample. Each port is intended to excite a distinct superposition of modes within the feed waveguide. At the interface between the multi-modal feed section and the sample it is then expected that the specific field distribution of each mode couples into the sample producing a distinct field pattern therein. It is favorable that each port is linked to a distinct field pattern in the sample, analogously to the port of a close coupling coil array. Since the waveguide of the feed section must have the similar geometrical dimensions as the bore (0.58 m inner diameter) in order to fit into it, it is as such not able to carry enough modes as the bore itself. In order to lower the cut off frequency, in some cases even selectively of certain modes, multiple methods are known in microwave theory applying either dielectric fillings [31], conductive structures [32], or metamaterials [33]. In this work a dielectric filling was employed which was shown to be effective in enabling field propagation in MRI systems [34]. In comparison to the other options the losses in the dielectric are low due to the low conductivity of available materials at these frequencies. A uniform dielectric filling of the entire inner volume of circular waveguide lowers the cut-off frequency of each mode according to the induced shrinkage of the free wavelength:

$$\omega_c(\epsilon_r) = \frac{1}{\sqrt{\epsilon_r}}\omega_c(1). \tag{6.2}$$

According to this formula a uniform dielectric filling with a relative ϵ_r of about 5.3 would be sufficient to allow at least 8 modes to propagate in a circular waveguide of 0.56 m in diameter. However, dielectric materials in that range would either be very expensive, bulky or heavy when needed to fill the entire volume of the waveguide. Furthermore, the cutoff frequencies of the TE modes would be lowered by the same amount as those of the TM modes, although the TM modes would have the beneficial property for NMR excitation, that the magnetic field is transverse and therefore NMR active. In the case of an inhomogeneous material distribution inside a waveguide, the modal structure can in general not be deduced directly from the modal structure of the empty waveguide. However, if the structure of the dielectric filling becomes small compared to the wavelength, the average macroscopic effects of a mesoscopically inhomogeneous material on electromagnetic waves can be described by a uniform material with appropriate effective dielectric material parameters. Therefore, the very complex field distributions inside the filled waveguide is approximated on a larger scale by the modes of a waveguide with a uniform filling that has an appropriate effective permittivity. This approximation becomes valid in the limit of very small scaled (compared to the wavelength), equably distributed inhomogeneities. This effective permittivity can in principle be estimated either based directly on the filling material properties and distribution by the usage of the Maxwell-Garnett formula [35, 36], or ex-post by explicitly simulating the modal structure of the waveguide with and without insert and using Eq. 6.2 for the calculation of the net effective permittivity for each mode:

$$\epsilon_{\text{eff}} = \left(\frac{\omega_c(\text{empty})}{\omega_c(\text{filled})} \right)^2 . \tag{6.3}$$

Both approaches allow capturing the complex interactions appearing in the mesoscopic scale of the dielectric's structure by its net effects, and will be compared for the given setup.

6.2.3 Methods

Construction of the feed waveguide section

The feed waveguide was made of a PE tube of 2 m length and an outer diameter of 560 mm. The PE tube was upholstered with a brass mesh made of 0.25 mm wire as shown in Fig. 6.7. The tube was inserted coaxially into the bore supported by two sliding groves fitting into the rails of the bore liner. In order to maintain a closed conductive surface around the waveguide, 0.5 mm copper sheets were clinched onto the waveguide to fit the shape of the groove. The copper sheets were screwed together with the brass mesh to the PE tube using 8 mm nylon screws. On the feeding end of the waveguide a PVC disk covered by the same brass mesh as the waveguide itself was mounted using 6 mm nylon screws in order to terminate this end of the waveguide with a short circuit and to enable mounting the feeding ports. The brass mesh of the end cap was electrically contacted to the mesh covering the PE tube by soldering copper leads to both. These leads are then pressed onto each other when fastening the mounting screws of the end cap. The entire construction was supported by a wooden frame equipped with wheels facilitating the insertion of the waveguide into the bore.

To lower the cutoff frequencies of higher order modes, a structured dielectric insert was constructed. It consisted of 52 PMMA tubes of 2 m length, an inner diameter of 34 mm and 3 mm wall thickness and filled with distilled water ($\epsilon_r = 81, \sigma = 0.0001\,{}^{\text{S}}\!/\!_{\text{m}}$). The tubes were arranged on a Cartesian grid with a pitch of 58 mm. Two circular pressboard plates trued up in the waveguide former each equipped with 42 mm holes positioned the PMMA tubes. The effect of the dielectric insert, the resulting modal field distribution and the corresponding cutoff frequencies were calculated using the 2D Finite Element Method (FEM) based

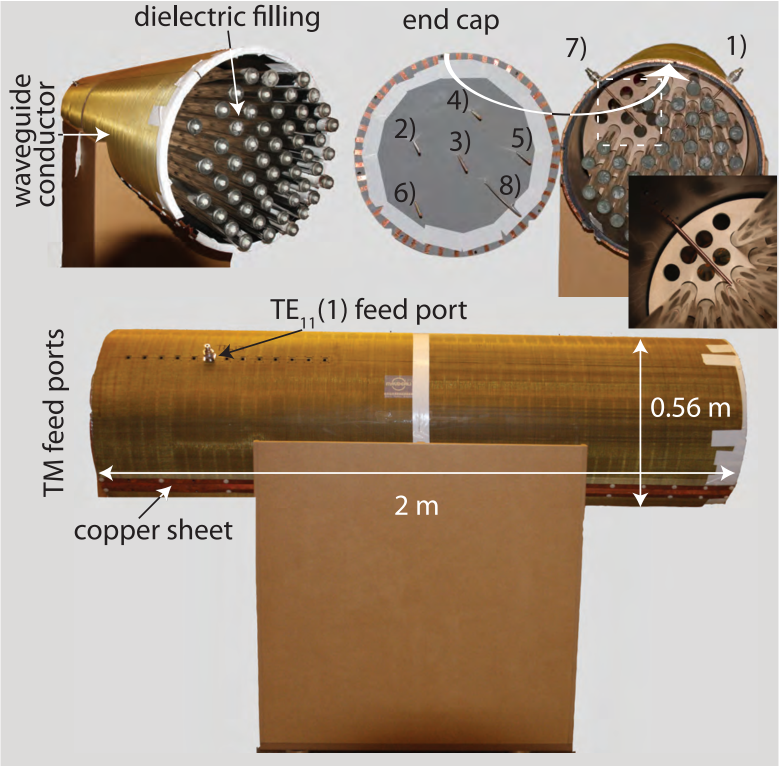

Figure 6.7: Photos of the feed waveguide section. The upper left image shows the end of the feed waveguide section that is entered into the magnet bore. The opposite end of the waveguide is depicted in the upper right image. The backplane is opened to show the feed stubs targeting (1) $TE_{11}(2)$ having a length of 195 mm, (2) $TM_{11}(1)$ (220 mm), (3) TM_{02} (230 mm), (4) $TM_{11}(2)$ (165 mm), (5) $TM_{21}(1)$ (195 mm), (6) $TM_{21}(2)$ (190 mm) and (7) $TE_{11}(1)$ (195 mm) plus the feed loop (8) for TM_{01} ($130{\times}100\,mm^2$). The lower image shows the feed section from the side.

eigenmode analysis of the commercial software package COMSOL (Stockholm, Sweden). Based on the resulting cut-off frequencies with and without dielectric insert, the effective permittivity of the dielectric filling has been calculated for each mode using Eq. 6.3. The results of these simulations are collected in Table 1 for all modes potentially propagating at the proton Larmor frequency for 7T. The 6 TM modes exhibiting the lowest cut-off frequencies among all TM modes were targeted to be selectively fed each by a dedicated port. The two lowest TE modes (TE_{11}) were targeted in addition because all the propagating TM modes have no magnetic field at the center. The shift of the cut-off frequencies of all TM modes is much larger than that of the TE modes. This results in an effective permittivity for all TM modes of about 23.5, which corresponds roughly to the volume average of the dielectric permittivity inside the waveguide. The TE modes are apparently almost unaffected by the dielectric insert which is represented by the very low effective permittivity of about 1.6. From these design studies it was concluded, that the dielectric insert as presented is able to carry at least one mode for each of the 8 available channels.

Mode selective feed

In order to achieve spatial field diversity among the 8 ports intended to be used, each port needs to excite the propagating modes inside the waveguide as orthogonal as possible with respect to the other ports. Since the modes themselves are spatially orthogonal, it was considered to be a good start, to target a single mode for each port.

All ports consisted of 7/16 series panel connectors (Huber & Suhner AG, Pfaeffikon SZ, Switzerland) screwed onto the brass mesh of the waveguide which had a cut out for the center conductor. With the exception of TM_{01}, all modes were fed by copper stubs with a diameter of 7 mm screwed onto the center conductor of the before mentioned panel connectors. The placement of the stubs was deduced from field simulations of the targeted modes (see Fig. 6.6b). These simulations were carried out using the COMSOL 2D FEM mode solver with the dielectric inserts in the volume of the waveguide. In the case of degenerate modes TM_{nm}/TE_{nm}, the mounting points of the ports formed a $90\,/n$ angle with the axis of the waveguide. Generally the exciters were positioned in order to maximally couple into the target mode. Although no explicit suppression of other modes can be achieved in general, it was expected that the coupling into the other modes is significantly lower ensuring high field diversity among the ports. The feed stubs of the TM modes were mounted in z-direction on the backplane, since the electric fields of all TM modes have a longitudinal component in contrast to the TE modes. The lateral position of each stub on the backplane was chosen such that the targeted mode exhibits a purely longitudinal electric field aligning with the current running on the stub. The TM_{01} mode was fed by a loop made of a handformable cable (SUCOFORM 47 CU from Huber & Suhner AG) whose outer conductor was soldered to the center conductor of the panel connector. The position of the loop was chosen to enclose the radial zero line of the TM02 minimizing the coupling to this mode. The positions of the stubs for the TE_{11} modes were located a quarter effective wavelength distant from the endcap, which turned out to be 500 mm. The individual ports were matched for the feed section installed on the system filled with 52 PMMA tubes and a cylindrical phantom filled with tissue simulating liquid (20 cm in diameter, 30 cm in length, $\epsilon_r = 56$, $\sigma = 0.78\,{}^{\mathrm{S}}\!/_{\mathrm{m}}$) placed in the isocentre of the bore 10 cm distant from the PMMA tubes. The matching was adjusted by the length of the feed stubs and the circumference for the TM_{01} loop.

Each port was equipped with a custom made, low voltage active transmit receive switch with integrated preamplifier (MGA53453, Agilent, Santa Clara, California) delivering an isolation of more than 60 dB in transmission and a gain of about 18.5 dB in reception. The insertion loss for transmission was below 0.3 dB and the noise figure of the entire unit was about 1.5 dB.

Imaging experiments

All imaging experiments were carried out using a Philips Achieva 7T scanner (Philips Healthcare, Cleveland, Oh.) equipped with an 8 channel parallel transmission unit (MultiX, Philips Hamburg, Germany). For the imaging experiments, the peak power of each amplifier output was limited to nominally 500 W and the time average power of all 8 channels maximally 100 W in total. Two cylindrical phantoms were employed, a cylinder filled with simulating tissue dielectric properties (20 cm in diameter, 30 cm in length, $\epsilon_r = 56$, $\sigma = 0.78\,{}^{\mathrm{S}}\!/\!_{\mathrm{m}}$) and a cylinder filled with saline water (20 cm in diameter, 34 cm in length, $\epsilon_r = 81$, $\sigma = 0.84\,{}^{\mathrm{S}}\!/\!_{\mathrm{m}}$). In order to reproduce imaging conditions similarly to in-vivo cases, a watermelon with a diameter of about 20 cm has been used. While the phantoms have been placed in the isocenter of the magnet, the feeding waveguide was slid into the bore of the magnet reaching up to a distance of 35 cm from the isocenter. In order to acquire the images of the field distribution inside the feed section, the feed section was pushed about 30 cm beyond the isocenter into the working area of the gradient coil.

In order to acquire the sensitivities for each port in transmission and reception, a low flip angle, gradient echo recalled 2D imaging sequence with a slow repetition time of 100 ms was used, preventing strong saturation effects distorting the reference data. The resolution of the images acquired was 2 mm at a slice thickness of 5 mm and the field of view encoded was 300 mm for the 20 cm cylindrical phantom and 450 mm for imaging the field distribution excited by each port inside the feed waveguide section itself. The data retrieved from each voxel therefore consisted of 8×8 complex intensities, to which the bilinear model describing the ideal dependence of the signal on the transmission and reception sensitivities was fitted using Singular Value Decomposition. By this fit the transmission and reception sensitivity maps were estimated on a point-wise basis. Data of the noise floor was acquired using identical parameters for the recording as they were used for imaging the sensitivity maps.

RF shims were calculated on the basis of the retrieved transmission sensitivity maps of the slice by optimizing the magnitude distribution of the excitation to match the target distribution. In order to solve for the optimum amplitude and phase values for each port, a generic minimum search function was employed (fmin, Matlab, The MathWorks, Natick, MA).

In order to determine the net efficiency of the novel setup, B_1^+ maps have been acquired in the cylindrical water phantom in three transverse slices. The tissue simulating liquid could not be employed because it exhibits strong chemical shift induced peak splitting hampering the acquisition of reliable field maps. The sequence used is described in [37] and was executed with a repetition time of 200 ms and with a duration of the B_1^+ sensitizing pulse of 10 ms. A 64×64 matrix has been acquired with a field of view of 250 mm for the transversal slices. Due to the large field of view, the field map had to be acquired taking the effect of strong local off-resonances into account. The local off-resonance has been estimated by the phase difference of two gradient echo images acquired with an echo time difference of 0.5 ms. Outliers from the fitting of the B_1^+ maps have been removed by the application of a median filter. For a power efficient field measurement, an RF shim has been calculated in each slice based on low flip angle gradient echo acquisitions as described above. The phases of the waveforms applied to each channel have been calculated in order to provide maximum total excitation over the slice for the sagital slice and the two transversal slices taken in the middle of the phantom and towards the feet end. For the top slice the field has been maximized in one pixel as indicated in the results section using the phase based method described in Ref. [38]. The B_1^+ maps of the individual channels have been acquired using the interferometric approach described in Refs. [37, 39]. The forward power delivered to each port of the feed section has been kept constant for all B_1^+ mapping experiments and was measured for each channel. The power delivered to a port was determined by a spectrum analyzer (FSL 9 kHz . . . 3 GHz, Rhode & Schwartz, Germany) that was connected to a branch line hybrid with a coupling of -20 dB to the forward wave going into the port. For each flip angle, the power of the B_1^+ sensitizing rectangular pulse was measured after analog demodulation at the carrier frequency of the pulse using the built in unit of the spectrum analyzer. The measured power was then scaled to account for the branch line coupler and cable losses which were measured separately by a network analyzer (Agilent ENA E5071C).

The parallel imaging performance has been evaluated on the basis of the receive sensitivity maps and noise data measured on the cylindrical phantom filled with tissue simulating liquid. The sensitivities have been calculated by the method described above. The g-factor maps have been calculated in 2D according to [12] including the measured noise covariance data with undersampling in the vertical and horizontal dimension.

The watermelon has been positioned at the isocenter of the scanner. In order to prevent longitudinal standing waves inside the melon, the tissue dielectric cylindrical phantom has been placed joining the watermelon in a distance of 10 cm in the supposed propagation direction coaxially within the bore. Using this setup it was assumed that the waves incident on the watermelon are guided out of it and get partially adsorbed in the lossy cylinder and radiate out of the bore. Therefore the standing wave ratio in the melon is expected to decrease. After the acquisition of the sensitivity maps for transmission and reception of each channel in the central transversal slice, an RF shim targeting uniform excitation has been calculated. Applying this shim setting a higher resolution image (0.7 mm in-plane) has been acquired on the same slice with a repetition time of 16 ms within 5 minutes duration. The SENSE reconstructed images for different reduction factors have been generated from the corresponding full data.

The dependence of the parallel imaging performance on the modal structure and the number of supported modes inside the feeding waveguide was assessed experimentally. Sensitivity maps were acquired in the central transverse slice of the cylindrical phantom filled with tissue dielectric liquid. Then a certain number of dielectric PMMA tubes have been removed according to the drawings in Fig. 6.12. The retraction of the dielectric filling has been chosen as such to maintain the rotational symmetries of the waveguide and of the targeted modes. The number of modes propagating at the NMR center frequency was calculated for each scenario by the 2D FEM eigenmode analysis using COMSOL. Since the effective permittivity in the waveguide and therefore the wavelength the modes but also their field distribution in the direct vicinity of the feed stubs is drastically changing for each setup, the matching had to be adapted separately for every experiment. In order not to change the geometrical situation inside the waveguide, L-matching networks consisting of an appropriate fixed value shunt capacitor and a 50 Ω cable for phase adjustment was attached to the ports exhibiting a reflection coefficient of more than 6 dB. For each setup, the full scattering matrix was measured using network analyzer.

6.2.4 Results

Mode selective feeding

The matched stub lengths resulted in a length in between 165 mm and 230 mm and in a circumference of 360 mm for the loop exciter (see Fig. 6.7). The ports of the feed system could be matched to the feed line in the loaded case with an average reflection of -11 dB, a minimum reflection of -33 dB and maximum reflection of -6 dB. The coupling between the ports was -14.5 dB on average and below -9.1 dB for all ports. In the case no sample was present inside the bore, the mean reflection even decreased to -14 dB but the mean coupling increased to -13 dB without any adjustments to the matching configuration. The magnitudes of all entries of the S-matrix are plotted in Fig. 6.13.

Parallel transmission

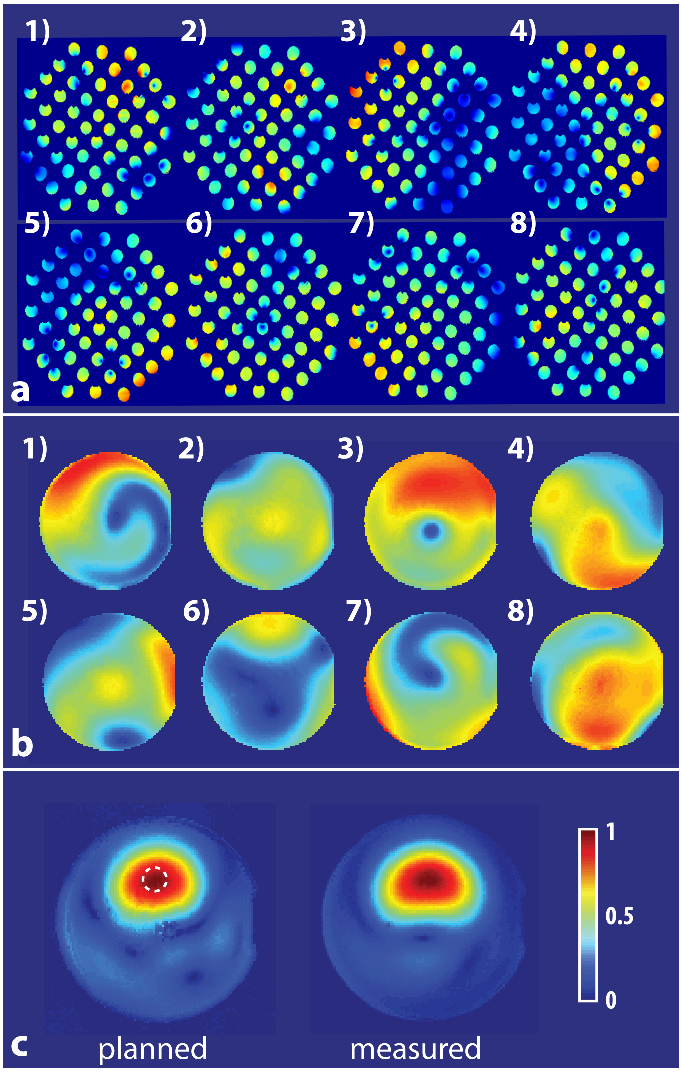

Figure 6.8: Results from multi-channel transmission. a) shows a transverse slice of the relative excitation strength inside the feed waveguide section when sending power into the port corresponding to the numbering in Fig. 6.7. The relative excitation patterns inside the cylindrical phantom are plotted in b) correspondingly to a). Basic RF shimming is demonstrated by focusing the excitation in the dashed circle based on signal intensity obtained by low flip angle, gradient echo recalled calibration scans on the presented transverse slice. Figure c) shows a comparison between the calculated image intensity and the measured one when scanning with the actual RF shim.

The relative amplitudes of the excitation produced by driving each port individually can be seen in Fig. 6.8 a) and b) in a transversal slice across the feed section and in the tissue simulating cylindrical phantom respectively. From visual inspection, it can be seen that the field patterns do not directly match to the targeted modes inside an ideal waveguide. However, it is also visible that the field patterns excited by each port are distinct from each other inside the waveguide as well as in the phantom. Especially the field patterns produced by channel 1 and 7 exhibit a very prominent swirl structure. The results from RF shimming trying to localize the excitation field within a given spot can be seen in Fig. 6.8c) in which the net intensity of the low flip angle gradient echo images are plotted.

They show a high degree of correspondence between the calculated superposition of the complex gradient echo images acquired with every individual port excited and the actually measured image with parallel excitation using all channels. The

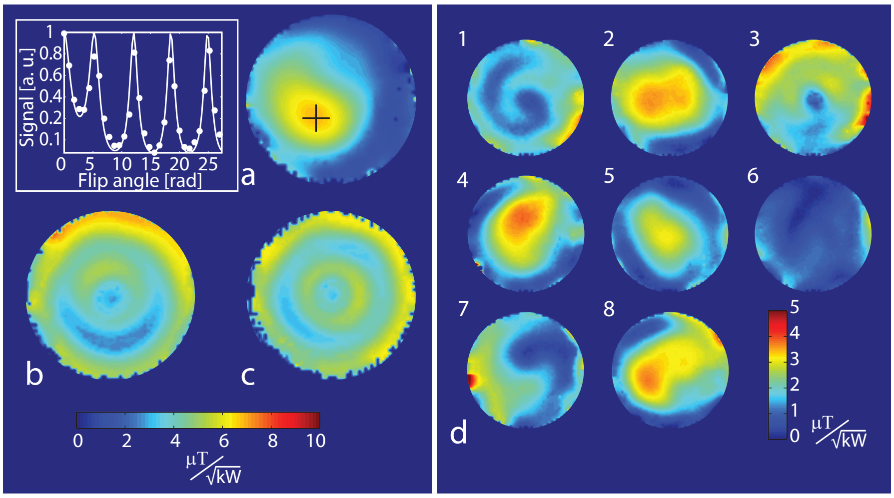

Figure 6.9: B_1^+ maps in a large cylindrical lossy phantom. Three axially evenly distributed transverse slices have been measured to cover the phantom. Image a) shows a B_1^+ map taken in the upper third of the phantom towards the feed section, b) in the middle of the phantom and c) towards the feet end of the bore. The plot on the left of a) shows the signal retrieved for the different saturation pulse flip angle (dots) in the pixel marked by the cross in a) and the fitted signal curve (solid line) showing more than 4 revolutions in nutation within 10 ms. The B_1^+ maps have been measured applying an individual RF shim for each slice. The B_1^+ maps of the 8 individual channels are shown in d) measured in the same slice as a).

B_1^+ maps acquired can be seen in Fig. 6.9. The maximum achieved field strength was $6.9\,{}^{\mu\mathrm{T}}/_{\sqrt{kW}}$ in the slice closest to the feed system corresponding to a nutation frequency of about 400 Hz when applying the maximally measured total power of 1.9 kW summed over all ports. This is also demonstrated by the plot in Fig. 6.9 showing the signal change induced by a 10 ms saturation prepulse of varying flip angle. The power of the block pulse used for this sequence was for each port below 235 W. In slice c, acquired the furthest away from the feed system, the maximum field intensity reduced to about $5.3\,{}^{\mu\mathrm{T}}/_{\sqrt{kW}}$ not considering all points that are further away from the center axis than two third of the cylinder's radius. The B_1^+ maps of the individual channels (Fig. 6.9 d) show distinct field patterns similarly to Fig. 6.8 b) with a peak value of $3.9\,{}^{\mu\mathrm{T}}/_{\sqrt{kW}}$ in channel 4.

Parallel imaging

The individual receive sensitivities of each channel measured in the waveguide feed section and in the cylindrical phantom can be seen in Fig. 6.10 a and b. Analogously to the transmit sensitivities, also the receive sensitivities do not show a one to one correspondence to the principal modes of the waveguide either in the waveguide feed section or in the phantom. However, the field patterns exhibit high geometrical diversity. This is in line with the good parallel imaging performance; the g-factor maps in Fig. 6.10 c show that even for rather high acceleration factors up to 3, the maximum g-factor stays below 3 and exhibit moderate further increase towards even higher acceleration.

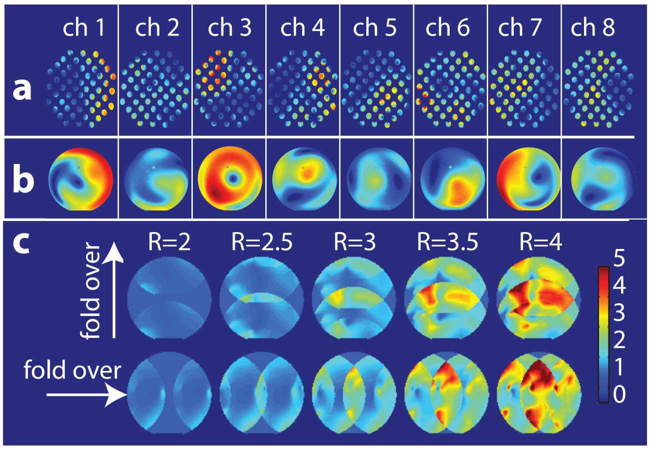

Figure 6.10: Parallel imaging performance. The relative receive sensitivities of each port as numbered in Fig. 6.7 inside the feed section are plotted in a). b) shows the corresponding sensitivities on a transverse slice through the cylindrical phantom. The g-factor maps obtained for 2D Cartesian SENSE with reduction factor R along the given fold-over direction are shown in c).

A similar result can be seen for the central transverse slice taken from a watermelon. The receive sensitivities measured (see Fig. 6.11 a) exhibit a distinct pattern for each port. The combined image of all receive channels acquired with an RF shim targeted for uniformity is depicted in Fig. 6.11 b, showing good SNR and contrast over the entire slice. Note that the center brightening is most probably caused by strong local signal enhancements in the melon. This assumption is supported by the caustic pattern of this brightening and similarly bright spots outside the central region and in the skin of the melon. RF non-uniformities, being usually very smoothly varying over space, are therefore an improbable cause for these bright pixels. The accelerated images shown in Fig. 6.11 c exhibit a tolerable noise enhancement for moderate acceleration factors of 2.5. Most artifacts induced by the acceleration occur at the boundaries of the areas with strong signal voids induced by the air filled cavities in the melon. These problems are therefore attributed to the determination of the coil sensitivities that needed to be extrapolated over these boundaries. In the image calculated from a highly reduced data set with a reduction factor of 4, shown in Fig. 6.11 d, regions with stronger noise

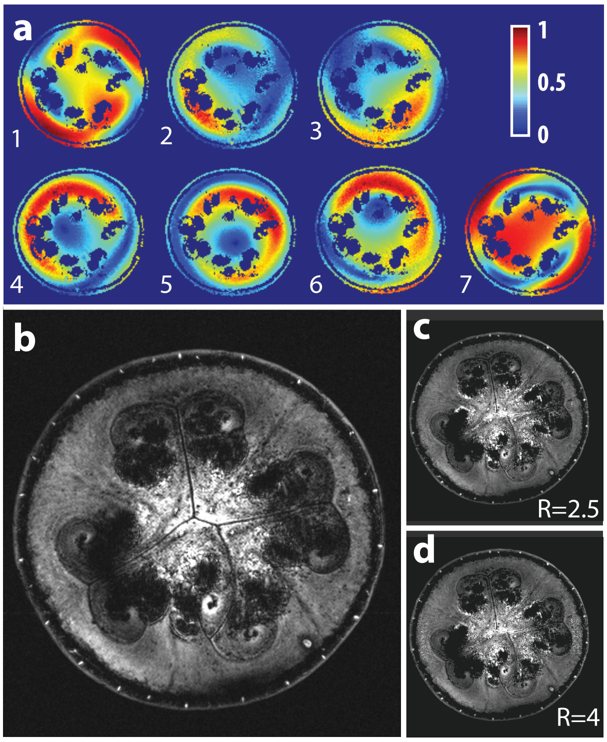

Figure 6.11: Parallel transmission and imaging on an in-vivo like sample. In a) the relative receive sensitivities of all ports driven by stubs only (therefore channel 8 was excluded) were calculated based on low flip angle gradient echo recalled calibration scans. Based on the same data an RF shim targeting a uniform excitation throughout the slice was calculated and measured as shown in b). Please notice, that the strong brightening in the center of the image is probably mostly based on a signal enhancement inside the sample due to its very caustic appearance. Corresponding SENSE accelerated images calculated based on b) are shown in c) and d) for different acceleration factors.

enhancement emanating from the unfolding process become visible. The most affected regions are found at the image center as well as close to the surface on the left and on the right side of the image.

The upper half of Fig. 6.12 shows the dielectric distribution inside the feed section used to study the dependence of the parallel imaging performance on the number of modes supported in the feed waveguide section. The number of propagating modes, i.e. modes that have a cut-off frequency below 298 MHz, was determined in the simulations to drop from 17 for the 52 rod configuration, to 13 modes for 36 rods, 10 modes for 24 rods and still 5 modes using only 12 rods in the bore. In line with the theoretical estimation (Table 1), the empty feed waveguide was not found to be able to carry any propagating RF waves at the NMR frequency. This was experimentally confirmed by the fact that no matching of any channel could be achieved as well as no quantifiable NMR signal could be acquired with this configuration. Fig. 6.13 shows the resulting matching, coupling and noise correlations among the individual channels for the four different dielectric insert configurations with 12 to 52 rods. The values of the matching and coupling stay within a comparable range for all situations and result in a similar over all noise correlation. However, the parallel imaging performance shows significant differences. At low acceleration factors ($R < 4$), astonishingly the configuration with

Table 6.1: Overview of the propagating modes in the feed waveguide. The cutoff frequencies are compared for the case of the empty waveguide and for the structured dielectric insert. This yielded the effective ϵ for each mode. Furthermore, the longitudinal wavelength of each mode is denoted.

fundamental mode	target port	f emtpy [MHz]	f filled [MHz]	effective ϵ	λ filled [m]
TM_{01}	8	411	85	23.4	1.04
TM_{11}	2, 4	645	136	23.1	1.13
TM_{21}	5, 6	876	187	21.9	1.29
TM_{02}	3	942	193	23.8	1.32
TM_{31}		1089	225	23.4	1.53
TE_{11}	1 ,7	314	246	1.6	1.78
TM_{12}		1196	248	23.3	1.81
TM_{41}		1293	266	23.6	2.23
$TM_{22}(1)$		1435	284	25.5	3.32
TM_{03}		1476	291	25.7	4.67
$TM_{22}(2)$		1435	297	23.3	12.29

12 rods shows the lowest mean g-factor and also one of the lowest maximum values over the slice chosen (see Fig. 6.12). However, for higher acceleration factors, the g-factor shows a strong increase beyond a certain reduction factor. The arrows correspondingly colored to the traces mark this critical point. It can be seen that the critical reduction factor is the higher of number of propagating modes in the feed waveguide was. Going along with this, the g-factor of the waveguide section carrying 17 modes is the lowest starting from a reduction factor of 4.5.

6.2.5 Discussion & Conclusion

The current implementation of a multi-channel transmit and receive travelling wave system showed that remote excitation and detection of NMR with significantly distinct sensitivity patterns is feasible. The setup proved to have high tolerance to high incident RF power because the feed structure itself did not contain any fixed or tunable lumped elements such as capacitors. Furthermore, variable-loading situations had a minor influence on the tuning and matching of the setup because the structure itself provided larger bandwidth than usually employed narrow band matching networks. Compared to close coupling array structures no conductors or lumped elements were present in the patient section of the bore. This reduces the risk of high local electric fields eminating from them penetrating the sample and generating high local power deposition.

The chosen structured high dielectric insert showed the advantages of lower cost and weight compared to a homogeneous dielectric filling with lower microscopic permittivity but equivalent effectiveness. Experiments showed, that even a minor amount of dielectric filling of only 12 water filled rods provides significant spatial diversity among the ports. Moreover, the structuring made selectively more transverse magnetic modes available for excitation and reception by lowering their cut-off frequencies below the NMR frequency. This finding reflects that the effective permittivity is much higher for the TM modes (ϵ_{TM}) than for the TE modes (ϵ_{TE}). The effective dielectric constants among the TM and among the TE modes is found to be each reasonably constant as shown by Table 1. Since the electric fields of the TM modes are longitudinal and those of TE modes are transverse at cutoff, they can be considered to span the main axes of the anisotropic effective permittivity tensor ϵ with the eigenvalues given by the effective permittivity of the corresponding mode:

$$\epsilon = \begin{pmatrix} \epsilon_{TE} & 0 & 0 \\ 0 & \epsilon_{TE} & 0 \\ 0 & 0 & \epsilon_{TM} \end{pmatrix}. \tag{6.4}$$

Interestingly, the permittivity acting on the longitudinal field components (ϵ_{TM}) correspond very well to the average volume permittivity in the waveguide ($\epsilon = 23$). The permittivity seen by the net transverse field (ϵ_{TE}) can be approximately explained by the Maxwell-Garnett formula [25, 26] yielding $\epsilon = 1.7$. The equality of the effective material parameters of the resulting from the simulation and from the Maxwell-Garnett equation shows that such a dielectric insert can be described as a mesoscopic material filling the waveguide. This description delivers usable approximations of the propagation properties of the modes inside the waveguide without calculating the actual microscopic field distribution in the structured material. It is predicted by the Maxwell-Garnett formula, that the macroscopic permittivity of such a material is rather low up to very high filling fractions of the high dielectric material, mainly because of the polarization of the dielectric inclusions shielding most of the high dielectric bulk material against the external field. According to these findings, the net transverse permittivity of the dielectric insert can be increased by either increasing the permittivity of the dielectric or increasing its volume fraction but interestingly also by inverting the distribution of the dielectric permittivity, i.e. filling the small PMMA tubes with air and the rest of the volume in the waveguide with water. This would generate according to Maxwell-Garnett, a very high net transverse permittivity (ϵ_{TE}) almost as high as volume average permittivity yielding ϵ_{TM}. In such a setup it would therefore be expected, that the TE modes would lower their cut-off frequency similar to the TM modes.

Although the targeted modes of the basic modal structure of a circular waveguide could not each be fed with a high selectivity, the achieved spatial diversity between the individual ports was demonstrated to be high enough for basic RF shimming operation such as for targeted spatial excitation as well as for rendering the flip angle highly uniform across larger objects such as the water melon shown in Fig. 6.11. The low selectivity of the feed structure with regards to the basic modes of an ideal circular waveguide has possibly three main reasons: First, the exciters were designed for simple fabrication and matching and not to explicitly suppress the coupling into other modes, but to efficiently couple to the targeted mode. Second, it is expected that the modal structure inside a waveguide filled by such a rather coarsely structured dielectric as implemented here - the diameter of the PMMA tubes corresponds to one quarter of the free wavelength in the dielectric - differs rather strongly from the ideal mode patterns of the uniform waveguide. Especially in the case of a close proximity of the individual rods, the resulting field distribution is strongly dominated by the mesoscopic field structure. And third, the size of the feeding stubs and loops were chosen for best matching to the impedance of the feed line when inserted in the structured waveguide. While this approach renders the before mentioned advantage that no additional matching network is needed, the resulting stubs become rather long. This is expected to increase the coupling among the stubs as well as decreasing the geometrical decoupling to the modes that are not targeted because of the metallic surfaces of the exciters disturbing the field pattern of the modes. Of course, a finer structuring and using shorter feed stubs is expected to increase the selectiveness of the ports into their particular mode. Nevertheless, it has to be pointed out, that mode selectivity as such is not the ultimate goal for the application to parallel MRI, but the ability to excite and receive highly distinct sensitivity distribution by each port with independent noise contributions.

By using several modes of a waveguide in order to RF shim the transverse field distribution it must be considered that each of the contributing modes can have a different axial wavelength. On the upside, this potentially provides the possibility for axial RF encoding from a single ended travelling wave system. On the potential downside, neglecting losses and reflections, each single mode propagating in the waveguide would produce an axially uniform excitation, but the superposition of two or more non degenerated modes would not. This would prevent an algorithm calculating an RF shim from choosing modes with different longitudinal wavelengths for volumes with an axial extent of comparable size of the resulting interference modulation between the two modes. However, for the application in current MRI systems this problem is very moderate; the wavenumber of the resulting envelope modulation is given by twice the difference of the longitudinal wavenumbers of the superimposing basic modes. For the modes targeted with the current feed section the shortest modulation wavelength resulting (superposing TM_{01} and TE_{11}) in a distance between the nulls of about $2.7\,\mathrm{m}$, which is much longer than the usable range of current high field magnets and gradient coils. Furthermore, attenuation and reflection induced RF field non-uniformities will probably be more dominant.

Although the baseline SNR of RF detectors with such a high coverage is probably too low in general to make parallel imaging acceleration useful for many applications, the explored RF encoding capability holds good prospects for parallel transmission applications such as acceleration of spatially-(spectrally) selective pulses. Nevertheless, the parallel transmission and imaging experiments showed that the basic RF encoding capability of the travelling wave setup is almost comparable to close coupling arrays if the object is electrically large and except close to its surface. The close coupling arrays offer the possibility of strongly focused excitation and reception in the quasi stationary near-field, which is beyond the resolution achieved in the far field, but for the same reason also limited to the surface of the sample. However, the RF encoding capability of the current setup could be further enhanced by either selectively coupling to more propagating modes or by feeding RF waves into the imaging area from the opposite side of the bore. The latter approach would be especially interesting for parallel imaging. As mentioned in [10, 11], each mode propagating in the waveguide modulates the received signal with an axial phase gradient depending on the axial wavelength and propagation direction. This phase gradient could readily be used for spatial encoding.

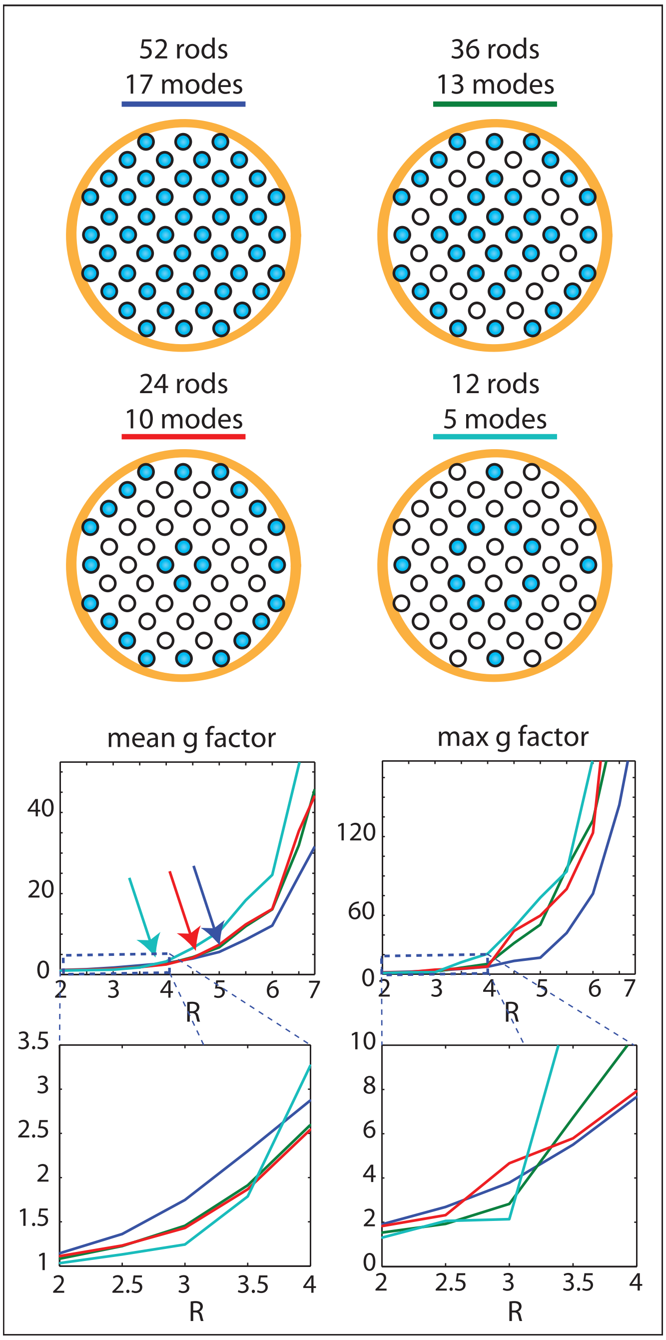

Figure 6.12: Dependence of the parallel imaging performance on the dielectric filling of the waveguide. The schematics on the top show the distribution of dielectric fillings (blue denotes that a dielectric fill was present) that have been studied and the number of modes that the waveguide should be allowed to carry according to the simulations. The lower part shows the dependence of the g-factor on the reduction factor for the different setups for a transverse slice through the cylindrical phantom as coded by the colors in the top part. The arrows show the onset of a steep increase in the curve of the g-value versus the reduction factor that can be found at higher acceleration the more modes present in the waveguide (the green and the red arrow overlap). For low g-factors however, the sparse fillings show a better performance as shown by the zoomed in plots on the bottom of the figure.

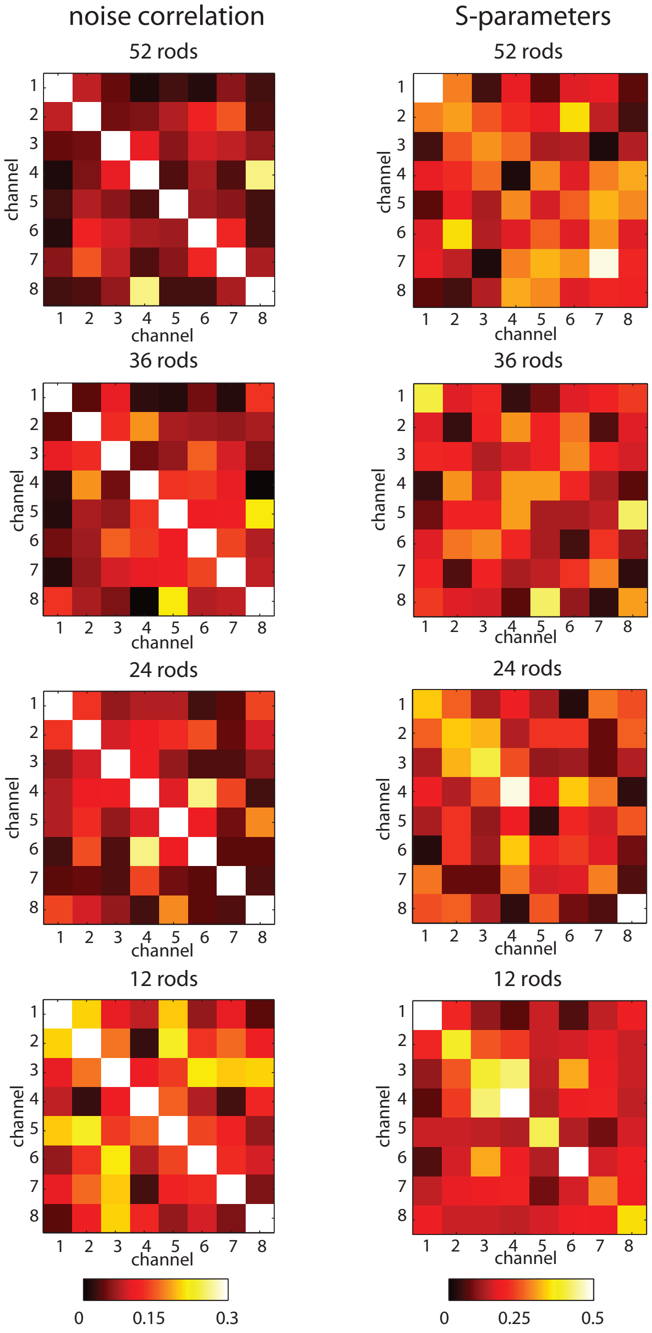

Figure 6.13: Magnitude of the noise correlation and the S-parameters found for all channels depending on the dielectric filling shown in Fig. 6.12. It can be seen that in average the noise correlation and the coupling between the channels is only slightly enhanced by the reduction of the modes inside the feed section.

Bibliography

[1] Hayes CE, Edelstein WA, Schenk JF, Mueller OM, and Eash M. An efficient, highly homogeneous radiofrequency coil for whole-body NMR imaging at 1.5 T. J Magn Reson 1985; 63:622–628.

[2] Tropp J. Theory of the birdcage resonator. J Magn Reson 1989; 82:51–62.

[3] Roemer PB, Edelstein WA, Hayes CE, Souza SP, and Mueller OM. The NMR phased array. Magn Reson Med 1990; 16(2):192–225.

[4] Vaughan JT, Hetherington HP, Otu JO, Pan JW, and Pohost GM. High frequency volume coils for clinical NMR imaging and spectroscopy. Magn Reson Med 1994; 32(2):206–218.

[5] Vaughan T, DelaBarre L, Snyder C, Tian J, Akgun C, Shrivastava D, Liu W, Olson C, Adriany G, Strupp J, Andersen P, Gopinath A, Moortele P-Fvd, Garwood M, and Ugurbil K. 9.4T human MRI: Preliminary results. Magn Reson Med 2006; 56(6):1274–1282.

[6] Atkinson IC, Renteria L, Burd H, Pliskin NH, and Thulborn KR. Safety of Human MRI at Static Fields Above the FDA 8T Guideline: Sodium Imaging at 9.4T Does Not Affect Vital Signs or Cognitive Ability. J Magn Reson Imag 2007; 26:1222–1227.

[7] Bogdanov G and Ludwig R. Coupled microstrip line transverse electromagnetic resonator model for high-field magnetic resonance imaging. Magn Reson Med 2002; 47(3):579–593.

[8] Harpen MD. Cylindrical coils near self-resonance. Magn Reson Med 1993; 30(4):489–493.

[9] Hoult DI. The principle of reciprocity in signal strength calculations: a mathematical guide. Conc Magn Reson 2000; 12:173–187.

[10] Brunner DO and Pruessmann KP. Reciprocity Relations in Travelling Wave MRI. In Proc Intl Soc Magn Reson Med 2009. p. 2943; Honolulu, Hawaii; 2009.

[11] Brunner DO and Pruessmann KP. Phase delay effects in travelling-wave MRI. In Proc ESMRMB 2009. p. 347; Antalya, Turkey; 2009.

[12] Pruessmann KP, Weiger M, Scheidegger MB, and Boesiger P. SENSE: sensitivity encoding for fast MRI. Magn Reson Med 1999; 42:952–962.

[13] Gulla AF and Budil DE. Engineering and Design Concepts for Quasioptical High-Field Electron Paramagnetic Resonance. Conc Magn Reson B 2004; 22B(1):15–36.

[14] Boyd RW. Nonlinear Optics. San Diego. Elsevier Science; 2003.

[15] Kurnit NA, Abella ID, and Hartmann SR. Observation of a Photon Echo. Phys Rev Lett 1964; 13(19):567–568.

[16] Armstrong JA, Bloembergen N, Ducuing J, and Pershan PS. Light Waves at the Boundary of Nonlinear Media. Phys Rev 1962; 128:606–622.

[17] McCall SL and Hahn EL. Self-Induced Transperancy. Phys Rev 1969; 183(2):457–490.

[18] Bock NA, Konyer NB, and Henkelman RM. Multiple-mouse MRI. Magn Reson Med 2003; 49(1):158–167.

[19] Webb AG, Collins CM, Versluis MJ, Kan HE, and Smith NB. MRI and localized proton spectroscopy in human leg muscle at 7 tesla using longitudinal traveling waves. Magnetic Resonance in Medicine 2010; 63(2):297–302.

[20] Christ A, Kainz W, Hahn E, Honegger K, Rascher W, Janka R, Bautz W, Kiefer B, Schmitt P, Hollenbach HP, Chen J, Shen JX, Neufeld E, Oberle M, and Kuster N. Development of CAD Based Anatomical Human Body Models of Two Adults and Two Children. In European BioElectromagnetics Association 2007; Bordeaux, France; 2007.

[21] Wiesinger F, Moortele P-FVd, Adriany G, Zanche ND, Ugurbil K, and Pruessmann KP. Parallel imaging performance as a function of field strength - An experimental investigation using electrodynamic scaling. Magn ResonMed 2004; 52(5):953–964.

[22] Adriany G, Van de Moortele P-F, Wiesinger F, Moeller S, Strupp JP, Andersen P, Snyder C, Zhang X, Chen W, Pruessmann KP, Boesiger P, Vaughan T, and Ugurbil K. Transmit and receive transmission line arrays for 7 Tesla parallel imaging. Magn Reson Med 2005; 53(2):434–445.

[23] Vaughan JT, Snyder CJ, DelaBarre LJ, Bolan PJ, Tian J, Bolinger L, Adriany G, Andersen P, Strupp J, and Ugurbil K. Whole-body imaging at 7T: Preliminary results. Magn Reson Med 2009; 61(1):244–248.

[24] Katscher U, Boernert P, Leussler C, and van den Brink JS. Transmit SENSE. Mag Res Med 2003; 49(1):144–150.

[25] Setsompop K, Alagappan V, Gagoski B, Witzel T, Polimeni J, Potthast A, Hebrank F, Fontius U, Schmitt F, Wald LL, and Adalsteinsson E. Slice-selective RF pulses for in vivo B1 inhomogeneity mitigation at 7 tesla using parallel RF excitation with a 16-element coil. Magn Reson Med 2008; 60(6):1422–1432.

[26] van den Berg CAT, van den Bergen B, Kamer JBVd, Raaymakers BW, Kroeze H, Bartels LW, and Lagendijk JJW. Simultaneous B_1 homogenization and specific absorption rate hotspot suppression using a magnetic resonance phased array transmit coil. Magn Reson Med 2007; 57(3):577–586.

[27] Brunner DO, Paska J, Froehlich J, and Pruessmann KP. Travelling-wave MRI: Initial results of in-vivo head imaging at 7T. In Proc Intl Soc Magn Reson Med 2009. p. 500; Honolulu, Hawaii, USA; 2009.

[28] Jackson JD. Classical Electrodynamics. New York. Wiley; 1999.

[29] Brunner DO, Zanche ND, Froehlich J, Paska J, and Pruessmann KP. Travelling wave nuclear magnetic resonance. Nature 2009; 475(7232):994–998.

[30] Pozar DM. 4.7 Excitation of waveguides - Electric and magnetic currents. In Microwave engineering second edition. John Wiley & Sons Inc.; New York; 1998.

[31] Meier PJ and Wheeler HA. Dielectric-Lined Circular Waveguide with Increased Usable Bandwidth. IEEE Trans Mircowave Theory and Techniques 1964; 12(2):171–175.

[32] Lubkowski G, Damm C, Bandlow B, Schuhmann R, Schuessler M, and Weiland T. Waveguide miniaturization using spiral resonators and dipole arrays; 2006.

[33] Hrabar S. Waveguide Experiments to Characterize Properties of SNG and DNG Metamaterials. In Nader Engheta Richard W. Ziolkowski, editor, *Metamaterials*; p. 87–111. 2006.

[34] van den Berg CAT, van den Bergen B, Bartels LW, and Lagendijk JJW. Using the natural resonant modes of the RF cavity for whole body excitation at 7 T . In ISMRM Workshop on Advances in High Field MRI 2007; Asilomar, California, USA; 2007.

[35] Maxwell Garnett JC. Colours in Metal Glasses and Metallic Films. Phil Trans R Soc Lond A 1904; 203:385–420.

[36] Wu F and Whites KW. Computation of static effective permittivity for a multiphase lattice of cylinders. Electromagnetics 2001; 21(2):97–114.

[37] Brunner DO and Pruessmann KP. B_1^+ Interferometry for the Calibration of RF Transmitter Arrays. Magn Reson Med 2009; 61(6):1480–1488.

[38] Van de Moortele P, Snyder C, DelaBarre L, Adriany G, Vaughan J, and Ugurbil K. Calibration tools for RF shim at very high field with multiple element RF coils: from ultra fast local relative phase to absolute magnitude B1+ mapping. In Proc Intl Soc Magn Reson Med 2007. p. 1676; Berlin; 2007.

[39] Nehrke K and Boernert P. Improved B1-Mapping for Multi RF Transmit Systems. In Proc. Intl Soc Magn Reson Med 2008. p. 353; Toronto; 2008.

List of Publications

[1] Brunner DO and Pruessmann KP. Enforcing strict constraints in multiple-channel RF pulse optimization. In Proc Intl Soc Mag Reson Med 2007. p. 1690; Berlin; 2007.

[2] Brunner DO, Schweizer S, and Pruessmann KP. Fast mapping of highly inhomogeneous RF fields. In Proc Intl Soc Magn Reson Med 2007. p. 353; Berlin; 2007.

[3] Brunner DO, Zanche ND, Froehlich J, Baumann D, and Pruessmann KP. A symmetrically fed microstrip coil array for 7T. In Proc Intl Soc Magn Reson Med 2007. p. 448; Berlin; 2007.

[4] DeZanche N, Brunner DO, and Pruessmann KP. An Inexpensive versatile RF power splitter, attenuator and phase-shifting system for array transmit at 7T. In Minnesota High-Field Workshop 2007. p. 87; Minnesota; 2007.

[5] Froehlich J, Baumann D, Brunner DO, Pruessmann KP, and Vahldieck R. Computational analysis and validation of coil arrays for whole-brain mr-imaging at 7 t; 2007.

[6] Brunner DO, DeZanche N, Paska J, Froehlich J, and Pruessmann KP. Traveling wave MR on a whole-body system. In Proc Intl Soc Magn Reson Med 2008. p. 434.

[7] Brunner DO and Pruessmann KP. Increasing bandwidth of spatially selective transmit SENSE pulses using constrained optimization. In Proc Intl Soc Mag Reson Med 2008. p. 635; Toronto; 2008.

[8] Brunner DO and Pruessmann KP. A Matrix Approach for Mapping Array Transmit Fields in Under a Minute. In Proc Intl Soc Magn Reson Med 2008. p. 354; Toronto; 2008.

[9] Brunner DO, Zanche ND, and Pruessmann KP. A Comparison of Matching Strategies for RF Transmission Arrays Based on Network Theory. In Proc Intl Soc Magn Reson Med 2008. p. 143; Toronto; 2008.

[10] De Zanche N, Nordmeyer-Massner JA, Brunner DO, and Pruessmann KP. Noise Correlation and Coupling Mechanisms: A Comparison of Overlapped and Non-Overlapped Surfaces Coils. In Proc Intl Soc Magn Reson Med 2008. p. 1073; Toronto; 2008.

[11] Brunner DO and Pruessmann KP. An Interferometric Approach for B1 Mapping of RF Transmitter Arrays. In Proc ESMRMB 2008. p. 94; Valencia, Spain; 2008.

[12] Brunner DO, DeZanche N, Paska J, Frohlich J, and Pruessmann KP. Travelling-wave MR: Comparison with a volume resonator at 7T. In Proc ESMRMB 2008. p. 91; Valencia; 2008.

[13] Wyss M, Brunner DO, Morel A, and Pruessmann KP. T1 contrast in the human brain at 7T. In Proc ESMRMB 2008. p. 252; Valencia; 2008.

[14] Brunner DO, Nordmeyer-Massner JA, and Pruessmann KP. Information Theory in MRI. In Proc Intl Soc Magn Reson Med 2009. p. 2978; Honolulu, Hawaii, USA; 2009.

[15] Brunner DO, Paska J, Froehlich J, and Pruessmann KP. SAR assessment of transmit arrays: Deterministic calculation of worst- and best-case performance. In Proc Intl Soc Magn Reson Med 2009. p. 4803; Honolulu, Hawaii, USA; 2009.

[16] Brunner DO, Paska J, Froehlich J, and Pruessmann KP. Travelling-wave MRI: Initial results of in-vivo head imaging at 7T. In Proc Intl Soc Magn Reson Med 2009. p. 500; Honolulu, Hawaii, USA; 2009.

[17] Brunner DO and Pruessmann KP. Reciprocity Relations in Travelling Wave MRI. In Proc Intl Soc Magn Reson Med 2009. p. 2943; Honolulu, Hawaii; 2009.

[18] Paska J, Froehlich J, Brunner DO, Pruessmann KP, and Vahldieck R. Field Superposition Method for RF Coil Design. In Proc Intl Soc Magn Reson Med 2009. p. 3038; Honolulu, Hawaii, USA; 2009.

[19] Paska J, Froehlich J, Brunner DO, Pruessmann KP, and Vahldieck R. Verification of RF EM field simulations with direct EM field measurement. In Proc ESMRMB 2009. p. 193; Antalya, Turkey; 2009.

[20] Schirra CO, Brunner D, Keupp J, Razavi R, Schaeffter T, and Kozerke S. Compressed Sensing for Highly Accelerated 3D Visualization of 19F-Catheters. In Proc Intl Soc Magn Reson Med; volume 2009 2009. p. 4405; Honolulu, Hawaii, USA; 2009.

[21] Wyss M, Brunner DO, Morel A, and Pruessmann KP. T1 contrast in the human brain at 7 Tesla. In Proc Intl Soc Magn Reson Med 2009. p. 2759; Honoulu, Hawaii, USA; 2009.

[22] Brunner DO, Paska J, Frohlich J, and Pruessmann KP. Exact calculation of the worst-case local SAR and the highest safe B_1^+ of a transmitter array. In Proc ESMRMB 2009. p. 194; Antalya, Turkey; 2009.

[23] Brunner DO, Nordmeyer-Massner JA, and Pruessmann KP. An information theory approach to array detection in MRI. In Proc ESMRMB 2009. p. 322; Antalya, Turkey; 2009.

[24] Brunner DO and Pruessmann KP. Phase delay effects in travelling-wave MRI. In Proc ESMRMB 2009. p. 347; Antalya, Turkey; 2009.

[25] Brunner DO, Zanche ND, Froehlich J, Paska J, and Pruessmann KP. Travelling wave nuclear magnetic resonance. Nature 2009; 475(7232):994–998.

[26] Brunner DO and Pruessmann KP. B_1^+ Interferometry for the Calibration of RF Transmitter Arrays. Magn Reson Med 2009; 61(6):1480–1488.

[27] Paska J, Froehlich J, Brunner DO, Pruessmann KP, and Vahldieck R. A field superposition method for rf coil design; 2009.

[28] Brunner DO, Grassberger C, and Pruessmann KP. Optimization of conductor geometries of small RF loop coils for ultra high field applications. In Proc Intl Soc Magn Reson Med 2010. p. 3814; Stockholm; 2010.

[29] Brunner DO and Pruessmann KP. SVD based calibration of transmit arrays. In Proc Intl Magn Reson Med 2010. p. 242; Stockholm, Sweden; 2010.

[30] Brunner DO, Paska J, Froehlich J, and Pruessmann KP. Travelling Wave Parallel Imaging. 2010. p. 646; Stockholm; 2010.

[31] Graesslin I, Steiding C, Annighoefer B, Weller J, Biederer S, Brunner D, Homann H, Schweser F, Katscher U, Pruessmann K, and Börnert P. Local SAR constrained Hotspot Reduction by Temporal Averaging in Parallel Transmission. In Proc Intl Soc Magn Reson Med 2010. p. 4932; Stockholm; 2010.

[32] Paska J, Brunner DO, Froehlich J, and Pruessmann KP. A travelling wave setup for parallel transmission. In Proc Intl Soc Magn Reson Med 2010. p. 3795.

[33] Pavan M, Vannesjö SJ, Barmet C, Brunner DO, and Pruessmann KP. Frequency-Division Multiplexing for Concurrent imaging and Field Monitoring. In Proc Intl Soc Magn Reson Med 2010. p. 1538.

[34] van Lier AL, Raaijmakers AJ, Brunner DO, Klomp DW, Pruessmann KP, Lagendijk JJ, and Berg CAvd. Propagating RF phase: a new contrast to detect local changes in conductivity. In Proc Intl Soc Magn Reson Med 2010. p. 2864; Stockholm; 2010.

[35] Brunner DO and Pruessmann KP. Optimal Design of Multiple-Channel RF Pulses Under Strict Power and SAR Constraints. Magn Reson Med 2010; 63(5):1280–1291.

[36] Fuchs A, Henning A, Brunner D, and Boesiger P. Compensation of Offresonance Magnetization Transfer Artifact in SPECIAL at 7T. In Proc Intl Soc Magn Reson Med 2010. p. 3383; Stockholm; 2010.

Acknowledgements

This work is the result of more than 4 years of research at the Institute for Biomedical Engineering at the University and ETH Zurich with contributions of all members of the lab. I am much obliged that I had the occasion to work in such an inspiring atmosphere and to enjoy the great spirit within this institute. I want to address my special thanks to:

Prof. Dr. Klaas P. Pruessmann for giving me the opportunity to work in his group, for his introduction into MRI, for thoroughly revising all hypotheses and manuscripts that came up and especially for his open minded and trustful guidance that is key to the productive, creative and enjoyable atmosphere in the group.

Prof. Dr. Nicola De Zanche for his introduction into radio frequency electronics, MR hardware and Engineering approaches. I gladly remember many interesting and also diverting discussions. He is always the greatest help one can rely on getting something running, 8 channel arrays and Golf IIIs.

Dr. Christoph Barmet for his help with MR reconstruction problems and many interesting discussions. Special thanks for sharing the office with me what certainly not every tidy and well organized scientific worker could manage.

Dr. Jürg Froehlich for establishing the fruitful collaboration between the MR and his group. His knowledge and help with field theoretical questions was key to many discoveries and devolvements made.

Jan Paska for his work done on the simulations which provided us insight into the complex structures of radio frequency fields.

Michael Wyss for sharing his great experience in in-vivo work and clinical applications.

Dr. Jurek Nordmeyer-Massner for many interesting and sincere discussion about more than RF and for his incredible organization and orientation skills especially in most turbulent times.

Matteo Pavan for his collaboration in the lab and his help to find the way in the gigantic jungle of semiconductors.

Dr. Bertram Wilm, Georgios Katsikatos, Maximilian Häberlin, Johnna S. Vannesjö, and Lars Kasper for inspiring collaborations in the group of Klaas Prüssmann.

Dr. Susanne Heinzer-Schweizer for her help in validation of the B_1^+ mapping. Her optimism and great enthusiasm were essential to the inspiring atmosphere in the MR group.

Dr. Anke Henning for her collaboration on the MultiX system.

The Philips Multix Team with Dr. Ingmar Grsšlin, Dr. Peter Börnert, Dr. Ullrich Katscher, Giel Mens and many others for successful and trustful collaboration about multi-channel transmission.

Dr. Roger Lüchinger and Dr. Dieter Meier for keeping the MR running and getting it running again when I finished my measurement.

Dr. Hendrik Mandelkow for many very interesting and fruitful discussions about MRI and the world a bit further away from the isocenter.

Caroline Reischauer, Robert Vorburger, Jelena Curcic for many inspiring discussions and for maintaining the most important infrastructure of the institute - the coffee corner.

All members of the IBT and IFH for many discussions and a great working atmosphere.

Dr. Nico C. A. T. van den Berg for many fruitful discussion and collaborations. Having likeminded people in the community is crucial to the development of ideas and I appreciated all the unbiased and interesting discussions.

Astrid L. H. M. W. van Lier for the interesting collaboration about the B_1^+ mapping applications.

Dr. Gregor Adriany for sharing with us his great experience about TR-arrays he collected over the years in Minnesota.

Prof. Dr. Andrew G. Webb and Prof. Dr. John M. Pauly for co-examining this work with great care and effort.

Curriculum Vitae

I was born on March 23rd, 1980 as the son of Michèle and Otto Brunner in Männedorf, Zürich, Switzerland. I've attended the Gymnasium in Wattwil receiving the matura type c (scientific and mathematical focus) in 1999. I qualified for the International Physics Olympiad in Padova as a member of the Swiss team in the same year receiving an honorable mention. From autumn 1999 I stood in an internship at TECAN AG as an application engineer in the field of micro fluidics for a year and proceeded in part time working on the development of lab automatization solutions after starting my studies of physics at the Swiss Federal Institute of Technology (ETH) in Zurich in autumn 2000. By spring 2003 I joined the mathematics group as a teaching assistant. In summer 2003, I joined the group of Prof. Dr. G. Kostorz at the Institute for Applied Physics for a semester thesis in the field of material sciences entitled *Fabrication and Characterization of a Ni-Mn-Ga Mono-Crystal*. In the line with my studies in the field of condensed matter physics, I joined the group of Prof. Dr. K. Ensslin at the Institute for Solid State Physics for a semester thesis *Magnetic Focusing in Parabolic Quantum Wells* as well as for my Diploma thesis *Local Investigation of a Quantum Point Contact Using an Atomic Force Microscope* analyzing properties of quantized charge transport in structures in the nanometer scale. I received my diploma in solid state physics from ETH in 2005 joining the same year the Institute for Biomedical Engineering at the University and ETH Zurich in the group of Prof. Dr. K. Prüssmann as a PhD student and research assistant.